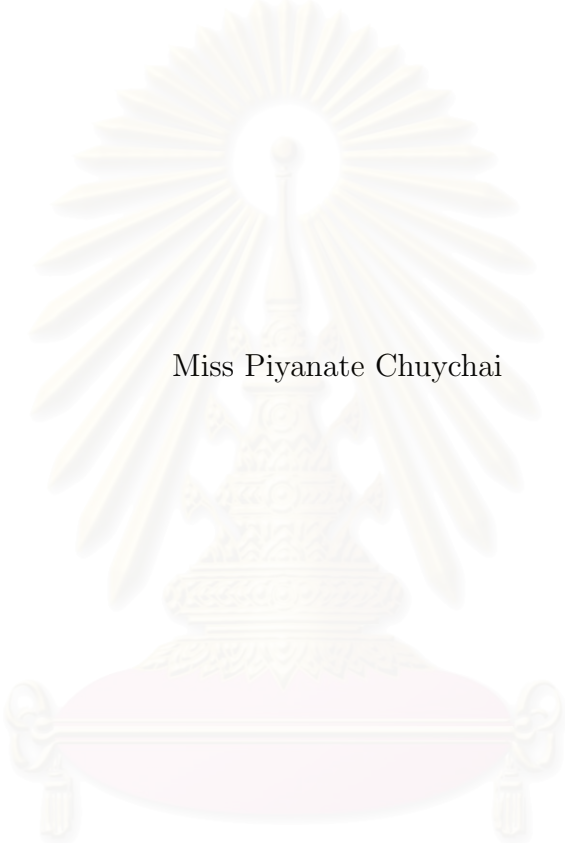


MODELS OF RANDOM MAGNETIC FIELDS AND SOME IMPLICATIONS  
FOR TURBULENCE STRUCTURE AND PARTICLE  
TRANSPORT IN THE HELIOSPHERE



Miss Piyanate Chuychai

A Dissertation Submitted in Partial Fulfillment of the Requirements

for the Degree of Doctor of Philosophy in Physics

Department of Physics

Faculty of Science

Chulalongkorn University

Academic Year 2004

ISBN 974-17-6583-5

แบบจำลองของสนามแม่เหล็กอย่างสม่ำเสมอและผลที่ตามมาเกี่ยวข้องกับโครงสร้างของ  
ความปั่นป่วนและการขนส่งอนุภาคในเฮลิโอสเฟียร์



นางสาว ปิยนตร นุชฉาย

สถาบันวิทยบริการ

วิทยานิพนธ์นี้เป็นส่วนหนึ่งของการศึกษาตามหลักสูตรปริญญาวิทยาศาสตรดุษฎีบัณฑิต

จุฬาลงกรณ์มหาวิทยาลัย

สาขาวิชาฟิสิกส์ ภาควิชาฟิสิกส์

คณะวิทยาศาสตร์ จุฬาลงกรณ์มหาวิทยาลัย

ปีการศึกษา 2547

ISBN 974-17-6583-5

ลิขสิทธิ์ของจุฬาลงกรณ์มหาวิทยาลัย

Thesis Title	MODELS OF RANDOM MAGNETIC FIELDS AND SOME IMPLICATIONS FOR TURBULENCE STRUCTURE AND PARTICLE TRANSPORT IN THE HELIOSPHERE
By	MISS PIYANATE CHUYCHAI
Field of Study	Physics
Thesis Advisor	Patcha Chatraphorn, Ph.D.
Thesis Co-advisor	Associate Professor David Ruffolo, Ph.D.
Thesis Co-advisor	Professor William H. Matthaeus, Ph.D.

---

Accepted by the Faculty of Science, Chulalongkorn University in Partial  
Fulfillment of the Requirements for the Doctor 's Degree

..... Dean of the Faculty of Science  
(Professor Piamsak Menasveta, Ph.D.)

THESIS COMMITTEE

..... Chairman  
(Ahpisit Ungkitchanukit, Ph.D.)

..... Thesis Advisor  
(Patcha Chatraphorn, Ph.D.)

..... Thesis Co-advisor  
(Associate Professor David Ruffolo, Ph.D.)

..... Thesis Co-advisor  
(Professor William H. Matthaeus, Ph.D.)

..... Member  
(Associate Professor Mayuree Natenapit, Ph.D.)

..... Member  
(Boonchoat Paosawatyanong, Ph.D.)

..... Member  
(Tanin Nutaro, Ph.D.)

นางสาวปิยนตร นุชฉาย : แบบจำลองของสนามแม่เหล็กอย่างสุ่มและผลที่ตามมาที่เกี่ยวข้องกับโครงสร้างของความปั่นป่วนและการขนส่งอนุภาคในเฮลิโอสเฟียร์. (MODELS OF RANDOM MAGNETIC FIELDS AND SOME IMPLICATIONS FOR TURBULENCE STRUCTURE AND PARTICLE TRANSPORT IN THE HELIOSPHERE) อ. ที่ปรึกษา : อ. ดร. ปัจฉา ฉัตรภรณ์, อ.ที่ปรึกษาร่วม : รศ. ดร. เดวิด รูฟโฟโล และ Prof. William H. Matthaeus 196 หน้า. ISBN 974-17-6583-5.

เราพิจารณาเส้นสนามแม่เหล็กอย่างสุ่มในแบบจำลองสององค์ประกอบของสนามแม่เหล็กปั่นป่วนซึ่งประกอบด้วยองค์ประกอบแบบสองมิติและแบบแผ่น (2D+slab) แบบจำลองนี้เป็นแบบจำลองที่เหมาะสมสำหรับสนามแม่เหล็กในใจกลางระหว่างดาวเคราะห์ เราพัฒนาทฤษฎีสำหรับการฟุ้งของเส้นสนามแม่เหล็กในสนามแม่เหล็กปั่นป่วนแบบไม่สมมาตรรอบแกนสนามแม่เหล็กเฉื่อย (non-axisymmetric turbulence) ผลเฉลยอยู่ในรูปแบบสองสมการพหุนามในสองตัวแปรและสามารถใช้ได้สำหรับขนาดความปั่นป่วนใดๆ เรายังได้ศึกษาการแยกตัวของสองเส้นสนามแม่เหล็กในสนามแม่เหล็กปั่นป่วนแบบสมมาตรรอบแกนสนามแม่เหล็กเฉื่อย (axisymmetric turbulence) เชิงวิเคราะห์ เราพบบริเวณที่มีการฟุ้งสองช่วง นั่นคือการฟุ้งแบบช้าในช่วงเริ่มแรกและการฟุ้งแบบเร็วในช่วงระยะทางไกลๆ เรายืนยันทฤษฎีที่พัฒนาขึ้นมาด้วยการจำลองเชิงตัวเลข นอกจากนี้เราอธิบายปรากฏการณ์ dropout ของการขนส่งอนุภาคพลังงานสูงที่มาจากดวงอาทิตย์ โดยใช้เส้นทางของเส้นสนามแม่เหล็กเป็นตัวแทนของศูนย์กลางการเคลื่อนที่ของอนุภาค ในงานวิจัยนี้เราเสนอแนวความคิดสถิติแบบขึ้นกับเงื่อนไขเริ่มต้น (conditional statistics) นั่นคือขึ้นกับฟังก์ชันศักย์ขององค์ประกอบสองมิติที่จุดเริ่มต้นของเส้นสนามแม่เหล็ก เราทำการจำลองซึ่งสนับสนุนความคิดนี้ ผลที่ได้แสดงว่าเส้นสนามแม่เหล็กที่เริ่มต้นบริเวณใกล้จุดโอ (O-point) ถูกกักชั่วคราวในเกาะสองมิติ ขณะที่ เส้นสนามแม่เหล็กที่เริ่มต้นบริเวณใกล้จุดเอ็กซ์ (X-point) ฟุ้งอย่างรวดเร็วออกจากเกาะสองมิติ เมื่อเรากำหนดฟังก์ชันศักย์ขององค์ประกอบสองมิติให้ง่ายขึ้นโดยใช้ฟังก์ชันเกาส์เซียน เราพบว่าสนามแบบสองมิติที่แรงทำให้การเดินสุ่มของสนามแม่เหล็กช้าลงภายในเกาะสองมิติ ซึ่งสอดคล้องกับทฤษฎี quasilinear ที่เราสร้างขึ้น งานวิจัยนี้ทำให้เราเข้าใจการขนส่งอนุภาคในเฮลิโอสเฟียร์ได้ดีขึ้น และยังสามารถนำไปประยุกต์ใช้กับระบบอื่นๆที่มีลักษณะใกล้เคียงกันได้อีกด้วย

ภาควิชา ฟิสิกส์  
สาขาวิชา ฟิสิกส์  
ปีการศึกษา 2547

ลายมือชื่อนิพนธ์.....  
ลายมือชื่ออาจารย์ที่ปรึกษา.....  
ลายมือชื่ออาจารย์ที่ปรึกษาร่วม.....  
ลายมือชื่ออาจารย์ที่ปรึกษาร่วม.....

## 4273815523 : MAJOR PHYSICS

KEY WORD: DIFFUSION / MAGNETIC FIELD / RANDOM WALK / TURBULENCE

PIYANATE CHUYCHAI : MODELS OF RANDOM MAGNETIC FIELDS AND SOME IMPLICATIONS FOR TURBULENCE STRUCTURE AND PARTICLE TRANSPORT IN THE HELIOSPHERE. THESIS ADVISOR : PATCHA CHATRAPORN, Ph.D., THESIS COADVISOR : ASSOC. PROF. DAVID RUFFOLO, Ph.D., PROF. WILLIAM H. MATTHAEUS, Ph.D., 196 pp. ISBN 974-17-6583-5.

We consider the magnetic field line random walk in the two-component model of magnetic turbulence (2D+slab), which is a reasonable model for magnetic fields in interplanetary space. We develop the theory for the diffusion of field lines in non-axisymmetric 2D+slab turbulence. The solution is in the form of non-perturbative coupled bi-quadratic equations. The separation of two adjacent field lines in 2D+slab axisymmetric turbulence has also been analytically examined in this research. We found two diffusive regimes, with slow diffusion at short distances and fast diffusion in the long distance limit. The theories have been verified by the numerical simulations. Furthermore, we also explain the dropout phenomena of solar energetic particle transport by representing the field line trajectories in 2D+slab turbulence as a guiding center motion of the particles. Here, the idea of conditional statistics is introduced, in which we propose that the field line trajectories depend on the topology of the potential function of 2D turbulence at the starting point. We perform numerical simulations, which support our idea. The results show that field lines starting near O-points are temporarily trapped within 2D islands while the field lines initially located near X-points rapidly diffuse away from 2D islands. When we simply set the 2D potential function as a Gaussian, we found that the strong 2D field can suppress the random walk of field lines inside in 2D islands and derive a quasilinear theory to explain this. This research provides a better understanding of the transport of particles in the heliosphere and can be applied to other similar systems.

Department: Physics

Student's signature.....

Field of study: Physics

Advisor's signature.....

Academic year 2004

Co-advisor's signature.....

Co-advisor's signature.....

# Acknowledgements

First of all, I wish to sincerely express my gratitude to my co-advisors, Assoc. Prof. David Ruffolo and Prof. William H. Matthaeus, for always giving me supervision and encouragement during my graduate study. I have learned a lot of physics and computer techniques from them. Without their guidance, I could not finish this work. The experience of working with them will be very useful to my future career. I am also grateful to Dr. Patcha Chatraphorn, my advisor, for her help and many suggestions.

I would like to give my gratitude to my thesis committee, Dr. Ahpisit Ungkitchanukit, Assoc. Prof. Mayuree Natenapit, Dr. Boonchoat Paosawatyanong, and Dr. Tanin Nutaro, for their comments and suggestions.

I would like to thank the Thailand Research Fund very much for giving me financial support through the Royal Golden Jubilee Fellowship for the Ph.D. program and an additional grant to build a 9-node cluster. It is really helpful to this research and it will also benefit research in this area in the future.

Much help during the work was provided by many people. I would like to thank Dr. Gang Qin, Dr. Shyamsundar Parhi, and Mr. Nimal Seenu for discussion and suggestions about physics and computer skills. For setting up the cluster, there are many people who helped and gave advice, i.e., Dr. Pablo Dmitruk, Mr. Walt Dabell, Dr. Tawun Remsungnen, Mr. Chestha Rattanapan, Mr. Paisan Tooprakai, Mr. Kittipat Malakit, and Mr. Jakapan Meechai. I want to thank people in the Space Physics and Energetic Particles Lab very much for their help and discussion. I would like to give a special thanks to Miss Khuttiya Chalapat and Miss Lugsanee Pinyo for their helps.

Finally I would like to thank my family that always supports and takes care of me, also all of my teachers who taught me good things, and my friends who were always beside me when I was discouraged.

# Contents

	page
<b>Abstract in Thai</b> .....	iv
<b>Abstract in English</b> .....	v
<b>Acknowledgements</b> .....	vi
<b>Contents</b> .....	vii
<b>List of Figures</b> .....	x
<b>List of Tables</b> .....	xxiv
<b>Chapter 1 Introduction</b> .....	1
1.1 Introduction .....	1
1.2 Objectives .....	3
1.3 Procedure and Outline .....	4
1.4 Usefulness of This Work .....	5
<b>Chapter 2 Theoretical Background</b> .....	6
2.1 Turbulence .....	6
2.2 Kolmogorov Spectrum .....	7
2.3 Solar Wind and Interplanetary Magnetic Field .....	9
2.4 The 2D+Slab Model of Magnetic Field Turbulence .....	14
2.5 Correlation Function and Power Spectrum .....	19
2.6 Correlation Length .....	21
2.7 Field Line Random Walk .....	26
<b>Chapter 3 Numerical Methods</b> .....	35
3.1 Generating Turbulent Magnetic Fields .....	35
3.2 Tracing the Magnetic Field Lines .....	44
3.3 The Diffusion Coefficients: Comparison between Numerical and Theoretical results .....	50
3.3.1 Computation of Field Line Random Walk	

# Contents (cont.)

	page
for Slab Turbulence .....	50
3.3.2 Computation of Field Line Random Walk for 2D+Slab Turbulence.....	61
<b>Chapter 4 Non-axisymmetric Field Line Random Walk .....</b>	<b>71</b>
4.1 Introduction .....	71
4.2 Analytic Theory .....	72
4.3 Interpretation.....	78
4.4 Numerical Confirmation.....	82
4.4.1 2D and Slab Spectra.....	83
4.4.2 Simulations and Results.....	85
4.5 Summary.....	92
<b>Chapter 5 Field Line Separation .....</b>	<b>94</b>
5.1 Introduction .....	94
5.2 Analytic Theory .....	100
5.3 Interpretation.....	106
5.4 Numerical Confirmation .....	116
5.5 Summary.....	122
<b>Chapter 6 Conditional Statistics .....</b>	<b>127</b>
6.1 Introduction and Observations.....	127
6.2 Explanation of Dropouts.....	131
6.3 Inhibition of Random Walk by Systematic Flows in Two Dimensions.....	140
6.3.1 Magnetic Field Model.....	140
6.3.2 Diffusion Theory .....	141



## Contents (cont.)

	page
6.3.3 Numerical Experiments.....	145
6.4 Summary.....	163
<b>Chapter 7 Conclusions .....</b>	<b>165</b>
<b>References .....</b>	<b>169</b>
<b>Appendices .....</b>	<b>177</b>
<b>Appendix A Test of Accuracy of Streamline Code     for Constant + Slab Fields .....</b>	<b>178</b>
A.1 The Equation of Motion and Analytical Solutions.....	179
A.2 Relative Error .....	181
A.3 Results and Discussion .....	181
<b>Appendix B Numerical Evaluation of Analytical     Expression for Field Line Separation .....</b>	<b>188</b>
<b>Appendix C Fitting the Data from     <i>Ulysses</i> Spacecraft .....</b>	<b>190</b>
<b>Appendix D Trajectories of Magnetic Field Lines     in Gaussian 2D Field.....</b>	<b>194</b>
<b>Vitae.....</b>	<b>196</b>

# List of Figures

Figure	Page
Figure 2.1	The spectrum of turbulence from Kolmogorov's theory ..... 10
Figure 2.2	Fast and slow solar wind observed by the Ulysses spacecraft under the solar minimum conditions. The lines are interpreted as a polar plot of solar wind speed vs. direction and the picture shows the superposition of an extreme ultraviolet view of solar magnetic field lines and coronal streamer observations at different radii. The speed of the solar wind at low latitudes was slower than at higher latitudes (McComas et al. 1998) ..... 11
Figure 2.3	The structures of the solar wind and the interplanetary magnetic field ..... 12
Figure 2.4	Schematic diagram of the structure of the current sheet. (Image credit: NRC, 2004) ..... 14
Figure 2.5	Orbit of a charged particle following a turbulent magnetic field line. The thick line is the particle trajectory and the thin line is the magnetic field line ..... 15
Figure 2.6	Illustration of the slab fluctuation, which depends only on the $z$ coordinate. The arrows demonstrate the slab fluctuation $\vec{b}^{slab}$ ..... 17

# List of Figures (cont.)

Figure	Page
Figure 2.7	18
<p>Schematic contour plot of <math>a(x, y)</math>. The solid arrows show the 2D field, <math>\vec{b}^{2D}</math>, and the dashed arrows show examples of the directions of <math>\vec{\nabla}a(x, y)</math> for both positive and negative potential functions. The 2D field must lie along the equipotential lines of the potential function. For a positive potential function, the 2D field is in a counter-clockwise direction, while a 2D field having a negative potential function is in the clockwise direction . . . . .</p>	
Figure 2.8	22
<p>The correlation function <math>R_{xx}^{slab}(z)</math> and its relationship with the correlation length <math>\ell_c</math> . . . . .</p>	
Figure 3.1	39
<p>Example of a slab power spectrum [Eq. (3.2)] . . . . .</p>	
Figure 3.2	40
<p>Contour plots of 2D turbulence and their spectra. Note that all length scales in the figures (A)-(F) are in units of <math>\ell_z</math>, which is 0.027 AU . . . . .</p>	
Figure 3.3	41
<p>Shape of the 2D spectrum for Figure 3.2(A) . . . . .</p>	
Figure 3.4	41
<p>Shape of the 2D spectrum for Figure 3.2(B) . . . . .</p>	
Figure 3.5	42
<p>Shape of the 2D spectrum for Figure 3.2(C) . . . . .</p>	
Figure 3.6	42
<p>Shape of the 2D spectrum for Figure 3.2(D) . . . . .</p>	
Figure 3.7	43
<p>Shape of the 2D spectrum for Figure 3.2(E) . . . . .</p>	
Figure 3.8	43
<p>Shape of the 2D spectrum for Figure 3.2(F) . . . . .</p>	
Figure 3.9	46
<p>Example of two trajectories of magnetic field lines in pure slab turbulence . . . . .</p>	

## List of Figures (cont.)

Figure	Page
Figure 3.10	Example of a trajectory of a magnetic field line in pure 2D turbulence.....47
Figure 3.11	Example of a magnetic field line in 2D+slab turbulence ..... 48
Figure 3.12	Diagram of steps in the field line simulations.....49
Figure 3.13	Schematic of a simulated field line. The dotted line represents the data from the simulations at each $z$ . Suppose we trace a field line over only $10d$ , where $d$ is the print out step size. We can see that the number of samples for $\Delta z = 1d$ is equal to ten while for $\Delta z = 10d$ there is only one sample for this field line ..... 52
Figure 3.14	Example of the plot between $\langle(\Delta x)^2\rangle$ of 1,000 field lines and $\Delta z$ when we set $N_z = 2^{22}$ , $L_z = 100,000\ell_z$ and $\delta b/B_0 = 0.5$ ..... 52
Figure 3.15	Illustration of the free streaming region, $\langle\Delta x^2\rangle \propto (\Delta z)^2$ , when $\Delta z \lesssim \ell_c$ ..... 53
Figure 3.16	Periodicity effect when we trace the magnetic field lines over three simulation boxes. Here, we set $N_z = 2^{22}$ , $L_z = 10,000\ell_z$ and $\delta b/B_0 = 0.5$ . We can obviously see that the relation between $\langle(\Delta x)^2\rangle$ and $\Delta z$ is not linear for large $\Delta z$ . It is back to zero every one box length. Usually we avoid this numerical artifact by using only a few percent of the box length $L_z$ ..... 53
Figure 3.17	Comparison of $D_\perp$ from theory and from numerical simulations versus $\delta b^2/B_0^2$ ..... 55

## List of Figures (cont.)

Figure	Page
Figure 3.18	Diffusion coefficients from simulations (solid lines) and expected values from discrete theory (dashed lines) for $\delta b/B_0 = 0.1$ .....56
Figure 3.19	Diffusion coefficients from simulations (solid lines) and expected values from discrete theory (dashed lines) for $\delta b/B_0 = 0.3$ .....57
Figure 3.20	Diffusion coefficients from simulations (solid lines) and expected values from discrete theory (dashed lines) for $\delta b/B_0 = 0.5$ .....58
Figure 3.21	Diffusion coefficients from simulations (solid lines) and expected values from discrete theory (dashed lines) for $\delta b/B_0 = 0.7$ .....59
Figure 3.22	Diffusion coefficients from simulations (solid lines) and expected values from discrete theory (dashed lines) for $\delta b/B_0 = 0.9$ .....60
Figure 3.23	Comparison of $D_{\perp}$ from theory and numerical simulations versus $\delta b/B_0$ , for $f_s = 0.2$ .....63
Figure 3.24	Comparison of $D_{\perp}$ from theory and numerical simulations versus $f_s$ , for $\delta b/B_0 = 0.5$ .....63
Figure 3.25	The solid lines show the diffusion coefficient from the simulations of each component and the dashed lines show the value expected from continuous theory (dashed lines) and from discrete theory (dotted lines) for $\delta b/B_0 = 0.3$ and $f_s = 0.2$ .....64
Figure 3.26	The solid lines show the diffusion coefficient from the simulations of each component and the dashed lines show the value expected from continuous theory (dashed lines) and from discrete theory (dotted lines) for $\delta b/B_0 = 0.5$ and $f_s = 0.2$ .....65

# List of Figures (cont.)

Figure	Page
Figure 3.27	66
<p>The solid lines show the diffusion coefficient from the simulations of each component and the dashed lines show the value expected from continuous theory (dashed lines) and from discrete theory (dotted lines) for <math>\delta b/B_0 = 0.9</math> and <math>f_s = 0.2</math> . . . . .</p>	
Figure 3.28	67
<p>The solid lines show the diffusion coefficient from the simulations of each component and the dashed lines show the value expected from continuous theory (dashed lines) and from discrete theory (dotted lines) for <math>\delta b/B_0 = 0.5</math> and <math>f_s = 0.5</math> . . . . .</p>	
Figure 3.29	68
<p>The solid lines show the diffusion coefficient from the simulations of each component and the dashed lines show the value expected from continuous theory (dashed lines) and from discrete theory (dotted lines) for <math>\delta b/B_0 = 0.5</math> and <math>f_s = 0.9</math> . . . . .</p>	
Figure 4.1	75
<p>Contours of constant power <math>A(k_x, k_y)</math> of the 2D potential function for the axisymmetric case and for the type of non-axisymmetric 2D turbulence we consider . . . . .</p>	
Figure 4.2	84
<p>Contours of constant power of the 2D potential function for the axisymmetric case and for the type of non-axisymmetric 2D turbulence we consider in terms of the ellipticity parameter <math>\xi</math> . . . . .</p>	

# List of Figures (cont.)

Figure	Page
Figure 4.3	Relationship between the autocorrelation $A(k_x, k_y)$ and the potential function $a(x, y)$ . The scales of the $A(k_x, k_y)$ plot indicate the number of modes in $(k_x, k_y)$ space and the contour plots of $a(x, y)$ in the right panel are only small pieces cut from the large simulation area ..... 89
Figure 4.4	Diffusion coefficients from theory and simulations for $E^{slab} : E^{2D} = 20 : 80$ when we vary only the ellipticity $\xi$ ..... 90
Figure 4.5	Diffusion coefficients from theory and simulations for $E^{slab} : E^{2D} = 80 : 20$ when we vary only the ellipticity $\xi$ ..... 91
Figure 5.1	Illustration of the magnetic field line random walk perpendicular to the mean field ( $\Delta x$ ), displacement between nearby field lines ( $X \equiv x_2 - x_1$ ), and their separation ( $\Delta X \equiv X - X_0$ ). The present work calculates the mean squared separation vs. distance along the mean field ..... 96
Figure 5.2	Schematic of two random field lines and definition of various quantities ..... 101

## List of Figures (cont.)

Figure	Page
Figure 5.3	
Schematic of the separation of field lines, i.e., the change in displacement $(X, Y)$ between two field lines for a small initial displacement $(X_0, 0)$ . a) 2D turbulence is strongly correlated only for displacements within the dashed circle, of less than a perpendicular coherence length $\ell_{\perp}$ . Panels b-d illustrate the distribution of field line displacements with increasing $\Delta z$ . b) Slow diffusive separation. c) Superdiffusive separation. d) Fast diffusive separation.....	
	102
Figure 5.4	
Examples of the field line random walk $\langle \Delta x^2 \rangle$ and separation $\langle \Delta X^2 \rangle$ as a function of $\Delta z$ , the distance along the mean magnetic field. The random walk is dominated by a) the 2D component of turbulence, b) the slab component of turbulence. Solid lines indicate diffusive behavior, dashed lines indicate superdiffusion. Dotted lines, for reference, show the extension of the long-distance behavior. Ordinates in units of $\ell_{\perp}^2$ , abscissae in units of $\ell_c$ . (See text for details) .....	
	109
Figure 5.5	
Coefficients of diffusive separation, $D_{sx}$ (thick lines) and $D_{sy}$ (thin lines), as a function of $\Delta z$ for the slab-dominated case of Figure 5.4b and various initial displacements $X_0$ , with $x$ -quantities in units of $\ell_{\perp}$ and $z$ -quantities in units of $\ell_c$ .....	
	110



## List of Figures (cont.)

Figure	Page
Figure 5.6	
Coefficients of diffusive separation derived from computer simulations, $D_{sx}$ (thick solid line) and $D_{sy}$ (thin solid line), compared with $D_{sx} = D_{sy}$ from analytic calculations (dashed line), as a function of $\Delta z$ , for a random walk dominated by the 2D component of turbulence. Here we set the total fluctuation to be $B_0^2/4$ with a 50:50 ratio of slab to 2D energies. The long-distance limit is the régime of fast diffusive separation. ....	
	118
Figure 5.7	
Coefficients of diffusive separation derived from computer simulations, $D_{sx}$ (thick solid line) and $D_{sy}$ (thin solid line), compared with $D_{sx} = D_{sy}$ from analytic calculations (dashed line), as a function of $\Delta z$ , for a random walk dominated by the 2D component of turbulence. Here we set the total fluctuation to be $B_0^2/4$ with a 20:80 ratio of slab to 2D energies. The long-distance limit is the régime of fast diffusive separation. ....	
	120
Figure 5.8	
Coefficients of diffusive separation derived from computer simulations, $D_{sx}$ (thick solid line) and $D_{sy}$ (thin solid line), compared with those from analytic calculations (thick dashed line and thin dashed line, respectively), as a function of $\Delta z$ , for a random walk dominated by the slab component of turbulence, in the régime of slow diffusive separation. ....	
	121

## List of Figures (cont.)

Figure	Page
Figure 5.9	122
<p><math>\langle R^2 \rangle</math> plot of the slab-dominated case as in Figure 5.8 (<i>thick solid line</i>). The data have the best fit with the curve (<i>dashed line</i>) <math>\langle R^2 \rangle = 9.97 \times 10^{-5} \exp(z/6.57 \times 10^5)</math>.....</p>	
Figure 6.1	129
<p><i>Left panel:</i> Two impulsive flare events observed by <i>ACE</i> spacecraft which occurred during 1999 January 9-10. a) Energy of H-Fe ions (in units of MeV/nucleon) vs. arrival time. b) The intensity was highly variable (on a log scale). c) Interplanetary magnetic field angle in the geocentric solar ecliptic (GSE) <i>x-y</i> plane. d) Interplanetary magnetic field angle normal to the GSE <i>x-y</i> plane. <i>Right panel:</i> Example event of the solar energetic particles associated with a CME and an interplanetary shock. a) Energy of oxygen ions (in units of MeV/nucleon) vs. arrival time. b) The intensity variation was not observed in this event. c) Interplanetary magnetic field angle in the GSE <i>x-y</i> plane. d) Interplanetary magnetic field angle normal to the GSE <i>x-y</i> plane. (Image credit: Mazur et al. 2000).....</p>	
Figure 6.2	130
<p>The location of <i>Ulysses</i> during during Day 250, 2000 - Day 17, 2001. (Image credit: McKibben et al. 2001) .....</p>	
Figure 6.3	130
<p>Flux of <math>\sim 30</math>-70 MeV protons vs. time observed by <i>IMP-8</i> and <i>Ulysses</i>. The axes on the top show the <i>Ulysses</i> position and connection longitude relative to that of the Earth. (Image credit: McKibben et al. 2001).....</p>	

## List of Figures (cont.)

Figure	Page
Figure 6.4	
Contour plot of the potential function for a representation of the 2D turbulence component. The magnetic field due to this component follows contours of constant potential. Field lines near O-points are trapped within topological “islands,” while field lines near X-points or outside islands rapidly travel to other locations. In the solar wind, magnetic field lines undergo an additional random walk due to the slab component of turbulence, which allows them to eventually escape from islands surrounding	
O-points .....	132
Figure 6.5	
Scatter plot of the 10,000 locations of magnetic field lines that are initially (at $z = 0$ ) located within a circle (simulating the region where particles are injected due to an impulsive solar flare). At intermediate $z$ values, field lines within islands of the 2D turbulence (around the O-points shown in Figure 6.4) remain trapped, while field lines in other regions spread rapidly. This explains the filamentary distribution of particles as indicated by dropout features. At large $z$ values all field lines diffuse rapidly, explaining the <i>Ulysses</i> and <i>IMP-8</i> observations of SEP diffusion throughout the inner solar system .....	136

## List of Figures (cont.)

Figure	Page
Figure 6.6	137
Scatter plot of the 10,000 field lines which are initially distributed uniformly through the entire simulation region. The field lines are still uniformly random over any distance. This simulation corresponds to the energetic particles from CME-driven and interplanetary shocks.....	
Figure 6.7	139
Illustration of interplanetary magnetic field lines populated with solar energetic particles (SEP) from a localized source region near the Sun, as expected for an impulsive solar flare. In the 2D+slab model of solar wind turbulence, some field lines are trapped in filaments corresponding to the small-scale topology, i.e., islands of the 2D turbulence, out to Earth orbit, while interstitial field lines spread laterally to large angular distances. This leads to the observed “core” region of SEP with dropouts and an extended “halo” region.....	
Figure 6.8	147
Orbit in the $x - y$ plane of a selected field line that lies deep in the trapping island, showing the predominantly cyclic trajectory, which gradually is transported out of the trapping region, whereupon the motion becomes highly irregular, and is an almost unconstrained random walk.....	

# List of Figures (cont.)

Figure	Page
Figure 6.9	Plot of the radial coordinate $r = \sqrt{x^2 + y^2}$ of a field line vs. the parallel coordinate. At short distances the radial position remains near its initial value $r = 15$ . After around $z = 150$ the field line breaks out of the trapping structure and random walks with a much larger amplitude. .... 148
Figure 6.10	Plot of $\langle \Delta r^2 \rangle / (2z)$ vs. $z$ , which confirms the theory at small radius, where the dashed line is the theoretical value. .... 149
Figure 6.11	$D_{rr}$ vs. $r_0$ expected from quasilinear theory ..... 150
Figure 6.12	$D_{eff}$ vs. $r_0$ as derived from Figure 6.11 by equation 6.28 ..... 150
Figure 6.13	$R'(z)$ vs. $z$ , showing how the field lines spread from starting points near the center when we set $\sigma = 10$ . .... 151
Figure 6.14	Illustration of the definitions of $r_c$ and $L_{trap}^{max}$ for $\sigma = 10$ and $\ell_z = 1$ ..... 152
Figure 6.15	Critical radius $r_c$ vs. $b_{2D}^2/B_0^2$ . The dashed line is the average value ..... 153
Figure 6.16	Critical radius $r_c$ vs. $b_{slab}^2/B_0^2$ . The dashed line is the average value ..... 154
Figure 6.17	Critical radius $r_c$ vs. $\sigma$ . The dashed line is the best linear fit to the data. .... 155
Figure 6.18	Snapshot of 10,000 field lines in Gaussian 2D field + slab turbulence at each $z$ . Here we set $\sigma = 1$ for the 2D field. .... 156

## List of Figures (cont.)

Figure		Page
Figure 6.19	Critical radius $r_c$ vs. $\ell_z$ . The dashed line is the best power-law fit .....	157
Figure 6.20	Critical radius $r_c$ vs. $\ell_z$ . The dashed line is the best logarithmic fit .....	158
Figure 6.21	$L_{trap}^{max}$ vs. $b_{2D}^2/B_0^2$ and the best power-law fit .....	159
Figure 6.22	$L_{trap}^{max}$ vs. $b_{slab}^2/B_0^2$ and the best power-law fit .....	160
Figure 6.23	$L_{trap}^{max}$ vs. $\sigma$ and the best power-law fit .....	161
Figure 6.24	$L_{trap}^{max}$ vs. $\ell_z$ and the best power-law fit .....	162
Figure A.1	Accuracy of particle orbits in a uniform magnetic field at various $r_{acc}$ .....	183
Figure A.2	Accuracy of particle orbits in a uniform magnetic and electric fields at various $r_{acc}$ .....	183
Figure A.3	Overlay of Figures A.1 (black) and A.2 (gray) .....	184
Figure A.4	Accuracy of particle orbits in a uniform magnetic field when we use $r_{acc} = 10^{-5}$ .....	184
Figure A.5	Accuracy of particle orbits in a slab magnetic field with $\delta b/B_0 = 0$ .....	185
Figure A.6	Accuracy of particle orbits in a slab magnetic field with $\delta b/B_0 = 0.001$ .....	185
Figure A.7	Accuracy of particle orbits in a slab magnetic field with $\delta b/B_0 = 0.01$ .....	186

## List of Figures (cont.)

Figure	Page
Figure A.8 Accuracy of particle orbits in a slab magnetic field with $\delta b/B_0 = 0.1$ .....	186
Figure A.9 Accuracy of particle orbits in a slab magnetic field with $\delta b/B_0 = 1.0$ .....	187
Figure A.10 Accuracy of particle orbits in a slab magnetic field at $t = 10^3$ gyroperiods and various $\delta b/B_0$ .....	187
Figure C.1 The coordinates of an Archimedean spiral magnetic field line connected to the Sun.....	191
Figure C.2 The dots shows the data from <i>Ulysses</i> on November 8-26, 2000 and the line is the function from the Reid profile that can best fit the data .....	193

# List of Tables

Table	Page
Table 3.1 Comparison between diffusion coefficients from theory and simulation .....	54
Table 3.2 Comparison between the diffusion coefficient from theory and simulations for $E_{slab} : E_{2D} = 20:80$ when we vary $\delta b/B_0$ .....	70
Table 3.3 Comparison between the diffusion coefficient from theory and simulations for $\delta b/B_0 = 0.5$ when we vary $f_s$ .....	70
Table 4.1 Discrete theory and simulation results for the diffusion coefficients and their differences when we vary $f_x$ , $\ell_{zx}$ , for $\ell_{zy}$ .....	86
Table 4.2 Comparison between numerical results and theoretical results of the diffusion coefficients for 20% slab and 80% 2D energies when $\xi$ is varied .....	87
Table 4.3 Comparison between numerical results and theoretical results of the diffusion coefficients for 80% slab and 20% 2D energies when $\xi$ is varied .....	88
Table 4.4 Discrete theory and simulation values and their differences when we vary all non-axisymmetry parameters .....	92
Table 5.1 Types of Separation of Two Magnetic Field Lines in Two-Component Turbulence .....	107



# Chapter 1

## Introduction

### 1.1 Overview

Turbulence is an interesting phenomenon that we can easily observe in nature. It also appears at the surface of the Sun and in the interplanetary medium. The atmosphere of the Sun consists of hot gas and magnetic fields. It has three layers: the photosphere is the inner layer, the chromosphere is above the photosphere, and the corona extends beyond the chromosphere into interplanetary space. The Sun's gravity cannot hold on to the outer layer since the temperature is very high (over 1,000,000 K). Therefore, a turbulent ionized gas flow called the solar wind escapes continuously from the outer layer of the Sun into the entire heliosphere, that is, the region influenced by the Sun. When the solar wind flows out from the Sun, it drags the Sun's magnetic field into interplanetary space. Thus, the interplanetary magnetic field is also turbulent. In what is called "solar activity," there are explosions at the surface that eject solar energetic particles into space, most of which are charged particles. Since these particles affect the Earth, it is important to understand their transport from the Sun into space.

One aspect of that problem that has received substantial interest in astrophysics is the diffusion or transport of charged particles perpendicular to the magnetic field. From fundamental physics, we know that charged particles move around the magnetic field in helical orbits, so to a good approximation their guiding centers follow the traces of magnetic field lines. Therefore, another way

to study the transport of the particles is to aim to understand the diffusion or transport of random magnetic field lines in space, which is a primary influence on the direction of the particle motion.

There are many open issues about the random walk of magnetic field lines in interplanetary space. The first calculation of the random walk of the magnetic field lines in magnetic turbulence was presented by Jokipii (1966) and Jokipii & Parker (1968), who considered fluctuations that depend only on the distance along the mean field. A classic quasilinear calculation (Jokipii 1966) shows that the field line random walk is associated with the Fourier power at “zero wave number” of the turbulence and yields a simple expression for a diffusion coefficient proportional to the product of the energy density in the fluctuations and the correlation scale. There is also evidence that the behavior of the particle distribution can be better understood if we know the separation rate of the random field lines (Jokipii 1973). There are spacecraft observations from solar events (Mazur et al. 2000) showing that the intensity of solar energetic particles repeatedly disappears and reappears, events referred to as dropouts. The released particles follow neighboring field lines still trapped in the same flux tube up to and beyond a mean distance of 1 AU (the astronomical unit, AU, is defined as the distance from the Sun to the Earth). Some scientists believed that dropouts would be related to the rate of field line separation.

Over the past decade, understanding of the solar wind has improved (Matthaeus et al. 1990; Bieber et al. 1994). A useful model for solar wind turbulence is the two-component model that consists of a slab component that depends only on the distance along the mean field and a two-dimensional (2D) component that depends only on the two transverse directions (Bieber, Wanner, & Matthaeus

1996). The diffusion theory for the field line random walk in this 2D+slab model was developed by Matthaeus et al. (1995). They presented a calculation with a nonperturbative statistical approach to the diffusion coefficient of the field line random walk in axisymmetric magnetic field turbulence, representing diffusion of magnetic field lines in the directions perpendicular to the mean field. Those theoretical results were confirmed by numerical simulation (Gray et al. 1996).

In this dissertation, we use the 2D+slab model of magnetic field turbulence to find the diffusion coefficients of separation between two field lines in axisymmetric turbulence and the field line random walk in non-axisymmetric turbulence. We also study the trajectories of field lines in relation to the dropout events and find the conditional statistics for the trapping and escape of the field lines. Furthermore, a simple model of a 2D field plus a random slab field has been used to understand the more complex turbulent system.

## 1.2 Objectives

The objectives of this work are:

1. To analytically derive the diffusion coefficients for the non-axisymmetric field line random walk and axisymmetric field line separation in 2D+slab turbulence.
2. To numerically simulate 2D+slab field lines and calculate the diffusion coefficients for the field line random walk and field line separation.
3. To verify the analytical formulae with simulations.
4. To examine conditional statistics and trajectories of turbulent magnetic fields in space.

### 1.3 Procedure and Outline

In the theoretical work, we consider the magnetic field to be composed of a mean field and transverse fluctuations. We use the relations between the magnetic field line and the magnetic field to examine the diffusion coefficients along the transverse ( $x$  and  $y$ ) directions. We assume that the magnetic field is statistically homogeneous. We also assume the validity of the diffusion approximation and Corrsin's dependence hypothesis. In the numerical work, we generate many different random magnetic fields in wavenumber ( $k$ ) space and use Fourier transforms to transform them back into real space. In order to obtain the positions of the streamlines, we solve the field line differential equation by a numerical method. Next, we examine the statistics of field lines, in order to calculate the diffusion coefficients. After that, we compare analytical and simulation results. Finally, the results of the analysis will be discussed in the context of relevant spacecraft observations.

This dissertation is divided into seven chapters. An overview, review of previous work, objectives and usefulness of this work are introduced in the first chapter. Since we perform both theoretical and numerical work, we first present the theoretical background such as the properties of turbulent magnetic fields, a model of such fields, and the previous theory of the field line random walk in Chapter 2. Then the numerical methods that we use to trace the field lines and to analyze the data are described in the following chapter. We derive the random walk theory for non-axisymmetric turbulence and confirm its solutions by simulations, the details of which appear in Chapter 4. In Chapter 5, the theory of the separation of two adjacent field lines for axisymmetric 2D+slab turbulence is developed and confirmed by the computer simulations. Furthermore, the expla-

nation and the simulations of the dropout observations are shown in Chapter 6, leading us to study the inhibition of the random walk by systematic and turbulent flows. Finally, we conclude all of the work in the last chapter.

## 1.4 Usefulness of This Work

The developed theories and the simulation techniques can be applied to special cases of interest in the heliospheric transport of charged particles, such as dropouts of solar energetic particles, the solar modulation of cosmic rays, and particle acceleration at nearly perpendicular shocks. This research will also provide a better understanding of the transport of particles in the heliosphere.



# Chapter 2

## Theoretical Background

The essential basic knowledge that is useful in this work is presented in this chapter. We first describe the characteristics of turbulence and the spectrum of the turbulent motion. Since, in this dissertation, we focus on the turbulent magnetic field in space, then we briefly talk about the solar wind and interplanetary magnetic field in space. The model of the turbulent magnetic field that we use in our work is introduced in the next section. The system that we consider is random, so some statistic properties and some important length scales have been also discussed. The goal of this work is to study the random walk of the turbulent magnetic field lines; therefore, the methods of derivation of the diffusion coefficients of field lines are shown in the last section.

### 2.1 Turbulence

Turbulence is one type of fluid flow which is easily observed in everyday life such as the clouds in the sky, the water from the tap, the jet from the aircraft and the smoke from the cigarette. It is not only on the Earth that turbulent flows are found; the flows of plasma in stellar atmospheres and media between planets and stars are also turbulent. Since turbulent flow is random and irregular, we cannot exactly predict the motion of turbulence. We can only describe the statistics and the mean properties. However, it is not enough to say that the flow is turbulent if it has only randomness. Another important characteristic of turbulence is diffusivity which causes rapid mixing and increased rates of momentum, heat and mass transfer, much more effectively than molecular diffusion

and laminar flow. Turbulence always occurs at high Reynolds number, defined by  $Re \equiv UL/\nu$ , where  $U$  and  $L$  are characteristic velocity and length scales of the flow and  $\nu$  is the kinematic viscosity of the fluid. Although turbulence is powerful for transferring energy and increasing the rate of momentum transfer, it is always dissipative due to the viscosity of the fluid. Turbulence rapidly decays if no energy input is continuously maintained to the system. Therefore, the energy supply is necessary for the existence of turbulence. Three-dimensional vorticity fluctuations are also needed for turbulent flow. This means the flow must be rotational and three dimensional. Without these characteristics, the flow cannot transfer energy from the largest eddies to smallest eddies because of the absence of vortex stretching.

## 2.2 Kolmogorov Spectrum

The concept of an energy cascade from the largest scales to smallest scales in the turbulent flow was first introduced by Richardson (1922). The idea is that the energy is fed into the turbulence at the largest scales of motion. This energy is transferred to smaller and smaller scales until the smallest ones, and then the energy is dissipated due to the viscosity of the fluid. Suppose that we consider the eddies associated with the length scale  $\ell$  and velocity  $u$ . The time scale of these eddies is  $\ell/u$ . Since the energy is in the order of  $u^2$ , the rate of energy transfer (or dissipation rate) per unit mass  $\epsilon$  is of order  $u^3/\ell$ . For the largest scale, the length scale  $\ell_0$  and the velocity scale  $u_0$  are relevant to the characteristic size and velocity scale of the turbulent flow and they are independent of the viscosity. These are called “outer scales.” The idea of the energy cascade has been again considered and greatly developed by Kolmogorov

(1941a). He hypothesized that the small scales are statistically isotropic even though the large scales are anisotropic due to the boundary condition of the flow and the smallest scales depend only on two parameters, which are the dissipation rate  $\epsilon$  and the viscosity  $\nu$ . Therefore, from these hypotheses, the only forms for the smallest length, time, and velocity scales are  $\eta \equiv (\nu^3/\epsilon)^{1/4}$ ,  $\tau \equiv (\nu/\epsilon)^{1/2}$ , and  $v \equiv (\nu\epsilon)^{1/4}$  respectively. These smallest scales in turbulence are well known as the “Kolmogorov microscales” or “inner scales.” They are the smallest scales before the energy is dissipated by the viscosity. One easy way to derive these forms of the smallest scales is by using dimensional analysis. For instance, from Kolmogorov’s hypothesis we can write  $\eta = \nu^n \epsilon^m$ , where  $n$  and  $m$  are possibly fractional powers, which we do not know yet, and we already know the units of  $\nu$ , which are  $[L]^2/[T]$ , and  $\epsilon$ , which are  $[L]^2/[T]^3$ . (Note that  $[L]$  and  $[T]$  stand for the units of length and time, respectively.) Considering the units on both left and right hand sides,  $[L] = ([L]^2/[T])^n ([L]^2/[T]^3)^m$ . If we compare the powers of the units in the both sides, the equation is true when  $1 = 2n + 2m$  and  $0 = n + 3m$ . Finally we obtain  $n = 3/4$  and  $m = -1/4$ , which is the same as the form that Kolmogorov got for the smallest length scale. We can also use a similar process to get the smallest time and velocity scales.

Another important hypothesis for turbulence given by Kolmogorov is that in every turbulent flow the statistics of the motion of scale  $\ell$  in the range  $\ell_0 \gg \ell \gg \eta$ , called the “inertial range”, have a universal form, which can be only determined by  $\epsilon$  and does not depend on  $\nu$ . For the range of smaller scales than the inertial range, in which the viscosity affects the motion, we call this range the “dissipation range.”



Now we consider the spectrum in the inertial range. Usually we can write

$$\bar{u}^2 = \int_0^{\infty} S(k) dk, \quad (2.1)$$

where  $S(k)$  is the wave number spectrum and  $k$  is magnitude of the wave vector (here we assume that the turbulence is isotropic so the spectrum depends on the magnitude  $k$  only). Kolmogorov said that the spectrum in the initial range should depend on  $\epsilon$  and, of course, on  $k$ . Thus, from dimensional analysis, it is found that

$$S(k) \propto \epsilon^{2/3} k^{-5/3}, \quad (2.2)$$

where  $\ell_0^{-1} \ll k \ll \eta^{-1}$ . Then the spectrum of turbulence looks like that in Figure 2.1. This relation is universal for all turbulence and has been known as “Kolmogorov’s  $k^{-5/3}$  law.” We call a spectrum of turbulence that obeys this theory a “Kolmogorov spectrum.” Kolmogorov’s theory has been confirmed by many laboratory experiments and observations of turbulence in the oceans and atmosphere. The  $k^{-5/3}$  law is easily observed for phenomena at large Reynolds number because they have a wide inertial range.

## 2.3 Solar Wind and Interplanetary Magnetic Field

The solar wind is an ionized gas, or plasma, continuously flowing out from the Sun in all directions. The solar wind is not uniform but is rather a turbulent flow, since the Sun is active and always supplies the energy to the solar wind. It is composed of protons, electrons, and minor ions such as helium, carbon, nitrogen, and oxygen ions. The region where the solar wind originates is the corona, the outer atmosphere of the Sun. Because the temperature of the corona is very high and the Sun’s gravity cannot hold on to it, the material from the corona expands

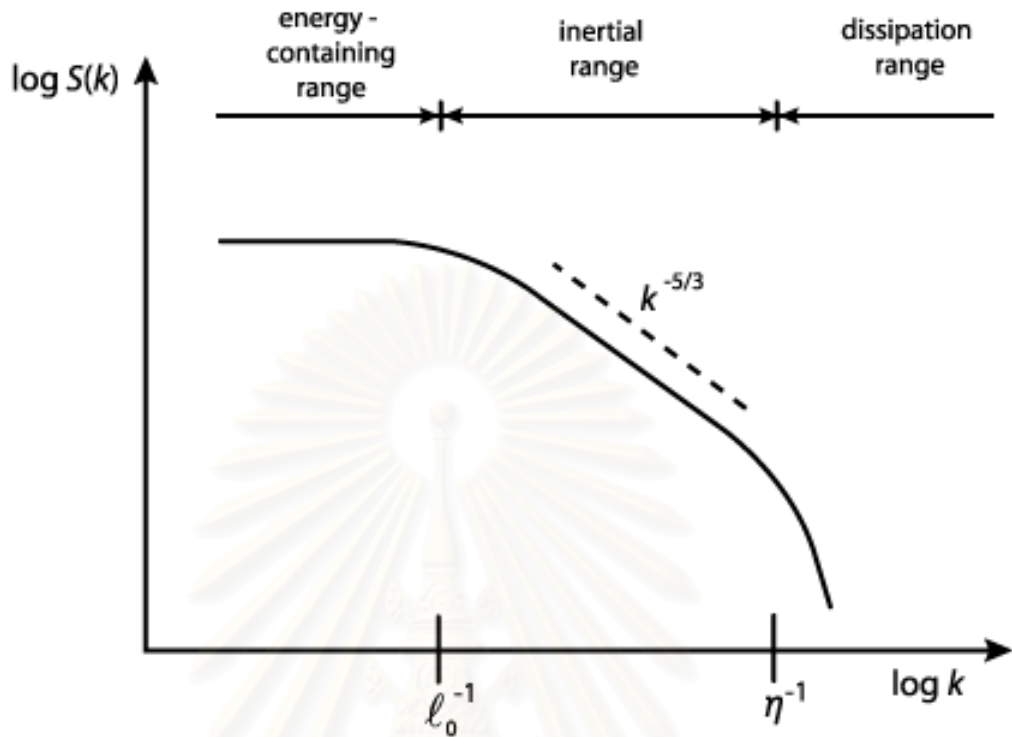


Figure 2.1: The spectrum of turbulence from Kolmogorov's theory.

into interplanetary space. However, the speed of the solar wind is not the same in all directions, as shown in Figure 2.2. The speed of the solar wind from the region where we observe coronal streamers and coronal loops, typically near the Sun's equator, is slower than from the regions with nearly radial magnetic fields, called coronal holes. For the slow wind, the speed is approximately 400 km/s near the Earth and the wind is highly variable, while the fast wind is at about 800 km/s and not highly variable. The solar wind expands through the entire solar system; therefore, its speed and density decrease when the distance from the Sun increases. The speed of the solar wind slows down slightly as it moves away from the Sun until it is terminated at the end of the solar system, where

the solar wind impacts the interstellar wind.

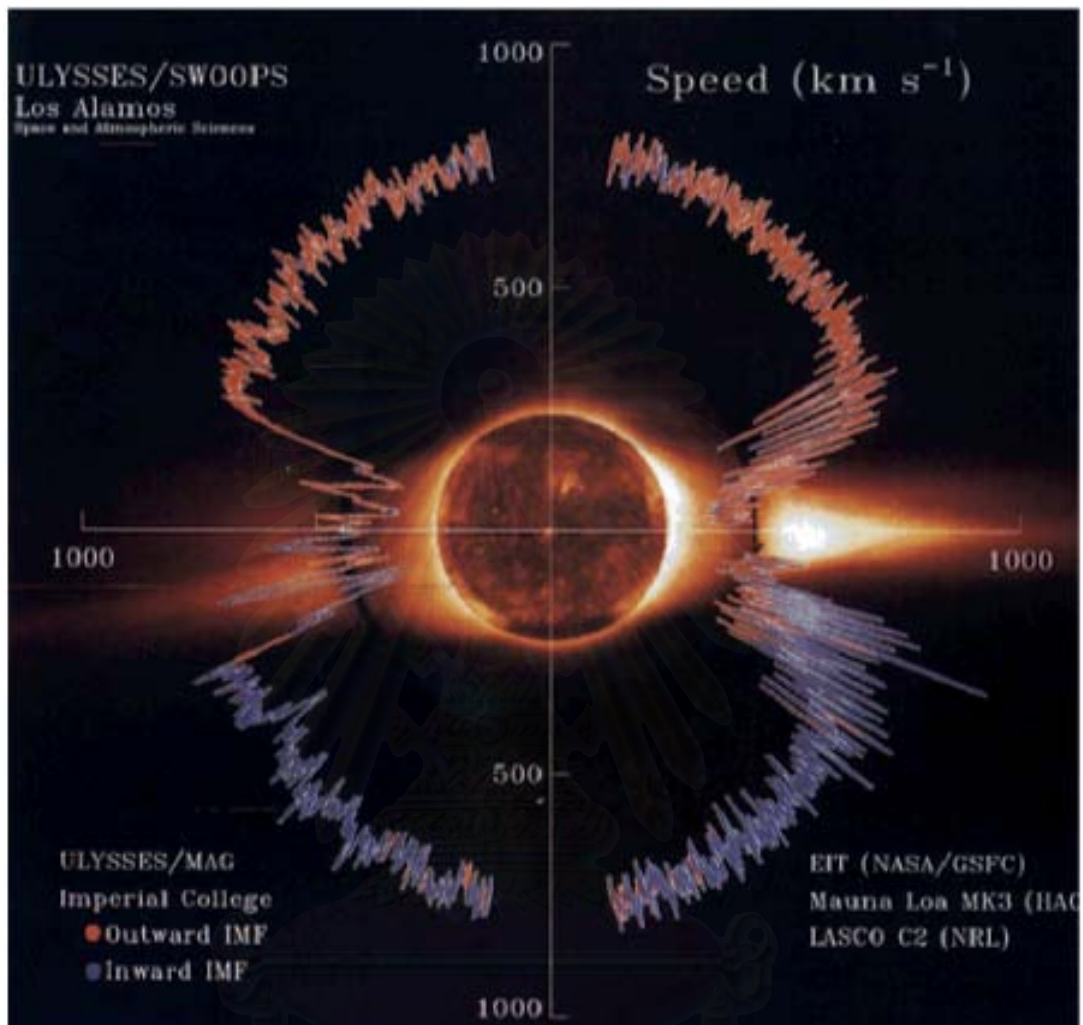


Figure 2.2: Fast and slow solar wind observed by the Ulysses spacecraft under the solar minimum conditions. The lines are interpreted as a polar plot of solar wind speed vs. direction and the picture shows the superposition of an extreme ultraviolet view of solar magnetic field lines and coronal streamer observations at different radii. The speed of the solar wind at low latitudes was slower than at higher latitudes (McComas et al. 1998).

The plasma that emanates with the solar wind also carries out the magnetic field from the Sun, then called the “interplanetary magnetic field (IMF).” Since the magnetic field is frozen in the solar wind everywhere in the solar system,

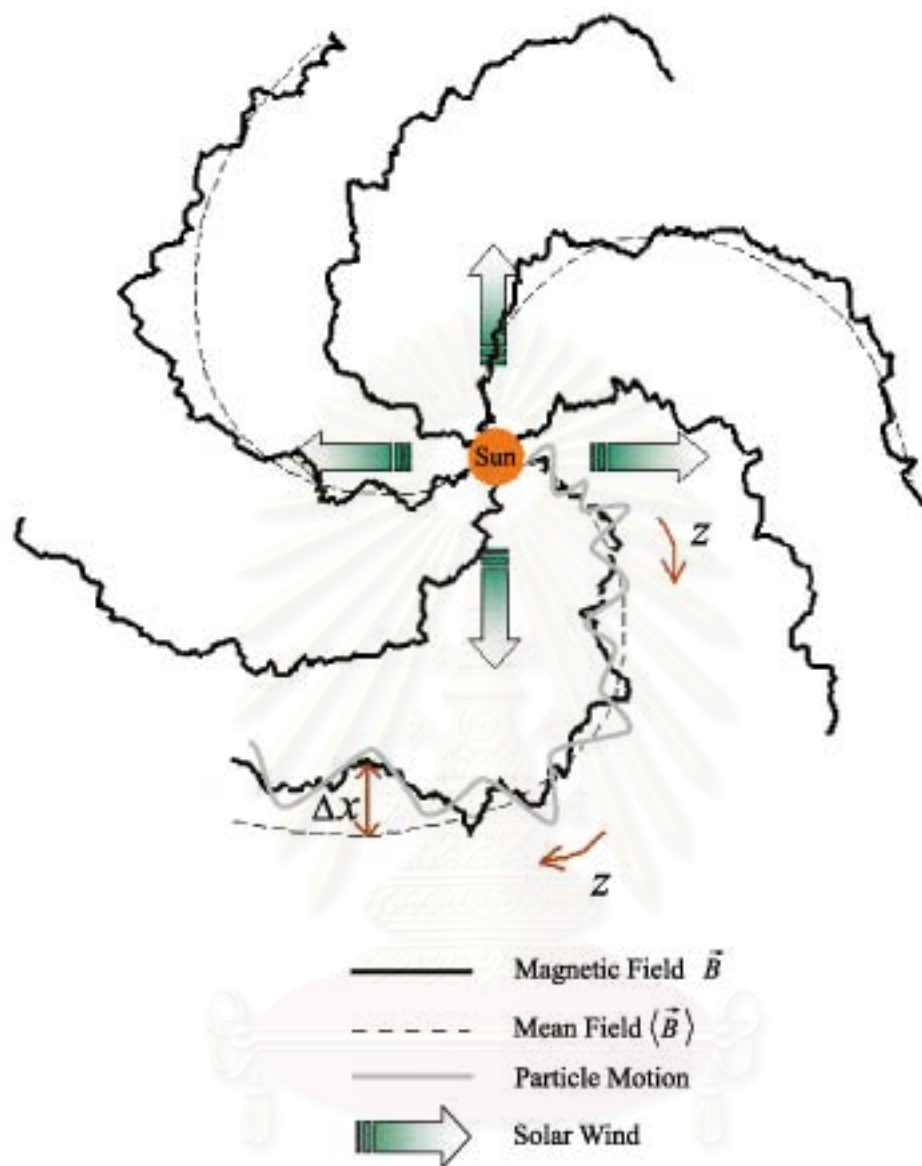


Figure 2.3: The structures of the solar wind and the interplanetary magnetic field.

the IMF receives characteristics from the solar wind too, e.g., the characteristics of turbulence. While the Sun rotates, the solar wind is escaping continuously from the Sun in approximately the radial direction and one foot of an interplanetary magnetic field line is tied to the Sun. Therefore, the shape of an IMF line looks

like an Archimedean spiral with fluctuations due to the turbulence as shown in Figure 2.3. The shape of IMF lines is similar to the streamlines of water from a garden sprinkler and the flow direction of the solar wind is comparable with the flow of water. Figure 2.2 the example of the direction of the IMF during the minimum activity of solar cycle. The direction of the IMF is different for northern and southern hemispheres. If the direction of the IMF is outward for the northern hemisphere, it is inward for the southern hemisphere. This is because the magnetic field of the Sun is different from the dipole magnetic field of the Earth. The magnetic polarities (north and south polarities) of the Sun are distributed over the entire surface of the Sun. Near each pole, there is one dominant polarity. From Figure 2.2, the outward magnetic polarity is the majority in the northern hemisphere and the inward magnetic polarity is a majority in the southern hemisphere. Near the equator, there are both polarities. That is why we often find magnetic loops of the Sun near the equator and open magnetic field lines near the poles. The footpoints are not fixed due to convection and differential rotation within the Sun as well as solar activity, moving the Sun's field lines until the opposite polarity dominates every 11 years (the solar cycle). However, the structure of the solar wind at solar maximum is much more complicated than during solar minimum (McComas et al. 2002). Instead of the solar wind flowing uniformly fast at high latitudes as during the solar minimum, it is slower and more highly variable at solar maximum. The corona holes at the poles shrink and finally disappear. The mixed polarities can also be found at high latitude. The magnetic field on the surface of the Sun becomes chaotic before the new cycle begins with a switch of magnetic field polarities.

Since northern and southern hemispheres have opposite magnetic polar-

ities, the surface where the interplanetary magnetic field change suddenly is a current sheet. This is located near the ecliptic plane but is wavy like a skirt (see Figure 2.4). The magnetic field in space is important to study because it affects the high energy particles released from the Sun, called solar energetic particles or SEPs. Since most SEPs are charged particles, they follow the magnetic field lines in helical orbits as shown in Figure 2.5. Thus, there is a connection between particle transport and the random walk of magnetic field lines in space.

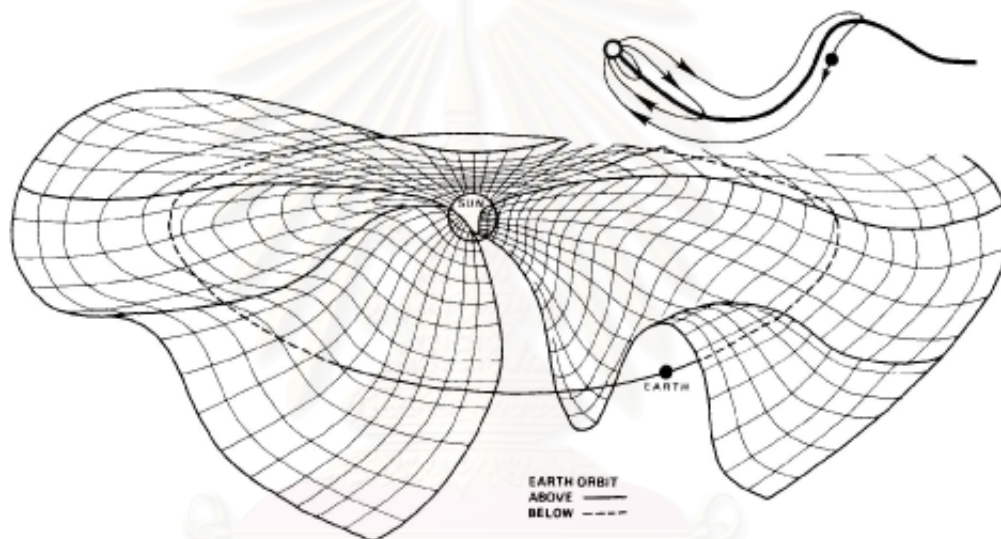


Figure 2.4: Schematic diagram of the structure of the current sheet. (Image credit: NRC, 2004)

## 2.4 The 2D+Slab Model of Magnetic Field Turbulence

The two-component model was motivated by the observation that solar wind fluctuations are concentrated at nearly parallel and nearly perpendicular wave numbers (Matthaeus, Goldstein, & Roberts 1990). For the parallel com-

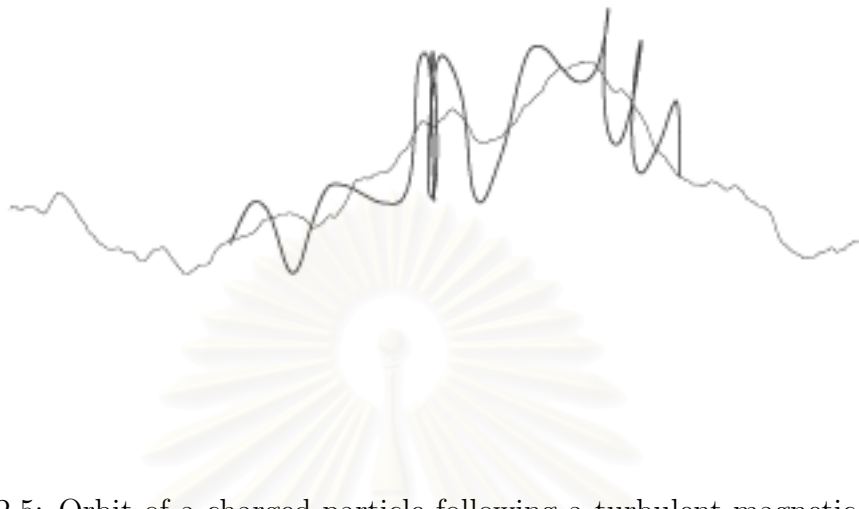


Figure 2.5: Orbit of a charged particle following a turbulent magnetic field line. The thick line is the particle trajectory and the thin line is the magnetic field line.

penent, the wave vector is parallel to the direction of the mean field and the fluctuation of the magnetic field in this component is perpendicular to both the parallel wave vector and the mean field. This is motivated by Alfvénic or slab-like waves in the solar wind propagating along the mean field. We call this component the “slab” component. Another component, which is motivated by laboratory experiments, is called “two-dimensional (2D)” turbulence, which has a wave vector perpendicular to the mean magnetic field. The magnetic fluctuation in this component is also perpendicular to both the wave vector and the mean field. This component gives long correlation lengths in the direction of the mean field. The analysis of solar wind data by Matthaeus, Goldstein, & Roberts (1990) showed that the power spectrum of the solar wind turbulence is composed of these two components. Furthermore, the two-component model provides a good explanation of the parallel transport of SEPs (Bieber et al. 1994; Bieber, Wan-

ner, & Matthaeus 1996; Dröge 2000), providing a solution to the long-standing discrepancy between theoretical and observed scattering mean free paths.

In the 2D+slab model of magnetic field turbulence, we assume

$$\vec{B} = \vec{B}_0 + \vec{b}(x, y, z), \quad (2.3)$$

where  $\vec{B}_0$  is a constant mean field in the  $z$  direction and  $\vec{b}$  is the transverse fluctuation. The magnetic field that we consider is static and homogeneous. That means the field does not depend on time and the statistical properties of the magnetic field are invariant under translations. The fluctuation  $\vec{b}$  is perpendicular to the mean field and  $\langle \vec{b} \rangle$  must be zero. According to the two-component model, the fluctuation in real space can be divided into two parts. In the slab component of turbulence,  $\vec{b}^{slab}$  depends only on  $z$ , the coordinate along the mean field while  $\vec{b}^{2D}$  for the 2D turbulence depends only on the perpendicular coordinates,  $x$  and  $y$ . Thus the fluctuation can be written as

$$\vec{b}(x, y, z) = \vec{b}^{2D}(x, y) + \vec{b}^{slab}(z). \quad (2.4)$$

For the two-dimensional component, we can write

$$\vec{b}^{2D}(x, y) = \vec{\nabla} \times [a(x, y)\hat{z}], \quad (2.5)$$

where  $a\hat{z}$  is a vector potential for the 2D component and  $a(x, y)$  can be called the potential function.

The slab and 2D fields are illustrated in Figures 2.6 and 2.7, respectively. From the definition of the slab field, the fluctuation depends only on  $z$ . Therefore, if we consider the slab fluctuation in the  $x$ - $y$  plane at each  $z$ ,  $\vec{b}^{slab}$  is the same along that plane but different from the field on other planes as shown in Figure 2.6. From (2.5), we can write 2D turbulence as  $\vec{b}^{2D} = \vec{\nabla} a(x, y) \times \hat{z}$ . From this relation,



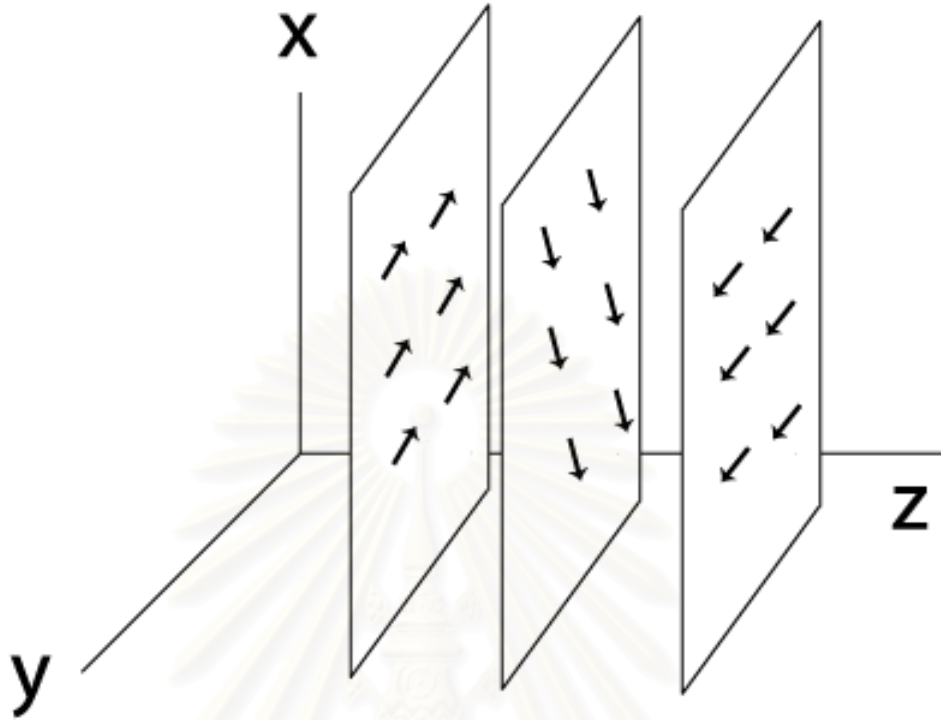


Figure 2.6: Illustration of the slab fluctuation, which depends only on the  $z$  coordinate. The arrows demonstrate the slab fluctuation  $\vec{b}^{slab}$ .

we can clearly see that the 2D field must be in the direction perpendicular to the gradient of the potential function and also to the  $z$  direction. Therefore, the direction of the 2D field must be along the equipotential line of  $a(x, y)$  as shown in Figure 2.7. A 2D field that has a positive value of  $a(x, y)$  is in a counter-clockwise direction while one that has a negative value has a clockwise direction.

Finally, from (2.3) and (2.4), we again write the total magnetic field,

$$\begin{aligned} \vec{B} = & B_0 \hat{z} + [b_x^{2D}(x, y) + b_x^{slab}(z)] \hat{x} \\ & + [b_y^{2D}(x, y) + b_y^{slab}(z)] \hat{y}. \end{aligned} \quad (2.6)$$

The total magnetic field for the two-component model includes the mean field, slab and 2D fields together, so it would be more complicated than when we

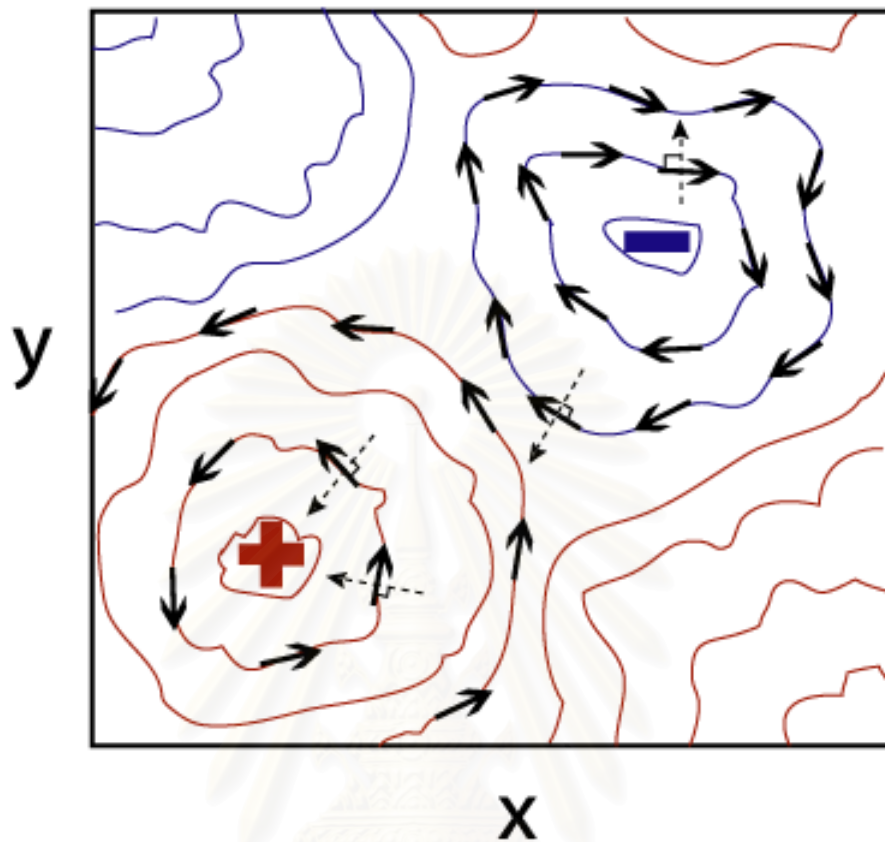


Figure 2.7: Schematic contour plot of  $a(x, y)$ . The solid arrows show the 2D field,  $\vec{b}^{2D}$ , and the dashed arrows show examples of the directions of  $\vec{\nabla}a(x, y)$  for both positive and negative potential functions. The 2D field must lie along the equipotential lines of the potential function. For a positive potential function, the 2D field is in a counter-clockwise direction, while a 2D field having a negative potential function is in the clockwise direction.

consider only slab or only 2D fields. The details of the 2D+slab turbulent field, such as how to generate the turbulent field and examples of 2D and slab field lines, will be discussed further in Chapter 3.

## 2.5 Correlation Function and Power Spectrum

Since we consider a turbulent magnetic field for which the field itself is random, it is hard to directly write the magnetic field as a function at each position. Therefore, we need statistical quantities to describe the random field. The only part that is a random quantity in our magnetic model is the fluctuation  $\vec{b}$ . One property that we already know from the previous section is  $\langle \vec{b} \rangle = 0$ , where  $\langle \ \rangle$  denotes the ensemble average, which is not enough information to describe the random system. An important statistical quantity that can give us the information on the spatial structure is the “two-point correlation” or “correlation function.” It is defined by

$$R_{ij}(\vec{x}, \vec{r}) = \langle b_i(\vec{x})b_j(\vec{x} + \vec{r}) \rangle, \quad (2.7)$$

where  $i$  and  $j$  are  $x$ ,  $y$ , and  $z$  components. For homogeneous turbulence, the correlation function is independent of  $\vec{x}$ , so we can write

$$R_{ij}(\vec{r}) = \langle b_i(0)b_j(\vec{r}) \rangle. \quad (2.8)$$

The correlation function tells us how the magnetic field at two different points is correlated. For example, if we consider any two points in the system, and let the vector between these two points be  $\vec{r}$ , when we calculate the correlation function in (2.8), the correlation function gives a high value when the magnetic field of these two points still in the same direction and it gives a low value or nearly zero when there is little or no relation between  $\vec{b}$  at those two points. The magnetic field at a given point  $\vec{x}$  should correlate more highly with itself than with that at other points. For example, if we consider the correlation function of the  $x$ -component, the highest value is

$$R_{xx}(0) = \langle b_x^2 \rangle. \quad (2.9)$$

The Fourier transform of the correlation function is called the “power spectrum”  $P_{ij}(\vec{k})$ ,

$$P_{ij}(\vec{k}) = \frac{1}{(\sqrt{2\pi})^3} \int_{-\infty}^{\infty} R_{ij}(\vec{r}) \exp(i\vec{k} \cdot \vec{r}) d^3\vec{r}, \quad (2.10)$$

where  $\vec{k}$  is the wave vector. We can rewrite the correlation function as the inverse Fourier transform,

$$R_{ij}(\vec{r}) = \frac{1}{(\sqrt{2\pi})^3} \int_{-\infty}^{\infty} P_{ij}(\vec{k}) \exp(-i\vec{k} \cdot \vec{r}) d^3\vec{k}, \quad (2.11)$$

and from (2.9) and (2.11), we can obviously see that

$$\langle b_x^2 \rangle = \frac{1}{(\sqrt{2\pi})^3} \int_{-\infty}^{\infty} P_{xx}(\vec{k}) d^3\vec{k}. \quad (2.12)$$

In our model, we have slab and 2D components for magnetic fluctuations, so the correlation functions for 2D and slab fluctuations are

$$R_{ij}^{2D}(x, y) = \langle b_i^{2D}(0, 0) b_j^{2D}(x, y) \rangle \quad (2.13)$$

and

$$R_{ij}^{slab}(z) = \langle b_i^{slab}(0) b_j^{slab}(z) \rangle. \quad (2.14)$$

We can also find the power spectra for 2D and slab components,

$$P_{ij}^{2D}(k_x, k_y) = \frac{1}{2\pi} \int_{-\infty}^{\infty} \int_{-\infty}^{\infty} R_{ij}^{2D}(x, y) \exp[i(k_x x + k_y y)] dx dy \quad (2.15)$$

and

$$P_{ij}^{slab}(k_z) = \frac{1}{\sqrt{2\pi}} \int_{-\infty}^{\infty} R_{ij}^{slab}(z) \exp(ik_z z) dz. \quad (2.16)$$

The 2D fluctuation can be written in terms of the potential function  $a(x, y)$ , which is also a random function. The power spectrum corresponding to the autocorrelation  $\langle a(0, 0)a(x, y) \rangle$  is  $A(k_x, k_y)$ , that is,

$$\langle a(0, 0)a(x, y) \rangle = \frac{1}{2\pi} \int_{-\infty}^{\infty} \int_{-\infty}^{\infty} A(k_x, k_y) \exp[-i(k_x x + k_y y)] dk_x dk_y. \quad (2.17)$$

Considering (2.5) in wave vector space, it is

$$\vec{b}^{2D}(k_x, k_y) = -i\vec{k} \times [a(k_x, k_y)] \hat{z}. \quad (2.18)$$

Eq. (2.18) yields

$$b_x(k_x, k_y) = -ik_y a(k_x, k_y) \quad (2.19)$$

$$b_y(k_x, k_y) = ik_x a(k_x, k_y), \quad (2.20)$$

and the relationship between  $P_{ii}^{2D}$  and  $b_i(k_x, k_y)$  is

$$P_{ii}^{2D}(k_x, k_y) = \frac{1}{2\pi V} |b_i(k_x, k_y)|^2, \quad (2.21)$$

where  $V$  is the total volume. Substituting (2.19) and (2.20) into (2.21), we have

$$P_{xx}^{2D}(k_x, k_y) = k_y^2 A(k_x, k_y) \quad (2.22)$$

$$P_{yy}^{2D}(k_x, k_y) = k_x^2 A(k_x, k_y), \quad (2.23)$$

where  $A(k_x, k_y) = |a(k_x, k_y)|^2 / (2\pi V)$ .

In practice, we specify the power spectrum instead of the correlation function because we can understand the implied physics. We will discuss more about the power spectrum we use in the next section and in Chapter 3.

## 2.6 Correlation Length

Other interesting quantities that are related to the correlation function and power spectrum are the length scales in slab and 2D turbulence. This section shows the derivation of the relationship between the correlation length ( $\ell_c$ ) for slab turbulence and parallel coherence length ( $\ell_z$ ). Another length scale that we should understand is the ultrascale ( $\tilde{\lambda}$ ), a length scale in 2D turbulence, which

is related to the perpendicular coherence length ( $\ell_{\perp}$ ). We first evaluate the slab correlation length, defined by

$$\ell_c = \frac{\int_0^{\infty} R_{xx}^{slab}(z) dz}{R_{xx}^{slab}(z=0)}. \quad (2.24)$$

Now from equation (2.9),  $R_{xx}^{slab}(z=0)$  is  $\langle b_{x,slab}^2 \rangle$ , the mean-square fluctuation  $\delta b_{x,slab}^2$ . One interpretation of equation (2.24) is that the area of the rectangle  $\ell_c \times R_{xx}^{slab}(0)$  equals the area under the  $R_{xx}^{slab}(z)$  plot as shown in Figure 2.8.

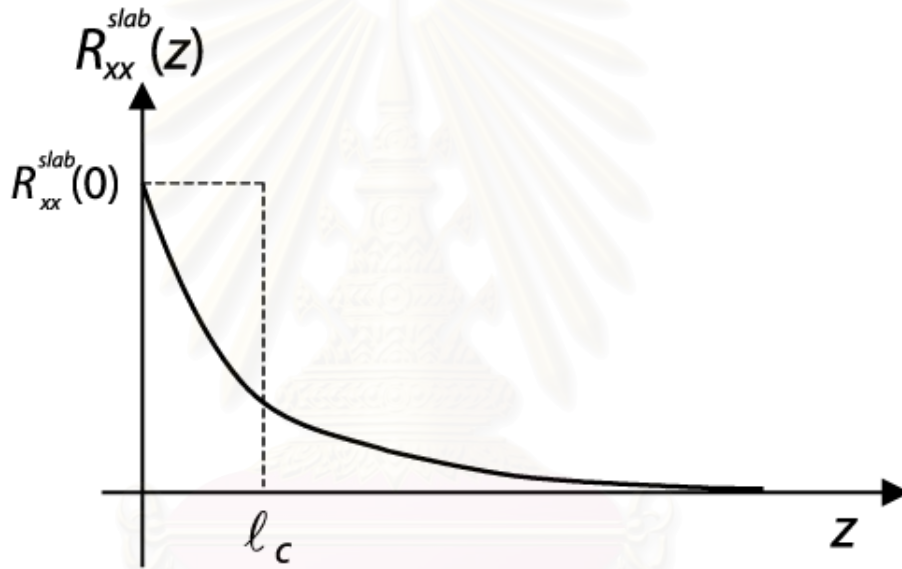


Figure 2.8: The correlation function  $R_{xx}^{slab}(z)$  and its relationship with the correlation length  $\ell_c$ .

The power spectrum, the Fourier transform of the correlation function, can then be written as

$$P_{xx}^{slab}(k_z) = \frac{1}{\sqrt{2\pi}} \int_{-\infty}^{\infty} R_{xx}^{slab}(z) \exp(ik_z z) dz. \quad (2.25)$$

Therefore, we can also write the correlation function in terms of the power spectrum

$$R_{xx}^{slab}(z) = \frac{1}{\sqrt{2\pi}} \int_{-\infty}^{\infty} P_{xx}^{slab}(k_z) \exp(-ik_z z) dk_z. \quad (2.26)$$

The function we use for the slab power spectrum in numerical simulations is

$$P_{xx}^{slab} = \frac{C_1}{[1 + (k_z \ell_z)^2]^{5/6}}, \quad (2.27)$$

where  $C_1$  is constant that can be calculated if we know the turbulence energy and  $\ell_z$  is the coherence length which is associated with  $k_{0z} = 1/\ell_z$ , where the spectrum bends over to the inertial range (similar to  $\ell_0$  in Figure 2.1). From (2.24), we rewrite the correlation function in terms of the power spectrum so it becomes

$$\ell_c = \frac{1}{\sqrt{2\pi}} \frac{\int_0^\infty \int_{-\infty}^\infty P_{xx}^{slab}(z) \exp(-ik_z z) dk_z dz}{\delta b_{x,slab}^2}. \quad (2.28)$$

Integrating over  $z$  and using  $\delta(k) = \int_{-\infty}^\infty \exp(-ikx) dx / (2\pi)$ , we get

$$\ell_c = \sqrt{\frac{\pi}{2}} \frac{\int_{-\infty}^\infty P_{xx}^{slab}(k_z) \delta(k_z) dk_z}{\delta b_{x,slab}^2} \quad (2.29)$$

$$= \sqrt{\frac{\pi}{2}} \frac{P_{xx}^{slab}(0)}{\delta b_{x,slab}^2}. \quad (2.30)$$

From (2.27), we can see that  $P_{xx}^{slab}(k_z = 0) = C_1$ . Therefore we have to find the constant  $C_1$  in terms of  $\ell_z$  and replace it into (2.30). Since

$$R_{xx}^{slab}(0) = \frac{1}{\sqrt{2\pi}} \int_{-\infty}^\infty P_{xx}^{slab}(z) dk_z, \quad (2.31)$$

we substitute the function of  $P_{xx}^{slab}$  as (2.27) into (2.31):

$$\delta b_{x,slab}^2 = \frac{1}{\sqrt{2\pi}} \int_{-\infty}^\infty \frac{C_1}{[1 + (k_z \ell_z)^2]^{5/6}} dk_z \quad (2.32)$$

$$C_1 = \frac{\sqrt{2\pi} \delta b_{x,slab}^2}{\int_{-\infty}^\infty [1 + (k_z \ell_z)^2]^{-5/6} dk_z}. \quad (2.33)$$

From Gradshteyn & Ryzhik (1980, p. 341),

$$\int_0^\infty \frac{x^{\mu-1}}{(p+qx^\nu)^{n+1}} dx = \frac{1}{\nu p^{n+1}} \left(\frac{p}{q}\right)^{\frac{\mu}{\nu}} \frac{\Gamma(\frac{\mu}{\nu}) \Gamma(1+n-\frac{\mu}{\nu})}{\Gamma(1+n)}, \quad (2.34)$$

where  $0 < \mu/\nu < n+1$ ,  $p \neq 0$ ,  $q \neq 0$ . In (2.33), we use  $\mu = 1$ ,  $\nu = 2$ ,  $n = -1/6$ ,  $p = 1$ , and  $q = (\ell_z)^2$ . Therefore

$$\int_{-\infty}^\infty \frac{1}{[1+(k_z \ell_z)^2]^{5/6}} dk_z = \frac{1}{\ell_z} \frac{\Gamma(\frac{1}{2})\Gamma(\frac{1}{3})}{\Gamma(\frac{5}{6})}. \quad (2.35)$$

Then

$$C_1 = \frac{\sqrt{2\pi}\Gamma(\frac{5}{6})}{\Gamma(\frac{1}{2})\Gamma(\frac{1}{3})} \delta b_{x,slab}^2 \ell_z, \quad (2.36)$$

and substituting  $C_1$ , which is  $P_{xx}^{slab}$ , into (2.30), we have

$$\ell_c = \frac{\Gamma(\frac{5}{6})\pi}{\Gamma(\frac{1}{2})\Gamma(\frac{1}{3})} \ell_z \quad (2.37)$$

$$= 0.747 \ell_z. \quad (2.38)$$

Then the relationship between  $\ell_c$  and  $\ell_z$  is

$$\ell_c = 0.747 \ell_z. \quad (2.39)$$

Next, we consider two other length scales: the ultrascale ( $\tilde{\lambda}$ ) and perpendicular coherence length ( $\ell_\perp$ ). Since the definition of the ultrascale (see more details in section 2.7) is

$$\tilde{\lambda} \equiv \sqrt{\frac{\langle a^2 \rangle}{\langle b_{2D}^2 \rangle}}, \quad (2.40)$$

we can write this in terms of the power spectrum  $A(k_\perp)$ ,  $P_{xx}^{2D}$ , and  $P_{yy}^{2D}$  as

$$\tilde{\lambda} = \sqrt{\frac{\frac{1}{2\pi} \int_{-\infty}^\infty \int_{-\infty}^\infty A(k_\perp) dk_x dk_y}{\frac{1}{2\pi} \int_{-\infty}^\infty \int_{-\infty}^\infty (P_{xx}^{2D} + P_{yy}^{2D}) dk_x dk_y}}. \quad (2.41)$$

Here, in numerical work, we use the power spectrum  $A(k_\perp)$  for 2D turbulence as

$$A(k_\perp) = \frac{C_2}{[1+(k_\perp \ell_\perp)^2]^{7/3}}, \quad (2.42)$$



where  $\ell_\perp$  is the perpendicular coherence length, which is associated with  $k_{0\perp} = 1/\ell_\perp$  (similar to  $\ell_0$  in Figure 2.1).

Note that the forms in (2.27) and (2.42) roll off to a constant at low  $k$ , and far above  $k_{0z}$  and  $k_{0\perp}$  they follow a Kolmogorov law, with the omnidirectional power spectrum (OPS) varying as  $k^{-5/3}$ . To see this, note that for slab (1D) fluctuations the OPS is simply  $P_{xx}^{slab} + P_{yy}^{slab}$ , which has the correct dependence, and for 2D fluctuations at a given magnitude  $k_\perp$ , the OPS  $\propto k_\perp (P_{xx}^{2D} + P_{yy}^{2D}) = k_\perp^3 A$ , which varies as  $k_\perp^{-5/3}$  for large  $k_\perp$ .

Next, we evaluate the numerator and the denominator in (2.41). We obtain

$$\begin{aligned}
\int_{-\infty}^{\infty} \int_{-\infty}^{\infty} A(k_\perp) dk_x dk_y &= C_2 \int_0^{2\pi} \int_0^\infty \frac{k_\perp}{[1 + (k_\perp \ell_\perp)^2]^{7/3}} dk_\perp d\theta \\
&= \frac{C_2 \pi}{\ell_\perp^2} \int_0^\infty \frac{1}{[1 + (k_\perp \ell_\perp)^2]^{7/3}} d(k_\perp \ell_\perp)^2 \\
&= \frac{C_2 \pi}{\ell_\perp^2} \int_0^\infty \frac{1}{(1 + U)^{7/3}} dU \\
&= \frac{C_2 \pi}{\ell_\perp^2} \frac{3}{4}
\end{aligned} \tag{2.43}$$

and

$$\begin{aligned}
\int_{-\infty}^{\infty} \int_{-\infty}^{\infty} (P_{xx}^{2D} + P_{yy}^{2D}) dk_x dk_y &= C_2 \int_0^{2\pi} \int_0^\infty A(k_\perp) k_\perp^2 k_\perp dk_\perp d\theta \\
&= \frac{C_2 \pi}{\ell_\perp^4} \int_0^\infty \frac{(k_\perp \ell_\perp)^2}{[1 + (k_\perp \ell_\perp)^2]^{7/3}} d(k_\perp \ell_\perp)^2 \\
&= \frac{C_2 \pi}{\ell_\perp^4} \int_0^\infty \frac{U}{(1 + U)^{7/3}} dU \\
&= \frac{C_2 \pi}{\ell_\perp^4} \int_0^\infty \left[ \frac{1}{(1 + U)^{4/3}} - \frac{1}{(1 + U)^{7/3}} \right] dU \\
&= \frac{C_2 \pi}{\ell_\perp^4} \frac{9}{4},
\end{aligned} \tag{2.44}$$

where  $U = (k_{\perp} \ell_{\perp})^2$ . Substituting (2.43) and (2.44) into (2.41), we finally have the relation between  $\tilde{\lambda}$  and  $\ell_{\perp}$  as

$$\tilde{\lambda} = 0.577 \ell_{\perp}. \quad (2.45)$$

Thus we can see that the correlation length and ultrascale depend on only coherence lengths and the shape of the power spectrum that we use.

## 2.7 Field Line Random Walk

To calculate the diffusion perpendicular coefficient of the field lines in 2D+slab turbulence is the objective of this section. The calculation was first performed by Matthaeus et al. (1995). This version of the derivation was published by Ruffolo, Matthaeus, and Chuychai (2004).

A magnetic field line is defined as a curve that is tangent everywhere to the magnetic field  $\vec{B}$ . If  $d\vec{l}$  is an arc length, the lines of force are defined by the differential equation,

$$d\vec{l} \times \vec{B} = 0. \quad (2.46)$$

In Cartesian coordinates,  $d\vec{l}$  is  $(dx, dy, dz)$  and  $\vec{B}$  is  $(B_x, B_y, B_z)$ . The equation of the magnetic field line can be determined by (2.46). From the differential equation, we have

$$\frac{dx}{B_x} = \frac{dy}{B_y} = \frac{dz}{B_z}. \quad (2.47)$$

In our model, we have  $\vec{B} = B_0 \hat{z} + b_x \hat{x} + b_y \hat{y}$ , so we obtain

$$\frac{dx}{b_x} = \frac{dy}{b_y} = \frac{dz}{B_0}. \quad (2.48)$$

From (2.48), we can calculate the perpendicular displacements  $\Delta x$  and  $\Delta y$  as

$$\Delta x(\Delta z) = x(\Delta z) - x(0) = \int_0^{\Delta z} \frac{b_x(x'(z'), y'(z'), z')}{B_0} dz' \quad (2.49)$$

$$\Delta y(\Delta z) = y(\Delta z) - y(0) = \int_0^{\Delta z} \frac{b_y(x'(z'), y'(z'), z')}{B_0} dz'. \quad (2.50)$$

The definition of the diffusion of field lines is similar to the diffusion of the random walk motion of particles, that is

$$\langle \Delta x^2 \rangle = 2\kappa \Delta t, \quad (2.51)$$

where  $\langle \Delta x^2 \rangle$  is the mean-square displacement of the particles,  $\kappa$  is the diffusion coefficient of the particles, and  $\Delta t$  is time. The diffusion coefficient appears in the diffusion equation,

$$\frac{\partial f}{\partial t} = \kappa \nabla^2 f, \quad (2.52)$$

where  $f$  is the distribution function. Thus, in general, we can define the perpendicular diffusion coefficient of the field lines as

$$D_{\perp} = \frac{\langle (\Delta \vec{x}_{\perp})^2 \rangle}{4\Delta z}, \quad (2.53)$$

where  $\Delta \vec{x}_{\perp}$  is the perpendicular displacement. This definition also obeys the diffusion equation

$$\frac{\partial f}{\partial z} = D_{\perp} \left( \frac{\partial^2 f}{\partial x^2} + \frac{\partial^2 f}{\partial y^2} \right). \quad (2.54)$$

Eq. (2.54) states that we are considering the diffusion of the density of magnetic field lines in perpendicular directions as it evolves along the distance  $z$ . To clearly understand how the magnetic field lines diffuse along the distance  $z$ , imagine that we are looking at a snapshot of the field lines in many representations of the turbulent magnetic field at each distance  $z$ . Therefore, we can view each field line as a point in the  $x$ - $y$  plane at a given  $z$ . Suppose  $f$  stands for the density of those field lines. The diffusion coefficient tells us how much these points spread out when the distance  $z$  changes.

We here assume the turbulence as isotropic, that is,  $\langle(\Delta x)^2\rangle = \langle(\Delta y)^2\rangle$ .

The perpendicular diffusion coefficient of the field lines is defined as

$$D_{\perp} = \frac{\langle(\Delta x)^2\rangle}{2\Delta z}. \quad (2.55)$$

Thus we calculate  $\langle(\Delta x)^2\rangle$  from (2.49),

$$\langle(\Delta x)^2\rangle = \frac{1}{B_0^2} \int_0^{\Delta z} \int_0^{\Delta z} \langle b_x(x'(z'), y'(z'), z') b_x(x''(z''), y''(z''), z'') \rangle dz' dz''. \quad (2.56)$$

We define  $\Delta x' = x'' - x'$ ,  $\Delta y' = y'' - y'$  and  $\Delta z' = z'' - z'$  and let the magnetic turbulence be homogeneous. Then (2.56) becomes

$$\langle(\Delta x)^2\rangle = \frac{1}{B_0^2} \int_0^{\Delta z} \int_{-z'}^{\Delta z - z'} \langle b_x(0, 0, 0) b_x(\Delta x'(\Delta z'), \Delta y'(\Delta z'), \Delta z') \rangle d\Delta z' dz'. \quad (2.57)$$

Continuing with the derivation, note that Lagrangian correlation functions such as  $\langle b_x(x', y', z') b_x(x'', y'', z'') \rangle$  differ from standard (Eulerian) correlation functions; in a Lagrangian ensemble average over representations of the magnetic turbulence, the positions themselves depend on the representation. However, it is possible to separate the statistics of the magnetic fluctuations from those of individual trajectories when the two positions are separated by more than a coherence length in the parallel or perpendicular direction. (Over smaller distances this is not necessarily accurate, e.g., straight line trajectories, with one spatial distribution, are associated with higher magnetic correlation than bending trajectories, which have a different spatial distribution.) This approximation, known as Corrsin's independence hypothesis (Corrsin 1959; Salu & Montgomery 1977; see also McComb 1990) can be expressed either in wave-vector space (as in Matthaeus et al. 1995) or in position space.

Here we demonstrate the implementation of Corrsin's hypothesis in position space. We consider the Lagrangian correlation function to be the Eulerian correlation function,  $R_{xx} \equiv \langle b_x(0,0,0)b_x(x,y,z) \rangle$ , weighted by the conditional probabilities of finding  $\Delta x'$  and  $\Delta y'$  after a given  $\Delta z'$ :

$$\begin{aligned} & \langle b_x(0,0,0)b_x(\Delta x'(\Delta z'), \Delta y'(\Delta z'), \Delta z') \rangle \\ &= \int_{-\infty}^{\infty} \int_{-\infty}^{\infty} R_{xx}(\Delta x', \Delta y', \Delta z') P(\Delta x'|\Delta z') P(\Delta y'|\Delta z') d\Delta x' d\Delta y' \end{aligned} \quad (2.58)$$

$$\begin{aligned} \langle \Delta x^2 \rangle &= \frac{1}{B_0^2} \int_0^{\Delta z} \int_{-z'}^{\Delta z - z'} \int_{-\infty}^{\infty} \int_{-\infty}^{\infty} R_{xx}(\Delta x', \Delta y', \Delta z') \\ &\quad \times P(\Delta x'|\Delta z') P(\Delta y'|\Delta z') d\Delta x' d\Delta y' d\Delta z' dz', \end{aligned} \quad (2.59)$$

where we invoke the statistical independence of  $\Delta x'$  and  $\Delta y'$ .

Another key assumption is that the condition probability distributions are Gaussian,

$$\begin{aligned} P(\Delta x'|\Delta z') &= \frac{1}{\sqrt{2\pi\sigma_x^2}} \exp\left[-\frac{(\Delta x')^2}{2\sigma_x^2}\right] \\ P(\Delta y'|\Delta z') &= \frac{1}{\sqrt{2\pi\sigma_y^2}} \exp\left[-\frac{(\Delta y')^2}{2\sigma_y^2}\right] \end{aligned} \quad (2.60)$$

where  $\sigma_x^2 = \langle \Delta x^2 \rangle$  and  $\sigma_y^2 = \langle \Delta y^2 \rangle$  are the variance of the distributions. Furthermore, we assume the variances are diffusive and statistically axisymmetric in the sense that

$$\langle (\Delta x)^2 \rangle = \langle (\Delta y)^2 \rangle = 2D_{\perp} |\Delta z'|, \quad (2.61)$$

where  $D_{\perp}$  is the desired perpendicular diffusion coefficient. The distributions in equation (2.60) guarantee the statistical independence assumed in equation (2.59). For slab or two-component turbulence, these assumptions are accurate

for sufficiently large  $\Delta z$ , by the central limit theorem. A check on the validity of the result is that  $\langle \Delta x^2 \rangle$  should be proportional to  $\Delta z$  in that limit, and as  $\Delta z$  decreases, violation of that proportionality indicates the limit of validity of the diffusion approximation. For example, at small  $\Delta z$ , over which  $\vec{b}$  is nearly constant, there is a “free-streaming” régime where field lines have nearly straight-line trajectories and  $\langle \Delta x^2 \rangle \propto (\Delta z)^2$ .

So far, our calculation of  $\Delta x^2$  has not yet specified the nature of the magnetic turbulence. Now let us focus on axisymmetric, two-component 2D+slab turbulence:

$$R_{xx}(\Delta x', \Delta y', \Delta z') = R_{xx}^{slab}(\Delta z') + R_{xx}^{2D}(\Delta x', \Delta y') \quad (2.62)$$

or in terms of power spectra,

$$\begin{aligned} R_{xx}^{slab}(\Delta z') &= \frac{1}{\sqrt{2\pi}} \int_{-\infty}^{\infty} P_{xx}^{slab}(k_z) e^{-ik_z \Delta z'} dk_z \\ R_{xx}^{2D}(\Delta x', \Delta y') &= \frac{1}{2\pi} \int_{-\infty}^{\infty} \int_{-\infty}^{\infty} P_{xx}^{2D}(k_x, k_y) e^{-ik_x \Delta x'} e^{-ik_y \Delta y'} dk_x dk_y. \end{aligned} \quad (2.63)$$

Then substituting equations (2.62) and (2.63) into equation (2.59), and separating slab and 2D contributions, we have

$$\begin{aligned} \langle \Delta x^2 \rangle_{slab} &= \frac{1}{\sqrt{2\pi}} \frac{1}{B_0^2} \int_{-\infty}^{\infty} P_{xx}^{slab}(k_z) \int_0^{\Delta z} \int_{-z'}^{\Delta z - z'} \left( \int_{-\infty}^{\infty} P(\Delta x' | \Delta z') d\Delta x' \right) \\ &\quad \times \left( \int_{-\infty}^{\infty} P(\Delta y' | \Delta z') d\Delta y' \right) e^{-ik_z \Delta z'} d\Delta z' dz' dk_z \end{aligned} \quad (2.64)$$

$$\begin{aligned} \langle \Delta x^2 \rangle_{2D} &= \frac{1}{2\pi} \frac{1}{B_0^2} \int_{-\infty}^{\infty} \int_{-\infty}^{\infty} P_{xx}^{2D}(k_x, k_y) \int_0^{\Delta z} \int_{-z'}^{\Delta z - z'} \left( \int_{-\infty}^{\infty} e^{-ik_x \Delta x'} P(\Delta x' | \Delta z') d\Delta x' \right) \\ &\quad \times \left( \int_{-\infty}^{\infty} e^{-ik_y \Delta y'} P(\Delta y' | \Delta z') d\Delta y' \right) d\Delta z' dz' dk_x dk_y. \end{aligned} \quad (2.65)$$

For the slab component of turbulence, in which  $R_{xx}^{slab}$  does not depend on  $\Delta x'$  or  $\Delta y'$ , the conditional probabilities simply integrate to 1, yielding

$$\langle \Delta x^2 \rangle_{slab} = \frac{1}{\sqrt{2\pi}} \frac{1}{B_0^2} \int_{-\infty}^{\infty} \int_0^{\Delta z} \int_{-z'}^{\Delta z - z'} P_{xx}^{slab}(k_z) e^{-ik_z \Delta z'} d\Delta z' dz' dk_z. \quad (2.66)$$

For the 2D component, we have

$$\begin{aligned} \int_{-\infty}^{\infty} e^{-ik_x \Delta x'} P(\Delta x' | \Delta z') d\Delta x' &= \int_{-\infty}^{\infty} \frac{e^{-ik_x \Delta x'}}{\sqrt{4\pi D_{\perp} |\Delta z'|}} \exp \left[ -\frac{(\Delta x')^2}{4D_{\perp} |\Delta z'|} \right] d\Delta x' \\ &= e^{-D_{\perp} k_x^2 |\Delta z'|}, \end{aligned} \quad (2.67)$$

and with the analogous formula for the  $\Delta y'$  integral, we obtain

$$\langle \Delta x^2 \rangle_{2D} = \frac{1}{2\pi} \frac{1}{B_0^2} \int_{-\infty}^{\infty} \int_{-\infty}^{\infty} \int_0^{\Delta z} \int_{-z'}^{\Delta z - z'} P_{xx}^{2D}(k_x, k_y) e^{-D_{\perp}(k_x^2 + k_y^2) |\Delta z'|} d\Delta z' dz' dk_x dk_y. \quad (2.68)$$

So far this derivation is equivalent to that of Matthaeus et al. (1995), except that we consider the exact limits of the  $\Delta z'$  integration, not approximating the limits as  $\pm\infty$ .

Now we may carry out the integration over  $\Delta z'$  and  $z'$  in equations (2.66) and (2.68), to obtain

$$\begin{aligned} \langle \Delta x^2 \rangle_{slab} &= \frac{1}{\sqrt{2\pi}} \frac{1}{B_0^2} \int_{-\infty}^{\infty} \frac{2[1 - \cos(k_z \Delta z)]}{k_z^2} P_{xx}^{slab}(k_z) dk_z \quad (2.69) \\ \langle \Delta x^2 \rangle_{2D} &= \frac{1}{2\pi} \frac{1}{B_0^2} \int_{-\infty}^{\infty} \int_{-\infty}^{\infty} \frac{2\Delta z P_{xx}^{2D}(k_x, k_y)}{D_{\perp}(k_x^2 + k_y^2)} \left[ 1 + \frac{e^{-D_{\perp}(k_x^2 + k_y^2)\Delta z} - 1}{D_{\perp}(k_x^2 + k_y^2)\Delta z} \right] dk_x dk_y \\ &= \frac{1}{2\pi} \frac{1}{B_0^2} \frac{2\Delta z}{D_{\perp}} \int_{-\infty}^{\infty} \int_{-\infty}^{\infty} \frac{P_{xx}^{2D}(k_x, k_y)}{k_{\perp}^2} [1 - g(D_{\perp} k_{\perp}^2 \Delta z)] dk_x dk_y, \end{aligned} \quad (2.70)$$

where  $k_{\perp}^2 \equiv k_x^2 + k_y^2$ , and  $g(u) \equiv (1 - e^{-u})/u$  behaves as a low-pass filter, i.e.,  $g(u) \approx 1$  for  $u \ll 1$  and monotonically declines to zero as  $u \rightarrow \infty$ . We then obtain an expression for the perpendicular diffusion coefficient for a single field line,  $D_{\perp} \equiv \langle \Delta x^2 \rangle / (2\Delta z)$ :

$$\begin{aligned} D_{\perp} &= \frac{1}{\sqrt{2\pi}} \frac{1}{B_0^2} \int_{-\infty}^{\infty} \frac{[1 - \cos(k_z \Delta z)]}{k_z^2 \Delta z} P_{xx}^{slab}(k_z) dk_z \\ &\quad + \frac{1}{2\pi} \frac{1}{B_0^2} \frac{1}{D_{\perp}} \int_{-\infty}^{\infty} \int_{-\infty}^{\infty} \frac{P_{xx}^{2D}(k_x, k_y)}{k_{\perp}^2} [1 - g(D_{\perp} k_{\perp}^2 \Delta z)] dk_x dk_y. \end{aligned} \quad (2.71)$$

Note that this formula is implicit in the sense that  $D_{\perp}$  appears on both sides of the equation, and non-perturbative in the sense that it applies for any  $P_{xx}^{slab}$  and  $P_{xx}^{2D}$ . Note also that a diffusion coefficient is only a valid concept when  $\langle \Delta x^2 \rangle \propto \Delta z$ , i.e., when this expression for  $D_{\perp}$  is constant in  $\Delta z$ . Next, we will show that this is indeed the case for sufficiently large  $\Delta z$ .

Equation (2.71) can be interpreted further when we consider that most observed power spectra of magnetic turbulence have power concentrated below and in the vicinity of a certain scale  $k_0$ , which is associated with a coherence scale,  $\ell = 1/k_0$ . Now if there is no 2D component, we have

$$D_{\perp}^{slab} = \frac{1}{\sqrt{2\pi}} \frac{1}{B_0^2} \int_{-\infty}^{\infty} \frac{[1 - \cos(k_z \Delta z)]}{k_z^2 \Delta z} P_{xx}^{slab}(k_z) dk_z. \quad (2.72)$$

Note that as  $\Delta z \rightarrow \infty$ ,

$$\frac{1 - \cos(k_z \Delta z)}{k_z^2 \Delta z} \rightarrow \pi \delta(k_z) \quad (2.73)$$

and

$$D_{\perp}^{slab} = \sqrt{\frac{\pi}{2}} \frac{P_{xx}^{slab}(0)}{B_0^2}. \quad (2.74)$$

This dependence, originally derived by Jokipii & Parker (1968), is approximately true for large  $\Delta z$ , i.e.,  $\Delta z \gg \ell_z = 1/k_{0z}$ , where  $\ell_z$  is a parallel coherence length, provided that  $P_{xx}^{slab}$  is roughly constant for  $k_z \ll k_{0z}$ . Equation (2.74) can also be expressed as

$$D_{\perp}^{slab} = \frac{\langle b_x^2 \rangle^{slab}}{B_0^2} \ell_c \quad (2.75)$$

for the correlation length  $\ell_c$ .

Next considering the limit of vanishing slab turbulence, we have  $D_{\perp} = D_{\perp}^{2D}$ , and

$$(D_{\perp}^{2D})^2 = \frac{1}{2\pi} \frac{1}{B_0^2} \int_{-\infty}^{\infty} \int_{-\infty}^{\infty} \frac{P_{xx}^{2D}(k_x, k_y)}{k_{\perp}^2} [1 - g(D_{\perp} k_{\perp}^2 \Delta z)] dk_x dk_y. \quad (2.76)$$



(A note on notation:  $D_{\perp}^{2D}$  refers to the perpendicular random walk in the limit of no slab turbulence, while  $\langle \Delta x^2 \rangle_{2D}$  refers to the contribution of 2D turbulence even if slab turbulence is present.) Since  $g$  acts as a low-pass filter,  $(1 - g)$  acts as a high-pass filter, which is close to 1 except that it becomes small within a “hole” in  $(k_x, k_y)$  space, for  $k_{\perp} \lesssim \sqrt{1/(D_{\perp} \Delta z)}$ . As  $\Delta z \rightarrow \infty$ , the width of this hole decreases, and our expression for  $D_{\perp}^{2D}$  is equivalent to that of Matthaeus et al. (1995). The effect of the hole around  $k_{\perp} = 0$  is negligible if its size is small compared with  $k_{0\perp}$ , so the expression

$$D_{\perp}^{2D} = \sqrt{\frac{1}{2\pi} \frac{1}{B_0^2} \int_{-\infty}^{\infty} \int_{-\infty}^{\infty} \frac{P_{xx}^{2D}(k_x, k_y)}{k_{\perp}^2} dk_x dk_y} \quad (2.77)$$

is valid for  $k_{0\perp}^2 D_{\perp} \Delta z \gg 1$ , i.e.,  $\langle \Delta x^2 \rangle \gg \ell_{\perp}$ , for perpendicular excursions greater than the scale  $\ell_{\perp} = 1/k_{0\perp}$ . Referring to the flux function (vector potential magnitude)  $a(x, y)$  for the 2D turbulence (see section 2.5), we have

$$P_{xx}^{2D}(k_x, k_y) = k_y^2 A(k_{\perp}) \quad \text{and} \quad P_{yy}^{2D}(k_x, k_y) = k_x^2 A(k_{\perp}), \quad (2.78)$$

where  $A(k_{\perp})$ , the (axisymmetric) power spectrum of  $a(x, y)$ , is defined as the Fourier transform of the correlation function  $\langle a(0, 0)a(x, y) \rangle$ . Then  $P_{xx}^{2D} + P_{yy}^{2D} = k_{\perp}^2 A$ , and assuming axisymmetry, the integral of  $P_{xx}^{2D}/k_{\perp}^2$  is half that of  $A$ . Thus we can relate  $D_{\perp}^{2D}$  to the variance of  $a(x, y)$ :

$$D_{\perp}^{2D} = \sqrt{\frac{1}{2\pi} \frac{1}{2B_0^2} \int_{-\infty}^{\infty} \int_{-\infty}^{\infty} A(k_{\perp}) dk_x dk_y} = \sqrt{\frac{\langle a^2 \rangle}{2B_0^2}}, \quad (2.79)$$

and finally we can define the “ultrascale”

$$\tilde{\lambda} \equiv \sqrt{\frac{\langle a^2 \rangle}{\langle b^2 \rangle^{2D}}}, \quad (2.80)$$

again yielding a form:

$$D_{\perp}^{2D} = \frac{\tilde{\lambda}}{\sqrt{2}} \frac{\sqrt{\langle b^2 \rangle^{2D}}}{B_0}. \quad (2.81)$$

By way of an analogy with hydrodynamic correlation functions (Batchelor 1953) we see that  $\tilde{\lambda}$  is the length associated with the curvature of the  $\langle aa' \rangle$  correlation at zero separation (see eq. [2.80]), and therefore may be thought of as the Taylor microscale or “inner scale” of the  $\langle aa' \rangle$  correlation function.

In summary, substituting equations (2.72) and (2.76) into equation (2.71) gives

$$D_{\perp} = D_{\perp}^{slab} + \frac{(D_{\perp}^{2D})^2}{D_{\perp}} \quad D_{\perp} = \frac{D_{\perp}^{slab}}{2} + \sqrt{\left(\frac{D_{\perp}^{slab}}{2}\right)^2 + (D_{\perp}^{2D})^2}, \quad (2.82)$$

for  $D_{\perp}^{slab}$  and  $D_{\perp}^{2D}$  as in equations (2.75) and (2.81), respectively (Matthaeus et al. 1995). We recall that this derivation assumes a diffusive random walk of the field line, which is only valid in the régime where  $\langle \Delta x^2 \rangle \propto \Delta z$ . This is true of the results for large  $\Delta z$  as given above, and evaluating  $\langle \Delta x^2 \rangle$  based on this formula for  $D_{\perp}$  verifies that the range of validity is for  $\sqrt{\langle \Delta x^2 \rangle}$  and  $\Delta z$  greater than the respective coherence lengths. This built-in check of the range of validity arises from not approximating the limits of  $d\Delta z'$  integration as  $\pm\infty$ . Equation (2.71) agrees with previous results while also providing a built-in check on the régime of validity. This will be important in the derivations of the non-axisymmetric field line random walk in Chapter 4 and the field-line separation in Chapter 5.

# Chapter 3

## Numerical Simulations

From the previous chapter, we can see that a key objective of the study of the random walk of turbulent field lines is to find the diffusion coefficients. An analytical method for studying the axisymmetric field line random walk was already shown in Section 2.7 (see also Ruffolo, Matthaeus, & Chuychai 2004), which reproduces the calculation of Matthaeus et al. (1995). In this chapter, we will present numerical techniques to simulate the axisymmetrically turbulent magnetic field lines and then directly compute their diffusion coefficients. To obtain the magnetic field lines, we first generate the turbulent magnetic field in the simulation box. The shapes of 2D and slab spectra are set in this part. The next section shows how to solve the field line equations by numerical methods. After we solve the field line equations, the outputs are positions along field line trajectories. Then we calculate the diffusion coefficients for pure slab and 2D+slab cases from the simulation data and compare them with the theoretical values. Moreover, the effects of the simulation box, representations of turbulent fields, and suitable length scale for simulated field lines are also discussed in this chapter.

### 3.1 Generating Turbulent Magnetic Fields

From (2.48), we can write the differential equation for the magnetic field line as

$$\begin{aligned}\frac{dx}{dz} &= \frac{b_x(x, y, z)}{B_0} \\ \frac{dy}{dz} &= \frac{b_y(x, y, z)}{B_0}.\end{aligned}\tag{3.1}$$

In order to solve the field line equations, we need to know the function of the magnetic field at each position. Since the system we consider is random and turbulent, it is not appropriate to specify the function for a magnetic field directly in position space. Therefore, the magnetic field components on the right hand sides of the field line equation are generated in wave number space ( $k$ -space) before conversion to real space. We instead define the power spectrum as a function in  $k$ -space, which is the Fourier transform of the magnetic correlation function  $R_{ij}(\vec{r}) = \langle b_i(0)b_j(\vec{r}) \rangle$ . The spectrum that we usually use for the magnetic turbulence is a Komolgorov spectrum over a wide range of wave numbers. The magnetic fluctuations in (3.1) are composed of slab and 2D turbulence. Because the slab turbulence depends only on  $z$  and the 2D turbulence depends on  $x$  and  $y$  positions, we separately generate them in  $k_z$  and  $(k_x, k_y)$  spaces, respectively. After that, the magnetic field in Fourier space is converted to position space by an inverse fast Fourier transform. For numerical computation, we cannot generate the magnetic fluctuations continuously in space due to the limitation of the computer. Thus the magnetic field is constructed only on the grid points in the simulation box. To avoid bias due to a periodicity effect (we will discuss this effect again in Section 3.3), we have to generate the magnetic field in a large (but finite) box. Therefore, in this part, the parameters that we need to input are the sizes in  $x$ ,  $y$ , and  $z$  directions of the simulation box ( $L_x$ ,  $L_y$ , and  $L_z$ ), the number of grid points ( $N_x$ ,  $N_y$ , and  $N_z$ ), the total root-mean-squared fluctuation ( $\delta b$ ), the fraction of 2D and slab energy, the shapes of the 2D and slab power spectra, and coherence lengths ( $\ell_z$  and  $\ell_\perp$ ).

For slab turbulence, we set the power spectrum for simulations as

$$P_{xx}^{slab}(k_z) = P_{yy}^{slab}(k_z) = \frac{C^{slab}}{[1 + (k_z \ell_z)^2]^{5/6}}, \quad (3.2)$$

where  $C^{slab}$  is a normalization constant that depends on the slab energy and  $\ell_z$  is the parallel coherence length. From the function of the slab spectrum, the slab magnetic fluctuations in  $k_z$  space are

$$b_x^{slab}(k_z) = \sqrt{P_{xx}^{slab}(k_z)} \exp[i\varphi(k_z)] \quad (3.3)$$

$$b_y^{slab}(k_z) = \sqrt{P_{yy}^{slab}(k_z)} \exp[i\varphi(k_z)], \quad (3.4)$$

where  $\varphi$  is a random phase number and  $k_z$  is a discrete number which is  $k_z = j2\pi/L_z$ , for  $j = 1, 2, 3, \dots, N_z/2 - 1$ . Eqs. (3.3) and (3.4) are used only for  $k_z > 0$ . The possible positive  $k_z$ -modes for slab turbulence lie between  $2\pi/L_z$  and  $N_z\pi/L_z$ . We consider not only the fluctuations at positive  $k_z$ -modes, but also the negative ones. The magnetic field in real space that we need is real, so the condition for the Fourier transform is  $b_i(-k_z) = [b_i(k_z)]^*$ , where  $i$  refers to the  $x$  or  $y$  component. For the case of  $j = N_z/2$ , with  $k_z = N_z\pi/L_z$ , for a discrete (periodic) FT we have

$$\begin{aligned} b_i^{slab}(k_z) &= b_i^{slab}(-k_z) \\ &= b_i^{slab}(k_z)^*, \end{aligned} \quad (3.5)$$

so we instead use

$$b_i^{slab}(k_z = \pi N_z/L_z) = \sqrt{P_{ii}^{slab}} \cos \varphi(k_z). \quad (3.6)$$

Since we use the inverse fast Fourier transform, the number of grid points  $N_z$  needs to be in the form  $2^N$ . Figure 3.1 shows an example of the slab power spectrum of (3.2). Next we pass  $b_x^{slab}(k_z)$  and  $b_y^{slab}(k_z)$  to inverse fast Fourier transforms in one dimension. What we obtain is  $b_x^{slab}(z)$  and  $b_y^{slab}(z)$  on the grid points, which means  $z = j(L_z/N_z)$ , where  $j = 0, 1, 2, \dots, N_z - 1$ .

$$A(k_{\perp}) = \frac{C^{2D}}{[1 + (k_{\perp}\ell_{\perp})^2]^{7/3}}. \quad (3.7)$$

According to (2.18), the 2D fluctuations in  $(k_x, k_y)$  are

$$b_x^{2D}(k_x, k_y) = -ik_y\sqrt{A(k_{\perp})}\exp[i\varphi(k_x, k_y)] \quad (3.8)$$

$$b_y^{2D}(k_x, k_y) = ik_x\sqrt{A(k_{\perp})}\exp[i\varphi(k_x, k_y)], \quad (3.9)$$

For 2D turbulence, we instead specify the power spectrum  $A(k_x, k_y)$  because the power spectra  $P_{xx}^{2D}(k_x, k_y)$  and  $P_{yy}^{2D}(k_x, k_y)$  can be written in terms of  $A(k_x, k_y)$  as shown by the relations (2.22) and (2.23). For the axisymmetric case, we set  $A(k_x, k_y)$  to be rotationally invariant in the  $k_x - k_y$  plane. The contours of constant  $A(k_x, k_y)$  are circles. The function of  $A(k_x, k_y)$  that we usually use in this work is in the form of (2.42), where  $\varphi(k_x, k_y)$  is a random phase and  $\varphi(-k_x, -k_y) = -\varphi(k_x, k_y)$  for the real values in  $b_x^{2D}(x, y)$  and  $b_y^{2D}(x, y)$ . Here,  $k_x$  and  $k_y$  are also discrete numbers, which are  $k_x = n(2\pi/L_x)$  and  $k_y = m(2\pi/L_y)$ , where  $n = 1, 2, 3, \dots, N_x/2$  and  $m = -N_y/2, \dots, -1, 0, 1, 2, 3, \dots, N_y/2$ , and the factor  $\exp[i\varphi(k_x, k_y)]$  is converted to  $\cos[\varphi(k_x, k_y)]$  where appropriate [see eq. (3.6)]. Note that  $N_x$  and  $N_y$  also need to be integer powers of 2. After that we use the inverse fast Fourier transform in two dimensions to transform them to  $b_x^{2D}(x, y)$  and  $b_y^{2D}(x, y)$  which are on the grid points in the  $x$ - $y$  plane of the simulation box. Furthermore, the inverse Fourier transform of the power spectrum  $A(k_x, k_y)$  yields the potential function  $a(x, y)$ . Figure 3.2 illustrates contour plots of the potential function  $a(x, y)$  associated with various functions  $A(k_{\perp})$  and various values of  $\ell_{\perp}$ . From this figure, we can see that the shape of the spectrum affects the contour plot of the 2D potential function and the size of 2D islands

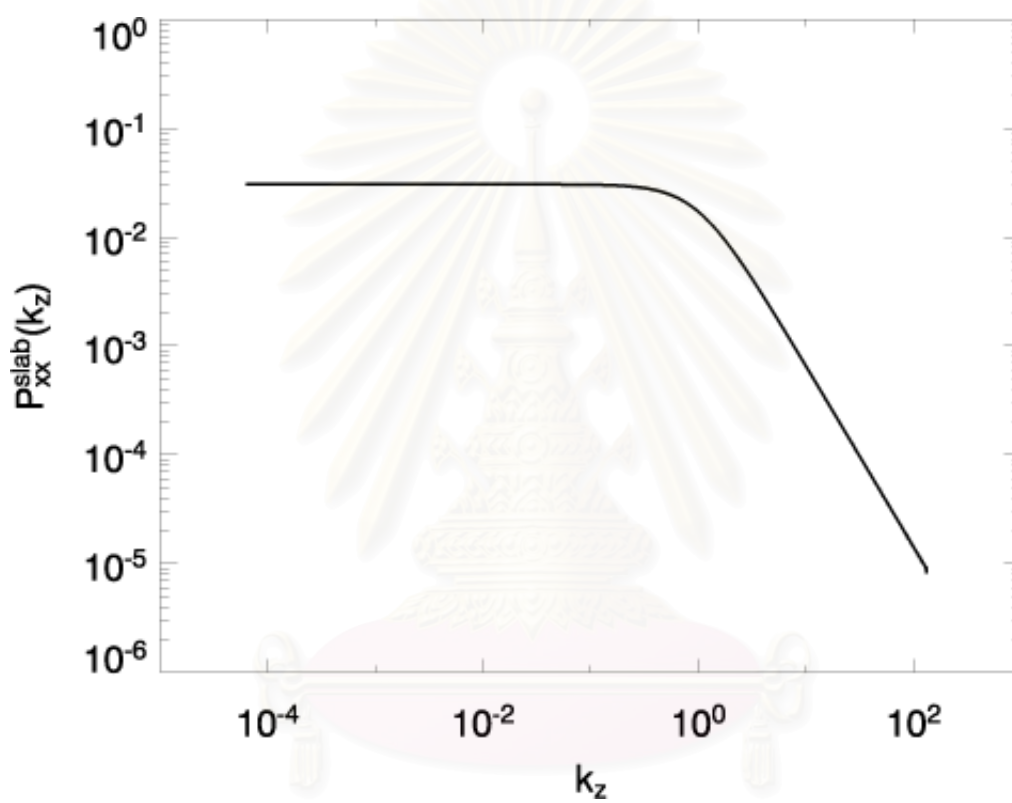


Figure 3.1: Example of a slab power spectrum [Eq. (3.2)].

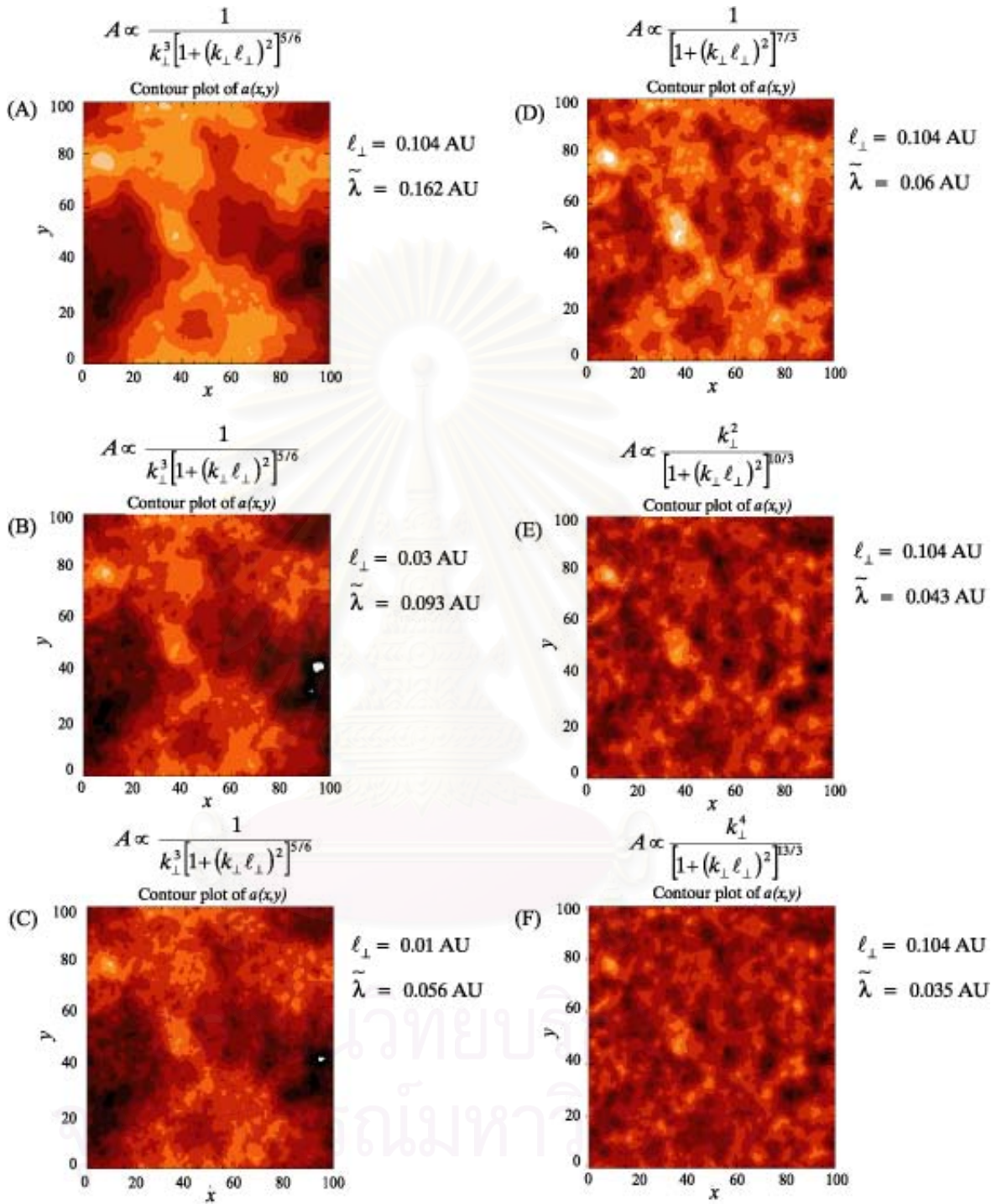


Figure 3.2: Contour plots of 2D turbulence and their spectra. Note that all length scales in the figures (A)-(F) are in units of  $\ell_z$ , which is 0.027 AU.



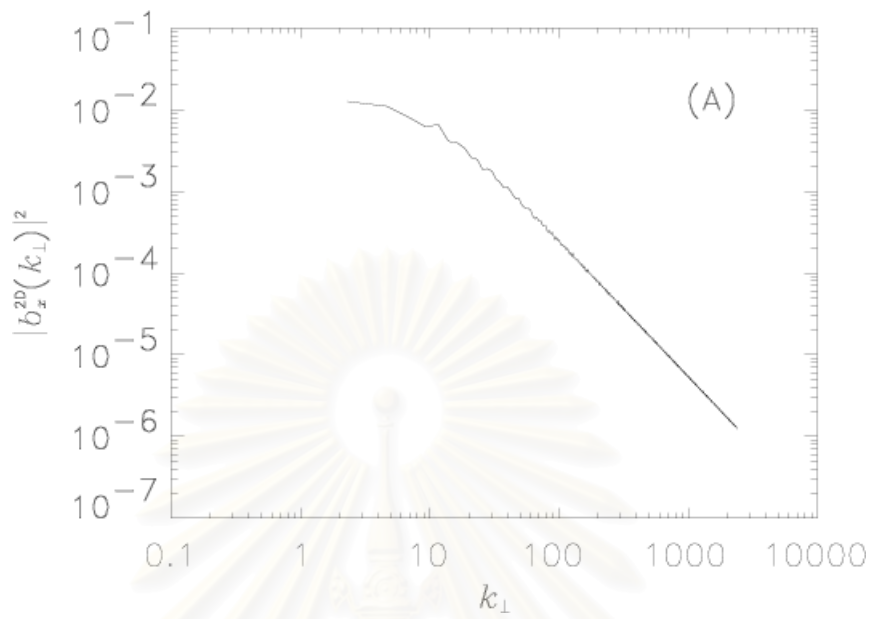


Figure 3.3: Shape of the 2D spectrum for Figure 3.2(A).

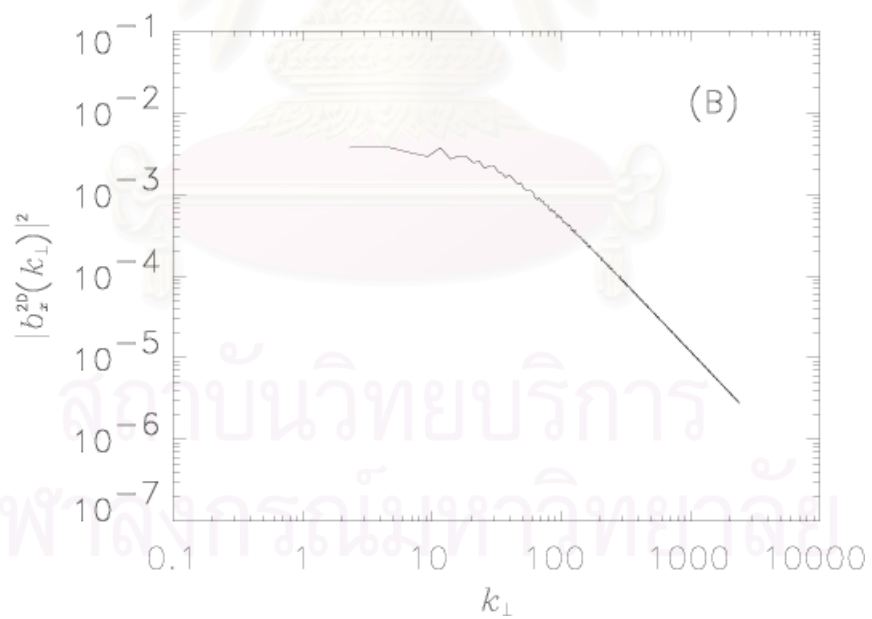


Figure 3.4: Shape of the 2D spectrum for Figure 3.2(B).

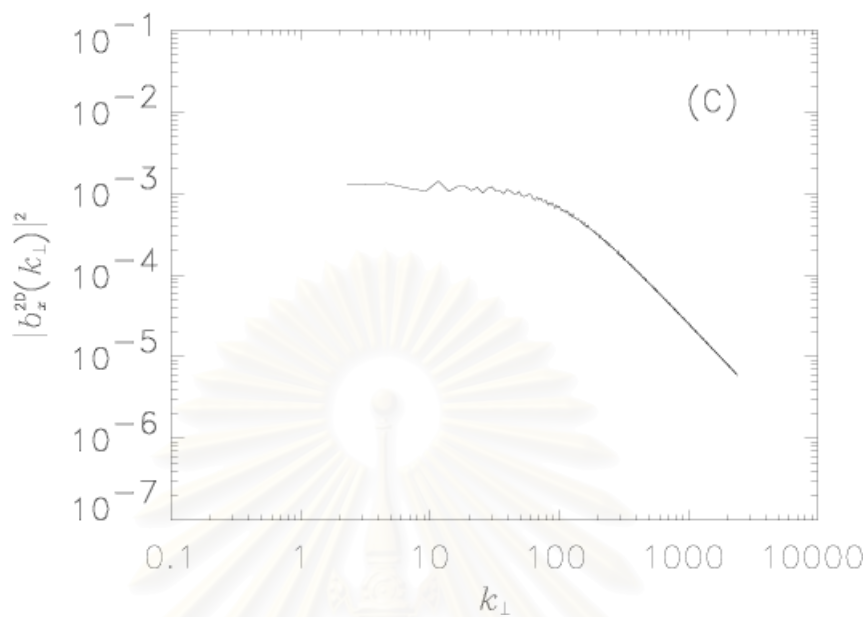


Figure 3.5: Shape of the 2D spectrum for Figure 3.2(C).

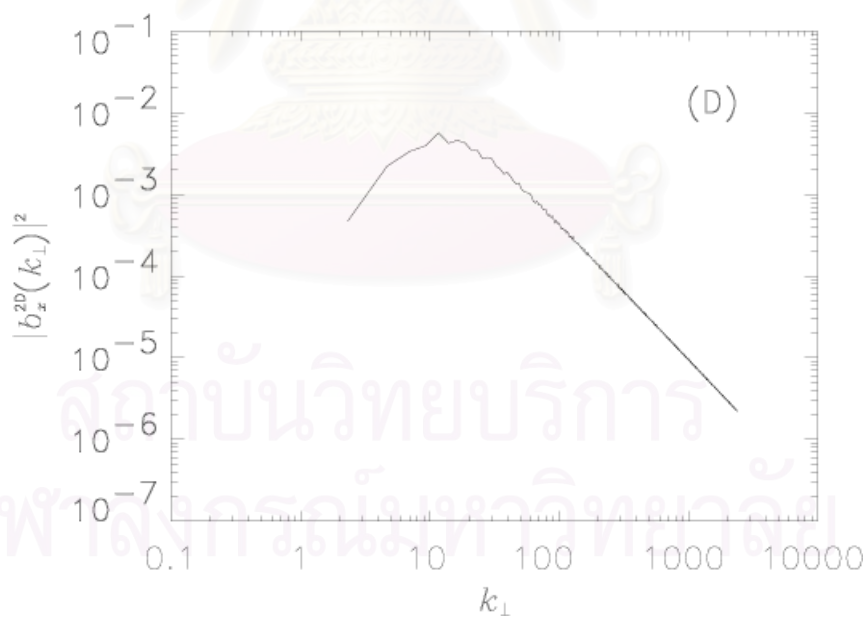


Figure 3.6: Shape of the 2D spectrum for Figure 3.2(D).

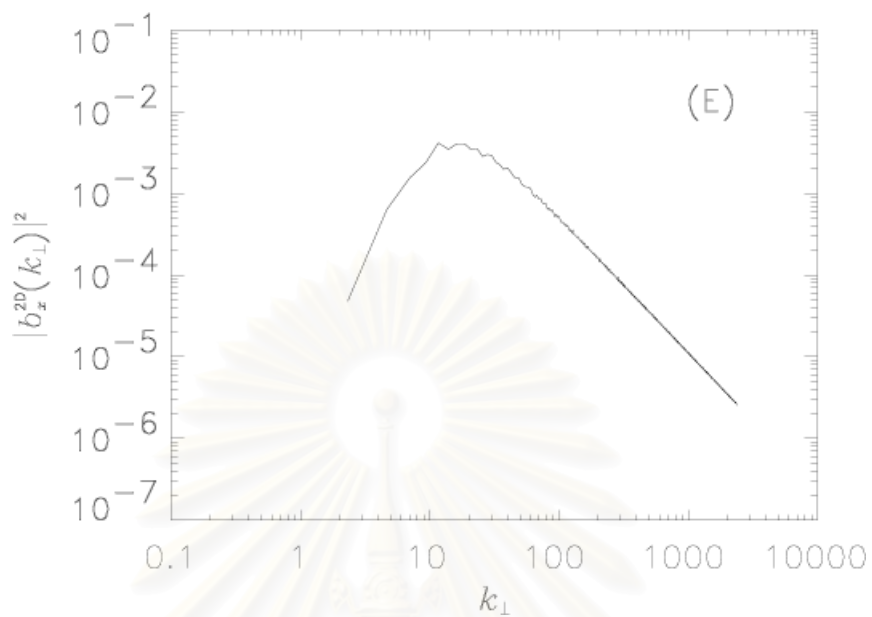


Figure 3.7: Shape of the 2D spectrum for Figure 3.2(E).

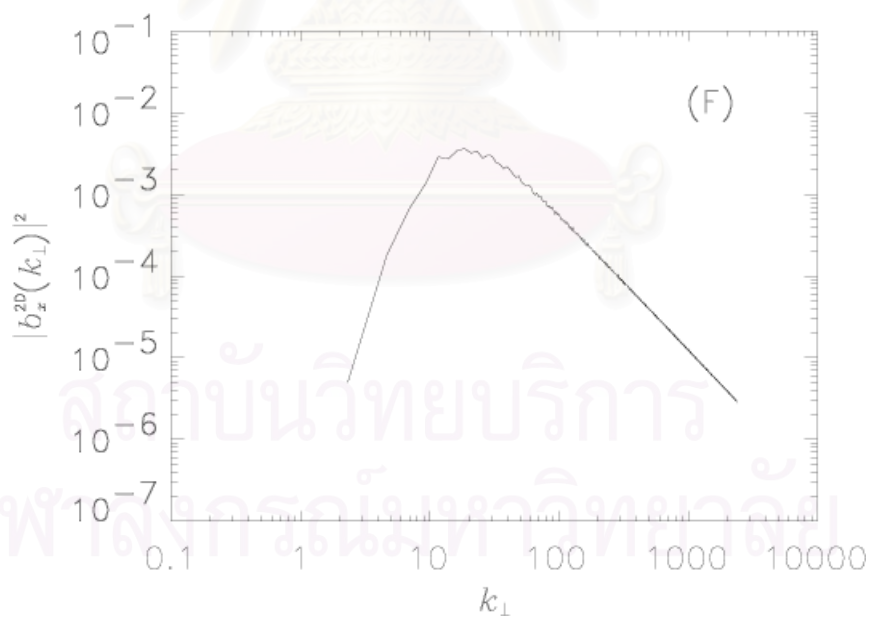


Figure 3.8: Shape of the 2D spectrum for Figure 3.2(F).

depends on  $\ell_{\perp}$  and  $\tilde{\lambda}$ . The plots of  $|b_x^{2D}(k_{\perp})|^2$  and  $k_{\perp}$  in Figures 3.3 to 3.8 come from the summation of  $|b_x^{2D}(k_x, k_y)|^2$  over all directions in the interval at each  $k_{\perp}$ . This quantity is proportional to the omnidirectional power spectrum (OPS), which we discussed before in Section 2.6.

## 3.2 Tracing the Magnetic Field Lines

Our initial aims of the numerical simulations are to trace the magnetic field lines in 2D+slab turbulence and to calculate the diffusion coefficients. In (3.1), we substitute 2D and slab fluctuations into  $b(x, y, z)$ . Thus, for field line tracing, we numerically solve the field line equations,

$$\begin{aligned}\frac{dx}{dz} &= \frac{b_x^{slab}(z) + b_x^{2D}(x, y)}{B_0} \\ \frac{dy}{dz} &= \frac{b_y^{slab}(z) + b_y^{2D}(x, y)}{B_0}.\end{aligned}\tag{3.10}$$

To solve the differential equations of field lines, what we have to know are the initial positions  $(x_0, y_0, z_0)$  of each field line and the function of the magnetic field at any position  $(x, y, z)$ . From the previous section, we have the 2D and slab magnetic fields only on a real-space grid in the simulation box. Therefore, we can compute the magnetic field at any position from nearest known points on the grid by using linear interpolation for slab turbulence and bi-linear interpolation to estimate the magnetic field at any position  $(x, y, z)$ . Outside the simulation box, we repeat the magnetic field inside the simulation box that we generate as a periodic function due to the Fourier transform.

For evaluation of the trajectories of field lines, we use a fourth-order Runge-Kutta method with adaptive time stepping regulated by a fifth-order error estimate step (Press et al. 1992) to solve the field line equations (3.10). With

this method, we can set the required accuracy ( $racc$ ), related to the relative error between a fifth-order Runge-Kutta and the embedded fourth-order Runge-Kutta methods. The outputs from solving field line equations are positions  $(x,y,z)$  along field line trajectories.

The numerical code that we use was developed by the group of Prof. William H. Matthaeus at Bartol Research Institute, University of Delaware, and I was a member of the development team. This code is a parallel implementation of a versatile algorithm for computation of streamlines, magnetic field lines, or charged particle trajectories (see Appendix A for a test of the code). The code works by programming the master node to pass out “jobs” to the worker nodes. Each job includes the initial data and some parameters. Load balancing is achieved in a standard way: When a node has finished a job, it asks the master if there is another job to do. The results of each job are written to disk.

Figures 3.9, 3.10, and 3.11 show samples of magnetic field trajectories in pure slab, pure 2D, and 2D+slab fields, respectively. We can clearly see from Figure 3.9 that the magnetic field lines in pure slab turbulence depend only on the  $z$ -component, not on  $x$ - or  $y$ -components. A field line in pure 2D turbulence follows a contour of the 2D potential function, which depends only on  $x$  and  $y$  coordinates. Therefore, the features of field lines in 2D+slab turbulence are a kind of combination between slab and 2D fields. Neither slab itself nor 2D itself is realistic because the field lines in slab turbulence are completely independent of  $x$  and  $y$ , while the field lines in the 2D turbulence are not diffusive at all. For 2D+slab turbulence, there is a field line random walk as observed in space as we already explained in Chapter 2. Finally, we again summarize the steps of numerical simulations by the diagram in Figure 3.12.

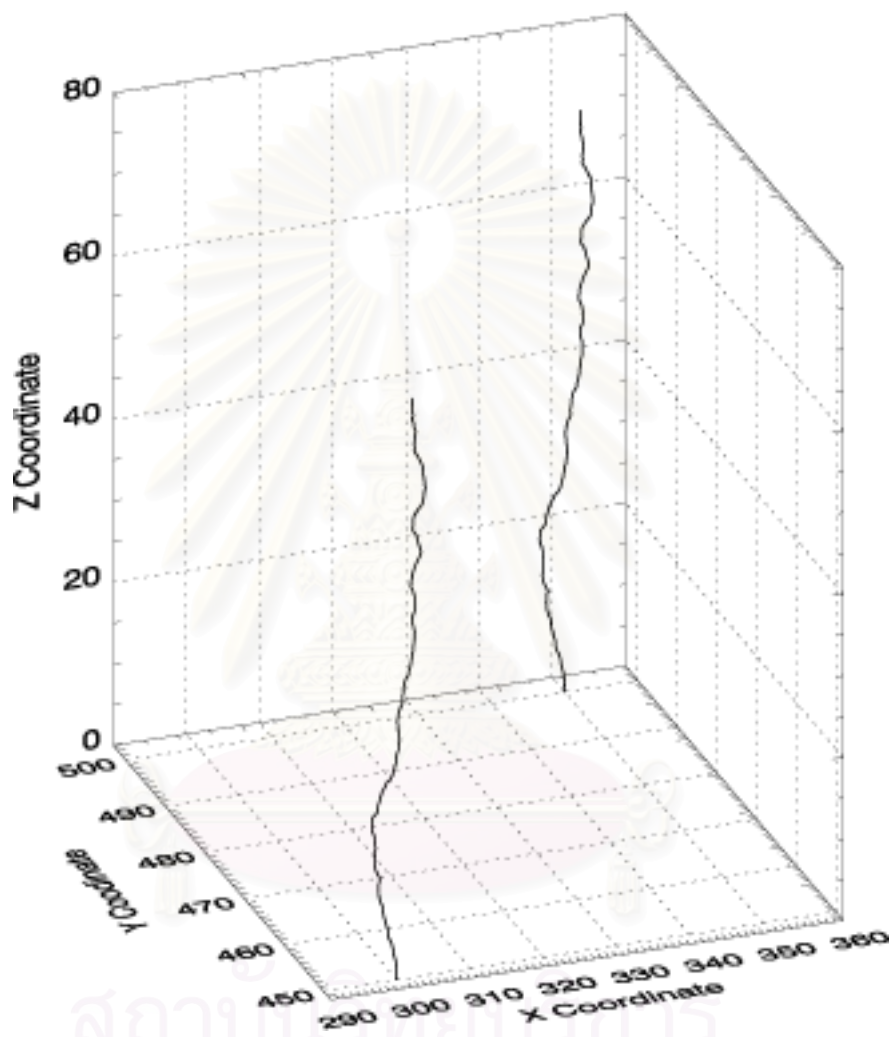


Figure 3.9: Example of two trajectories of magnetic field lines in pure slab turbulence.

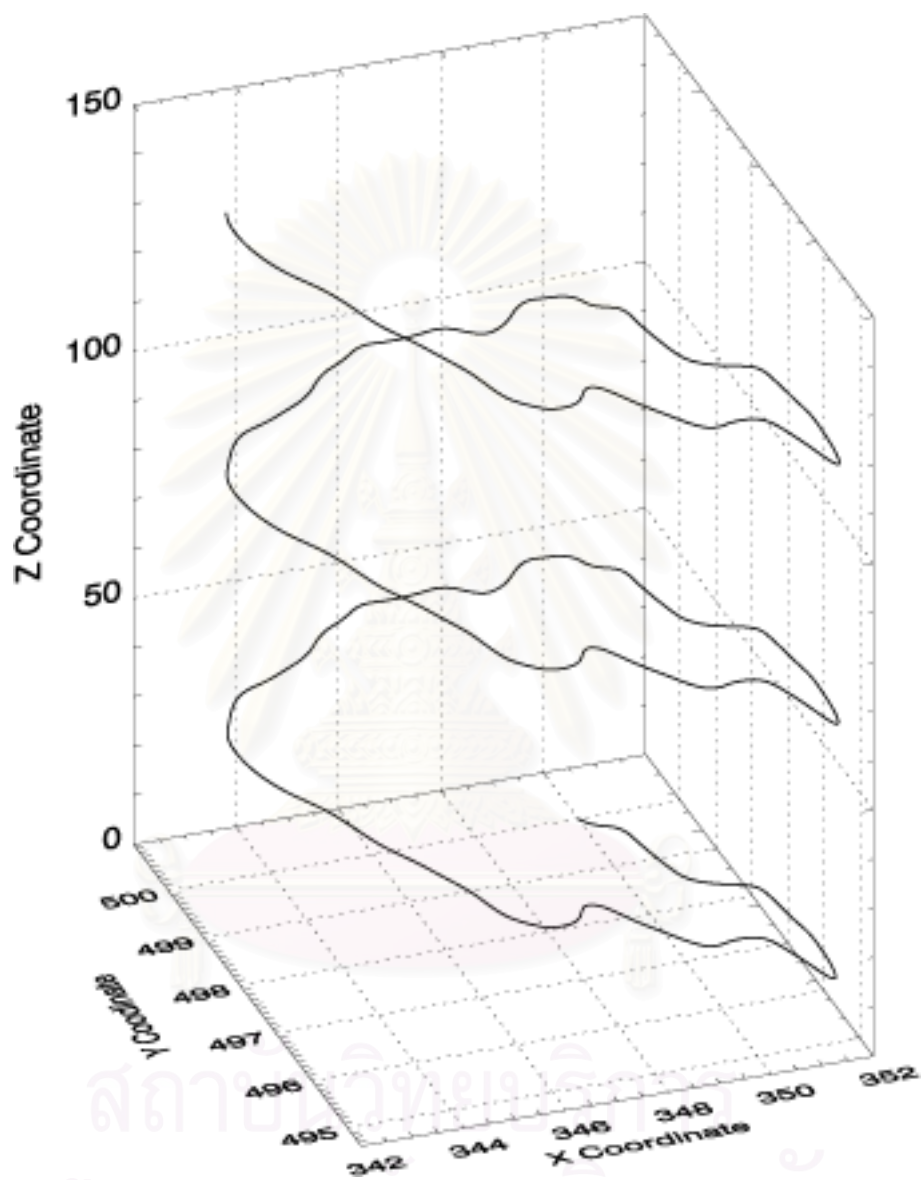


Figure 3.10: Example of a trajectory of a magnetic field line in pure 2D turbulence.

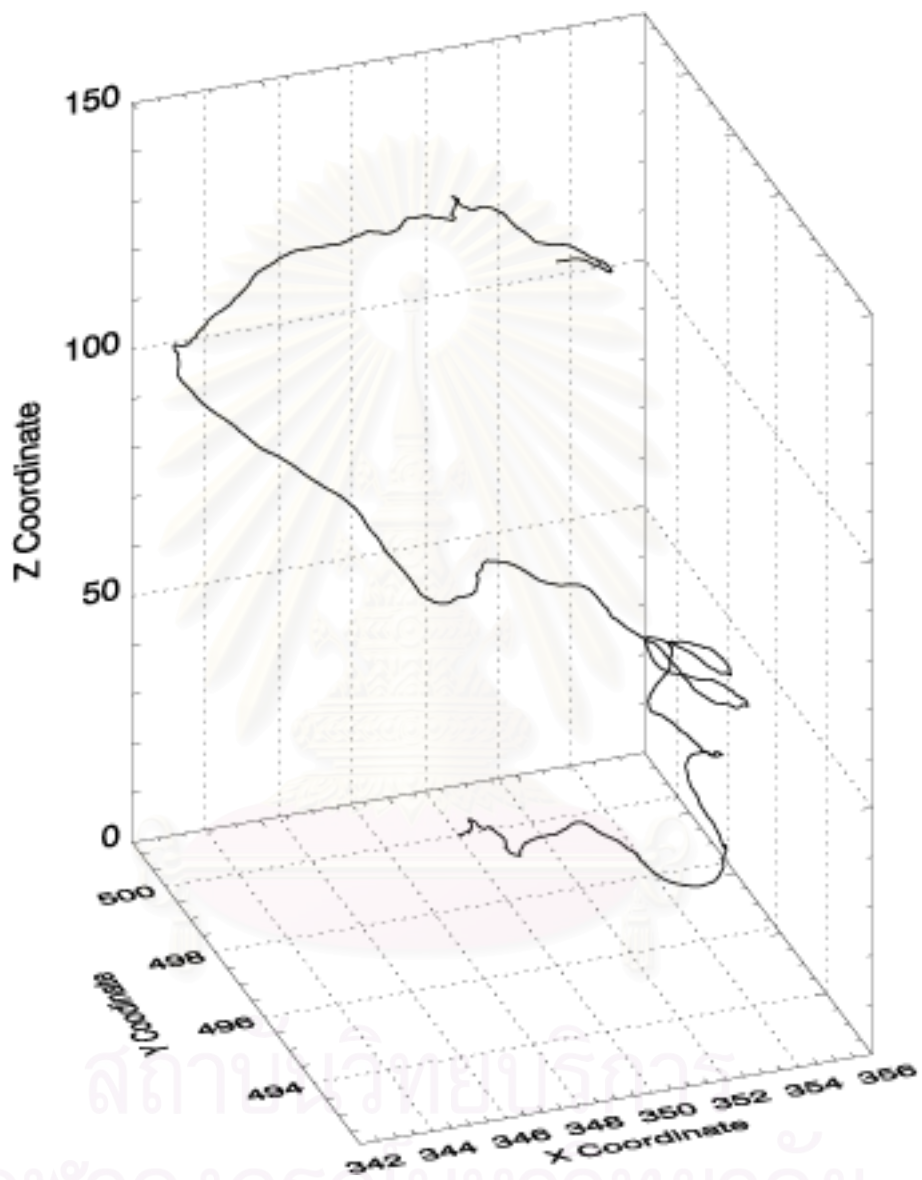


Figure 3.11: Example of a magnetic field line in 2D+slab turbulence.



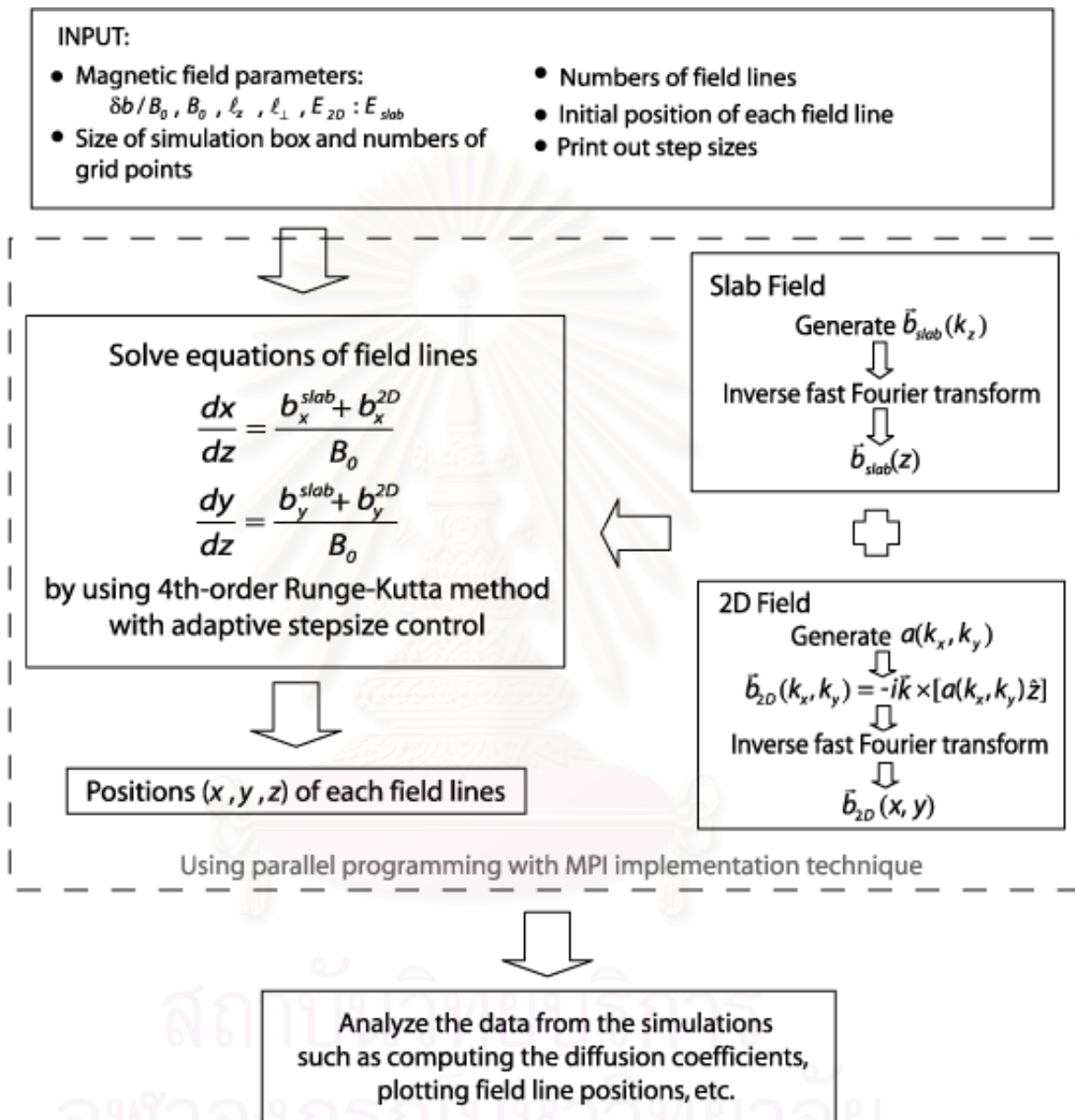


Figure 3.12: Diagram of steps in the field line simulations.

### 3.3 The Diffusion Coefficients: Comparison between Numerical and Theoretical Results

After we trace the magnetic field lines and get their positions, we analyze the data by plotting the trajectories or calculating the diffusion coefficients. For the diffusion coefficient computation, we should have a sufficient set of magnetic field lines and realizations to obtain good statistics. Thus, in our work, we usually trace many field lines (over 1,000 lines) for random initial positions and realizations of 2D turbulence in the simulation box. In this section, we show two cases of field line random walk computations. The first is for slab turbulence, in which the field line trajectories are purely diffusive, and another case is for 2D+slab, a case that is close to the nature of the interplanetary magnetic field. In this section, the length scales are all in parallel correlation scale units.

#### 3.3.1 Computation of Field Line Random Walk for Slab Turbulence

For the pure slab case, we generate 1,000 field lines in a large box with uniformly random initial positions of field lines in the box. To avoid the periodic effect, we set  $L_z = 100,000\ell_z$  and trace the field lines to only  $1/40$  of the box length. The number of grid points in the  $z$  direction ( $N_z$ ) is  $2^{22}$  points. The Kolmogorov spectrum at high  $k$  has been used for slab turbulence, according to

$$P_{xx}(k_z) = P_{yy}(k_z) = \frac{C}{[1 + (k_z\ell_z)^2]^{5/6}}. \quad (3.11)$$

In the simulations, we set  $\ell_z = 1$  and vary  $\delta b/B_0 = 0.1, 0.3, 0.5, 0.7,$  and  $0.9$ . After we simulate the field lines for each case, we directly compute  $\langle \Delta x^2 \rangle$  for each  $\Delta z$  from the data. That is we collect all  $(\Delta x)^2$  values for each  $\Delta z$  from the

field line data and then average them. For calculations over a limited range of  $z$ ,  $0 < z < z_{max}$ , we can compare field line locations at pairs of  $z$  values separated by  $0 < \Delta z < z_{max}$ . For small  $\Delta z$ , we have more samples than for large  $\Delta z$ , or we can say that we obtain the better statistics for small  $\Delta z$  than for large  $\Delta z$ . Figure 3.13 shows how we have better statistics for smaller  $\Delta z$ . Next we plot the graph between  $\langle(\Delta x)^2\rangle$  and  $\Delta z$  such as in Figure 3.14. If we plot Figure 3.14 in a log-log scale, shown as Figure 3.15, we can identify a free streaming region,  $\langle(\Delta x)^2\rangle \propto (\Delta z)^2$ , at  $\Delta z \lesssim \ell_c$ . Figure 3.16 illustrates the periodic effect when we trace the magnetic field lines over more than a simulation box (using periodic boundary conditions). To avoid this, we normally trace the field lines over only a few percent of the box length. After we have the data of  $\langle(\Delta x)^2\rangle$  vs.  $\Delta z$ , we calculate the derivative at each  $\Delta z$ , which is called the “running diffusion coefficient,”  $\tilde{D}_x$ . We compare it with the theoretical value,

$$D_{\perp}^{slab} = \frac{\ell_c \delta b^2}{2B_0^2}. \quad (3.12)$$

To easily see the comparison between theoretical and numerical values, we make another plot that is the partial average of the running diffusion coefficient. The partial average is simply  $\langle\Delta x^2\rangle/(2\Delta z)$ . It is the average of every earlier running diffusion coefficient up to the  $\Delta z$  we consider. If the running diffusion coefficient is nearly constant from 0 to  $\Delta z$ , the partial average is statistically more accurate.



Figure 3.13: Schematic of a simulated field line. The dotted line represents the data from the simulations at each  $z$ . Suppose we trace a field line over only  $10d$ , where  $d$  is the print out step size. We can see that the number of samples for  $\Delta z = 1d$  is equal to ten while for  $\Delta z = 10d$  there is only one sample for this field line.

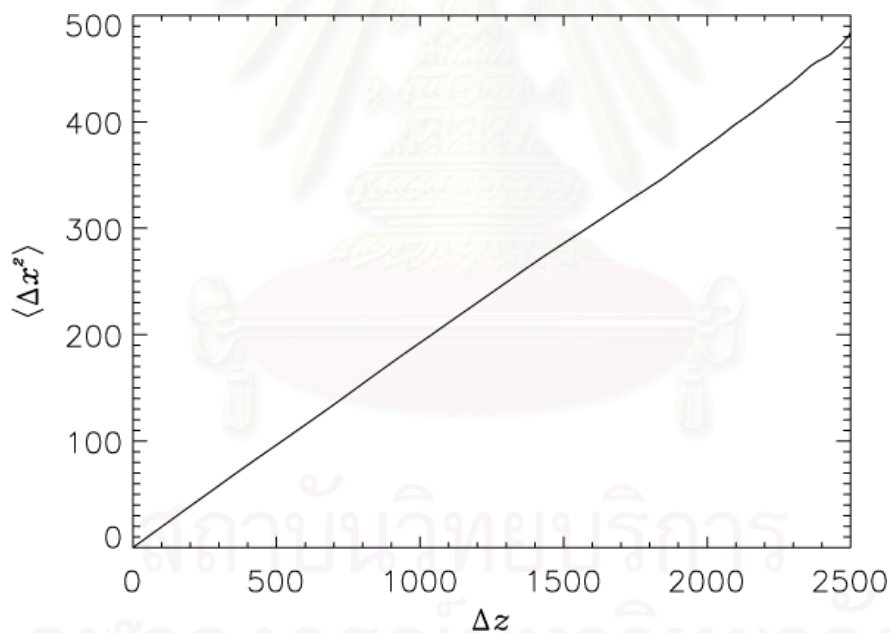


Figure 3.14: Example of the plot between  $\langle(\Delta x)^2\rangle$  of 1,000 field lines and  $\Delta z$  when we set  $N_z = 2^{22}$ ,  $L_z = 100,000\ell_z$  and  $\delta b/B_0 = 0.5$ .

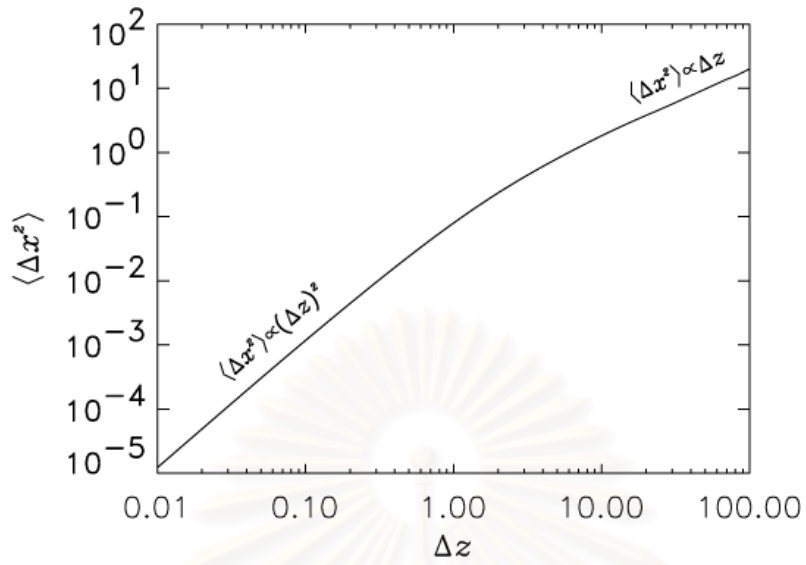


Figure 3.15: Illustration of the free streaming region,  $\langle \Delta x^2 \rangle \propto (\Delta z)^2$ , when  $\Delta z \lesssim \ell_c$ .

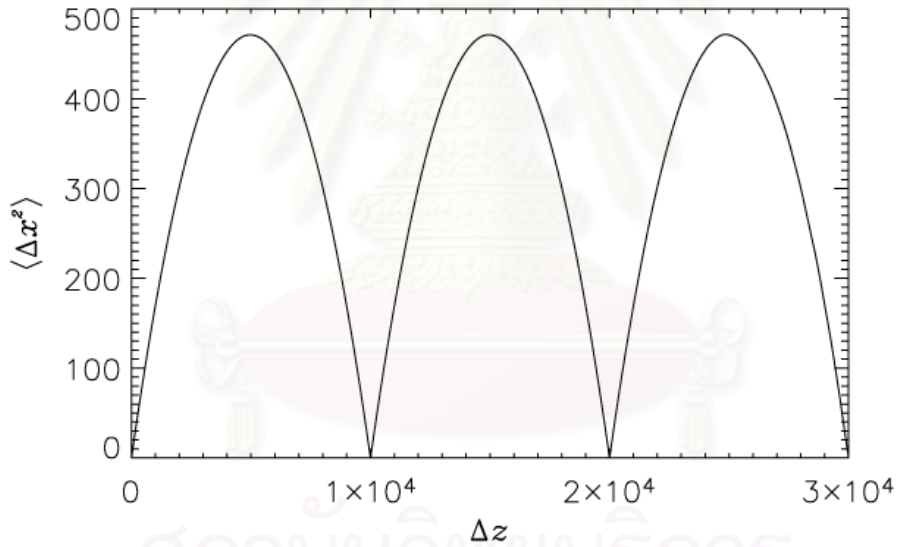


Figure 3.16: Periodicity effect when we trace the magnetic field lines over three simulation boxes. Here, we set  $N_z = 2^{22}$ ,  $L_z = 10,000\ell_z$  and  $\delta b/B_0 = 0.5$ . We can obviously see that the relation between  $\langle (\Delta x)^2 \rangle$  and  $\Delta z$  is not linear for large  $\Delta z$ . It is back to zero every one box length. Usually we avoid this numerical artifact by using only a few percent of the box length  $L_z$ .

A comparison between theory and numerical simulations is shown in Table 3.1 and Figure 3.17. The running diffusion coefficient of each case and the partial averages are shown in Figures 3.18-3.22. In Table 3.1, we show diffusion coefficients from two versions of the theory. One is the diffusion coefficient from the theory calculated from the integral Fourier transform like we presented in Chapter 2, which are the correlation length ( $\ell_c$ ) and the ultrascale ( $\tilde{\lambda}$ ) calculated from the integral Fourier transform such as equations (2.30) and (2.41), respectively. Another one is the diffusion coefficient from discrete theory in which the  $\vec{k}$ -integrals are replaced by discrete sums over  $\vec{k}$  modes used in the simulations. For the discrete theory, we can compute the diffusion coefficient for the slab component by using (2.30) but instead of considering the power spectrum at zero wave number, we use the power spectrum at the discrete  $k_z$  modes which are closest to zero wave number from the magnetic field data in  $k_z$  space. The diffusion coefficient from simulations is the average between the partial average of the running diffusion coefficients in  $x$  and  $y$  directions at  $\Delta z = 500$ .

Table 3.1: Comparison between diffusion coefficients from theory and simulation.

$\delta b/B_0$	$D_{\perp}$ theory	$D_{\perp}$ discrete theory	$D_{\perp}$ simulation
0.1	0.0037	0.0039	0.0039
0.3	0.0336	0.0351	0.0351
0.5	0.0934	0.0976	0.0974
0.7	0.1830	0.1913	0.1913
0.9	0.3025	0.3163	0.3157

From the results, we can see that the diffusion coefficients from numerical simulations of field line tracing basically agree with the theoretical values. From the running diffusion coefficient plot, we can observe free streaming behavior at the beginning ( $\Delta z \ll \ell_c = 0.747\ell_z$ ) and diffusive behavior for long  $\Delta z$  ( $\Delta z \gg$

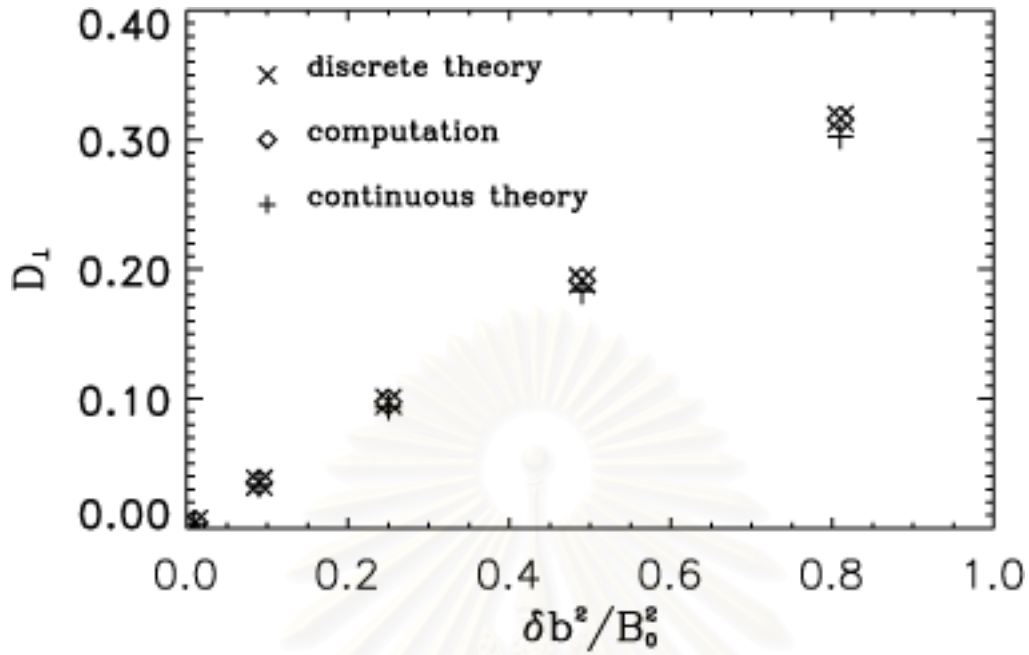


Figure 3.17: Comparison of  $D_{\perp}$  from theory and from numerical simulations versus  $\delta b^2 / B_0^2$ .

$\ell_c$ ). The large fluctuations in the running diffusion coefficient plot occur near the maximum  $\Delta z$  that we simulate because the number of data that we use to calculate the statistics for the diffusion coefficient is much smaller than for short  $\Delta z$ . The slight difference between the continuous and the discrete theories occurs since we directly compute the discrete theory from available wave vector modes in the generated magnetic field data while, in the continuous theory, we consider the continuous spectrum over all  $k_z$  space. The values of the diffusion coefficients from the simulations are closer to the discrete theory than to the continuous theory that uses Fourier integrals. This implies that the difference between simulations and continuous theory is mostly due to discretization error.

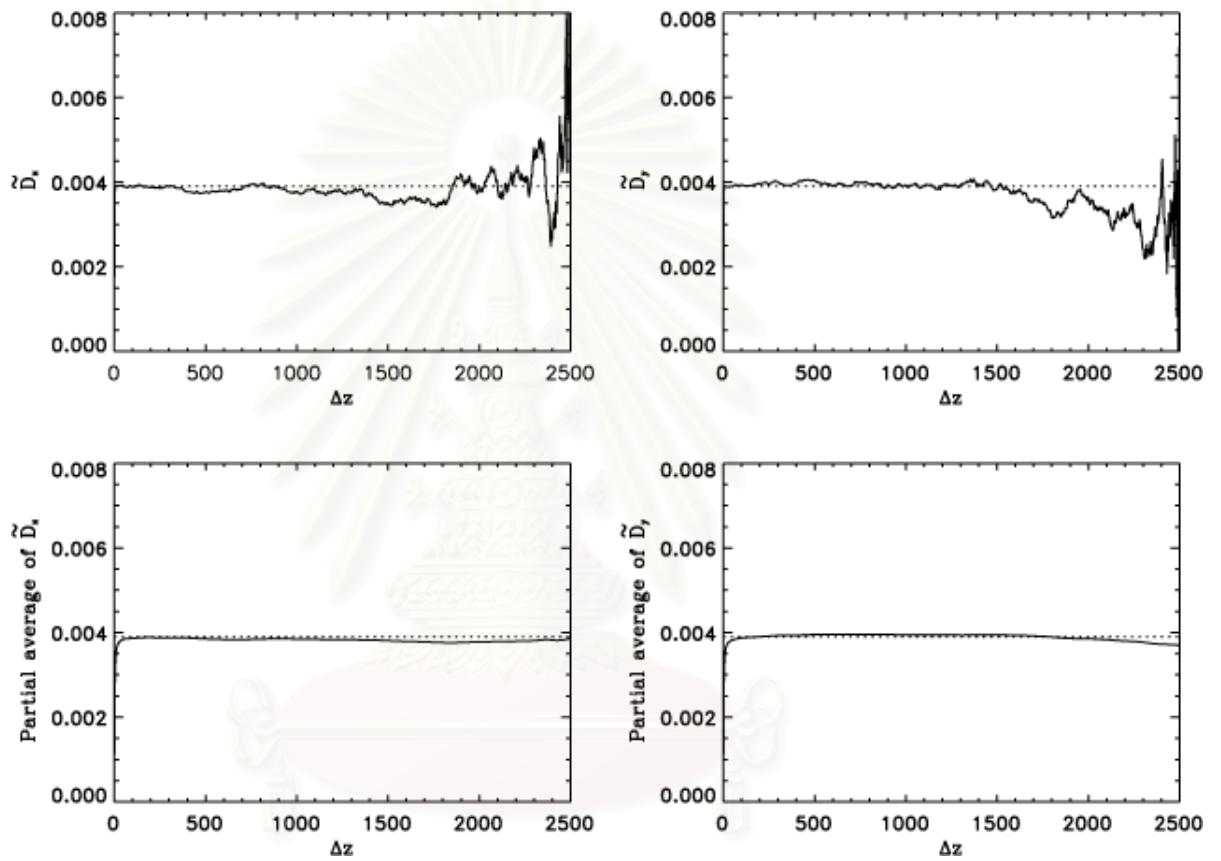


Figure 3.18: Diffusion coefficients from simulations (solid lines) and expected values from discrete theory (dashed lines) for  $\delta b/B_0 = 0.1$ .

จุฬาลงกรณ์มหาวิทยาลัย



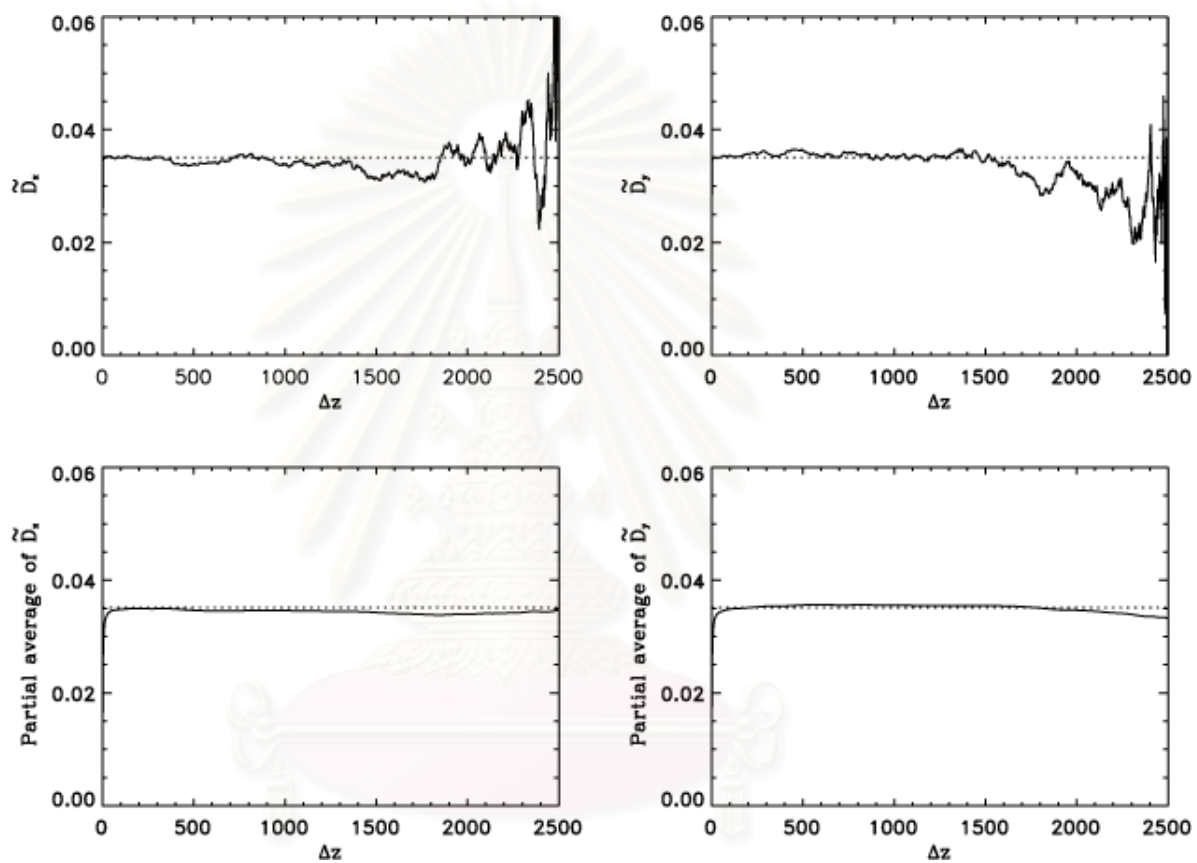


Figure 3.19: Diffusion coefficients from simulations (solid lines) and expected values from discrete theory (dashed lines) for  $\delta b/B_0 = 0.3$ .

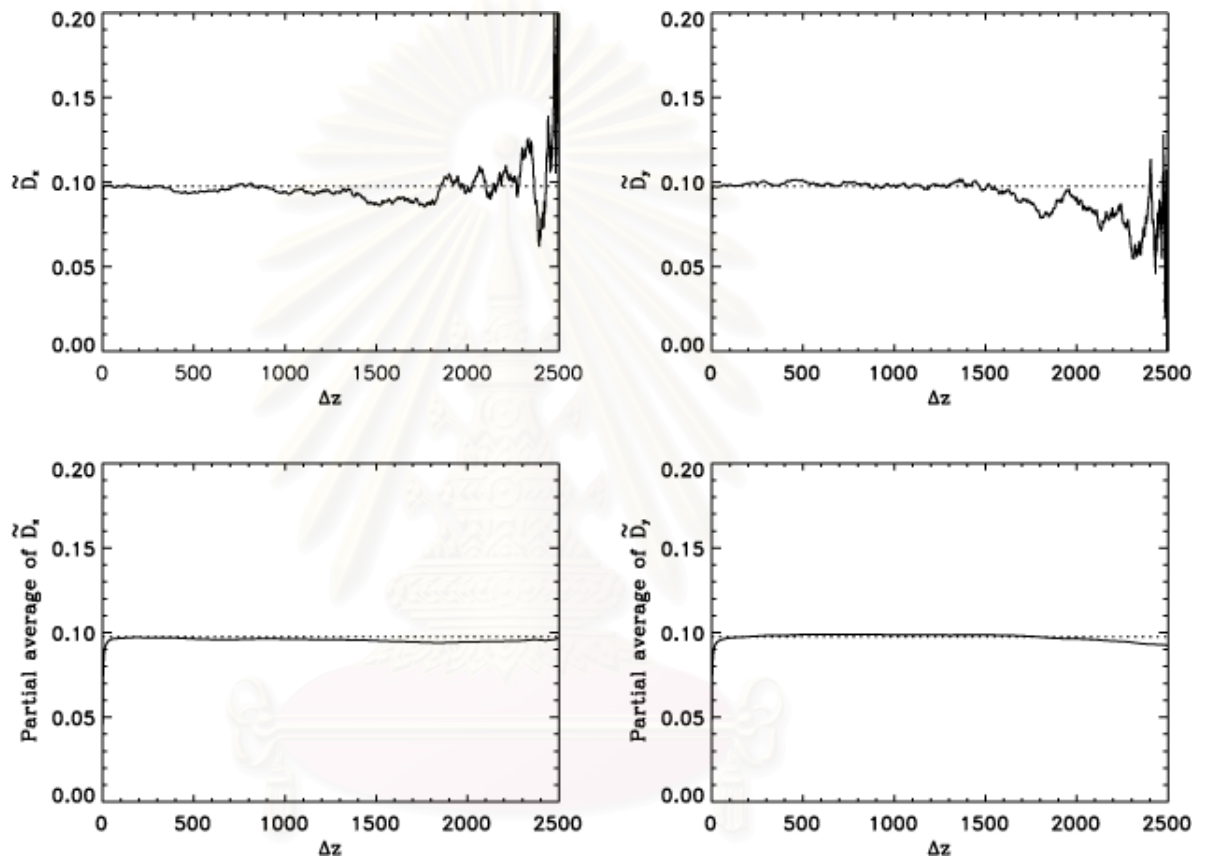


Figure 3.20: Diffusion coefficients from simulations (solid lines) and expected values from discrete theory (dashed lines) for  $\delta b/B_0 = 0.5$ .

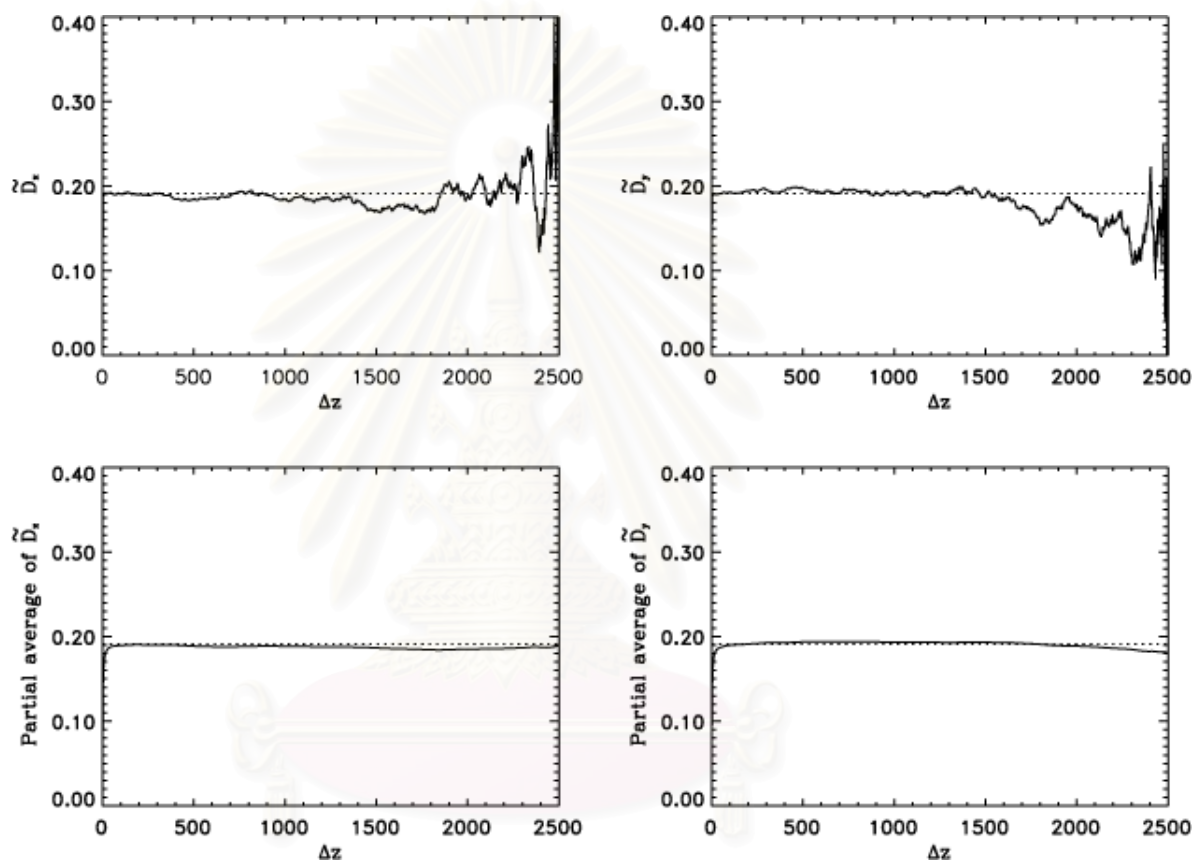


Figure 3.21: Diffusion coefficients from simulations (solid lines) and expected values from discrete theory (dashed lines) for  $\delta b/B_0 = 0.7$ .

จุฬาลงกรณ์มหาวิทยาลัย

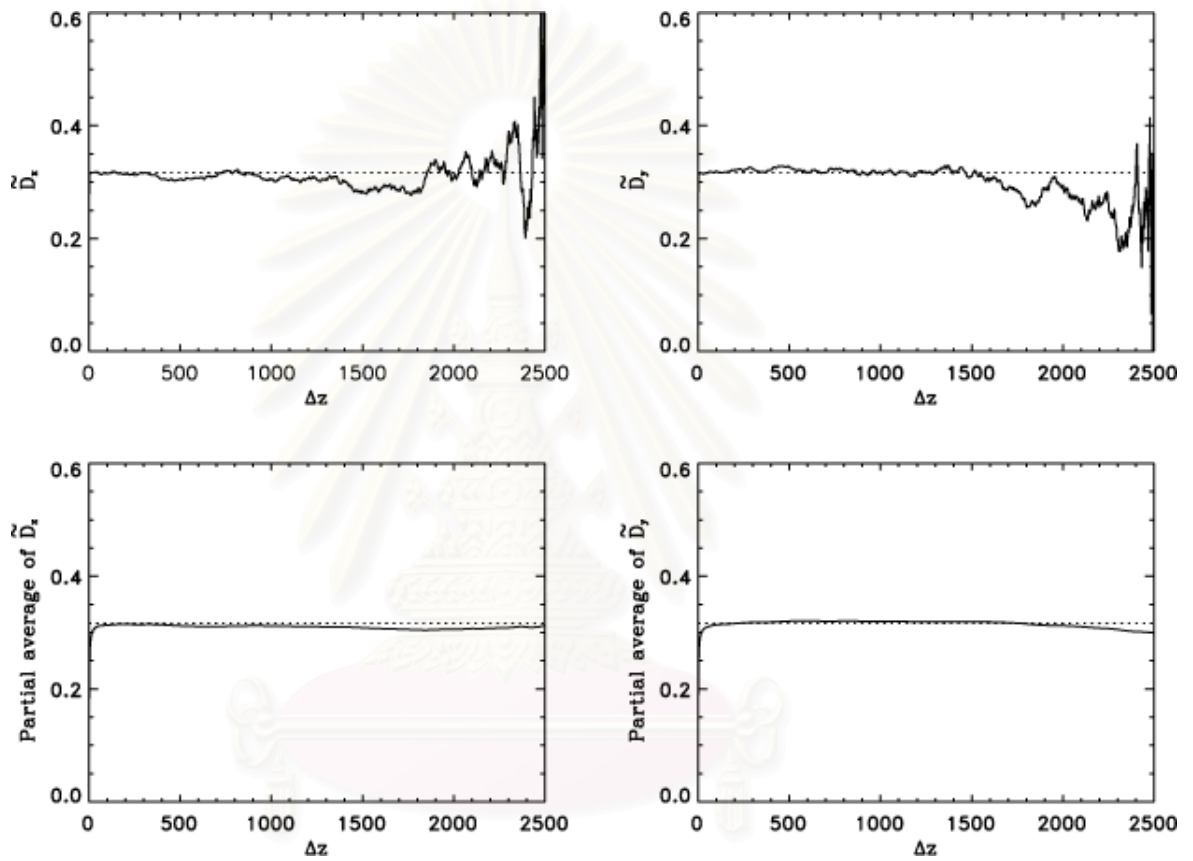


Figure 3.22: Diffusion coefficients from simulations (solid lines) and expected values from discrete theory (dashed lines) for  $\delta b/B_0 = 0.9$ .

จุฬาลงกรณ์มหาวิทยาลัย

### 3.3.2 Computation of Field Line Random Walk for 2D+Slab Turbulence

For 2D+slab turbulence, we trace 1,000 field lines in 200 realizations of the 2D field (5 field lines for each realization). The box sizes are  $L_z = 100,000\ell_z$  with  $N_z = 2^{22}$  points and  $L_x = L_y = 300\ell_z$  and  $N_x = N_y = 4,096$  points and we generate each field line over  $1/100$  of  $L_z$ . The magnetic power spectra for 2D+slab turbulence are

$$P_{xx}^{\text{slab}}(k_z) = P_{yy}^{\text{slab}}(k_z) = \frac{C_1}{[1 + (k_z\ell_z)^2]^{5/6}} \quad (3.13)$$

$$P_{xx}^{2D}(k_x, k_y) = \frac{C_2 k_y^2}{[1 + (k_{\perp}\ell_{\perp})^2]^{7/3}} \quad (3.14)$$

$$P_{yy}^{2D}(k_x, k_y) = \frac{C_2 k_x^2}{[1 + (k_{\perp}\ell_{\perp})^2]^{7/3}}, \quad (3.15)$$

where  $k_{\perp} = \sqrt{k_x^2 + k_y^2}$ ,  $C_1$  and  $C_2$  are normalization constants, and  $\ell_z$  and  $\ell_{\perp}$  are characteristic scale lengths. These kinds of spectra become Kolmogorov spectra at high  $k$ . For 2D spectra, they are associated with

$$A(k_{\perp}) = \frac{C_2}{[1 + (k_{\perp}\ell_{\perp})^2]^{7/3}}. \quad (3.16)$$

where  $A(k_{\perp})$  is the Fourier transform of the autocorrelation function of the vector potential. In the simulations, we set  $\ell_z = 1$  and  $\ell_{\perp} = 0.1$ . First, we vary  $\delta b/B_0 = 0.3, 0.5,$  and  $0.9$  and fix  $f_s = 0.2$  ( $f_s = \delta b_{\text{slab}}^2/\delta b^2$  is the fraction of slab energy). Then we vary the slab fraction  $f_s = 0.2, 0.5, 0.9$  and fix  $\delta b/B_0 = 0.5$ . When we get the field lines, we calculate the diffusion coefficient and compare with the theoretical result (Matthaeus et al. 1995),

$$D_{\perp} = \frac{D_{\perp}^{\text{slab}}}{2} + \sqrt{\left(\frac{D_{\perp}^{\text{slab}}}{2}\right)^2 + (D_{\perp}^{2D})^2}, \quad (3.17)$$

where  $D_{\perp}^{slab} = \ell_c \delta b_{slab}^2 / (2B_0^2)$  and  $D_{\perp}^{2D} = \tilde{\lambda} \delta b_{2D} / (\sqrt{2}B_0)$ , where  $\ell_c$  is the correlation length,  $\tilde{\lambda}$  is the ultrascale, which is equal to  $(\langle a^2 \rangle / (\delta b^2)^{2D})^{1/2}$ , and  $\delta b_{slab} = \sqrt{\langle b_{slab}^2 \rangle}$  and  $\delta b_{2D} = \sqrt{\langle b_{2D}^2 \rangle}$  are the root-mean-squared turbulent magnetic fields of slab and 2D components, respectively. From the spectra (3.13), (3.14) and (3.15), we get the relationships  $\ell_c = 0.747\ell_z$  and  $\tilde{\lambda} = 0.577\ell_{\perp}$ .

Tables 3.2 and 3.3 show the comparison between the diffusion coefficients from the numerical simulations ( $D_{\perp}$ ), which come from the average of  $D_x$  and  $D_y$  at  $\Delta z = 500$ , with the theoretical values for a continuous spectrum and a discrete spectrum when we vary  $\delta b/B_0$  and  $f_s$ . For the 2D component, we can write the diffusion coefficient from the discrete theory as

$$D_{\perp}^{2D} = \left( \sum_{k_{\perp}} \frac{|\vec{b}^{2D}(\vec{k}_{\perp})|^2}{2k_{\perp}^2 B_0^2} \right)^{1/2}. \quad (3.18)$$

The error reported in the Tables is the difference between  $D_{\perp}$  from discrete theory and  $D_{\perp}$  from the simulations. The results are plotted on a linear scale as Figures 3.23 and 3.24. The running diffusion coefficients are shown in Figures 3.25-3.29.

The 2D+slab simulations are more consistent with the discrete theory than the continuous theory that uses integral Fourier transforms. That is because, in the simulations, it is impossible to produce a power spectrum to infinitesimal  $\Delta k$ . For the 2D turbulence part, we are limited by the memory of the computer to treat  $N_x$  and  $N_y$  no greater than 4,096 points each. Therefore, we suggest comparing the simulations with the discrete theory. The errors compared with the discrete theory are within 15%, similar to the level of agreement obtained by Gray et al. (1996), so we can conclude that the simulations agree with the theory. In order to obtain this agreement, we have to ensure that we use a simulation box and realizations of 2D turbulence that are large enough and trace the magnetic field lines to only a few percent of the box length.

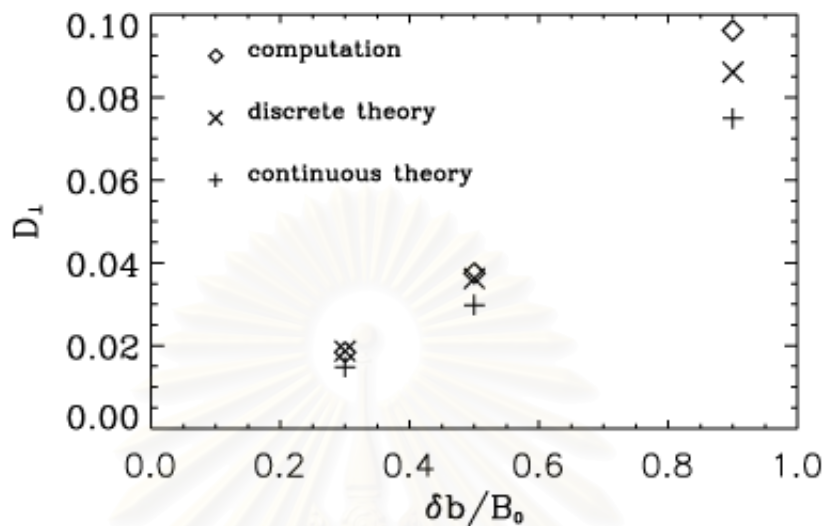


Figure 3.23: Comparison of  $D_{\perp}$  from theory and numerical simulations versus  $\delta b/B_0$ , for  $f_s = 0.2$ .

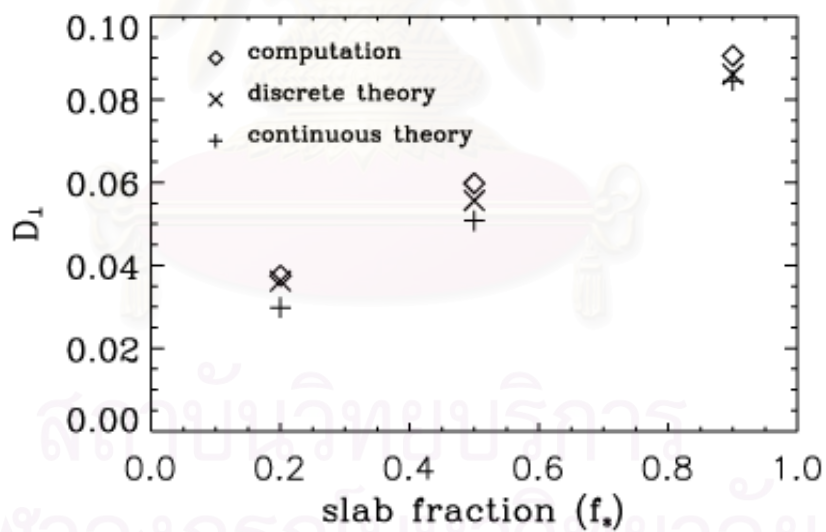


Figure 3.24: Comparison of  $D_{\perp}$  from theory and numerical simulations versus  $f_s$ , for  $\delta b/B_0 = 0.5$ .

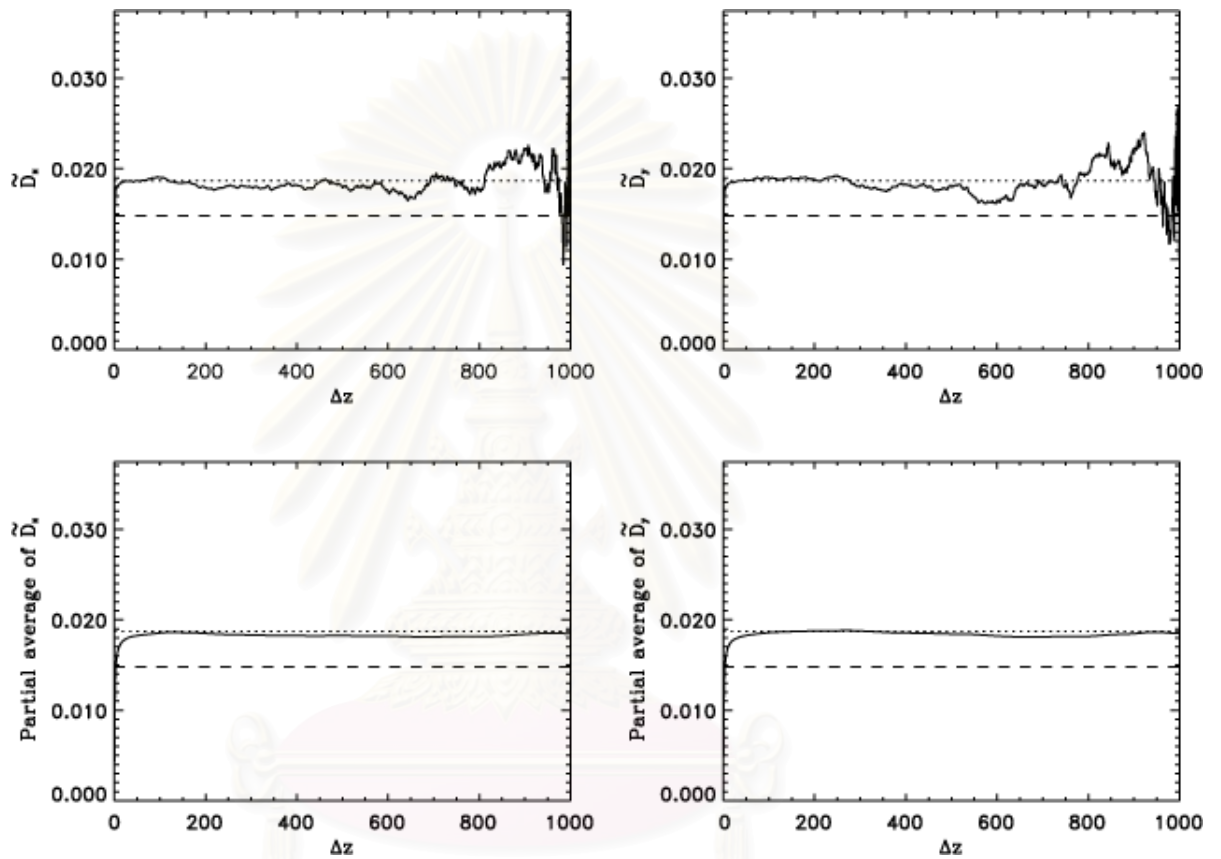


Figure 3.25: The solid lines show the diffusion coefficient from the simulations of each component and the dashed lines show the value expected from continuous theory (dashed lines) and from discrete theory (dotted lines) for  $\delta b/B_0 = 0.3$  and  $f_s = 0.2$ .

จุฬาลงกรณ์มหาวิทยาลัย



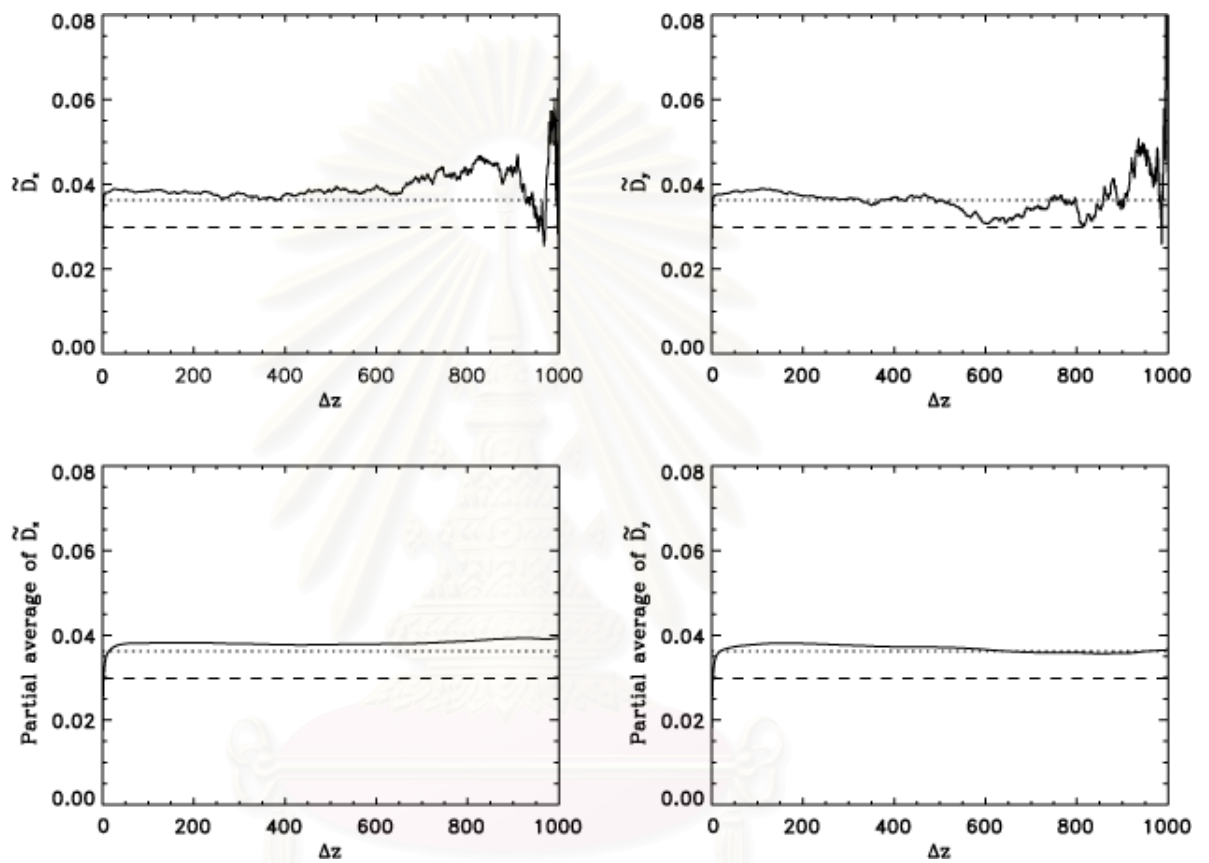


Figure 3.26: The solid lines show the diffusion coefficient from the simulations of each component and the dashed lines show the value expected from continuous theory (dashed lines) and from discrete theory (dotted lines) for  $\delta b/B_0 = 0.5$  and  $f_s = 0.2$ .

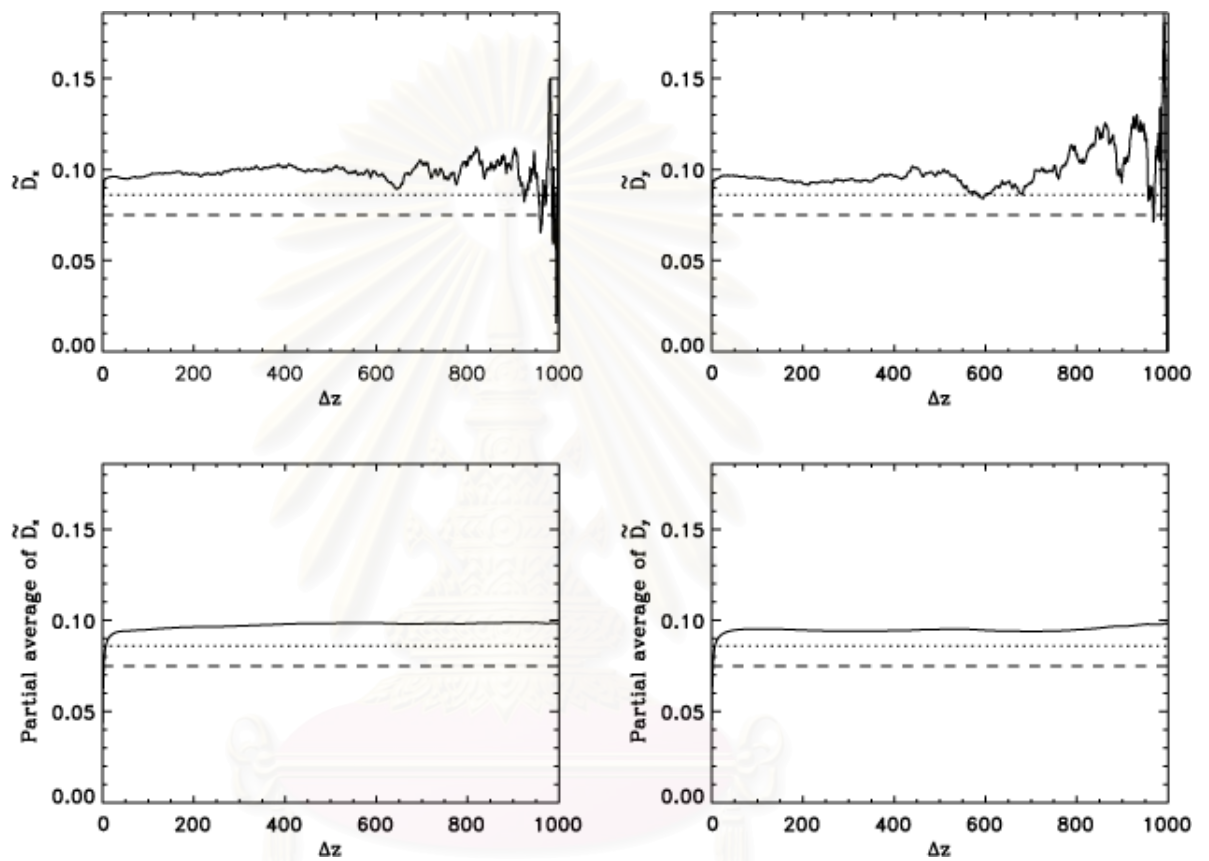


Figure 3.27: The solid lines show the diffusion coefficient from the simulations of each component and the dashed lines show the value expected from continuous theory (dashed lines) and from discrete theory (dotted lines) for  $\delta b/B_0 = 0.9$  and  $f_s = 0.2$

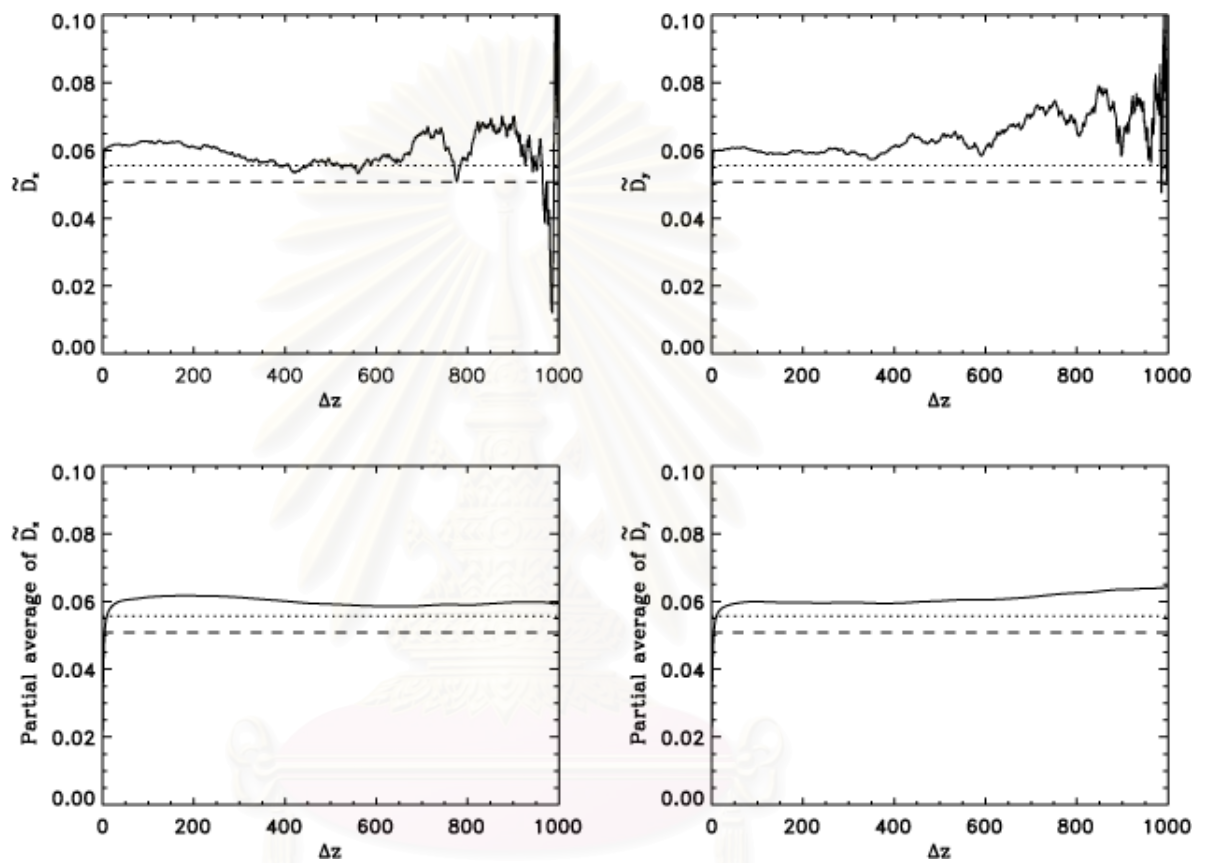


Figure 3.28: The solid lines show the diffusion coefficient from the simulations of each component and the dashed lines show the value expected from continuous theory (dashed lines) and from discrete theory (dotted lines) for  $\delta b/B_0 = 0.5$  and  $f_s = 0.5$ .

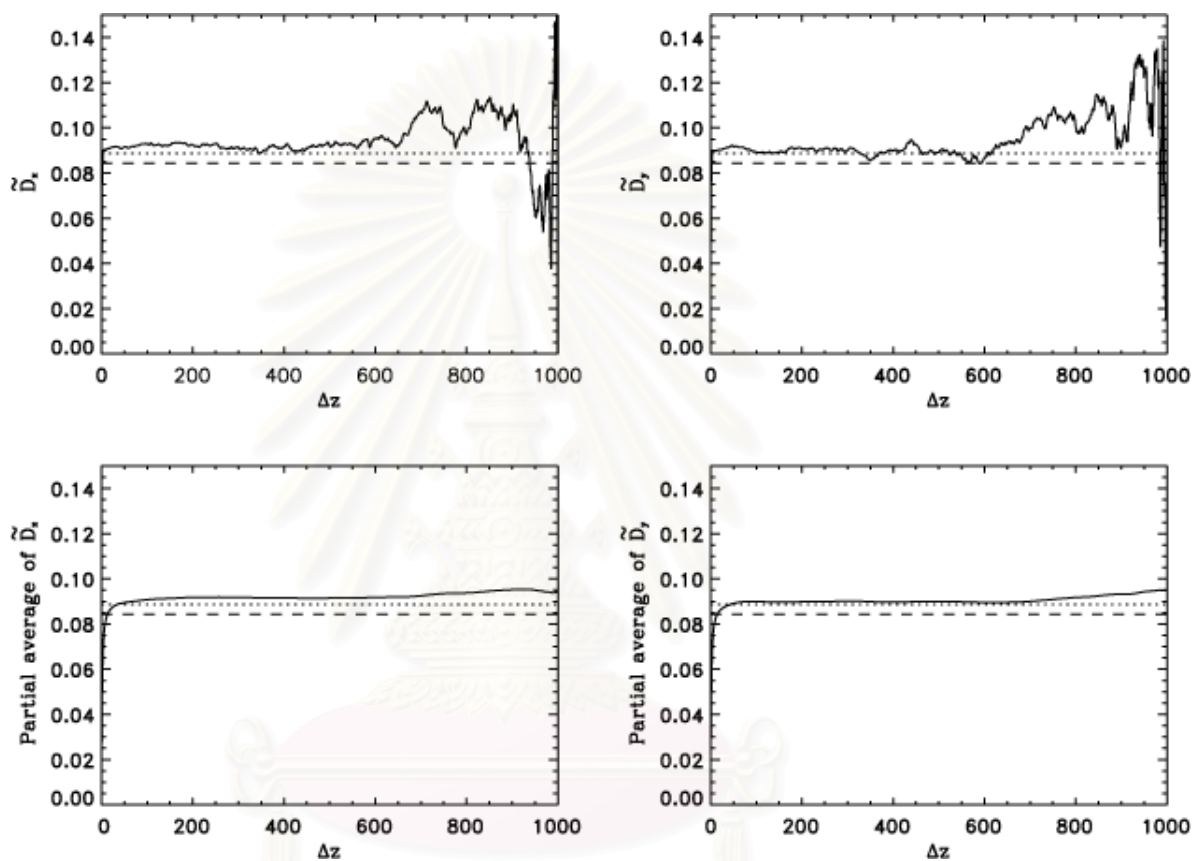


Figure 3.29: The solid lines show the diffusion coefficient from the simulations of each component and the dashed lines show the value expected from continuous theory (dashed lines) and from discrete theory (dotted lines) for  $\delta b/B_0 = 0.5$  and  $f_s = 0.9$ .

จุฬาลงกรณ์มหาวิทยาลัย

Table 3.2: Comparison between the diffusion coefficient from theory and simulations for  $E_{slab} : E_{2D} = 20:80$  when we vary  $\delta b/B_0$ .

$\delta b/B_0$	$D_{\perp}$ theory	$D_{\perp}$ discrete theory	$D_{\perp}$ simulation	% error
0.3	0.0148	0.0187	0.0184	1.63
0.5	0.0298	0.0363	0.0375	3.47
0.9	0.0749	0.0861	0.0962	11.73

Table 3.3: Comparison between the diffusion coefficient from theory and simulations for  $\delta b/B_0 = 0.5$  when we vary  $f_s$ .

$f_s$	$D_{\perp}$ theory	$D_{\perp}$ discrete theory	$D_{\perp}$ simulation	% error
0.9	0.0845	0.0861	0.0906	5.25
0.5	0.0508	0.0556	0.0598	7.46
0.2	0.0298	0.0363	0.0375	3.47

สถาบันวิทยบริการ  
จุฬาลงกรณ์มหาวิทยาลัย

# Chapter 4

## Non-axisymmetric Field Line Random Walk

### 4.1 Introduction

Although magnetic fluctuation properties in a turbulent plasma are usually assumed to be axisymmetric with respect to the mean field, there are indications that the variances of the fluctuation vectors may be non-axisymmetric in some cases of interest (Jokipii 1973; Jokipii et al. 1995; Burger & Hattingh 1998). Particular interest in the non-axisymmetric perpendicular diffusion and field line random walk derives from recent studies that suggest a possible role of enhanced latitudinal transport of cosmic rays at high heliographic latitudes (Jokipii et al. 1995; Burger & Hattingh 1998). The generalization to non-axisymmetry is immediate in quasilinear theory, since the diffusion coefficient is linear in the variances, but in general this is not in this case. In this chapter we develop a theory for the non-axisymmetric field line random walk in a more general non-perturbative scheme (Matthaeus et al. 1995) and perform the numerical simulations for several cases to verify the theory. The approach is useful for general transverse turbulence, although we apply it explicitly here to a two-component model of fluctuations that has been useful in solar wind and cosmic ray scattering studies (Matthaeus et al. 1990; Bieber et al. 1994, 1996). Our principal results are a general framework for the non-axisymmetric field line random walk as a set of coupled bi-quadratic equations, and perhaps more usefully, closed-form solutions

for several cases. The latter should find immediate application in heliospheric scattering problems such as cosmic ray modulation.

## 4.2 Analytic theory

The calculation of ensemble average diffusion coefficients is the objective of this chapter. For the non-axisymmetric case, the diffusion coefficients in  $x$  and  $y$  direction are defined as

$$D_x = \frac{\langle(\Delta x)^2\rangle}{2\Delta z} \quad (4.1)$$

$$D_y = \frac{\langle(\Delta y)^2\rangle}{2\Delta z}. \quad (4.2)$$

where  $\langle(\Delta x)^2\rangle \neq \langle(\Delta y)^2\rangle$ . We can explicitly make the parallel correlation length ( $\ell_c$ ) and slab fluctuations ( $\delta b_{slab}$ ) different in the  $x$  and  $y$  directions to make an anisotropic slab field. For 2D turbulence, the power spectrum  $A(k_x, k_y)$  for the axisymmetric case depends only on  $k_\perp = \sqrt{k_x^2 + k_y^2}$ , i.e., it is constant along circles in  $(k_x, k_y)$  space. To consider non-axisymmetric 2D turbulence, we suggest a form that is instead constant along ellipses in  $(k_x, k_y)$  space. For the analytic formulation, we still follow Matthaeus et al. (1995) and Ruffolo, Matthaeus, and Chuychai (2004) as we presented in Section 2.7 in order to obtain the diffusion coefficients. Therefore, we can write

$$\begin{aligned} \langle\Delta x^2\rangle &= \frac{1}{B_0^2} \int_0^{\Delta z} \int_{-z'}^{\Delta z - z'} \int_{-\infty}^{\infty} \int_{-\infty}^{\infty} R_{xx}(\Delta x', \Delta y', \Delta z') \\ &\quad \times P(\Delta x'|\Delta z')P(\Delta y'|\Delta z')d\Delta x'd\Delta y'd\Delta z'dz' \end{aligned} \quad (4.3)$$

and

$$\begin{aligned} \langle\Delta y^2\rangle &= \frac{1}{B_0^2} \int_0^{\Delta z} \int_{-z'}^{\Delta z - z'} \int_{-\infty}^{\infty} \int_{-\infty}^{\infty} R_{yy}(\Delta x', \Delta y', \Delta z') \\ &\quad \times P(\Delta x'|\Delta z')P(\Delta y'|\Delta z')d\Delta x'd\Delta y'd\Delta z'dz'. \end{aligned} \quad (4.4)$$

Here,  $R_{xx}$  and  $R_{yy}$  are different and we assume the probabilities in equations (4.3) and (4.4) to be Gaussian distributions as

$$P(\Delta x'|\Delta z') = \frac{1}{\sqrt{2\pi\sigma_x^2}} \exp\left[-\frac{(\Delta x')^2}{2\sigma_x^2}\right] \quad (4.5)$$

$$P(\Delta y'|\Delta z') = \frac{1}{\sqrt{2\pi\sigma_y^2}} \exp\left[-\frac{(\Delta y')^2}{2\sigma_y^2}\right], \quad (4.6)$$

where  $\sigma_x^2$  and  $\sigma_y^2$  are the variances in  $x$  and  $y$  components. For the non-axisymmetric field line random walk, we again apply the diffusion approximation for the variances, which are

$$\sigma_x^2 = \langle(\Delta x)^2\rangle = 2D_x|\Delta z'| \quad (4.7)$$

$$\sigma_y^2 = \langle(\Delta y)^2\rangle = 2D_y|\Delta z'|. \quad (4.8)$$

Therefore (4.5) and (4.6) are

$$P(\Delta x'|\Delta z') = \frac{1}{\sqrt{4\pi D_x|\Delta z'|}} \exp\left[-\frac{(\Delta x')^2}{4D_x|\Delta z'|}\right] \quad (4.9)$$

$$P(\Delta y'|\Delta z') = \frac{1}{\sqrt{4\pi D_y|\Delta z'|}} \exp\left[-\frac{(\Delta y')^2}{4D_y|\Delta z'|}\right]. \quad (4.10)$$

After that we integrate (4.3) and (4.4) over  $\Delta z'$  and  $z'$  and transform the correlation function in Fourier space. Finally, we obtain the coupled equations for  $D_x$  and  $D_y$  as

$$\begin{aligned} D_x &= \frac{\langle(\Delta x)^2\rangle}{2\Delta z} = \frac{1}{\sqrt{2\pi}} \frac{1}{B_0^2} \int_{-\infty}^{\infty} \frac{1 - \cos(k_z\Delta z)}{k_z^2\Delta z} P_{xx}^{slab}(k_z) dk_z \\ &+ \frac{1}{2\pi} \frac{1}{B_0^2} \int_{-\infty}^{\infty} \int_{-\infty}^{\infty} \frac{P_{xx}^{2D}(k_x, k_y)}{(D_x k_x^2 + D_y k_y^2)} [1 - g[(D_x k_x^2 + D_y k_y^2)\Delta z]] dk_x dk_y \end{aligned} \quad (4.11)$$

$$\begin{aligned} D_y &= \frac{\langle(\Delta y)^2\rangle}{2\Delta z} = \frac{1}{\sqrt{2\pi}} \frac{1}{B_0^2} \int_{-\infty}^{\infty} \frac{1 - \cos(k_z\Delta z)}{k_z^2\Delta z} P_{yy}^{slab}(k_z) dk_z \\ &+ \frac{1}{2\pi} \frac{1}{B_0^2} \int_{-\infty}^{\infty} \int_{-\infty}^{\infty} \frac{P_{yy}^{2D}(k_x, k_y)}{(D_x k_x^2 + D_y k_y^2)} [1 - g[(D_x k_x^2 + D_y k_y^2)\Delta z]] dk_x dk_y. \end{aligned} \quad (4.12)$$



When we choose a large  $\Delta z$ , (4.11) and (4.12) become

$$D_x - D_x^{slab} = \frac{1}{2\pi} \frac{1}{B_0^2} \int_{-\infty}^{\infty} \int_{-\infty}^{\infty} \frac{P_{xx}^{2D}(k_x, k_y)}{(D_x k_x^2 + D_y k_y^2)} dk_x dk_y \quad (4.13)$$

$$D_y - D_y^{slab} = \frac{1}{2\pi} \frac{1}{B_0^2} \int_{-\infty}^{\infty} \int_{-\infty}^{\infty} \frac{P_{yy}^{2D}(k_x, k_y)}{(D_x k_x^2 + D_y k_y^2)} dk_x dk_y, \quad (4.14)$$

where

$$D_x^{slab} = \sqrt{\frac{\pi}{2}} \frac{P_{xx}^{slab}(0)}{B_0^2} = \frac{\ell_x f_{sx} \delta b^2}{B_0^2} \quad (4.15)$$

$$D_y^{slab} = \sqrt{\frac{\pi}{2}} \frac{P_{yy}^{slab}(0)}{B_0^2} = \frac{\ell_y (1 - f_{sx}) \delta b^2}{B_0^2}. \quad (4.16)$$

where  $\ell_x$  and  $\ell_y$  are the correlation lengths in  $x$  and  $y$  directions respectively and  $f_{sx}$  is the fraction of slab energy in the  $x$  direction,  $f_{sx} = \langle b_x^2 \rangle^{slab} / \langle b^2 \rangle$ .

For the axisymmetric case,  $A(k_x, k_y)$  is constant along circles of constant  $\sqrt{k_x^2 + k_y^2}$  in  $(k_x, k_y)$  space. For the non-axisymmetric case, we assume an ellipse with a major axis  $\beta$  and a minor axis  $\alpha$ . Then, we can say that  $A(k_x, k_y)$  is constant along ellipses in  $(k_x, k_y)$  space of constant  $\sqrt{k_x^2/\alpha^2 + k_y^2/\beta^2}$ . See Figure 4.1 for a comparison between axisymmetric and non-axisymmetric cases. Therefore, for this case,  $A$  can be written as a function of  $\sqrt{k_x^2/\alpha^2 + k_y^2/\beta^2}$ . Rewriting equations (4.13) and (4.14) in terms of  $A$ ,

$$D_x - D_x^{slab} = \frac{1}{2\pi} \frac{1}{B_0^2} \int_{-\infty}^{\infty} \int_{-\infty}^{\infty} \frac{k_y^2 A \left( \sqrt{k_x^2/\alpha^2 + k_y^2/\beta^2} \right)}{(D_x k_x^2 + D_y k_y^2)} dk_x dk_y \quad (4.17)$$

$$D_y - D_y^{slab} = \frac{1}{2\pi} \frac{1}{B_0^2} \int_{-\infty}^{\infty} \int_{-\infty}^{\infty} \frac{k_x^2 A \left( \sqrt{k_x^2/\alpha^2 + k_y^2/\beta^2} \right)}{(D_x k_x^2 + D_y k_y^2)} dk_x dk_y. \quad (4.18)$$

Then we transform  $k_x$  to  $k'_x = k_x/\alpha$  and  $k_y$  to  $k'_y = k_y/\beta$ . The meaning of this is that we are looking at contours of  $A$  in  $(k'_x, k'_y)$  space in which the shape of the contour is a circle. This facilitates the integration. Therefore the equations

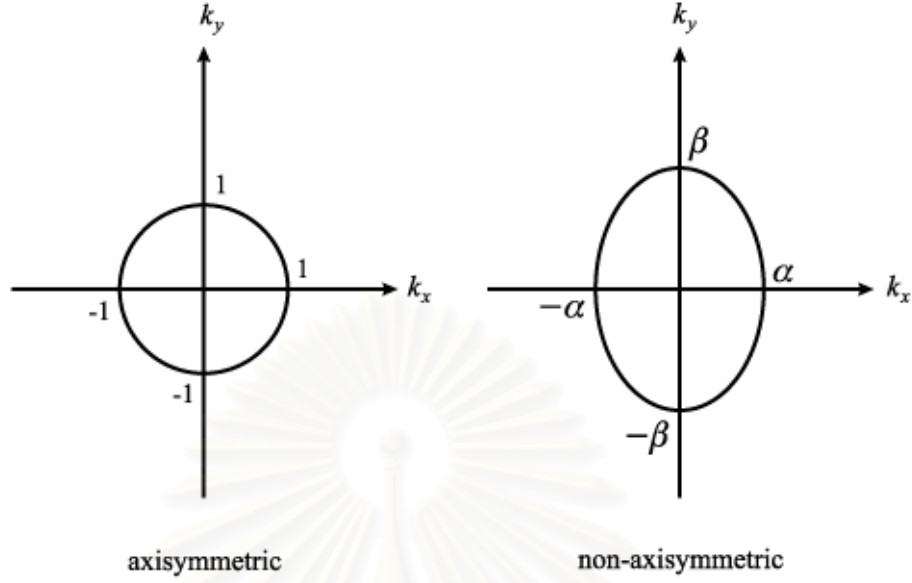


Figure 4.1: Contours of constant power  $A(k_x, k_y)$  of the 2D potential function for the axisymmetric case and for the type of non-axisymmetric 2D turbulence we consider.

above become

$$D_x - D_x^{slab} = \frac{1}{2\pi} \frac{1}{B_0^2} \int_{-\infty}^{\infty} \int_{-\infty}^{\infty} \frac{k_y^2 A(\sqrt{k_x'^2 + k_y'^2})}{(D_x \alpha^2 k_x'^2 + D_y \beta^2 k_y'^2)} d(\alpha k_x') d(\beta k_y') \quad (4.19)$$

$$D_y - D_y^{slab} = \frac{1}{2\pi} \frac{1}{B_0^2} \int_{-\infty}^{\infty} \int_{-\infty}^{\infty} \frac{k_x^2 A(\sqrt{k_x'^2 + k_y'^2})}{(D_x \alpha^2 k_x'^2 + D_y \beta^2 k_y'^2)} dk_x' dk_y'. \quad (4.20)$$

Next, write (4.19) and (4.20) in polar coordinates in  $k$ -space, where  $k'_\perp = \sqrt{k_x'^2 + k_y'^2}$ ,

$k'_x = k'_\perp \cos \theta$ , and  $k'_y = k'_\perp \sin \theta$ :

$$\begin{aligned} D_x - D_x^{slab} &= \frac{\alpha\beta}{2\pi B_0^2} \int_0^{2\pi} \int_0^\infty \frac{\beta^2 k'_\perp{}^2 \sin^2 \theta A(k'_\perp)}{(D_x \alpha^2 k'_\perp{}^2 \cos^2 \theta + D_y \beta^2 k'_\perp{}^2 \sin^2 \theta)} k'_\perp dk'_\perp d\theta \\ &= \frac{\alpha\beta}{2\pi B_0^2 D_x} \left(\frac{\alpha}{\beta}\right)^2 \int_0^\infty A(k'_\perp) k'_\perp dk'_\perp \int_0^{2\pi} \frac{1}{\cot^2 \theta + \left(\frac{D_y}{D_x}\right) \left(\frac{\beta^2}{\alpha^2}\right)} d\theta \end{aligned} \quad (4.21)$$

$$D_y - D_y^{slab} = \frac{\alpha\beta}{2\pi B_0^2} \int_0^{2\pi} \int_0^\infty \frac{\alpha^2 k'_\perp{}^2 \cos^2 \theta A(k'_\perp)}{(D_x \alpha^2 k'_\perp{}^2 \cos^2 \theta + D_y \beta^2 k'_\perp{}^2 \sin^2 \theta)} k'_\perp dk'_\perp d\theta$$

$$= \frac{\alpha\beta}{2\pi B_0^2 D_x} \int_0^\infty A(k'_\perp) k'_\perp dk'_\perp \int_0^{2\pi} \frac{1}{1 + \left(\frac{D_y}{D_x}\right) \left(\frac{\beta^2}{\alpha^2}\right) \tan^2 \theta} d\theta. \quad (4.22)$$

Since  $\int_0^\infty [1/(\cot^2 \theta + \rho^2)] d\theta = 2\pi/[\rho(\rho+1)]$  and  $\int_0^\infty [1/(1 + \rho^2 \tan^2 \theta)] d\theta = 2\pi/(1 + \rho)$  where  $\rho = (\sqrt{D_y/D_x})(\beta/\alpha)$  in our integrals, we get

$$D_x - D_x^{slab} = \left( \frac{\alpha\beta}{2\pi B_0^2} \int_0^\infty A(k'_\perp) k'_\perp dk'_\perp \right) \frac{\beta^2}{\alpha^2 D_x} \frac{1}{\left(\sqrt{\frac{D_y}{D_x}}\right) \left(\frac{\beta}{\alpha}\right) \left(1 + \left(\sqrt{\frac{D_y}{D_x}}\right) \left(\frac{\beta}{\alpha}\right)\right)} \quad (4.23)$$

$$D_y - D_y^{slab} = \left( \frac{\alpha\beta}{2\pi B_0^2} \int_0^\infty A(k'_\perp) k'_\perp dk'_\perp \right) \frac{1}{D_x} \frac{1}{\left(1 + \left(\sqrt{\frac{D_y}{D_x}}\right) \left(\frac{\beta}{\alpha}\right)\right)}. \quad (4.24)$$

Equations (4.23) and (4.24) become

$$(D_x - D_x^{slab}) \left( D_y + (\alpha/\beta) \sqrt{D_x D_y} \right) = \left( \frac{\alpha\beta}{B_0^2} \int_0^\infty A(k'_\perp) k'_\perp dk'_\perp \right) \quad (4.25)$$

$$(D_y - D_y^{slab}) \left( D_x + (\beta/\alpha) \sqrt{D_x D_y} \right) = \left( \frac{\alpha\beta}{B_0^2} \int_0^\infty A(k'_\perp) k'_\perp dk'_\perp \right). \quad (4.26)$$

Considering the quantity on the right hand side, let us call it

$$I = \frac{\alpha\beta}{B_0^2} \int_0^\infty A(k'_\perp) k'_\perp dk'_\perp. \quad (4.27)$$

Transforming  $k'_\perp$  back to  $k'_x$  and  $k'_y$  coordinates and then back again to  $k_x$  and  $k_y$ ,

$$\begin{aligned} I &= \frac{\alpha\beta}{2\pi B_0^2} \int_0^\infty A(k'_\perp) k'_\perp dk'_\perp \int_0^{2\pi} d\theta \\ &= \frac{\alpha\beta}{2\pi B_0^2} \int_{-\infty}^\infty \int_{-\infty}^\infty A(k'_\perp) dk'_x dk'_y \\ &= \frac{1}{2\pi B_0^2} \int_{-\infty}^\infty \int_{-\infty}^\infty A(k_x, k_y) dk_x dk_y \\ &= \frac{\langle a^2 \rangle}{B_0^2} = \left( \tilde{\lambda} \frac{b^{2D}}{B_0} \right)^2 \\ &= 2(D_\perp^{2D})^2 \end{aligned} \quad (4.28)$$

where  $\tilde{\lambda}$  is called the “ultrascale” [see equation (2.80)].

Finally we get the coupled equations for non-axisymmetric case

$$\begin{aligned} (D_x - D_x^{slab}) \left( D_y + \frac{\alpha}{\beta} \sqrt{D_x D_y} \right) &= I \\ (D_y - D_y^{slab}) \left( D_x + \frac{\beta}{\alpha} \sqrt{D_x D_y} \right) &= I. \end{aligned} \quad (4.29)$$

This set of equations also covers the axisymmetric case. For that case, we set  $\alpha = 1$  and  $\beta = 1$ , so the coupled equations reduce to

$$D_i = \frac{D_i^{slab}}{2} + \sqrt{\left( \frac{D_i^{slab}}{2} \right)^2 + (D_{\perp}^{2D})^2}. \quad (4.30)$$

To make the coupled equations (4.29) simpler for applications, we set  $\alpha$  to  $1/\sqrt{\xi}$  and  $\beta$  to  $\sqrt{\xi}$ , where  $\xi$  is an ellipticity parameter related to the anisotropy of 2D turbulence ( $\xi^2 = D_x^{2D}/D_y^{2D}$ ). That means that when we increase the major axis in the  $y$  direction, the minor axis in the  $x$  direction is decreased to conserve the area inside the ellipse contour. This case gives us a symmetry between  $D_x$  and  $D_y$ . Therefore, the general coupled equations become (Ruffolo, Chuychai, & Matthaeus 2001)

$$\begin{aligned} (D_x - D_x^{slab}) \left( D_y + \frac{\sqrt{D_x D_y}}{\xi} \right) &= I \\ (D_y - D_y^{slab}) \left( D_x + \xi \sqrt{D_x D_y} \right) &= I. \end{aligned} \quad (4.31)$$

These equations are straightforward to solve numerically for a given case of interest. Furthermore, it is possible to scale diffusion coefficients according to  $D_{\perp}$  and anisotropies according to  $\xi$  to reduce the above to equations that depend on only two parameters, allowing their limiting behavior to be readily elucidated.

### 4.3 Interpretation

While the coupled bi-quadratic equations (4.31) are not difficult to solve, for certain physical limits there are closed-form solutions with interesting interpretations. There are certain physical inputs one should specify for a given application, e.g., for solar modulation of galactic cosmic rays in different parts of the heliosphere, or anomalous cosmic ray acceleration at different parts of the solar wind termination shock. The “user” of this calculation should specify:

$B_0$ , the mean magnetic field,

$\delta b$ , the root-mean-squared turbulent magnetic field,

$f_s$ , the slab fraction of turbulent energy,

$\eta^2 \equiv f_{sx}/f_{sy}$ , the slab anisotropy,

$\ell_x$ , the correlation length of  $\delta b_x^{slab}$ ,

$\ell_y$ , the correlation length of  $\delta b_y^{slab}$ ,

$\tilde{\lambda}$ , the ultrascale (of 2D turbulence), and

$\xi$ , the anisotropy of 2D turbulence ( $\xi^2 = D_x^{2D}/D_y^{2D}$ ).

In many applications, direct measurements of these quantities are not available, so one must make educated guesses or *ad hoc* approximations. Here we present solutions of the general equations (4.31) for specific limits and approximations. Naturally, the simplest approximation is that either slab or 2D turbulence can be neglected. For the case that 2D turbulence is absent, we recover the Jokipii

and Parker (1968) results for slab turbulence,

$$D_i^{slab} = \frac{\ell_i f_{si} \delta b^2}{B_0^2} \quad (i = x, y), \quad (4.32)$$

where  $\ell_i$  and  $f_{si}$  are the correlation length and fraction of turbulent energy, respectively, of the  $i$ -component of slab turbulence. We also can write  $D_x^{slab}$  and  $D_y^{slab}$  in terms of  $\eta$  and  $f_s$  instead of  $f_{si}$ :

$$D_x^{slab} = \frac{\eta^2}{\eta^2 + 1} \frac{\ell_x f_s \delta b^2}{B_0^2} \quad (4.33)$$

$$D_y^{slab} = \frac{1}{\eta^2 + 1} \frac{\ell_y f_s \delta b^2}{B_0^2}. \quad (4.34)$$

Eqs. (4.33) and (4.34) yield  $\eta^2 = D_x^{slab}/D_y^{slab}$  when  $\ell_x = \ell_y$ . In limit that the slab fraction goes to zero, we have the field line diffusion coefficients

$$\begin{aligned} D_x^{2D} &= \xi D_\perp^{2D} \\ D_y^{2D} &= \frac{1}{\xi} D_\perp^{2D} \\ D_\perp^{2D} &= \frac{\tilde{\lambda} \delta b}{\sqrt{2} B_0}. \end{aligned} \quad (4.35)$$

Then we obviously see that  $\xi = \sqrt{D_x^{2D}/D_y^{2D}}$ .

Let us return to the case where 2D and slab turbulence are both present. If  $\eta$  and  $\xi$  are not known, a simple approximation is to set them equal ( $\eta = \xi$ ). Let us also set  $\ell_x = \ell_y$ . Thus we implicitly know that the anisotropy  $\delta = \sqrt{D_x/D_y}$  is also equal to  $\xi$ . Therefore, equations (4.31) decouple to these two equations:

$$\left( D_x - \frac{\xi^2}{\xi^2 + 1} \frac{\ell_x f_s \delta b^2}{B_0^2} \right) \left( \frac{D_x}{\xi^2} \right) = \frac{I}{2} \quad (4.36)$$

$$\left( D_y - \frac{1}{\xi^2 + 1} \frac{\ell_y f_s \delta b^2}{B_0^2} \right) (\xi^2 D_y) = \frac{I}{2}. \quad (4.37)$$

The solutions for this case are

$$D_x = \frac{1}{2} \left\{ \left( \frac{\xi^2}{\xi^2 + 1} \frac{\ell_x f_s \delta b^2}{B_0^2} \right) + \sqrt{\left( \frac{\xi^2}{\xi^2 + 1} \frac{\ell_x f_s \delta b^2}{B_0^2} \right)^2 + 4\xi^2 (D_\perp^{2D})^2} \right\} \quad (4.38)$$

$$D_y = \frac{1}{2} \left\{ \left( \frac{1}{\xi^2 + 1} \frac{\ell_x f_s \delta b^2}{B_0^2} \right) + \sqrt{\left( \frac{1}{\xi^2 + 1} \frac{\ell_x f_s \delta b^2}{B_0^2} \right)^2 + 4 \frac{(D_\perp^{2D})^2}{\xi^2}} \right\}. \quad (4.39)$$

The above solutions for  $D_x$  and  $D_y$  reduce to the form obtained by Matthaeus et al. (1995) as in (4.30). Furthermore, if all other input values are fixed but  $\eta$  and  $\xi$  both tend to 0 or  $\infty$ , then from (4.38) and (4.39) it can be shown that the 2D contribution dominates. That is, when  $\xi$  tends to zero,  $D_x \rightarrow \xi D_\perp^{2D}$  and  $D_y \rightarrow D_\perp^{2D}/\xi$  and when  $\xi$  goes to  $\infty$ ,  $D_x \rightarrow \xi D_\perp^{2D}$  and  $D_y \rightarrow D_\perp^{2D}/\xi$ . Thus if one employs such limits, say in the outer heliosphere where field fluctuations might become increasingly anisotropic (e.g., if “frozen in” the solar wind), then one must also use  $D_i \propto D_\perp^{2D} \propto \delta b_i/B_0$  (see eq. [2.81]).

For convenience in analyzing the coupled equations (4.31), we can rewrite all variables to compare with the 2D part, yielding

$$D'_\perp = \frac{D_\perp}{D_\perp^{2D}}, \quad D_\perp^{s'} = \frac{D_\perp^{slab}}{D_\perp^{2D}}, \quad (4.40)$$

$$\delta' = \frac{\delta}{\xi}, \quad \eta' = \frac{\eta}{\xi}, \quad (4.41)$$

where we define  $D_\perp$ ,  $D_\perp^{2D}$ , and  $D_\perp^{slab}$  as the geometric means  $\sqrt{D_x D_y}$ ,  $\sqrt{D_x^{2D} D_y^{2D}}$ , and  $\sqrt{D_x^{slab} D_y^{slab}}$ , respectively. Thus, for input values of  $D_\perp^{s'}$  and  $\eta'$ , we have two coupled equations with two known parameters and two unknown parameters  $D'_\perp$  and  $\delta'$ ,

$$D'_\perp \left( \frac{1}{\delta'} + 1 \right) (\delta' D'_\perp - \eta' D_\perp^{s'}) = 2 \quad (4.42)$$

$$D'_\perp (\delta' + 1) \left( \frac{D'_\perp}{\delta'} - \frac{D_\perp^{s'}}{\eta'} \right) = 2. \quad (4.43)$$

Now suppose that  $\eta \rightarrow \infty$ , while  $\xi$  is fixed. Since

$$D_{\perp}^{s'} = \frac{\sqrt{2}\ell}{\tilde{\lambda}} \frac{\eta}{\eta^2 + 1} \frac{f_s}{\sqrt{1 - f_s}} \frac{\delta b}{B_0} \quad (4.44)$$

$$\eta' D_{\perp}^{s'} = \frac{\sqrt{2}\ell}{\tilde{\lambda}} \frac{\eta^2}{\eta^2 + 1} \frac{1}{\xi} \frac{f_s}{\sqrt{1 - f_s}} \frac{\delta b}{B_0} \quad (4.45)$$

$$\frac{D_{\perp}^{s'}}{\eta'} = \frac{\sqrt{2}\ell}{\tilde{\lambda}} \frac{\xi}{\eta^2 + 1} \frac{f_s}{\sqrt{1 - f_s}} \frac{\delta b}{B_0}, \quad (4.46)$$

where  $\ell_x = \ell_y = \ell$ , the terms  $D_{\perp}^{s'}/\eta'$  and  $D_{\perp}^{s'}\eta'$  go to zero and a constant, respectively. Then the coupled equations become

$$D'_{\perp} \left( \frac{1}{\delta'} + 1 \right) (\delta' D'_{\perp} - \eta' D_{\perp}^{s'}) = 2 \quad (4.47)$$

$$D'_{\perp} (\delta' + 1) \left( \frac{D'_{\perp}}{\delta'} \right) = 2. \quad (4.48)$$

For this case, if  $D_{\perp}^{s'}\eta' \ll 1$  which implies  $D_x^{slab} \ll D_x^{2D}$ , the equations above are

$$D'_{\perp} \left( \frac{1}{\delta'} + 1 \right) (\delta' D'_{\perp}) = 2$$

$$D'_{\perp} (\delta' + 1) \left( \frac{D'_{\perp}}{\delta'} \right) = 2.$$

The solutions are  $D'_{\perp} \approx 1$  and  $\delta' \approx 1$ . That is, when  $\eta \rightarrow \infty$  and  $D_x^{slab} \ll D_x^{2D}$ , the diffusion coefficients tend to 2D values ( $D_i \approx D_i^{2D}$ ). If instead  $D_{\perp}^{s'}\eta' \gg 1$  which implies  $D_x^{slab} \gg D_x^{2D}$ , considering (4.47) we know that  $D'_{\perp}\delta'$  must be greater than  $D_{\perp}^{s'}\eta'$  because the left hand side of that equation needs to be positive. Thus  $\delta' > D_{\perp}^{s'}\eta'/D'_{\perp}$ . From (4.48), we can write

$$\delta' = \frac{D_{\perp}^{\prime 2}}{2 - D_{\perp}^{\prime 2}} \quad (4.49)$$

and also

$$D'_{\perp} = \sqrt{\frac{2}{1 + 1/\delta'}}. \quad (4.50)$$



Substituting (4.49) into (4.47), we see that

$$(\delta' - 1)D'_\perp = \eta' D_\perp^{s'} \gg 1. \quad (4.51)$$

Here we know from (4.49) that  $0 \leq D'_\perp < \sqrt{2}$ , so  $\delta' \gg 1$ . Therefore, from (4.50) and (4.51), we obtain  $D'_\perp \approx \sqrt{2}$  and  $\delta' \approx D_\perp^{s'} \eta' / \sqrt{2}$ . Converting these to diffusion coefficients, the solutions for the case where  $\eta \rightarrow \infty$  and  $D_x^{slab} \gg D_x^{2D}$  are  $D_x \approx D_x^{slab}$  and  $D_y \approx 2D_x^{2D} D_y^{2D} / D_x^{slab}$ , which is much lower than  $D_y^{2D}$ . The increased slab turbulence in the  $x$ -direction leads to *decreased*  $y$ -diffusion. That means when  $D_x^{slab}$  makes  $D_x$  very large, it decorrelates the random flights in the  $y$  direction and also decreases the mean free path in the  $y$  direction and  $D_y$ . If  $\eta$  instead goes to zero, the roles of  $x$ - and  $y$ -components are reversed. That is if  $D_y^{slab} \ll D_y^{2D}$ , then the diffusion coefficients tend to 2D values. If, on the other hand,  $D_y^{slab} \gg D_y^{2D}$ , then  $D_y \approx D_y^{slab}$  and  $D_x \approx 2D_x^{2D} D_y^{2D} / D_y^{slab}$ , which is much lower than  $D_x^{2D}$ .

Finally, we consider the case where  $\xi \rightarrow \infty$  for fixed  $\eta$ . If  $D_\perp^{slab} \gg D_\perp^{2D}$ , then  $D_i \approx D_i^{slab}$ . If  $D_\perp^{slab} \ll D_\perp^{2D}$ , then  $D_y \approx D_y^{slab}$  while  $D_x \approx 2D_x^{2D} D_y^{2D} / D_y^{slab}$ , which is again much lower than  $D_x^{2D}$ .

## 4.4 Numerical Confirmation

In the numerical work, we simulate field lines in a large box in which the magnetic field is turbulent in order to compute the  $x$ - and  $y$ - diffusion coefficients. For field line tracing, we numerically solve the field line equations,

$$\frac{dx}{dz} = \frac{b_x}{B_0} \quad \text{and} \quad \frac{dy}{dz} = \frac{b_y}{B_0}. \quad (4.52)$$

The magnetic field components on the right hand sides are generated in wave number space ( $k$ -space) before conversion to real space. Thus, first, we have

to specify the magnetic power spectrum in  $k$ -space. The steps to simulate the non-axisymmetric field lines are same as we presented in Chapter 3 except that we adapt the magnetic field generating routine to produce the non-axisymmetric fields.

#### 4.4.1 2D and Slab Spectra

In order to simulate non-axisymmetric turbulence, we construct the power spectra differently in  $x$  and  $y$  directions. For slab turbulence, we set the power spectrum for simulations as

$$P_{ii}^{slab}(k_z) = \frac{C_i^{slab}}{[1 + (k_z \ell_{zi})^2]^{5/6}}, \quad (i = x, y), \quad (4.53)$$

where  $C_i^{slab}$  is a normalization constant of the  $i$ -component which depends on the turbulence energy in  $x$  and  $y$  directions for slab part, and  $\ell_{zi}$  is the parallel correlation scale of the  $i$ -component. For the 2D component, we instead specify power spectrum  $A(k_x, k_y)$  because the power spectra  $P_{xx}^{2D}$  and  $P_{yy}^{2D}$  can be written as

$$\begin{aligned} P_{xx}^{2D}(k_x, k_y) &= k_y^2 A(k_x, k_y) \\ P_{yy}^{2D}(k_x, k_y) &= k_x^2 A(k_x, k_y). \end{aligned} \quad (4.54)$$

Then axisymmetry of 2D turbulence would imply that  $A$  depends only on the magnitude  $k_{\perp} = \sqrt{k_x^2 + k_y^2}$ , i.e., would be constant along circles in  $(k_x, k_y)$  space. Here, for non-axisymmetric 2D turbulence, we suggest a form in which  $A$  is instead constant along ellipses in  $(k_x, k_y)$  space, with an ellipticity parameter  $\xi$  defined as the aspect ratio as shown in Figure 4.2. Thus we can write  $A$  as a function of  $k'_{\perp} = \sqrt{\xi k_x^2 + k_y^2/\xi}$ . The function of  $A$  that we use for simulation is

$$A(k'_{\perp}) = \frac{C^{2D}}{[1 + (k'_{\perp} \ell_{\perp})^2]^{7/3}}. \quad (4.55)$$

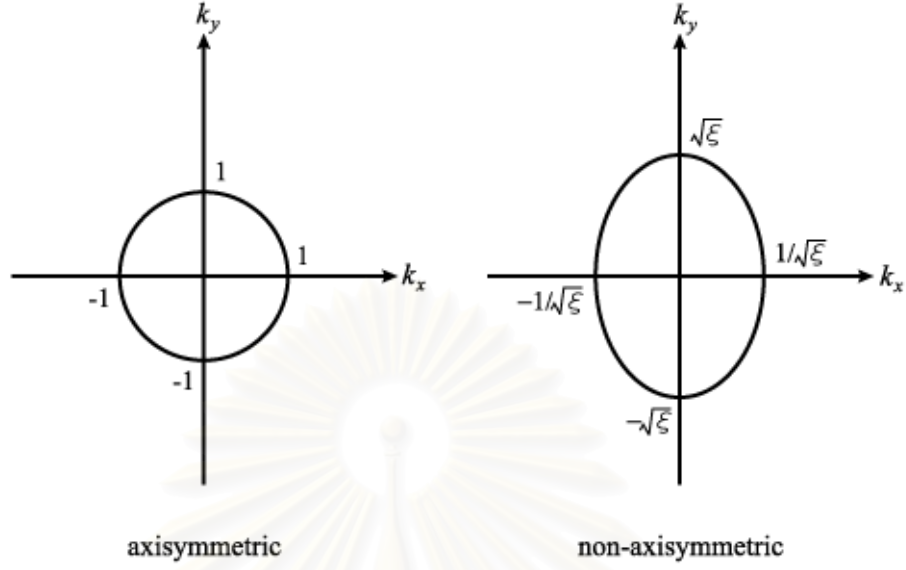


Figure 4.2: Contours of constant power of the 2D potential function for the axisymmetric case and for the type of non-axisymmetric 2D turbulence we consider in terms of the ellipticity parameter  $\xi$ .

This form of the 2D spectrum also permits the axisymmetric case when  $\xi = 1$ .

Now we have the spectra of magnetic turbulence. The relations between the magnetic field fluctuations and power spectra are

$$b_x^{slab}(k_z) = \sqrt{P_{xx}^{slab}} e^{i\phi(k_z)} \quad (4.56)$$

$$b_y^{slab}(k_z) = \sqrt{P_{yy}^{slab}} e^{i\phi(k_z)} \quad (4.57)$$

$$b_x^{2D}(k_x, k_y) = -ik_y \sqrt{A(k_x, k_y)} e^{i\phi(k_x, k_y)} \quad (4.58)$$

$$b_y^{2D}(k_x, k_y) = ik_x \sqrt{A(k_x, k_y)} e^{i\phi(k_x, k_y)}, \quad (4.59)$$

where  $\phi$  is a random phase number. After we have the magnetic fluctuations in  $k$ -space, we use inverse Fourier transforms to convert them to real space. Now we have the 2D and slab fluctuations in the simulation box. Next, the field line equation is solved by a fourth-order Runge-Kutta method with adaptive step

size control. After we get the positions of each field line, yielding the diffusion coefficients, we calculate  $\langle \Delta x^2 \rangle$  and  $\langle \Delta y^2 \rangle$  from the field line data and compute the running diffusion coefficients, i.e., the slope at each  $\Delta z$  in a plot of  $\langle \Delta x^2 \rangle$  or  $\langle \Delta y^2 \rangle$  vs.  $2\Delta z$ . The diffusion coefficient values from the numerical results come from the partial average of the running coefficient at  $\Delta z$  much greater than the correlation length. To ensure that we have enough of a sample for good statistics and to avoid periodicity effects, we randomly set starting points of the field lines in the box, change 2D realizations for every simulation, and trace the field lines to only a few percent of the box size.

#### 4.4.2 Simulations and Results

To verify the theory, we perform the simulations for three cases. For the first case, we confirm the theory for pure non-axisymmetric slab turbulence. In the second case, we simulate field lines in 2D+slab models that are non-axisymmetric only in the 2D component but isotropic in the slab component ( $D_x^{slab} = D_y^{slab}$ ). In the last case, the field lines are simulated in both non-axisymmetric 2D and slab fields. The results from simulations are compared with the discrete theory.

##### Case I: Non-axisymmetric Slab Turbulence without a 2D Component

We set  $L_x = L_y = L_z = 100,000\ell_{zx}$  and trace the field lines over only 2.5% of  $L_z$ . For the number of grid points, we set  $N_z = 2^{22} \approx 4$  million. The parameters governing anisotropy for this case are  $f_x$ ,  $\ell_{zx}$ , and  $\ell_{zy}$ . In the axisymmetric case, we usually set  $\ell_{zx} = \ell_{zy} = 1$  and  $f_x = f_y = 0.5$ , where  $f_x = \langle b_x^2 \rangle^{slab} / \langle b^2 \rangle^{slab}$  and  $f_y = \langle b_y^2 \rangle^{slab} / \langle b^2 \rangle^{slab}$ . Thus if we change these three parameters to other values, the system becomes non-axisymmetric. In this simulation we set  $\delta b/B_0=0.5$  as a

constant for all runs. Their values and differences are shown in Table 4.1. Clearly the simulation results match the theory quite closely.

Table 4.1: Discrete theory and simulation results for the diffusion coefficients and their differences when we vary  $f_x$ ,  $\ell_{zx}$ , for  $\ell_{zy}$ .

Run	$f_x$	$\ell_{zx}$	$\ell_{zy}$	$D_x$ theory	$D_y$ theory	$D_x$ sim.	$D_y$ sim.	$\Delta D_x$ (%)	$\Delta D_y$ (%)
1	0.50	1.0	1.0	0.09762	0.09762	0.09591	0.09632	-1.75	-1.33
2	0.25	1.0	1.0	0.04881	0.14644	0.04879	0.14400	-0.04	-1.67
3	0.75	1.0	1.0	0.14644	0.04881	0.14859	0.04815	+1.47	-1.35
4	0.50	1.0	2.0	0.09762	0.19200	0.09717	0.19738	-0.46	+2.80
5	0.50	1.0	0.5	0.09762	0.05016	0.09989	0.04875	+2.33	-2.81
6	0.50	2.0	1.0	0.19200	0.09762	0.19011	0.09640	-0.98	-1.25
7	0.50	0.5	1.0	0.05016	0.09762	0.04941	0.09661	-1.50	-1.03
8	0.75	1.0	2.0	0.14644	0.09600	0.14338	0.09625	-2.09	+0.26

## Case II: Non-axisymmetric 2D Turbulence with Axisymmetric Slab Turbulence

We keep all parameters for the slab component constant and axisymmetric, i.e.,  $f_x = 0.5f_s$ , where  $f_s$  is the fraction of slab energy,  $\ell_{zx}=1$ , and  $\ell_{zy}=1$ , and vary only the ellipticity  $\xi$  of  $A(k_x, k_y)$ . Figure 4.3 shows the relationship between the spectrum  $A(k_x, k_y)$  and potential function  $a(x, y)$  when we vary  $\xi$ . Therefore, in theory,  $D_x^{slab} = D_y^{slab}$  and they are constant for all of these runs. Moreover we set  $\ell_{\perp} = 1$  and  $\delta b/B_0 = 0.5$ , and perform two sets of simulations. One is for  $E^{slab} : E^{2D} = 20:80$  and another one is for  $E^{slab} : E^{2D} = 80:20$ . For the simulations, we trace 1,000 field lines in the large box with  $L_z = 100,000\ell_{zx}$  and  $L_x = L_y = 200\ell_{zx}$  and the numbers of grid points are  $N_x = N_y = 4,096$  and  $N_z = 2^{22}$ . The 2D realization is changed for every field line and the starting position of field lines is chosen randomly in the box. Tables 4.2 and 4.3 indicate

the numerical and theoretical values and the errors when we vary the ellipticity  $\xi$  for 20:80 and 80:20 cases. The theoretical values and numerical results for those two cases are plotted as Figures 4.4 and 4.5. For  $E^{slab} : E^{2D} = 20:80$ , we add two columns with kurtosis values of each component, which are  $\kappa^x = \langle \Delta x^4 \rangle / \langle \Delta x^2 \rangle^2$  and  $\kappa^y = \langle \Delta y^4 \rangle / \langle \Delta y^2 \rangle^2$ , to test for Gaussian distributions, which have a kurtosis of 3. We conclude that all kurtosis values are consistent with Gaussian distributions.

Table 4.2: Comparison between numerical results and theoretical results of the diffusion coefficients for 20% slab and 80% 2D energies when  $\xi$  is varied.

Run	$\xi$	$D_x$ theory	$D_y$ theory	$D_x$ sim.	$D_y$ sim.	$\Delta D_x$ (%)	$\Delta D_y$ (%)	$\kappa^x =$ $\frac{\langle \Delta x^4 \rangle}{\langle \Delta x^2 \rangle^2}$	$\kappa^y =$ $\frac{\langle \Delta y^4 \rangle}{\langle \Delta y^2 \rangle^2}$
1	0.25	0.0550	0.4038	0.0556	0.3767	+1.15	-6.72	2.90	3.05
2	1/3	0.0711	0.3748	0.0722	0.3449	+1.60	-7.98	3.00	3.01
3	0.5	0.1053	0.3172	0.1016	0.2771	-3.50	-12.64	3.01	2.95
4	2/3	0.1392	0.2692	0.1340	0.2386	-3.77	-11.36	3.15	3.05
5	1.0	0.2000	0.2000	0.1812	0.1778	-9.43	-11.10	3.09	2.97
6	1.5	0.2692	0.1392	0.2350	0.1310	-12.70	-5.88	3.04	3.01
7	2.0	0.3172	0.1053	0.2897	0.1021	-8.68	-3.02	2.98	2.93
8	3.0	0.3748	0.0711	0.3535	0.0699	-5.68	-1.73	3.02	2.95
9	4.0	0.4038	0.0550	0.3758	0.0572	-6.94	+4.07	3.02	2.89

Table 4.3: Comparison between numerical results and theoretical results of the diffusion coefficients for 80% slab and 20% 2D energies when  $\xi$  is varied.

Run	$\xi$	$D_x$ theory	$D_y$ theory	$D_x$ sim.	$D_y$ sim.	$\Delta D_x$ (%)	$\Delta D_y$ (%)
1	0.25	0.0923	0.1508	0.0894	0.1651	-3.20	+9.44
2	1/3	0.0991	0.1574	0.0984	0.1653	-0.69	+5.06
3	0.5	0.1122	0.1595	0.1155	0.1688	+2.91	+5.84
4	2/3	0.1241	0.1554	0.1283	0.1636	+3.38	+5.27
5	1.0	0.1418	0.1418	0.1439	0.1448	+1.51	+2.16
6	1.5	0.1554	0.1241	0.1640	0.1275	+5.58	+2.72
7	2.0	0.1597	0.1123	0.1653	0.1119	+3.49	-0.41
8	3.0	0.1574	0.0991	0.1700	0.0981	+8.02	-0.93
9	4.0	0.1508	0.0923	0.1622	0.0904	+7.51	-2.09

สถาบันวิทยบริการ  
จุฬาลงกรณ์มหาวิทยาลัย

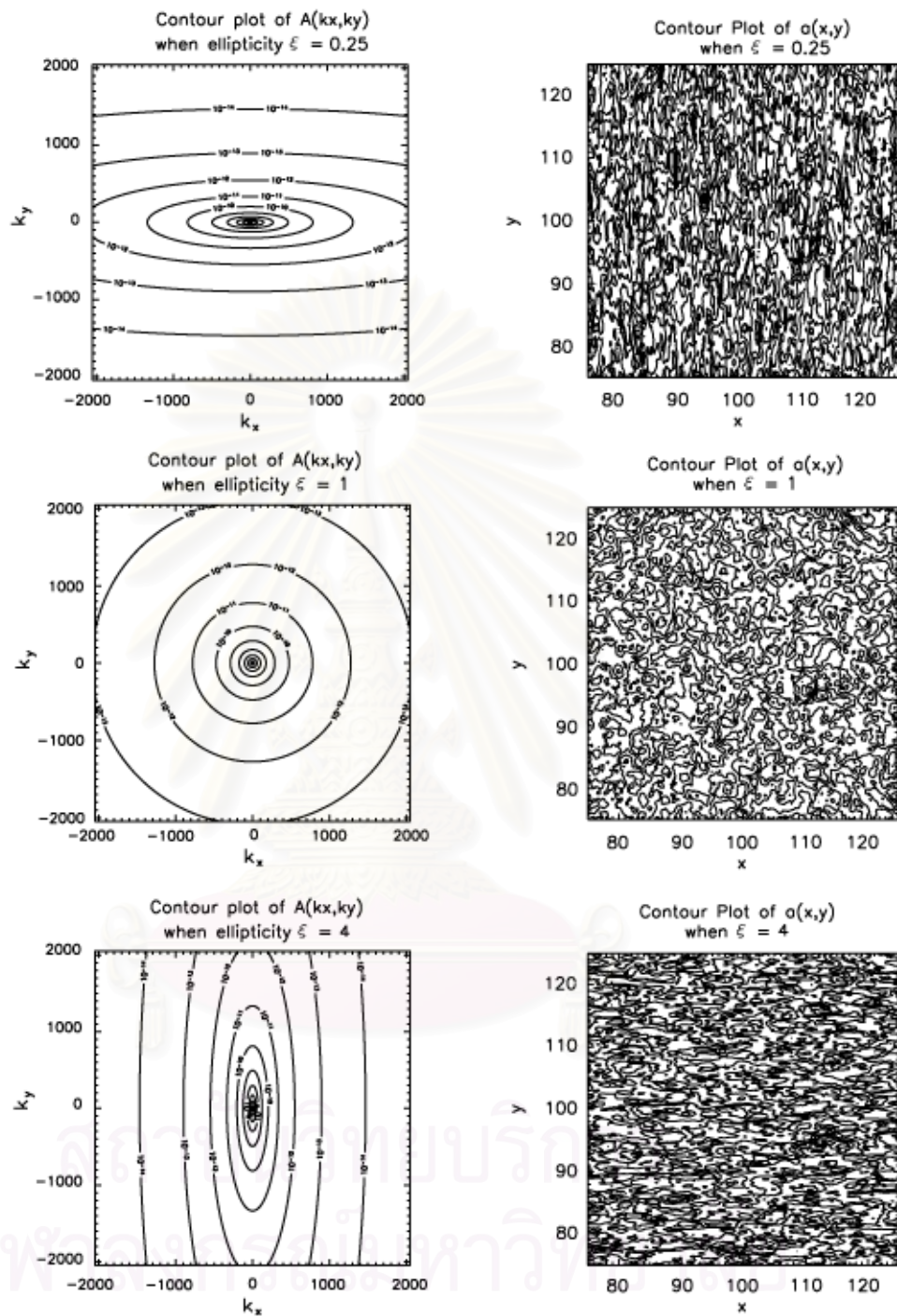


Figure 4.3: Relationship between the autocorrelation  $A(k_x, k_y)$  and the potential function  $a(x, y)$ . The scales of the  $A(k_x, k_y)$  plot indicate the number of modes in  $(k_x, k_y)$  space and the contour plots of  $a(x, y)$  in the right panel are only small pieces cut from the large simulation area.



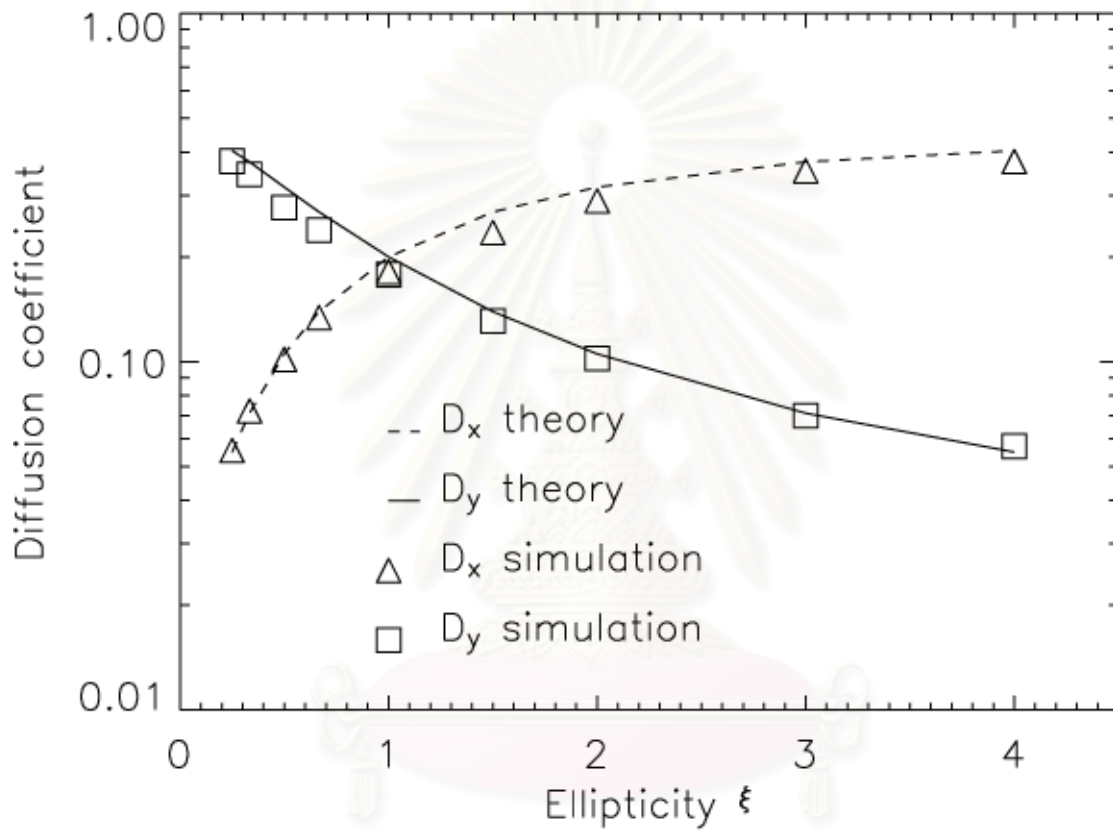


Figure 4.4: Diffusion coefficients from theory and simulations for  $E^{slab} : E^{2D} = 20 : 80$  when we vary only the ellipticity  $\xi$ .

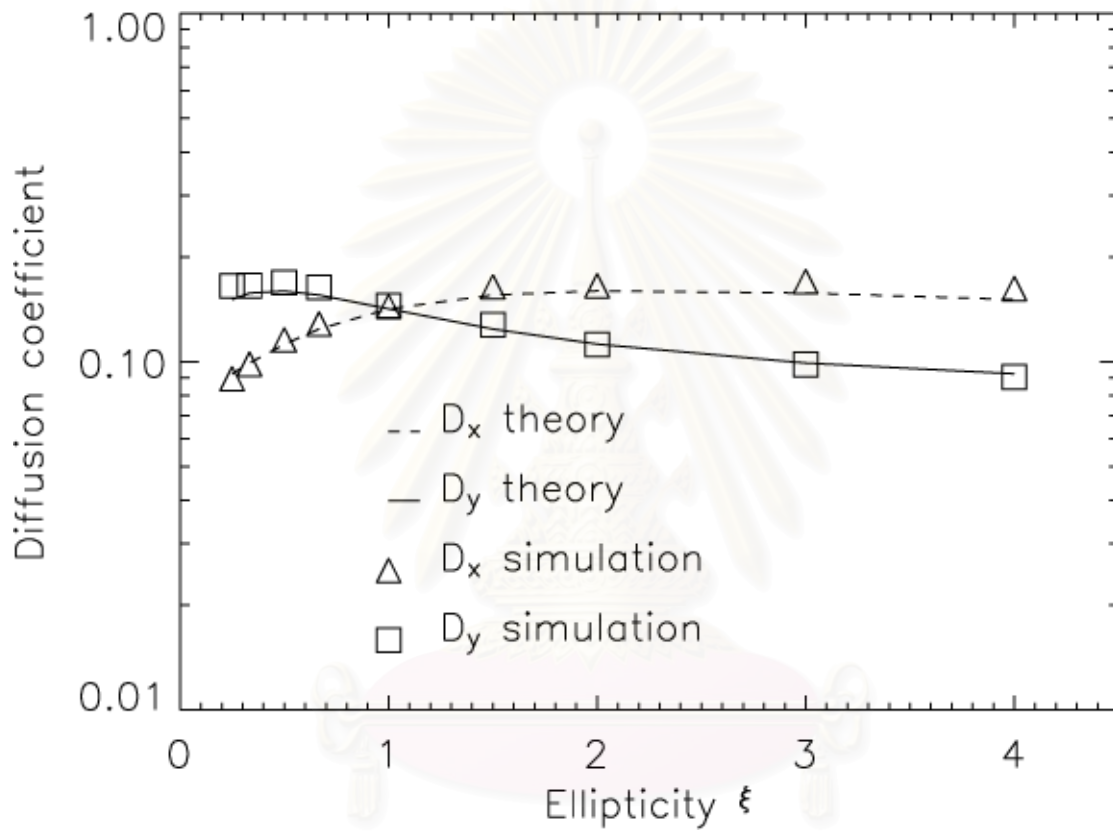


Figure 4.5: Diffusion coefficients from theory and simulations for  $E^{slab} : E^{2D} = 80 : 20$  when we vary only the ellipticity  $\xi$ .

จุฬาลงกรณ์มหาวิทยาลัย

### Case III: Non-axisymmetric Slab and 2D Turbulence

To be sure that the theory also works for the various cases in which both the slab and 2D turbulence are non-axisymmetric, we vary the parameters that cause non-axisymmetry of the 2D+slab turbulent field. We use the box size and other parameters as in case II but vary  $f_x/f_s$ ,  $\ell_{zx}$ ,  $\ell_{zy}$ , and  $\xi$ . Table 4.4 shows the results for this case.

Table 4.4: Discrete theory and simulation values and their differences when we vary all non-axisymmetry parameters.

$E_{slab} :$ $E_{2D}$	$f_x$	$\ell_{zx}$	$\ell_{zy}$	$\xi$	$D_x$ theory	$D_y$ theory	$D_x$ sim.	$D_y$ sim.	$\Delta D_x$ (%)	$\Delta D_y$ (%)
20:80	0.25	1.0	1.0	1.0	0.18260	0.21824	0.15744	0.20091	-13.78	-7.94
20:80	0.5	1.0	2.0	1.0	0.18881	0.22193	0.17234	0.20854	-8.72	-6.03
20:80	0.75	1.0	2.0	2.0	0.30971	0.11456	0.30420	0.10064	-1.78	-12.15
80:20	0.25	1.0	1.0	1.0	0.09353	0.19602	0.09823	0.19983	+5.02	+1.94
80:20	0.5	1.0	2.0	1.0	0.14387	0.19154	0.13487	0.21980	-6.26	+14.75
80:20	0.75	1.0	2.0	2.0	0.19869	0.10668	0.21412	0.10718	+7.77	+6.10

## 4.5 Summary

We analytically derive the diffusion coefficients in  $x$  and  $y$  directions for the non-axisymmetric field line random walk with using homogeneity, the diffusion approximation, and Corrsin's independent hypothesis. For slab turbulence, we make the parallel correlation lengths and slab fluctuations different in  $x$  and  $y$  directions and we suggest the form that the power spectrum  $A(k_x, k_y)$  is constant along ellipses in  $(k_x, k_y)$  space for the 2D turbulence. The solution is non-perturbative and in the simple form of coupled bi-quadratic equations. We also show the closed-form expressions for special cases of interest in the helio-

spheric transport of charge particles, such as solar modulation of cosmic rays and particle acceleration at a nearly perpendicular shock.

For the numerical simulations, we can see that the numerical results and theory have very good agreement. For the first case, pure non-axisymmetric slab turbulence, the simulations agree very well with the theory. The differences are less than 3%. It is interesting to note the discrepancy between simulations and theory when  $E_{slab} : E_{2D} = 20 : 80$  and the field is non-axisymmetric only in the 2D component. This is large (9%-13%) when  $\xi$  is near 1 and it drops when  $\xi \gg 1$  and  $\xi \ll 1$ . Moreover, the discrepancy in the direction that gives a large diffusion coefficient is always greater than that in the direction that gives a small number. When we decrease the fraction of turbulent energy in the 2D component to 20% ( $E_{slab} : E_{2D} = 80 : 20$ ), the differences between theory and numerical results decrease. It seems that the 2D energy affects the discrepancy between theory and simulations. However, the differences are still within 15%, which is similar that obtained in Gray et al. (1996). Furthermore, the theory is also verified in the case where both slab and 2D turbulence are non-axisymmetric. According to the numerical simulations, the theory of field line random walk in non-axisymmetric 2D and slab turbulence, which is based on the assumptions of homogeneity, a Gaussian distribution and the diffusion approximation, and Corrsin's independent hypothesis, works very well. In addition, the topology of the potential function of 2D turbulence is important for further understanding of the diffusion of field lines. Finally, the theory and numerical simulations can be applied to various astrophysical situations, especially in the solar wind, in order to study the diffusion of the field lines and charged particles.

# Chapter 5

## Field Line Separation

### 5.1 Introduction

The random walk of individual magnetic field lines relative to the mean magnetic field and the rate of separation of nearby field lines are key issues in defining the topology and structure of random magnetic fields in magnetohydrodynamic (MHD) turbulence. The statistics of such a random walk are often central to understanding the diffusion of energetic charged particles perpendicular to the mean magnetic field in astrophysical plasmas (Jokipii 1966; Jokipii & Parker 1968). Perpendicular diffusion is an important component of the solar cycle dependent modulation of Galactic cosmic rays (Parker 1965; Moraal 1976; Cane et al. 1999; Reinecke et al. 2000). Determining the rate of perpendicular diffusion of energetic particles in the heliosphere may be crucial in distinguishing between two popular models for explaining the dramatic observations by the ULYSSES spacecraft of apparent corotating interaction region (CIR) modulation of Galactic and anomalous cosmic rays (Kunow et al. 1995; McKibben et al. 1995; Simpson et al. 1995) and acceleration of low energy electrons and ions (Sanderson et al. 1995; Simnett et al. 1995) at higher heliospheric latitudes than where CIRs were observed, i.e., the models of Kóta & Jokipii (1995) and Fisk (1996). Other issues of energetic particle transport in the heliosphere may rely upon details of perpendicular diffusion, such as the poor access of Galactic cosmic rays into a corona mass ejection (Cane et al. 1994) that can account for the deep minima

of Forbush decreases, or energetic particle acceleration at a nearly perpendicular shock (Jokipii 1987; Jokipii et al. 1993; Kirk et al. 1996; Jones et al. 1998).

On the other hand, there are also situations in which the behavior of distributions of energetic charged particles might be better understood in terms of the mutual separation of field lines than by the random walk of individual field lines (Jokipii 1973). Indeed for an initially concentrated distribution of particles (assumed to be following field lines) to spread in the directions perpendicular to the mean magnetic field requires that the field lines threading the distribution mutually separate; a correlated wandering of nearby field lines would just displace the particle distribution without distorting it. Figure 5.1 illustrates the random walk perpendicular to the mean field ( $\Delta x$ ), the displacement between nearby field lines ( $X \equiv x_2 - x_1$ ), and their separation  $\Delta X \equiv X - X_0$ . In the extreme case that two turbulent field lines are completely decorrelated, the mean squared separation would be twice the mean squared random walk. On the other hand, two nearby field lines could follow highly correlated trajectories with a mutual separation much lower than the displacement from the mean field, as represented by the lower two field lines in Figure 5.1. Therefore field line separation is a sensitive probe of the dissimilarity of nearby field lines and the transverse structure of magnetic turbulence.

One application of calculating the field line separation is to address the long-recognized phenomenon of “channeling” or sudden changes in the fluxes of solar energetic particles (SEP), which has been revisited by recent, detailed measurements of Mazur et al. (2000), who refer to such events as “dropouts.” These are presumably due to sudden changes in magnetic connection to a spatially localized injection region. This picture requires that field lines that are adjacent

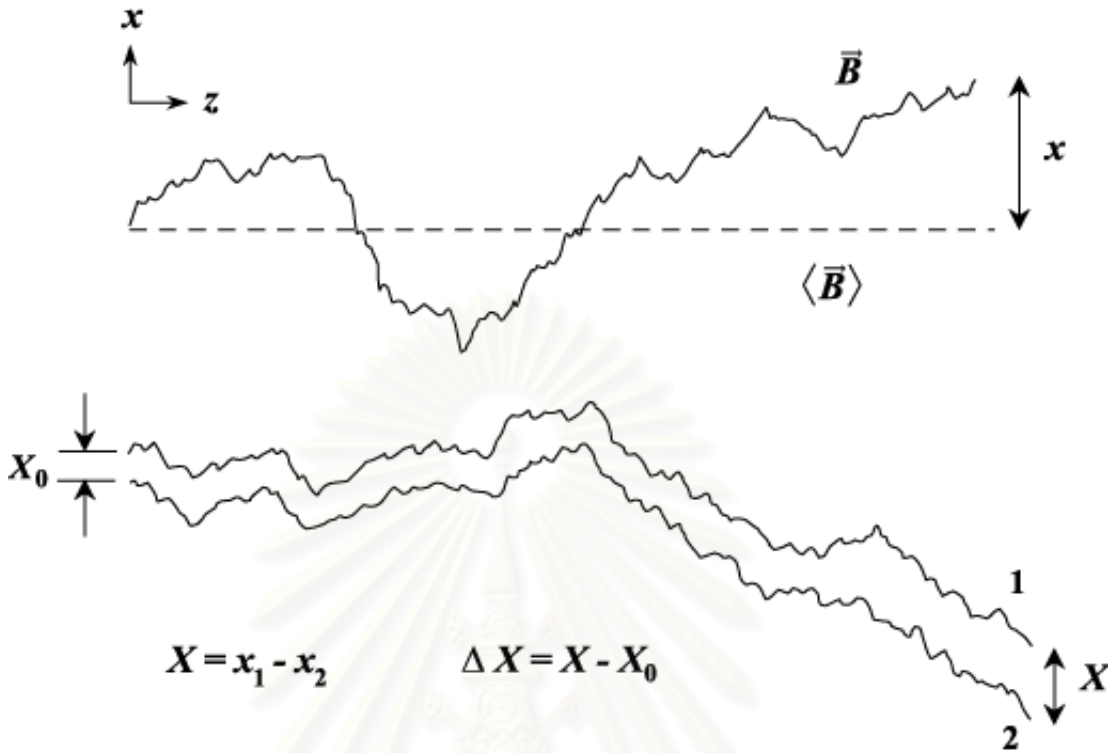


Figure 5.1: Illustration of the magnetic field line random walk perpendicular to the mean field ( $\Delta x$ ), displacement between nearby field lines ( $X \equiv x_2 - x_1$ ), and their separation ( $\Delta X \equiv X - X_0$ ). The present work calculates the mean squared separation vs. distance along the mean field.

when near the Sun remain confined to localized flux tubes out to distances  $\sim 1$  AU along the mean field.

In particular, Mazur et al. (2000) identify episodes of dramatic SEP intensity changes on an average timescale of 3 hr, corresponding to a spatial (longitudinal) scale of 0.03 AU. Giacalone et al. (2000) point out that if there is effectively no turbulent random walk, one can understand dropouts in terms of the field line random walk due to photospheric motions. This leads to the question: Why is there no apparent turbulent random walk? There certainly is turbulence in the interplanetary medium. One might expect a longitudinal diffu-

sion of field lines (due to the 2D component of solar wind fluctuations) to a scale of  $(\Delta x)_{\text{rms}} = \sqrt{2D_{\perp}\Delta z}$ , where the diffusion coefficient of the turbulent random walk is  $D_{\perp} = (b/B_0)(\tilde{\lambda}/\sqrt{2})$  (Matthaeus et al. 1995) and  $\tilde{\lambda}$  is the “ultrascale” or “mesoscale,” inferred from observations to be  $\sim 0.2$  AU (Matthaeus, Smith, & Bieber 1999). For a typical root-mean-squared turbulent magnetic field of half the mean field,  $b = 0.5B_0$ , the expected longitudinal scale of the turbulent random walk is 0.37 AU, which would wash out the observed dropouts. One possible explanation might be that the separation of nearby field lines, which controls the spread of particles from a small injection region near the Sun, could be much slower than the turbulent random walk relative to the mean field, as illustrated in Figure 5.1. This issue, which will be discussed again in Section 5.5, is just one example of an astrophysical problem related to the separation of nearby magnetic field lines.

The theory of the separation of adjacent field lines has been examined by Jokipii (1973) and Zimbardo et al. (1984). This issue has been recognized as relevant to physical processes in fusion plasmas (e.g., Rechester & Rosenbluth 1978; Kadomtsev & Pogutse 1979; Isichenko 1991a, 1991b), the solar corona (e.g., Similon & Sudan 1989), energetic particle transport in the heliosphere (Erdős et al. 1997, 1999), cosmic ray transport and acceleration in the Galaxy (Barge, Millet, & Pellat 1984; Chandran 2000), and thermal conduction in galaxy clusters (Maron, Chandran, & Blackman 2004). Much attention has been devoted in the past to description of the exponential separation of field lines (Rechester & Rosenbluth 1978; Kadomtsev & Pogutse 1979), in the régime of small separation before the field lines undergo independent random walks, owing to the relationship of that phenomenon to mixing in ergodic theory (Zaslavsky & Chirikov 1972) and



stochastic instability in general. In the present paper we will be mainly concerned with régimes of diffusive behavior, although we will comment on the relationship between these two views of field line separation. The length scale along the mean field over which field lines separate by a perpendicular coherence scale is relevant to incompressible MHD turbulence (Goldreich & Sridhar 1997; Lithwick & Goldreich 2001).

Apart from the observational issues discussed above, there are also a number of theoretical issues that provide motivation for reconsidering field line separation in a “realistic” (or, at least, observationally motivated) three-dimensional model magnetic field. For example, one feature of turbulence structure that has become recognized in recent years (Jones et al. 1998) is that models that are one dimensional (“slab”) or that admit even one ignorable coordinate give rise to pathological statistical representations of particle transport. There are also indications that the stochastic instability of field lines has a character in models having small numbers of coherent modes that contrasts strongly with its character in a continuum of incoherent modes (Rax & White 1992). It is reasonable to anticipate that such differences would impact the onset and nature of diffusion. One is cautioned, then, that some properties that emerge from simplified models of field line separation should not be taken as rigorous, especially in the light of better understood properties from observations and turbulence simulations. An example is the rather general identification of the correlation scale with the exponential separation scale (e.g., Sagdeev et al. 1988), although this is not a well understood relationship (Rechester & Rosenbluth 1978). Similarly, the identification of the correlation scale of magnetic fluctuations with the correlation scale of the *spatial gradients* of the fluctuations (Isichenko 1991a) is manifestly incorrect

for turbulence having distinct inner and outer scales. Moreover for homogeneous turbulence, the correlation scale of derivatives, i.e., the Taylor microscale, may differ from the fluctuation correlation scale by orders of magnitude (Batchelor 1953). This difference is at least three or four orders of magnitude in the solar wind (Matthaeus & Goldstein 1982). Finally we note that the realm of applicability of the perturbative quasi-linear (QLT) limit is often expressed (Isichenko 1991a) in terms of a dimensionless (Kubo) number  $R = (b/B_0)(\lambda_{\parallel}/\lambda_{\perp})$ , where  $\lambda_{\parallel}$  and  $\lambda_{\perp}$  are, respectively, correlation scales in the directions parallel to and perpendicular to the large scale mean magnetic field  $B_0$ . QLT is supposed to be accurate when  $R \ll 1$ . While qualitatively correct, we can see that a criterion based solely upon  $R$  cannot be complete, in view of the fact that the contribution to field line diffusion due to a quasi-two-dimensional component of the turbulence (Matthaeus et al. 1995) depends upon not  $\lambda_{\perp}$  but a distinct scale (the “ultrascale,” see below) that characterizes large-scale transverse magnetic structure.

In the following sections we re-examine the theory of the separation of adjacent field lines in astrophysical MHD turbulence, in light of improved understanding of solar wind turbulence in recent years (Matthaeus, Goldstein, & Roberts 1990; Bieber et al. 1994). We consider field line separation in two-component turbulence consisting of a slab component that varies only along the mean field, as well as a two-dimensional component that varies only in the two transverse directions, which has been shown to serve as a useful model of solar wind turbulence (Bieber, Wanner, & Matthaeus 1996). This turbulence model can also be viewed as a concrete example that is representative of anisotropic turbulence in general, i.e., turbulence that varies differently along or perpendic-

ular to the mean magnetic field. We proceed using a non-perturbative approach similar to that which has been used previously (Matthaeus et al. 1995; Gray et al. 1996) to examine the field line random walk. The main development of the analytical theory for the field line separation has been done by Assoc. Prof. David Ruffolo and Prof. William H. Matthaeus. The analytic results are verified by computer simulations, which is the part on which I concentrated. We then consider their astrophysical implications. We already published this work in the *Astrophysical Journal* (Ruffolo, Matthaeus, & Chuychai 2004).

## 5.2 Analytic theory

In this section, we derive the separation of two magnetic field lines in two-component 2D+slab turbulence. Now we consider the lateral coordinates of two different field lines,  $x_1(z)$ ,  $y_1(z)$ ,  $x_2(z)$ , and  $y_2(z)$ , expressing the displacement between them by  $X \equiv x_1 - x_2$  and  $Y \equiv y_1 - y_2$  (see Figures 5.1 and 5.2). Without loss of generality, we consider  $X(z = 0) = X_0$  and  $Y(z = 0) = 0$ , i.e., the  $x$ -direction is defined to be along the displacement between the two field lines at  $z = 0$ . Then the separation of the field lines is expressed as the change in displacement,  $(\Delta X, \Delta Y)$ , as a function of distance  $\Delta z$  along the mean magnetic field.

Note that although the turbulence can be assumed to be statistically homogeneous and axisymmetric in position space  $(x, y)$ , the same cannot be said for displacement space  $(X, Y)$  (see Figure 5.3). In particular, when considering the correlation between the 2D component of the turbulent field,  $\vec{b}^{2D}$ , at the positions of the two field lines, there is a fundamental difference between a distance much less than  $\ell_\perp$  (strong correlation) and a distance much greater than  $\ell_\perp$  (weak

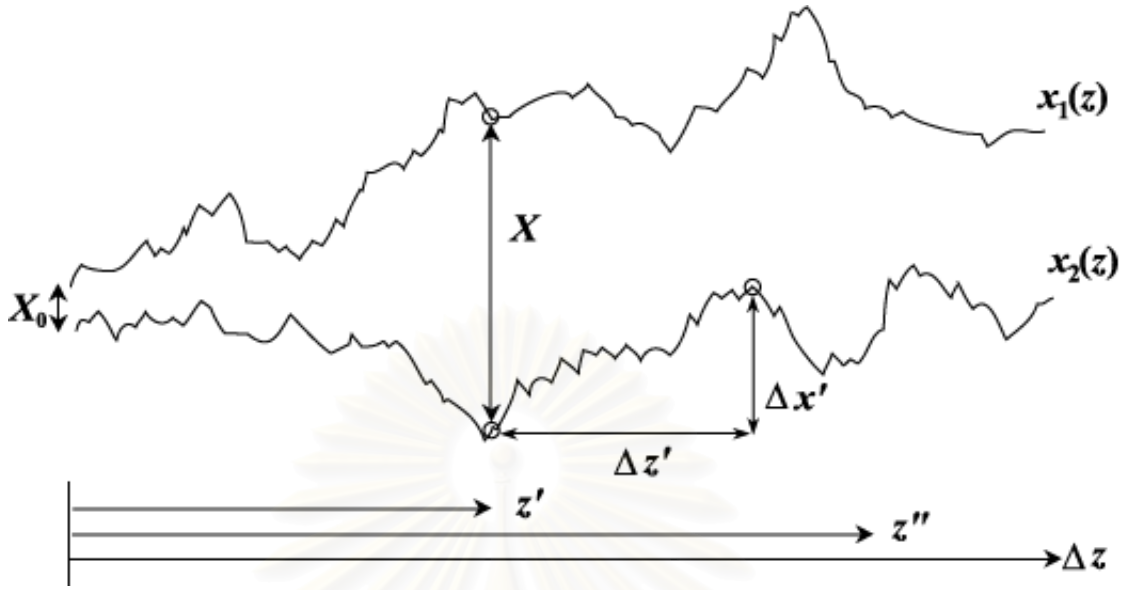


Figure 5.2: Schematic of two random field lines and definition of various quantities.

correlation). When we define the initial displacement as  $(X_0, 0)$ , then the separation in the two directions,  $\Delta X$  and  $\Delta Y$ , need not be statistically identical, as we will show mathematically in this section. Physically,  $\Delta X$  initially represents a changing distance between the two field lines, while  $\Delta Y$  initially implies a changing orientation of the displacement (Figure 5.3). After a large  $\Delta z$ , when  $\sqrt{\langle \Delta X^2 \rangle}$  and  $\sqrt{\langle \Delta Y^2 \rangle}$  are both much greater than  $\ell_\perp$ , the separation becomes axisymmetric, with  $\sqrt{\langle \Delta X^2 \rangle} \approx \sqrt{\langle \Delta Y^2 \rangle}$ .

Let us first treat  $\Delta X$ , the  $x$ -separation between two field lines after a distance  $\Delta z$ , which can be expressed as (Jokipii 1973):

$$\Delta X = \Delta x_1 - \Delta x_2 = \frac{1}{B_0} \int_0^{\Delta z} [b_x(x'_1, y'_1, z') - b_x(x'_2, y'_2, z')] dz'. \quad (5.1)$$

Then we have

$$\langle \Delta X^2 \rangle = \frac{1}{B_0^2} \int_0^{\Delta z} \int_0^{\Delta z} \langle b_x(x'_1, y'_1, z') b_x(x''_1, y''_1, z'') \rangle dz' dz''$$

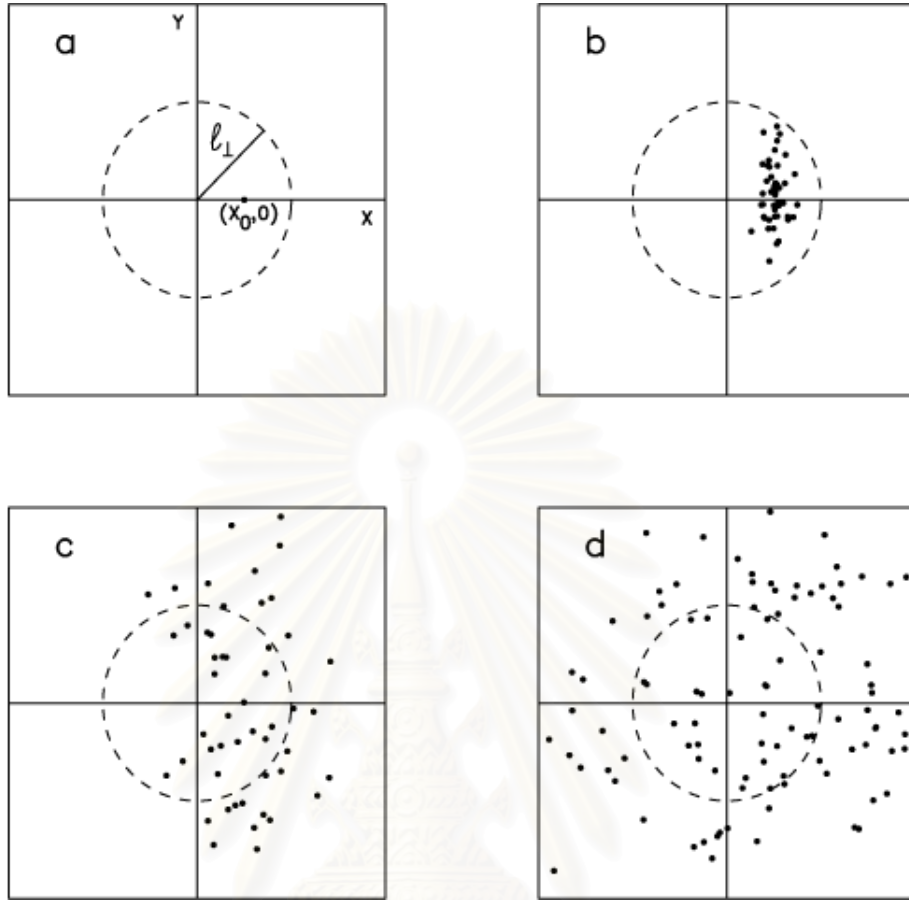


Figure 5.3: Schematic of the separation of field lines, i.e., the change in displacement  $(X, Y)$  between two field lines for a small initial displacement  $(X_0, 0)$ . a) 2D turbulence is strongly correlated only for displacements within the dashed circle, of less than a perpendicular coherence length  $\ell_{\perp}$ . Panels b-d illustrate the distribution of field line displacements with increasing  $\Delta z$ . b) Slow diffusive separation. c) Superdiffusive separation. d) Fast diffusive separation.

$$\begin{aligned}
 & + \frac{1}{B_0^2} \int_0^{\Delta z} \int_0^{\Delta z} \langle b_x(x'_2, y'_2, z') b_x(x''_2, y''_2, z'') \rangle dz' dz'' \\
 & - \frac{1}{B_0^2} \int_0^{\Delta z} \int_0^{\Delta z} \langle b_x(x'_1, y'_1, z') b_x(x''_2, y''_2, z'') \rangle dz' dz'' \\
 & - \frac{1}{B_0^2} \int_0^{\Delta z} \int_0^{\Delta z} \langle b_x(x'_2, y'_2, z') b_x(x''_1, y''_1, z'') \rangle dz' dz''. \quad (5.2)
 \end{aligned}$$

From the symmetry of “1” and “2” indices, we have

$$\langle \Delta X^2 \rangle = 2I_{11} - 2I_{12}, \quad (5.3)$$

where we define

$$I_{11} = \langle \Delta x^2 \rangle = \frac{1}{B_0^2} \int_0^{\Delta z} \int_0^{\Delta z} \langle b_x(x'_1, y'_1, z') b_x(x''_1, y''_1, z'') \rangle dz' dz'', \quad (5.4)$$

$$I_{12} = \frac{1}{B_0^2} \int_0^{\Delta z} \int_0^{\Delta z} \langle b_x(x'_1, y'_1, z') b_x(x''_2, y''_2, z'') \rangle dz' dz''. \quad (5.5)$$

Since slab fluctuations are independent of  $x$  and  $y$  coordinates, the contributions of slab turbulence to  $I_{11}$  and  $I_{12}$  are equal. Thus the direct slab contributions to  $\langle \Delta X^2 \rangle$  cancel, which makes sense because in pure slab turbulence the two field lines maintain a constant relative displacement at all  $z$ . This leaves us with

$$\langle \Delta X^2 \rangle = 2\langle \Delta x^2 \rangle_{2D} - \frac{2}{B_0^2} \int_0^{\Delta z} \int_0^{\Delta z} \langle b_x^{2D}(x'_1, y'_1, z') b_x^{2D}(x''_2, y''_2, z'') \rangle dz' dz''. \quad (5.6)$$

An equation for  $\langle \Delta Y^2 \rangle$  can be obtained by the substitutions  $\Delta X \rightarrow \Delta Y$ ,  $\Delta x \rightarrow \Delta y$ , and  $b_x \rightarrow b_y$ ; with the assumption of axisymmetry in  $x$  and  $y$ , we have  $\langle \Delta x^2 \rangle = \langle \Delta y^2 \rangle$ . Note that although the direct slab contributions have cancelled, the presence of slab turbulence still affects the results in that both terms on the right hand side of (5.6) implicitly involve the total perpendicular diffusion coefficient,  $D_\perp = \langle \Delta x^2 \rangle / (2\Delta z)$  (including the slab contribution).

The calculation of the field line separation for a given  $\Delta z$  proceeds as in Section 2.7. With the assumption of homogeneity, and again treating  $\Delta X$  first,

$$\begin{aligned} \langle \Delta X^2 \rangle &= 2\langle \Delta x^2 \rangle_{2D} \\ &\quad - \frac{2}{B_0^2} \int_0^{\Delta z} \int_{-z'}^{\Delta z - z'} \langle b_x^{2D}(0, 0, 0) b_x^{2D}(\Delta x'_2 - X', \Delta y'_2 - Y', \Delta z') \rangle d\Delta z' dz'. \end{aligned} \quad (5.7)$$

Suppressing “2” subscripts, and using the simplified notation  $X' \rightarrow X$ ,  $Y' \rightarrow Y$ , and  $z' \rightarrow z$ , we have

$$\begin{aligned} \langle \Delta X^2 \rangle &= 2\langle \Delta x^2 \rangle_{2D} \\ &\quad - \frac{2}{B_0^2} \int_0^{\Delta z} \int_{-z}^{\Delta z-z} \langle b_x^{2D}(0,0,0) b_x^{2D}(\Delta x' - X, \Delta y' - Y, \Delta z') \rangle d\Delta z' dz. \end{aligned} \quad (5.8)$$

Here the displacement between  $x_2''$  and  $x_1'$  is expressed in terms of displacements from a common point  $x_2'$  as shown in Figure 5.2. Then Corrsin’s hypothesis and the assumption of independence of  $X$  and  $Y$  displacements allow us to write

$$\begin{aligned} \langle \Delta X^2 \rangle &= 2\langle \Delta x^2 \rangle_{2D} - \frac{2}{B_0^2} \frac{1}{2\pi} \int_{-\infty}^{\infty} \int_{-\infty}^{\infty} P_{xx}^{2D}(k_x, k_y) \\ &\quad \times \left\{ \int_0^{\Delta z} \left[ \int_{-z}^{\Delta z-z} \left( \int_{-\infty}^{\infty} e^{-ik_x \Delta x'} P(\Delta x' | \Delta z') d\Delta x' \right) \right. \right. \\ &\quad \times \left. \left( \int_{-\infty}^{\infty} e^{-ik_y \Delta y'} P(\Delta y' | \Delta z') d\Delta y' \right) d\Delta z' \right] \left[ \int_{-\infty}^{\infty} e^{ik_x X} P(X|z) dX \right] \\ &\quad \times \left. \left[ \int_{-\infty}^{\infty} e^{ik_y Y} P(Y|z) dY \right] dz \right\} dk_x dk_y. \end{aligned} \quad (5.9)$$

We can evaluate the three square-bracketed expressions in turn, making use of Gaussian and diffusive conditional probability distributions. In the first, the  $\Delta x'$  and  $\Delta y'$  integrals (inside parentheses) can be evaluated as in (2.67), after which the  $\Delta z'$  integral is straightforward:

$$\begin{aligned} &\int_{-z}^{\Delta z-z} \left( \int_{-\infty}^{\infty} e^{-ik_x \Delta x'} P(\Delta x' | \Delta z') d\Delta x' \right) \left( \int_{-\infty}^{\infty} e^{-ik_y \Delta y'} P(\Delta y' | \Delta z') d\Delta y' \right) d\Delta z' \\ &\quad = \frac{1}{D_{\perp} k_{\perp}^2} \left( 2 - e^{-D_{\perp} k_{\perp}^2 (\Delta z - z)} - e^{-D_{\perp} k_{\perp}^2 z} \right). \end{aligned} \quad (5.10)$$

For the second bracketed expression, we note that  $X = X_0 + \Delta X$ , where  $X_0$  is the initial displacement between the two field lines. Then

$$\begin{aligned} \int_{-\infty}^{\infty} e^{ik_x X} P(X|z) dX &= e^{ik_x X_0} \int_{-\infty}^{\infty} e^{ik_x \Delta X} P(\Delta X|z) d\Delta X \\ &= e^{ik_x X_0} e^{-D_{sx} k_x^2 z}, \end{aligned} \quad (5.11)$$

again making use of (2.67), where  $D_{sx} \equiv \langle \Delta X^2 \rangle / (2\Delta z)$  is the diffusion coefficient for the  $x$ -separation of two magnetic field lines. The third bracketed expression is similar:

$$\int_{-\infty}^{\infty} e^{ik_y Y} P(Y|z) dY = e^{-D_{sy} k_y^2 z}. \quad (5.12)$$

We note that defining the initial displacement as  $(X_0, 0)$  breaks the axisymmetry of  $\Delta X$  and  $\Delta Y$  (see also Figure 5.3), so  $D_{sx}$  and  $D_{sy}$  may be distinct.

Substituting (2.70), (2.78), and (5.10)-(5.12) into (5.9), and performing the  $z$ -integration, we obtain a complete expression for  $\langle \Delta X^2 \rangle$ :

$$\begin{aligned} \langle \Delta X^2 \rangle = & \frac{8\Delta z^2}{\langle \Delta x^2 \rangle} \frac{1}{2\pi B_0^2} \int_{-\infty}^{\infty} \int_{-\infty}^{\infty} \frac{k_y^2 A(k_{\perp})}{k_{\perp}^2} \left\{ 1 - g(\langle \Delta x^2 \rangle k_{\perp}^2 / 2) \right. \\ & - e^{ik_x X_0} \left[ g(\langle \Delta X^2 \rangle k_x^2 / 2 + \langle \Delta Y^2 \rangle k_y^2 / 2) \right. \\ & - \frac{1}{2} g'(\langle \Delta X^2 \rangle k_x^2 / 2 + \langle \Delta Y^2 \rangle k_y^2 / 2, \langle \Delta x^2 \rangle k_{\perp}^2 / 2) \\ & \left. \left. - \frac{1}{2} g(\langle \Delta X^2 \rangle k_x^2 / 2 + \langle \Delta Y^2 \rangle k_y^2 / 2 + \langle \Delta x^2 \rangle k_{\perp}^2 / 2) \right] \right\} dk_x dk_y, \end{aligned} \quad (5.13)$$

where  $g'(u, v) \equiv (e^{-u} - e^{-v}) / (v - u)$  is a two-dimensional low-pass filter that approaches 1 when and only when both  $u \ll 1$  and  $v \ll 1$ . The analogous expression for  $\langle \Delta Y^2 \rangle$  is

$$\begin{aligned} \langle \Delta Y^2 \rangle = & \frac{8\Delta z^2}{\langle \Delta x^2 \rangle} \frac{1}{2\pi B_0^2} \int_{-\infty}^{\infty} \int_{-\infty}^{\infty} \frac{k_x^2 A(k_{\perp})}{k_{\perp}^2} \left\{ 1 - g(\langle \Delta x^2 \rangle k_{\perp}^2 / 2) \right. \\ & - e^{ik_x X_0} \left[ g(\langle \Delta X^2 \rangle k_x^2 / 2 + \langle \Delta Y^2 \rangle k_y^2 / 2) \right. \\ & - \frac{1}{2} g'(\langle \Delta X^2 \rangle k_x^2 / 2 + \langle \Delta Y^2 \rangle k_y^2 / 2, \langle \Delta x^2 \rangle k_{\perp}^2 / 2) \\ & \left. \left. - \frac{1}{2} g(\langle \Delta X^2 \rangle k_x^2 / 2 + \langle \Delta Y^2 \rangle k_y^2 / 2 + \langle \Delta x^2 \rangle k_{\perp}^2 / 2) \right] \right\} dk_x dk_y, \end{aligned} \quad (5.14)$$



which differs from  $\langle \Delta X^2 \rangle$  only in that  $k_y^2 A(k_\perp)$  is replaced by  $k_x^2 A(k_\perp)$ .

In terms of diffusion coefficients, we have

$$\begin{aligned}
 D_{sx} = & \frac{2}{D_\perp} \frac{1}{2\pi B_0^2} \int_{-\infty}^{\infty} \int_{-\infty}^{\infty} \frac{k_y^2 A(k_\perp)}{k_\perp^2} \left\{ 1 - g(D_\perp k_\perp^2 \Delta z) \right. \\
 & - e^{ik_x X_0} \left[ g(D_{sx} k_x^2 \Delta z + D_{sy} k_y^2 \Delta z) \right. \\
 & - \frac{1}{2} g'(D_{sx} k_x^2 \Delta z + D_{sy} k_y^2 \Delta z, D_\perp k_\perp^2 \Delta z) \\
 & \left. \left. - \frac{1}{2} g(D_{sx} k_x^2 \Delta z + D_{sy} k_y^2 \Delta z + D_\perp k_\perp^2 \Delta z) \right] \right\} dk_x dk_y. \quad (5.15)
 \end{aligned}$$

and

$$\begin{aligned}
 D_{sy} = & \frac{2}{D_\perp} \frac{1}{2\pi B_0^2} \int_{-\infty}^{\infty} \int_{-\infty}^{\infty} \frac{k_x^2 A(k_\perp)}{k_\perp^2} \left\{ 1 - g(D_\perp k_\perp^2 \Delta z) \right. \\
 & - e^{ik_x X_0} \left[ g(D_{sx} k_x^2 \Delta z + D_{sy} k_y^2 \Delta z) \right. \\
 & - \frac{1}{2} g'(D_{sx} k_x^2 \Delta z + D_{sy} k_y^2 \Delta z, D_\perp k_\perp^2 \Delta z) \\
 & \left. \left. - \frac{1}{2} g(D_{sx} k_x^2 \Delta z + D_{sy} k_y^2 \Delta z + D_\perp k_\perp^2 \Delta z) \right] \right\} dk_x dk_y. \quad (5.16)
 \end{aligned}$$

### 5.3 Interpretation

Fortunately the low-pass filters  $g$  and  $g'$  facilitate the interpretation of the general behavior of the mean squared separation between two magnetic field lines, described by  $\langle \Delta X^2 \rangle$  and  $\langle \Delta Y^2 \rangle$  as functions of distance along the mean field,  $\Delta z$ . The behavior of  $\langle \Delta X^2 \rangle$  is summarized in Table 5.1; that of  $\langle \Delta Y^2 \rangle$  is similar.

Table 5.1: Types of Separation of Two Magnetic Field Lines in Two-Component Turbulence

Random walk and separation <sup>a</sup>	Distance range	Type of separation
$\ell_{\perp}^2 \ll \langle \Delta x^2 \rangle$ and $\langle \Delta X^2 \rangle$	Long $\Delta z$	Fast diffusive separation
$\langle \Delta X^2 \rangle \sim \ell_{\perp}^2 \ll \langle \Delta x^2 \rangle$	Intermediate $\Delta z$ (only for $D_{\perp}^{2D} \ll D_{\perp}^{slab}$ )	Superdiffusive
$\langle \Delta X^2 \rangle \ll \ell_{\perp}^2 \ll \langle \Delta x^2 \rangle$	Intermediate $\Delta z$ (only for $D_{\perp}^{2D} \ll D_{\perp}^{slab}$ )	Slow diffusive separation
$\langle \Delta x^2 \rangle$ and $\langle \Delta X^2 \rangle \lesssim \ell_{\perp}^2$	Short $\Delta z$	Non-diffusive <sup>b</sup>

<sup>a</sup> $\langle \Delta x^2 \rangle$  is the mean squared “random walk,” the perpendicular displacement of a single magnetic field line relative to the mean field.  $\langle \Delta X^2 \rangle$  is the mean squared separation between two magnetic field lines. See also Figure 5.1.

<sup>b</sup>If  $D_{\perp}^{2D} \ll D_{\perp}^{slab}$ , non-diffusive behavior applies at a short distance  $\Delta z \lesssim \ell_z$  regardless of the magnitudes of  $\langle \Delta x^2 \rangle$  and  $\langle \Delta X^2 \rangle$ .

The interpretation presented in this section has been confirmed by numerical evaluation of (2.64), (2.65), (5.13), and (5.14) with the Mathematica program (Wolfram Research, Inc.). Results for specific numerical examples are shown in Figures 5.4 and 5.5; see Appendix B for details, including the turbulence parameters. Figure 5.4 shows  $\langle \Delta x^2 \rangle$  and  $\langle \Delta X^2 \rangle$  as a function of  $\Delta z$ , with a log-log scale, so diffusive behavior corresponds to lines of slope 1, with the diffusion coefficient as half the intercept at  $\log \Delta z = 0$ . Régimes of diffusive behavior are highlighted with solid lines. Figure 5.5 shows diffusion coefficients  $D_{sx}$  and  $D_{sy}$  as a function of  $\Delta z$ , so here diffusive behavior corresponds to the flat portions of the curves. We must point out that the assumptions underlying our quantitative derivation are invalid if the behavior is non-diffusive. However, we can draw the qualitative conclusion that superdiffusive behavior “connects” the two diffusive régimes in Figures 5.4b and 5.5.

The régimes of behavior of the mean squared separation are controlled by the low-pass filters  $g$  and  $g'$ . The arguments of  $g$  and  $g'$  depend on quantities such as  $\langle \Delta x^2 \rangle k_{\perp}^2$  or  $\langle \Delta X^2 \rangle k_x^2$ , and the  $k_x$  and  $k_y$  integrals are dominated by the region with  $k_{\perp} \lesssim k_{0\perp}$ , so the different régimes of behavior are defined by whether  $\langle \Delta x^2 \rangle$  and  $\langle \Delta X^2 \rangle$  are greater or less than the perpendicular coherence length squared,  $\ell_{\perp}^2 = 1/k_{0\perp}^2$ .

First we consider the case where  $\langle \Delta x^2 \rangle \gg \ell_{\perp}^2$  and  $\langle \Delta X^2 \rangle \gg \ell_{\perp}^2$ , which occurs at long distances  $\Delta z$ . In this case, all the  $g'$  and  $g$  terms tend to zero, and we have

$$\begin{aligned} \langle \Delta X^2 \rangle = \langle \Delta Y^2 \rangle &= 2\langle \Delta x^2 \rangle_{2D} \\ D_{sx} = D_{sy} &= 2 \frac{(D_{\perp}^{2D})^2}{D_{\perp}} \end{aligned}$$

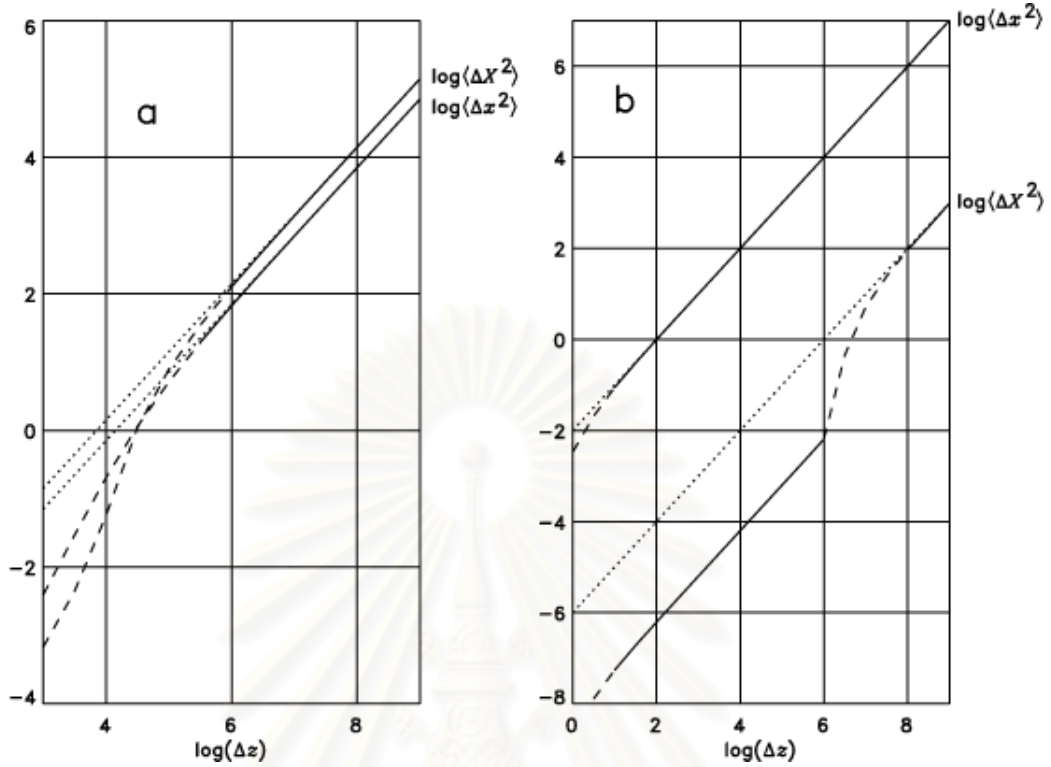


Figure 5.4: Examples of the field line random walk  $\langle \Delta x^2 \rangle$  and separation  $\langle \Delta X^2 \rangle$  as a function of  $\Delta z$ , the distance along the mean magnetic field. The random walk is dominated by a) the 2D component of turbulence, b) the slab component of turbulence. Solid lines indicate diffusive behavior, dashed lines indicate superdiffusion. Dotted lines, for reference, show the extension of the long-distance behavior. Ordinates in units of  $\ell_\perp^2$ , abscissae in units of  $\ell_c$ . (See text for details.)

$$\begin{aligned}
 &= \frac{1}{D_\perp} \frac{\langle a^2 \rangle}{B_0^2} \\
 &= \frac{\tilde{\chi}^2 \langle b^2 \rangle^{2D}}{D_\perp B_0^2}. \tag{5.17}
 \end{aligned}$$

We see that in the long-distance limit, the field line separation is axisymmetric, independent of the starting displacement  $X_0$ , and diffusive with a diffusion coefficient twice as great as the 2D contribution to the random walk. This behavior, which we refer to as fast diffusive separation, can be seen in the long-distance régimes of Figures 5.4 and 5.5. Note that for the case of a slab-dominated random

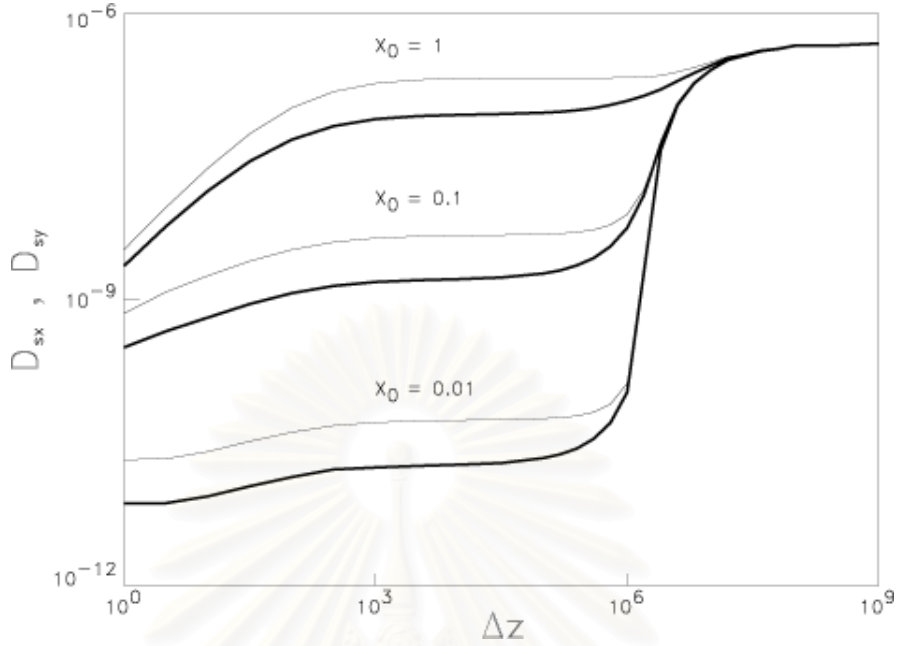


Figure 5.5: Coefficients of diffusive separation,  $D_{sx}$  (thick lines) and  $D_{sy}$  (thin lines), as a function of  $\Delta z$  for the slab-dominated case of Figure 5.4b and various initial displacements  $X_0$ , with  $x$ -quantities in units of  $\ell_\perp$  and  $z$ -quantities in units of  $\ell_c$ .

walk ( $D_\perp^{slab} \gg D_\perp^{2D}$ ),

$$D_{sx} = D_{sy} \approx \frac{2\tilde{\lambda}^2 \langle b^2 \rangle^{2D}}{\ell_c \langle b^2 \rangle^{slab}}, \quad (5.18)$$

and for a 2D-dominated random walk we have

$$D_{sx} = D_{sy} \approx \tilde{\lambda} \frac{\sqrt{2\langle b^2 \rangle^{2D}}}{B_0}. \quad (5.19)$$

To understand these results for fast diffusive separation, recall from Section 5.1 that if two turbulent field lines were completely uncorrelated, undergoing independent random walks, the mean squared separation  $\langle \Delta X^2 \rangle$  would be twice the mean squared random walk  $\langle \Delta x^2 \rangle$  of one field line. In the 2D+slab model of turbulence, only the 2D component decorrelates in the perpendicular directions, so we can understand why the fast diffusive separation in the long-distance limit

is twice as great as the 2D contribution to the random walk. Since this régime involves large separations and decorrelation of the 2D turbulence at the two field lines, as shown in Figure 5.3d, we can also understand why this behavior is axisymmetric (with  $\langle \Delta X^2 \rangle = \langle \Delta Y^2 \rangle$ ) and independent of the initial displacement between the field lines,  $X_0$ .

Paradoxically, equation (5.17) implies that when the slab turbulent energy  $\langle b^2 \rangle^{slab}$  is increased,  $D_{\perp}$  increases and the coefficient of diffusive separation *decreases* (as does the 2D contribution to  $D_{\perp}$ ; see eq. [2.82]). This is illustrated by Figures 5.4a and 5.4b, which differ only in the amplitude of slab turbulence (see Appendix B for details). An interpretation of this effect is that rapid lateral excursions due to slab turbulence quickly decorrelate the “random flights” in the relative excursions of the two field lines,  $\Delta X$  and  $\Delta Y$ . The random flights depend on 2D turbulence and hence  $x$  and  $y$ , which change more rapidly with increased slab turbulence. This yields a shorter mean free  $z$ -distance in the motion of one field line relative to another, hence the lower coefficient of diffusive separation.

Now let us consider what happens as  $\Delta z$  decreases. In the long-distance limit, we have fast diffusive separation where  $\langle \Delta X^2 \rangle = 2\langle \Delta x^2 \rangle_{2D}$ . In the case where the 2D component dominates the random walk,  $D_{\perp}^{2D} \gtrsim D_{\perp}^{slab}$ , we indeed have  $\langle \Delta X^2 \rangle \approx 2\langle \Delta x^2 \rangle$ . That implies that these two quantities both reach  $\ell_{\perp}^2$  at about the same distance  $\Delta z$  (Figure 5.4a). When  $\langle \Delta x^2 \rangle \lesssim \ell_{\perp}^2$  and  $\langle \Delta X^2 \rangle \lesssim \ell_{\perp}^2$ , then the low-pass filters  $g$  and  $g'$  switch on, our expressions for  $\langle \Delta x^2 \rangle_{2D}$  and  $\langle \Delta X^2 \rangle$  instead vary as  $(\Delta z)^2$ , and our derivation is no longer valid in this régime. This indeed happens at short distances  $\Delta z$  even if the 2D component does not dominate the random walk. Physically, we expect such behavior in the “free-streaming” limit where  $\vec{b}$  is nearly unchanged in direction. Such non-diffusive

behavior, the last case listed in Table 5.1, can be seen at low  $\Delta z$  in Figures 5.4 and 5.5.

Therefore, when the 2D component dominates the random walk, the two quantities  $\langle \Delta X^2 \rangle$  and  $\langle \Delta x^2 \rangle$  are of the same order of magnitude. On the other hand, if the slab component dominates the random walk, we can have the field line random walk much greater than the field line separation, because the slab fluctuations directly contribute to the former but not the latter. Furthermore, it is possible to have

$$\langle \Delta X^2 \rangle \ll \ell_\perp^2 \ll \langle \Delta x^2 \rangle, \quad (5.20)$$

which is intermediate to the short-distance and long-distance régimes described above. In this case, two nearby field lines follow highly correlated trajectories with a mutual separation much lower than the displacement from the mean field, as represented by the lower two field lines in Figure 5.1. We refer to this behavior as “slow diffusive separation.”

Referring to (5.13-5.16), and recalling that the integrals are dominated by  $k_\perp \lesssim k_{0\perp} = 1/\ell_\perp$ , we have  $g' \rightarrow 0$  and  $g \rightarrow 0$ , with the exception that  $g(\langle \Delta X^2 \rangle k_\perp^2 / 2) \rightarrow 1$ , so

$$D_{sx} = \frac{2}{D_\perp} \frac{1}{2\pi B_0^2} \int_{-\infty}^{\infty} \int_{-\infty}^{\infty} \frac{k_y^2 A(k_\perp)}{k_\perp^2} (1 - e^{ik_x X_0}) dk_x dk_y \quad (5.21)$$

$$D_{sy} = \frac{2}{D_\perp} \frac{1}{2\pi B_0^2} \int_{-\infty}^{\infty} \int_{-\infty}^{\infty} \frac{k_x^2 A(k_\perp)}{k_\perp^2} (1 - e^{ik_x X_0}) dk_x dk_y. \quad (5.22)$$

Recall that  $A$  is the power spectrum of  $a(x, y)$ , i.e., the Fourier transform of the autocorrelation function  $\langle a(0, 0)a(x, y) \rangle$ . Thus the directionally averaged coefficient of slow diffusive separation is

$$D_s \equiv \frac{D_{sx} + D_{sy}}{2} = \frac{1}{D_\perp} \frac{\langle a^2 \rangle - \langle a(0, 0)a(X_0, 0) \rangle}{B_0^2}. \quad (5.23)$$

This expression for  $D_s$  varies linearly with the autocorrelation of the flux function  $a$  at the initial displacement between the field lines, and has a direct physical interpretation. If the field lines are initially far apart with  $X_0 \gg \ell_\perp$ , so that the correlation  $\langle a(0,0)a(X_0,0) \rangle \rightarrow 0$ , then we recover the expression for fast diffusive separation (eq. [5.17]). Physically, this refers to the separation between two field lines for uncorrelated 2D turbulence (and perfectly correlated slab turbulence, at the same  $z$  coordinate), and there is no difference from the fast diffusive separation régime. On the other hand, for  $X_0 \lesssim \ell_\perp$ , field lines are initially close together with a substantial correlation in the flux function  $a$ , and the coefficient of diffusive separation is slower in this régime.

Transforming (5.23) to obtain

$$D_s = \frac{1}{D_\perp} \frac{\langle [a(X_0,0) - a(0,0)]^2 \rangle}{2B_0^2}, \quad (5.24)$$

we see that this expression is also related to the mean squared difference between  $a$  at the positions of the two field lines. Note that  $a(X_0,0) - a(0,0)$  can be interpreted as  $\int_1^2 \vec{b}^{2D} \cdot \hat{n} dl$ , where  $dl$  is the line element along any curve connecting the locations of field lines 1 and 2 and  $\hat{n}$  is the 2D normal to that curve, i.e., the 2D magnetic flux threading any such curve. There is an interesting similarity between this expression and (5.17) for fast diffusive separation, which will be explored further in a future report.

Another property of slow diffusive separation is that it is non-axisymmetric, i.e.,  $\langle \Delta Y^2 \rangle > \langle \Delta X^2 \rangle$ . Recalling that the axisymmetry is broken by defining the initial displacement as  $(X_0, 0)$ ,  $\Delta X$  initially refers to the change in the distance between the two field lines, while  $\Delta Y$  implies a changing orientation of the displacement (Figure 5.3). Mathematically, in the limit of small  $X_0$ , and with a



transformation to polar coordinates  $(k_{\perp}, \varphi)$ , equations (5.21) and (5.22) become

$$\begin{aligned} D_{sx} &= \frac{1}{D_{\perp}} \frac{X_0^2}{2\pi B_0^2} \left[ \int_0^{2\pi} \sin^2 \varphi \cos^2 \varphi d\varphi \right] \int_0^{\infty} k_{\perp}^3 A(k_{\perp}) dk_{\perp} \\ D_{sy} &= \frac{1}{D_{\perp}} \frac{X_0^2}{2\pi B_0^2} \left[ \int_0^{2\pi} \cos^4 \varphi d\varphi \right] \int_0^{\infty} k_{\perp}^3 A(k_{\perp}) dk_{\perp}. \end{aligned} \quad (5.25)$$

The bracketed integrals are  $(1/4)\pi$  and  $(3/4)\pi$ , respectively, so for small  $X_0$  the ratio of  $\langle \Delta Y^2 \rangle$  to  $\langle \Delta X^2 \rangle$  is 3 : 1. Using the relation  $k_{\perp}^2 A = P_{xx}^{2D} + P_{yy}^{2D}$ , we have

$$\begin{aligned} D_{sx} &= \frac{1}{8} \frac{1}{D_{\perp}} \frac{\langle b^2 \rangle^{2D}}{B_0^2} X_0^2 \\ D_{sy} &= \frac{3}{8} \frac{1}{D_{\perp}} \frac{\langle b^2 \rangle^{2D}}{B_0^2} X_0^2, \end{aligned} \quad (5.26)$$

or in terms of the correlation of  $a$ , we have

$$\begin{aligned} D_{sx} &= \frac{1}{2} \frac{1}{D_{\perp}} \frac{\langle a^2 \rangle - \langle a(0,0)a(X_0,0) \rangle}{B_0^2} \\ D_{sy} &= \frac{3}{2} \frac{1}{D_{\perp}} \frac{\langle a^2 \rangle - \langle a(0,0)a(X_0,0) \rangle}{B_0^2}. \end{aligned} \quad (5.27)$$

Note that when  $\langle a^2 \rangle - \langle a(0,0)a(X_0,0) \rangle$  is expanded in terms of  $X_0$ , odd terms vanish by symmetry and the leading term is of order  $X_0^2$ . Numerical values of  $D_{sx}$  and  $D_{sy}$  are shown in Figure 5.5 for various values of  $X_0$  (in units of  $\ell_{\perp}$ ).

Figure 5.3 also illustrates the transition between slow diffusive separation and fast diffusive separation, for a slab-dominated random walk and for  $X_0 \lesssim \ell_{\perp}$ . When the two field lines are closer than  $\ell_{\perp}$ , the 2D fluctuations are strongly correlated, leading to slow diffusive separation. The distribution of the field line separation is non-axisymmetric, preferentially changing the direction of the displacement instead of the distance. This is related to the motion of field lines subject to 2D turbulence: at any given position, two field lines are typically both rotating around the same 2D ‘‘island.’’ The mutual random walk is suppressed by

the temporary confinement of field lines within a perpendicular coherence length. When the distance is of order  $\ell_{\perp}$ , the 2D fluctuations decorrelate and the rate of separation increases. This is a régime of superdiffusion that bridges between the slow diffusive separation and fast diffusive separation (also seen in Figures 5.4 and 5.5). Then for distances much greater than  $\ell_{\perp}$  one obtains the long-distance limit of fast diffusive separation, which is axisymmetric and independent of  $X_0$ . The various régimes of field line separation of summarized in Table 5.1.

In Figure 5.5, it is seen that the onset of superdiffusive behavior occurs at a certain  $\Delta z$  value, independent of  $X_0$ . This is similar to the behavior of the mean separation vs.  $z$  in Figure 2 of Maron et al. (2004). This can be understood in terms of a universal curve of  $\langle R^2 \rangle$  vs.  $z$ , defined by the following ansatz:

$$\frac{d\langle R^2 \rangle}{dz} = 4 D_s(\langle R^2 \rangle). \quad (5.28)$$

Here the function  $D_s(\langle R^2 \rangle)$  is a running diffusion coefficient, related but not necessarily identical to the diffusion coefficient derived earlier, and  $\langle R^2 \rangle$  refers to the mean squared distance between the two field lines,

$$\langle R^2 \rangle \equiv \langle X^2 \rangle + \langle Y^2 \rangle = X_0^2 + \langle \Delta X^2 \rangle + \langle \Delta Y^2 \rangle. \quad (5.29)$$

The value of  $D_s(\langle R^2 \rangle)$  is set to  $D_s(X_0^2)$  from the slow diffusive separation régime (in which  $\langle \Delta X^2 + \Delta Y^2 \rangle \ll X_0^2$  and  $\langle R^2 \rangle \approx X_0^2$ ) as given by (5.23). The above ansatz proposes that  $D_s$  is a function only of  $\langle R^2 \rangle$  and not on the details of the displacement distribution, which is particularly accurate for slow diffusive separation and the onset of superdiffusion [e.g., equation (5.26) shows that  $D_s \propto X_0^2$ , so replacing  $X_0^2$  by the mean  $\langle R^2 \rangle$  leaves  $D_s$  nearly unchanged]. Then the choice of  $X_0$  is viewed as the choice of a starting point  $(z_0, \langle R^2 \rangle = X_0^2)$  along the universal curve, with  $\langle \Delta X^2 + \Delta Y^2 \rangle = \langle R^2 \rangle - X_0^2$  and  $\Delta z = z - z_0$ . This

model can approximately reproduce the results in Figure 5.5 for slow diffusive separation and the onset of superdiffusion. In that range, using  $D_{\perp} \approx D_{\perp}^{slab}$  and from (2.75) and (5.26), we have

$$D_s(\langle R^2 \rangle) = \frac{\langle b^2 \rangle^{2D} \langle R^2 \rangle}{\langle b^2 \rangle^{slab} 2\ell_c}, \quad (5.30)$$

and solving (5.28) we obtain

$$\begin{aligned} \langle R^2 \rangle &= X_0^2 e^{\Delta z / \ell_g} \\ \langle \Delta X^2 + \Delta Y^2 \rangle &= X_0^2 (e^{\Delta z / \ell_g} - 1), \end{aligned} \quad (5.31)$$

where the exponential growth length along the mean magnetic field,

$$\ell_g = \frac{\ell_c \langle b^2 \rangle^{slab}}{2 \langle b^2 \rangle^{2D}}, \quad (5.32)$$

marks the end of the approximately linear dependence of  $\langle \Delta X^2 + \Delta Y^2 \rangle$  on  $\Delta z$ , i.e., the end of slow diffusive separation. In this way, the onset of superdiffusion can be viewed as part of a process of exponential growth of  $\langle R^2 \rangle$  as a function of  $z$ , which is an example of stochastic instability. The result (eq. [5.32]) amounts to a calculation of the Kolmogorov-Lyapunov length (Rechester & Rosenbluth 1978) for a slab-dominated two-component magnetic field turbulence mode.

## 5.4 Numerical confirmation

To confirm the conclusions of these analytic calculations, we also developed computer simulations of field line separation in 2D+slab turbulence. While the simulations inevitably involve some discretization and statistical errors, they do avoid the key assumptions of the analytic work (Corrsin's hypothesis, Gaussian probability distributions, and diffusive separation) and thus provide an independent check of their validity. Computer simulations are also useful for examining

the régimes in which our analytic expressions are not valid, i.e., where the field line separation is not diffusive. The basic methods and results are presented here, and more technical details can be found in Chapter 3.

The simulations involved two steps:

1) Generating representations of slab and 2D turbulence with desired statistical properties, such as a power spectrum that follows the Kolmogorov power-law over the inertial wavenumber range and rolls over in the energy-containing range, as observed for solar wind turbulence (Jokipii & Coleman 1968). (See (3.2) and (3.7) for mathematical expressions.) Random phases are used in wavenumber space, followed by inverse fast Fourier transforms to obtain  $\vec{b}^{slab}(z)$  and  $\vec{b}^{2D}(x, y)$ . The transforms in  $z$  used  $2^{23}$  ( $\approx 8.4 \times 10^6$ ) points, while the transforms in  $x$  and  $y$  used  $2^{12} = 4096$  points in each dimension.

2) Tracing magnetic field lines, i.e., solving the coupled ordinary differential equations

$$\frac{dx}{dz} = \frac{b_x(x, y, z)}{B_0} \quad \frac{dy}{dz} = \frac{b_y(x, y, z)}{B_0}. \quad (5.33)$$

We used a fourth-order Runge-Kutta method with adaptive time stepping regulated by a fifth-order error estimate step (Press et al. 1992). The  $D_{sx}$  and  $D_{sy}$  values were based on averages over 1000 pairs of field lines, and each pair was for a distinct realization of slab and 2D turbulence.

Now the key physical conclusions of the analytic work (Table 5.1) can be checked using the computer simulations. In the 2D-dominated case, where  $D_{\perp}^{2D} \gtrsim D_{\perp}^{slab}$ , we expect a non-diffusive (free-streaming) régime at short  $\Delta z$ , followed by fast diffusive separation at long  $\Delta z$  (where  $\langle \Delta x^2 \rangle \gtrsim \ell_{\perp}^2$ ). The analytic expression is expected to hold quantitatively for diffusive behavior in the long-

distance limit; in particular, the fast diffusive separation rate should be given by (5.17).

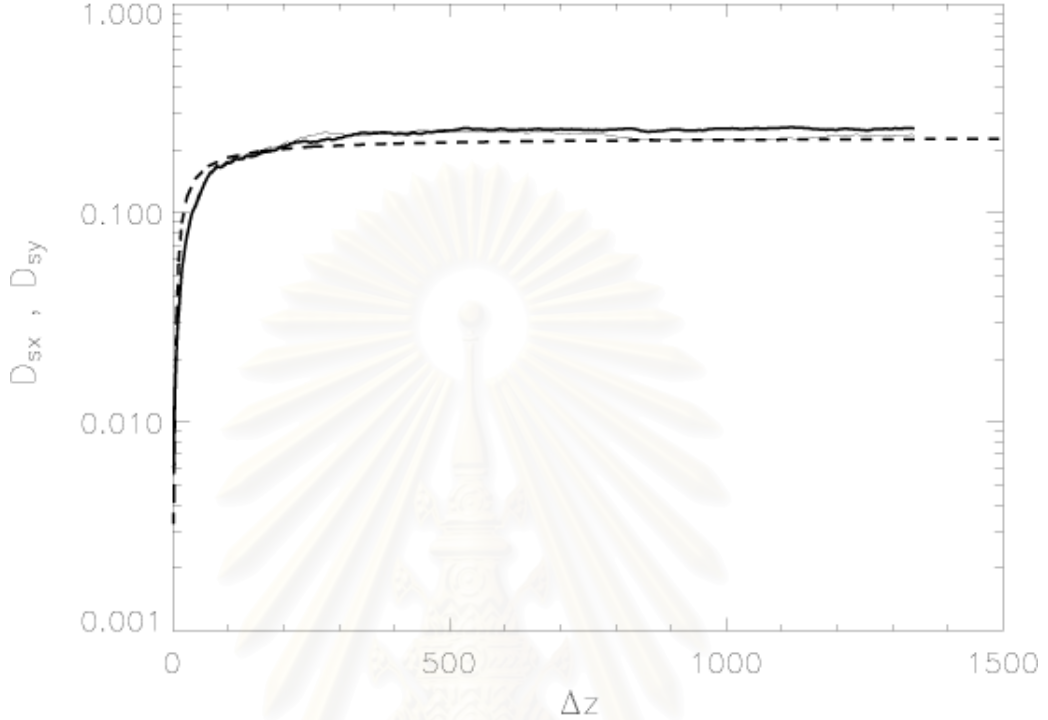


Figure 5.6: Coefficients of diffusive separation derived from computer simulations,  $D_{sx}$  (thick solid line) and  $D_{sy}$  (thin solid line), compared with  $D_{sx} = D_{sy}$  from analytic calculations (dashed line), as a function of  $\Delta z$ , for a random walk dominated by the 2D component of turbulence. Here we set the total fluctuation to be  $B_0^2/4$  with a 50:50 ratio of slab to 2D energies. The long-distance limit is the régime of fast diffusive separation.

Figure 5.6 shows a specific example of 2D-dominated behavior. Specifically, we used  $\langle b^2 \rangle^{2D} = \langle b^2 \rangle^{slab} = B_0^2/8$ ,  $X_0 = 0.1339$ , and other parameters as in Appendix B. These yield  $D_{\perp}^{2D} = 0.144$  and  $D_{\perp}^{slab} = 0.0625$ . The computational box sizes were  $L_z = 10^6 \ell_z$  and  $L_x = L_y = 200 \ell_z$ . The simulation results for  $D_{sx}$  (thick solid line) and  $D_{sy}$  (thin solid line) are compared with the analytic predictions for  $D_{sx}$  and  $D_{sy}$  from (5.15) and (5.16), which are indistinguishable in Figure 5.6 (dashed line). The difference of about 10% at large  $\Delta z$  represents

good quantitative agreement, given the simulation uncertainties. These include the statistical uncertainty, as estimated from the difference between simulation results for  $D_{sx}$  and  $D_{sy}$  and their stochastic variation with  $\Delta z$ , and the discretization error of about 6%, which we estimate by replacing continuous integration over  $\vec{k}$  in the analytic expressions with discrete sums over the  $\vec{k}$  modes used in the simulations. Note also that the analytic expression correctly identifies the  $\Delta z$  range where diffusive separation behavior begins, i.e., the lower limit of applicability of the diffusion approximation.

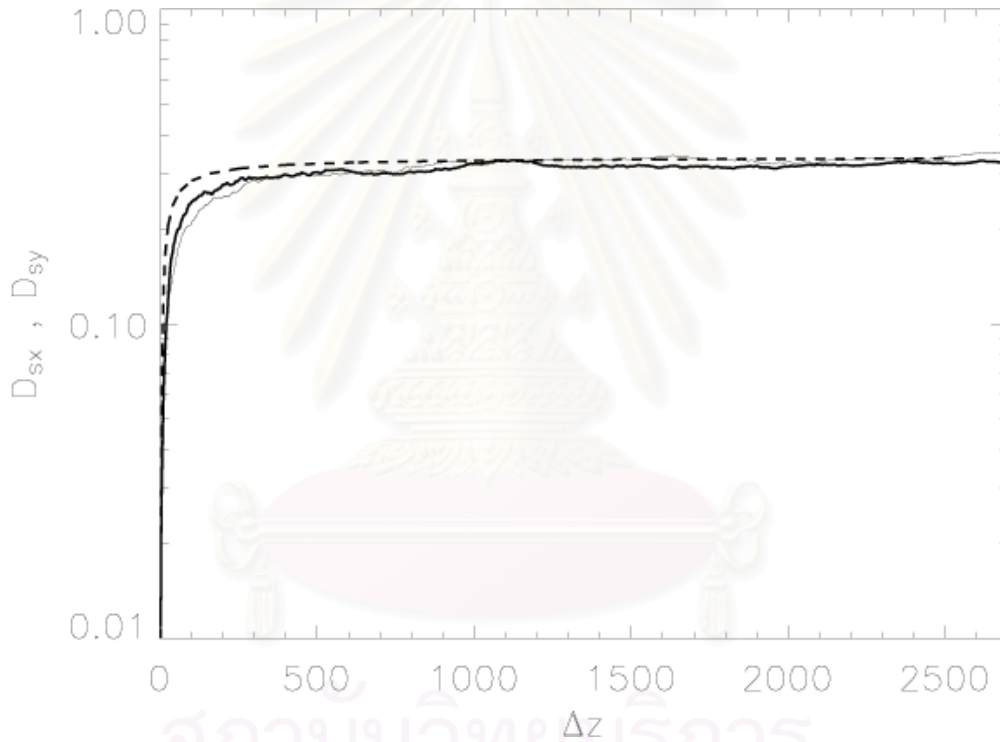


Figure 5.7: Coefficients of diffusive separation derived from computer simulations,  $D_{sx}$  (thick solid line) and  $D_{sy}$  (thin solid line), compared with  $D_{sx} = D_{sy}$  from analytic calculations (dashed line), as a function of  $\Delta z$ , for a random walk dominated by the 2D component of turbulence. Here we set the total fluctuation to be  $B_0^2/4$  with a 20:80 ratio of slab to 2D energies. The long-distance limit is the régime of fast diffusive separation.

Another simulation with the same total turbulent energy but a 20:80 ra-

ratio of  $\langle b^2 \rangle^{slab}$  to  $\langle b^2 \rangle^{2D}$  in Figure 5.7 showed a similar level of agreement. Indeed, agreement on the order of 15% was also found between computer simulations and analytic calculations for the field line random walk (Gray et al. 1996). In addition to the long-distance limit, another noteworthy feature of our 2D-dominated simulations is that in the free-streaming régime, there is non-axisymmetric separation,  $D_{sy} > D_{sx}$ , reminiscent of the analytic results in the slow diffusive régime for the slab-dominated case (see also Figure 5.3).

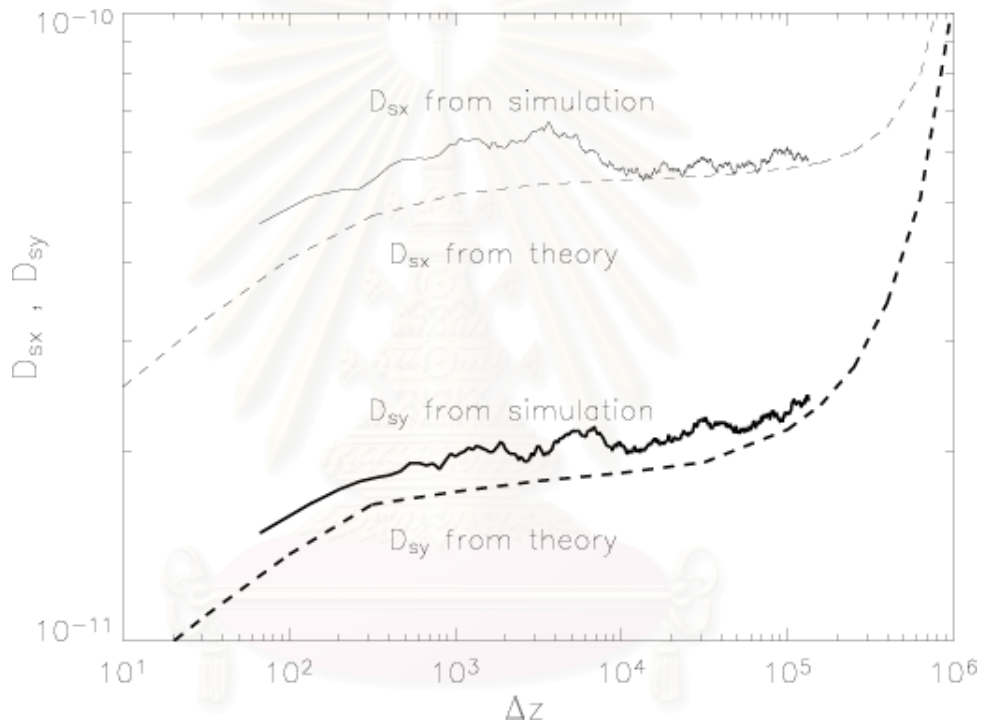


Figure 5.8: Coefficients of diffusive separation derived from computer simulations,  $D_{sx}$  (thick solid line) and  $D_{sy}$  (thin solid line), compared with those from analytic calculations (thick dashed line and thin dashed line, respectively), as a function of  $\Delta z$ , for a random walk dominated by the slab component of turbulence, in the régime of slow diffusive separation.

The interesting features of analytic results for the slab-dominated case ( $D_{\perp}^{slab} \gg D_{\perp}^{2D}$ ) are a régime of non-axisymmetric slow diffusive separation, with  $D_{sy} \approx 3D_{sx}$ , followed by a superdiffusive transition to fast diffusive separation in

the long-distance limit. (Note that the slow diffusion and onset of superdiffusion can also be expressed as an exponential separation phase; see Section 5.3.) We performed computer simulations for the same parameter values as in Figures 5.4b and 5.5, with the exception that  $X_0$  was set to 0.01. The computational box sizes were  $L_z = 2 \times 10^6 \ell_z$  and  $L_x = L_y = 200 \ell_z$ . The comparison with analytic calculations (Figure 5.8) demonstrates good agreement, with both simulation and analytic values flattening over the same range of  $\Delta z$  at the ratio  $D_{sy}/D_{sx} \approx 3$ . The difference of  $\sim 15\%$  is again of the same order as the statistical and discretization errors in the simulations (the latter is estimated at 10 to 15%) and is similar to that obtained by Gray et al. (1996).

Note that in the slab-dominated case, the slow diffusion and onset of superdiffusion can also be expressed as an exponential separation phase (see Section 5.3). When fitting the computational results for  $\langle R^2 \rangle = X_0^2 + \langle \Delta X^2 \rangle + \langle \Delta Y^2 \rangle$  to an exponential function of  $z$ , we find that the best fit is for  $\langle R^2 \rangle = 9.97 \times 10^{-5} \exp(z/6.57 \times 10^5)$  (see Figure 5.9). Referring to equation (5.31) and (5.32), the analytic expectation is  $\langle R^2 \rangle = X_0^2 \exp(z/\ell_g)$ , where for this case  $X_0^2 = 10^{-4}$  and  $\ell_g = 6.67 \times 10^5$ . Thus, the analytic and numerical calculations agree to within 0.3% for the prefactor and to within 1.5% for the exponential growth length,  $\ell_g$ .

## 5.5 Summary

We have developed an analytic formalism for the ensemble-averaged field line random walk and separation that does not assume a long-distance limit, i.e., in which fluctuations between the two field lines have not completely decorrelated. This is possible by retaining finite limits of integration in  $\Delta z'$ . The results of the analytic theory have been confirmed by numerical simulations, justifying the use



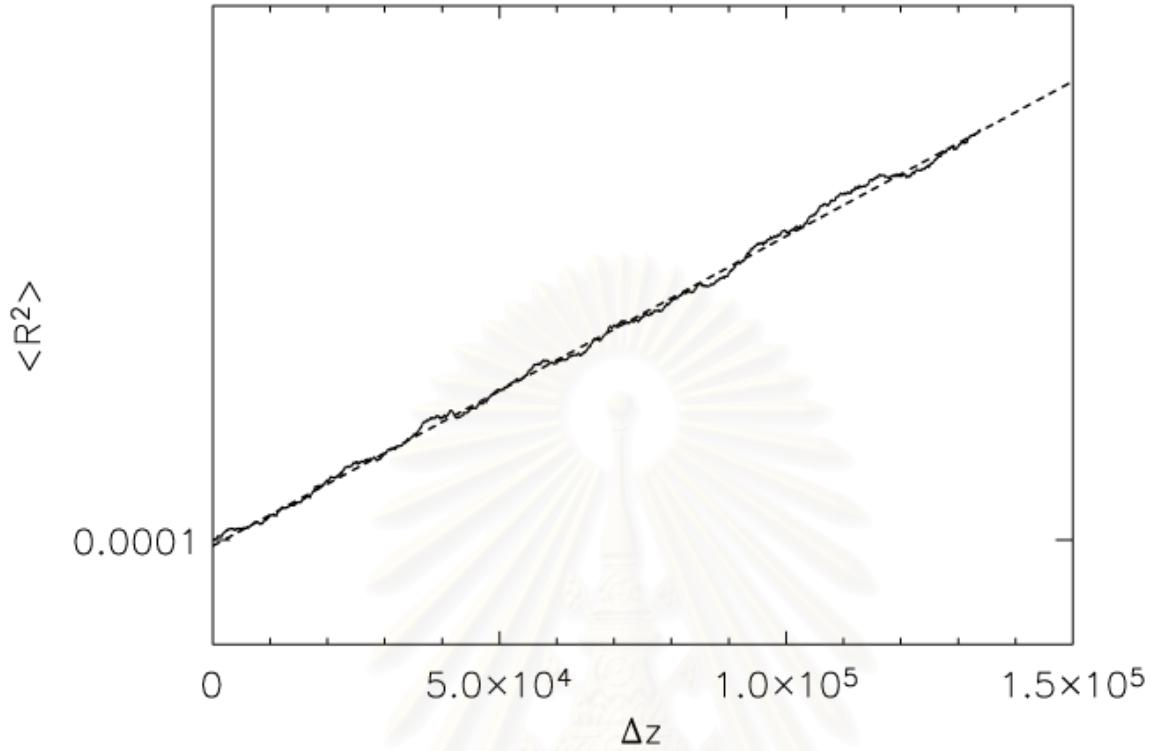


Figure 5.9:  $\langle R^2 \rangle$  plot of the slab-dominated case as in Figure 5.8 (*thick solid line*). The data have the best fit with the curve (*dashed line*)  $\langle R^2 \rangle = 9.97 \times 10^{-5} \exp(z/6.57 \times 10^5)$ .

of Corrsin's hypothesis.

The analytic results we have derived are non-perturbative in the sense that neither the total turbulent energy nor the turbulent energy of the slab or the 2D component is constrained to be small. The results are also not restricted to a specific functional form for the power spectrum. We are considering a particular case of anisotropic turbulence, in which power in  $\vec{k}$ -space is concentrated along the parallel axis and (axisymmetrically) along the perpendicular plane.

With its idealized and clear separation of parallel and perpendicular fluc-

tuations, the two-component magnetic turbulence model considered here is an archetype of highly anisotropic turbulence, which also serves as a useful model of turbulence in the solar wind (Matthaeus et al. 1990; Bieber et al. 1996) and has helped to quantitatively explain solar energetic particle transport (Bieber et al. 1994). In comparison, in the work of Jokipii (1973) all the turbulence is taken to decorrelate after a certain  $z$ -distance. In this sense it is like the slab component in our work, but differs in that it also contributes to field line separation. The results of Jokipii (1973) were generalized by Zimbardo et al. (1984) to other mean field geometries.

Our overall picture of diffusive separation at long distances and non-diffusive separation at short distances, with possible régimes of slow diffusion and superdiffusion in between, is qualitatively consistent with that presented by Isichenko (1991a, 1991b and references therein) for general magnetic turbulence. As discussed in the previous section, the slow diffusion and onset of superdiffusion in the mean squared separation  $\langle \Delta X^2 + \Delta Y^2 \rangle$  can be identified as an exponential growth of the mean squared distance between two field lines,  $\langle R^2 \rangle$ , as discussed by various authors (e.g., Skilling et al. 1974; Rechester & Rosenbluth 1978; Krommes 1978; Similon & Sudan 1989; Isichenko 1991a, 1991b and references therein). It was shown by Barghouty & Jokipii (1996) that the results of Jokipii (1973) can also be interpreted in such terms. In terms of the separation of field lines, we have shown that there is a régime that can be usefully considered as diffusive and non-axisymmetric in the perpendicular directions (slow diffusive separation; Figures 5.3-5.5 and 5.8).

In our detailed work for the particular case of two-component turbulence, we find a criterion for different types of field line separation behavior that is

somewhat different from that of Isichenko (1991a, 1991b). That work, as well as Krommes (1978) and Kadomtsev & Pogutse (1979), stressed a parameter  $R$  given (in our notation) by

$$R \sim (\sqrt{\langle b^2 \rangle} / B_0) (\ell_z / \ell_\perp), \quad (5.34)$$

sometimes called the Kubo number. On the other hand, our work identifies régimes of behavior that depend on  $D_\perp^{slab} / D_\perp^{2D}$ , the ratio of contributions to the field line random walk, which are in turn related to the amplitude of each component and the relevant distance scales. (Recall that  $D_\perp^{2D}$  contains  $\tilde{\lambda}$ , the ultrascale, which is in general distinct from the perpendicular coherence scale  $\ell_\perp$ .) Both  $D_\perp$  and  $D_s$  have different dependences for  $D_\perp^{slab} / D_\perp^{2D} \gg 1$  or  $\ll 1$  [compare equations (2.75) and (2.81), and equations (5.18) and (5.19)].

Can we reconcile the role of  $R$  in previous studies with the role of  $D_\perp^{slab} / D_\perp^{2D}$  in our work? We note that the previous work that considered  $R$  as a key parameter did not specifically consider turbulence with very different amplitudes for quasi-parallel and quasi-perpendicular wave vectors  $\vec{k}$ , apparently making the implicit assumption that those amplitudes are comparable. Indeed, the ratio

$$\frac{D_\perp^{slab}}{D_\perp^{2D}} = \frac{\langle b^2 \rangle^{slab} / B_0^2 \ell_c / 2}{\sqrt{\langle b^2 \rangle^{2D} / B_0} \tilde{\lambda} / \sqrt{2}} \quad (5.35)$$

reduces to  $R$  (modulo constants of order unity) in the case where  $\langle b^2 \rangle^{slab} \sim \langle b^2 \rangle^{2D}$  and  $\tilde{\lambda} \sim \ell_\perp$ . Therefore, we suggest that the ratio of contributions to  $D_\perp$  from quasi-parallel and quasi-perpendicular wave vectors  $\vec{k}$  may be a more general criterion for determining the behavior of field line separation in anisotropic turbulence.

The exponential growth rate for the mean squared distance, which has also been called the Kolmogorov entropy or topological entropy (see Appendix B

of Isichenko 1991b), is also found to be different for various cases of magnetic turbulence (Jokipii 1973; Barge et al. 1984; Similon & Sudan 1989; Isichenko 1991a, 1991b; Barghouty & Jokipii 1996; Maron et al. 2004), showing that general expressions are not always applicable to particular cases of interest. In our case of two-component turbulence, the exponential growth length, given by (5.32), is again related to the ratio between the amplitudes of slab and 2D components of the turbulent magnetic field, not only correlation lengths and the overall amplitude as suggested by Isichenko (1991a, 1991b).

Now let us return to a specific issue raised in Section 5.1: can observed dropouts (i.e., sharp spatial gradients) of solar energetic particles be explained by field line separation in the solar wind that is much slower than the field line random walk? Apparently not, because observed particle motion and magnetic turbulence in the solar wind are best modelled by a roughly 80:20 ratio in 2D:slab turbulent energy (Bieber et al. 1994, 1996), and  $\tilde{\lambda}$  is inferred from observations to be  $\sim 0.2$  AU (Matthaeus et al. 1999), so the derived value of  $D_{\perp}^{2D} = 0.37$  AU is about an order of magnitude higher than the slab contribution. This corresponds to a 2D-dominated random walk, the case of Figure 5.4a, and we expect fast diffusive separation ( $D_s \approx 2D_{\perp}^{2D}$ ) for distances greater than a parallel coherence length of  $\sim 0.02$  AU. Therefore, field line separation should correspond to uncorrelated random walks of two field lines starting in the same region. An alternative explanation of dropouts, corresponding to temporary trapping of field lines near O-points in the turbulence, is presented in Chapter 6.

In conclusion, we use non-perturbative analytic techniques based on the Corrsin independence hypothesis and computer simulations to investigate the separation of magnetic field lines in a two-component model of anisotropic tur-

bulence, which has proven to be a useful model of turbulence in the solar wind. In the long-distance limit, we predict “fast diffusive separation” with a diffusion coefficient  $D_s \approx 2(D_{\perp}^{2D})^2/D_{\perp}$ , where  $D_{\perp}$  refers to the perpendicular diffusion (random walk) of field lines relative to the mean magnetic field, and  $D_{\perp}^{2D}$  is for the case of vanishing slab turbulence. This has the counter-intuitive implication that increasing slab turbulence leads to a smaller  $D_s$ . If the random walk is dominated by the 2D component of turbulence, fast diffusive separation begins as soon as the random walk reaches a perpendicular coherence length  $\ell_{\perp}$ . However, if the slab component dominates the random walk, there is more interesting behavior at intermediate  $\Delta z$ . We find non-axisymmetric, slow diffusive separation at a rate related to the correlation of the flux function (vector potential) at the initial separation, followed by superdiffusive separation at  $\Delta z \gtrsim \ell_g$ , which increases up to the fast diffusive separation rate. The length  $\ell_g$  is identified with an exponential growth scale for the distance between neighboring magnetic field lines, which is related to the relative amplitudes of the slab and 2D components.

สถาบันวิทยบริการ  
จุฬาลงกรณ์มหาวิทยาลัย

# Chapter 6

## Conditional Statistics

### 6.1 Introduction and Observations

In general, energetic particles in space plasmas gyrate in helical orbits around magnetic field lines, and transport parallel to the mean magnetic field is more rapid than perpendicular transport (Parker 1963, p. 242). In particular, the interplanetary magnetic field is dragged outward from the Sun in a spiral pattern by the solar wind (Parker 1958), and the particles accelerated by violent events at the Sun (such as solar flares and coronal mass ejections) can rapidly travel to the observer when there is good magnetic connection between them. While spatial inhomogeneities in solar energetic particle (SEP) distributions have been known for decades, they have generally been reported as occasional, sharp features attributed to magnetic discontinuities, including shocks, magnetic sector boundaries, tangential discontinuities, fast/slow solar wind boundaries, large-scale flux tubes, and magnetic clouds (e.g., Scholer & Morfill 1975; Evenson, Meyer, & Yanagita 1982; Dröge, Wibberenz, & Klecker 1990; Sanderson et al. 2000). However, the “dropouts” recently observed by the *Advanced Composition Explorer* (*ACE*) spacecraft for a large number of impulsive solar events occur frequently (see Figure 6.1 in the left panel for examples of dropouts in impulsive solar flare events) and they are not correlated with the local interplanetary magnetic field (Mazur et al. 2000). Averaging over 25 events, the dropouts are associated with such small scales ( $\sim 0.03$  AU) that they cannot be attributed

to large-scale features and instead must be related to the small-scale structure of the interplanetary magnetic field (Mazur et al. 2000). Indeed, we argue that dropouts are a signature of the topology of magnetic turbulence in the solar wind and therefore are relevant to understanding magnetohydrodynamic (MHD) turbulence in general. Note that the dropouts cannot be observed in the energetic particles from gradual events, which are believed to be accelerated over large areas by interplanetary shocks driven by coronal mass ejections (CMEs), such as the event shown in the right panel of Figure 6.1.

In contrast, SEP from impulsive solar events serve as a good probe of lateral transport (in solar latitude and longitude) because they arise from a localized source (Reames, Cane, & von Rosenvinge 1990) associated with a group of sunspots. Lateral transport requires transport perpendicular to the mean magnetic field as a function of time, which is in turn attributed to the random walk of turbulent field lines as a function of distance along the mean field (Jokipii 1966). That substantial lateral transport occurs over a timescale of days is dramatized by recent observations of the same set of solar events by two spacecraft: the *Interplanetary Monitoring Platform 8 (IMP-8)* near Earth and *Ulysses* at 2 to 2.8 AU (see Figure 6.2 for the location of *Ulysses* during Day 250, 2000 - Day 17, 2001) (McKibben, Lopate, & Zhang 2001). The inferred magnetic footpoints of the two spacecraft were nearly opposite in solar longitude and also very different in solar latitude (equatorial for *IMP-8* and near the South Pole for *Ulysses*). Figure 6.3 presents time-dependent SEP fluxes observed by *IMP-8* and *Ulysses* that were very similar (in absolute terms) during the decay phases of the majority of the observed events. This indicates that SEP can undergo rapid lateral diffusion, spreading throughout the inner solar system within a few days.

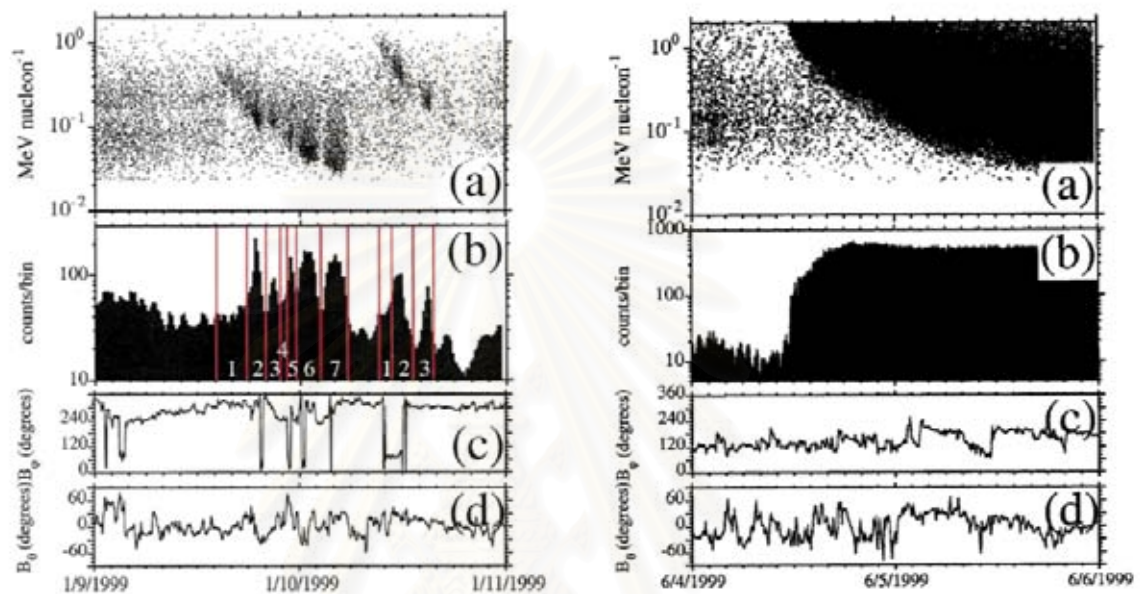


Figure 6.1: *Left panel:* Two impulsive flare events observed by *ACE* spacecraft which occurred during 1999 January 9-10. a) Energy of H-Fe ions (in units of MeV/nucleon) vs. arrival time. b) The intensity was highly variable (on a log scale). c) Interplanetary magnetic field angle in the geocentric solar ecliptic (GSE)  $x$ - $y$  plane. d) Interplanetary magnetic field angle normal to the GSE  $x$ - $y$  plane. *Right panel:* Example event of the solar energetic particles associated with a CME and an interplanetary shock. a) Energy of oxygen ions (in units of MeV/nucleon) vs. arrival time. b) The intensity variation was not observed in this event. c) Interplanetary magnetic field angle in the GSE  $x$ - $y$  plane. d) Interplanetary magnetic field angle normal to the GSE  $x$ - $y$  plane. (Image credit: Mazur et al. 2000)



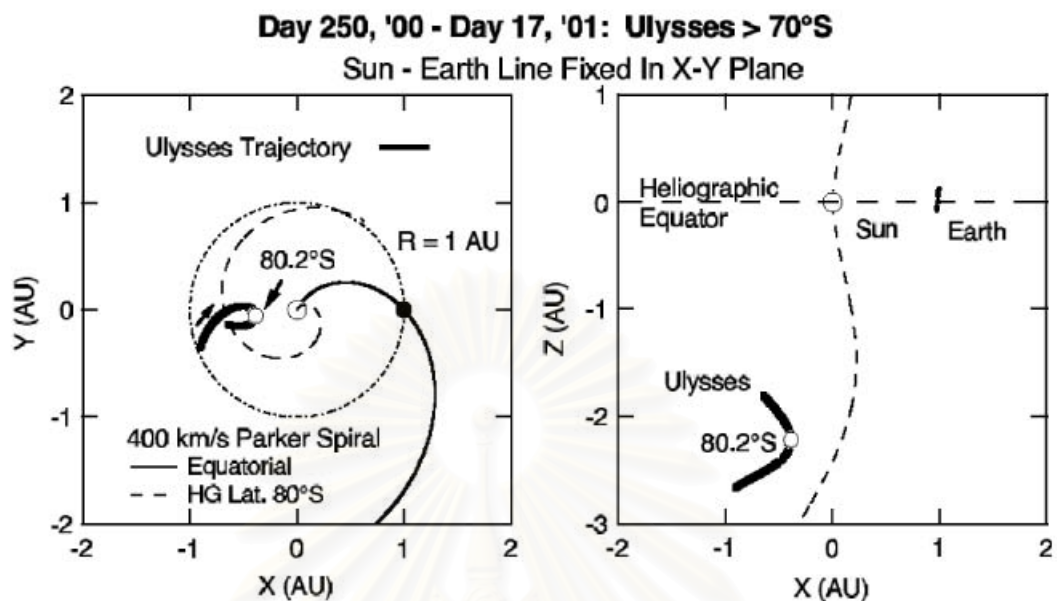


Figure 6.2: The location of *Ulysses* during during Day 250, 2000 - Day 17, 2001. (Image credit: McKibben et al. 2001)

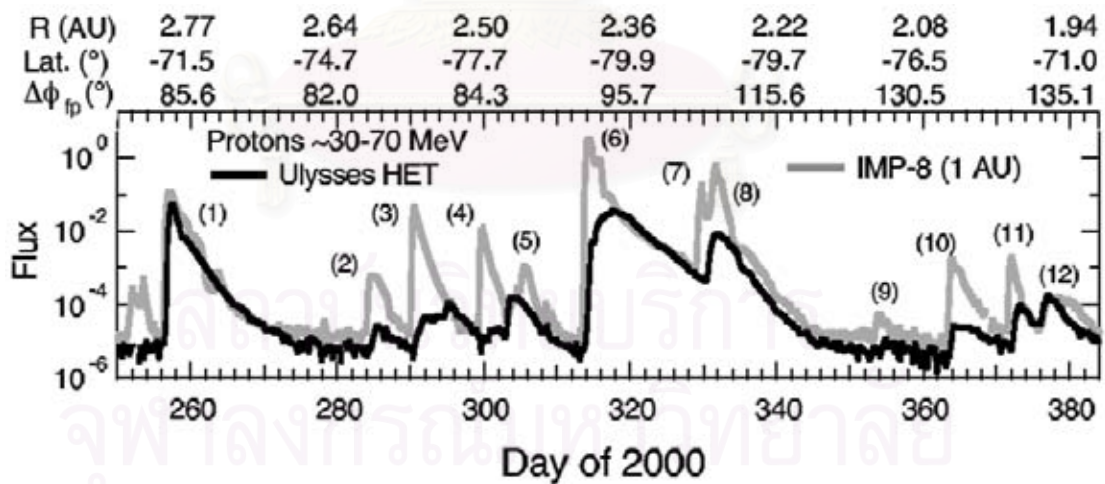


Figure 6.3: Flux of  $\sim 30$ -70 MeV protons vs. time observed by *IMP-8* and *Ulysses*. The axes on the top show the *Ulysses* position and connection longitude relative to that of the Earth. (Image credit: McKibben et al. 2001)

## 6.2 Explanation of Dropouts

The perpendicular transport of a diffusive nature cannot explain both the dropouts and the *IMP-8/Ulysses* observations; the latter, as well as previous multispacecraft observations (e.g., Palmer 1982 and references therein), imply such rapid diffusion that the small-scale dropouts would be washed out. It has been proposed that fluid motions at the solar surface lead to a field line random walk that is consistent with the dropouts (Giacalone, Jokipii, & Mazur 2000). As will be shown below, that type of random walk is too slow to explain the *IMP-8/Ulysses* observations.

Here we propose to reconcile these observations in terms of a two-component model of solar wind turbulence that has provided a useful explanation of both its magnetic statistics and the parallel transport of SEP. We show that in such a model, a certain fraction of low-energy SEP is temporarily trapped within small-scale topological structures in statistically homogeneous turbulence, ultimately escaping to diffuse at a much faster rate. This view of perpendicular transport can explain both the *ACE* observations of dropouts, over short timescales, and the *IMP-8/Ulysses* observations of rapid dispersion after a few days.

We next consider the characteristics of the two-component model of magnetic turbulence. For pure 2D turbulence, with no slab component, magnetic field lines can remain trapped near certain  $(x, y)$  coordinates because they always follow contours of constant  $a$ . As an example, Figure 6.4 shows a contour plot of  $a(x, y)$  for a specific representation of 2D turbulence that was generated to have desired statistical properties. The “O” symbols in Figure 6.4 indicate O-points [local maxima or minima in  $a(x, y)$ ] where the contours remain trapped within “islands” of the 2D turbulence (or filaments in three-dimensional space). We also

indicate X-points, i.e., saddle points of  $a(x, y)$ . This is an example of how turbulence with homogeneous statistical properties can have small-scale topological structure.

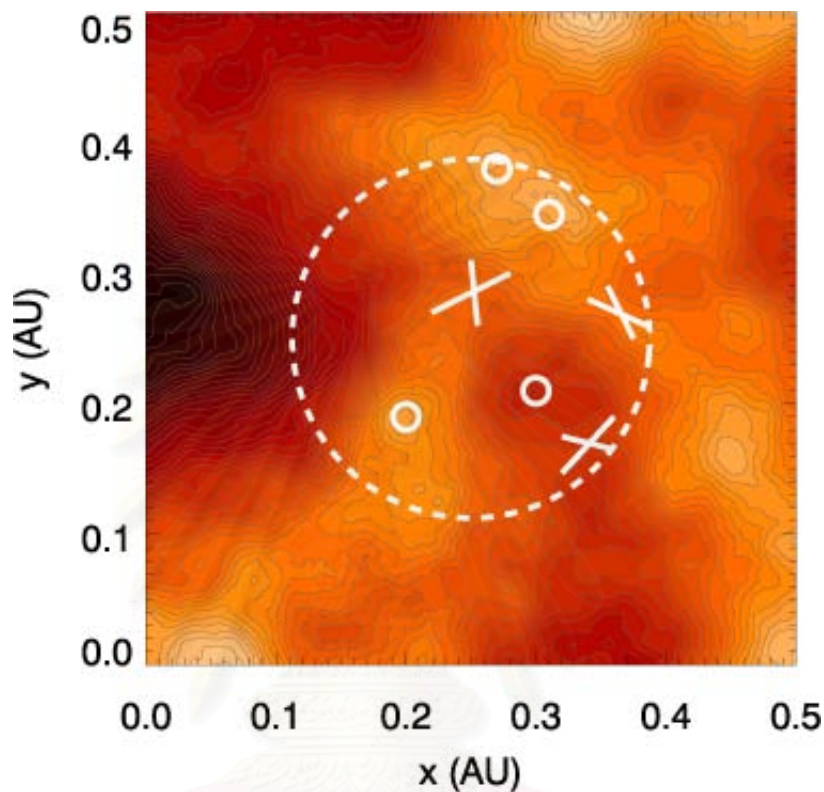


Figure 6.4: Contour plot of the potential function for a representation of the 2D turbulence component. The magnetic field due to this component follows contours of constant potential. Field lines near O-points are trapped within topological “islands,” while field lines near X-points or outside islands rapidly travel to other locations. In the solar wind, magnetic field lines undergo an additional random walk due to the slab component of turbulence, which allows them to eventually escape from islands surrounding O-points.

The ensemble average statistics of the field line random walk were calculated by Matthaeus et al. (1995). A diffusion coefficient,  $D$ , is defined by  $\langle \Delta x^2 \rangle = 2D\Delta z$ , where  $\Delta x$  is the change in a perpendicular coordinate over a distance  $\Delta z$  along the mean field. Each turbulence component is associated with

a value of  $D$ ; the overall value is  $D = D_{\text{slab}}/2 + \sqrt{(D_{\text{slab}}/2)^2 + (D_{2D})^2}$ . Under normal solar wind conditions,  $D_{\text{slab}}$  is very small ( $\approx 5 \times 10^{-4}$  AU). The total diffusion coefficient can be estimated from the *IMP-8* and *Ulysses* data sets.

For most solar events shown by McKibben et al. (2001), the 30-70 MeV proton time-intensity profiles at the two spacecraft are very similar, in shape as well as absolute magnitude, immediately after the peak in particle intensity. Only the event of 2000 November 8 (event 6 in Figure 6.3) shows a distinctly diffusive rise at *Ulysses* before matching *IMP-8* data in the decay phase. Therefore we have fit this most diffusive event, using a Reid profile (Reid 1964) centered at the Archimedean field line of the flare site at the radial distance of *Ulysses* (2.35 AU), to provide a lower bound on the particle diffusion coefficient  $\kappa_{\perp}$  (see the details of fitting in Appendix C). Based on this conservative estimate, the *IMP-8* and *Ulysses* observations require an SEP perpendicular diffusion coefficient of  $\kappa_{\perp} \geq 1.3 \times 10^{21} \text{ cm}^2 \text{ s}^{-1}$ , or  $\kappa_{\perp}/\beta \geq 4 \times 10^{21} \text{ cm}^2 \text{ s}^{-1}$ , where  $\beta$  is the particle speed divided by the speed of light. This is of the same order of magnitude as previous estimates (e.g., Parker 1963; Palmer 1982). Using the field line random walk concept (Jokipii 1966), which in itself yields an underestimate of  $D$  (Matthaeus et al. 2003), one obtains a total field line diffusion coefficient of  $D > 0.02$  AU, which is much greater than  $D_{\text{slab}}$ .

Therefore, the 2D component of turbulence dominates the ensemble average field line diffusion, and  $\Delta x_{rms} = \sqrt{\langle \Delta x^2 \rangle} > 0.2$  AU at Earth orbit. However, such ensemble average statistics cannot apply to observations of dropouts, because the dropouts correspond to filamentation over  $\sim 0.03$  AU, which would be completely washed out by such rapid diffusion.

Instead of ensemble average statistics, let us now consider conditional

statistics, depending on the initial location of a magnetic field line. If a field line is near an O-point, within an island of the 2D turbulence (see Figure 6.4), the 2D contribution to the random walk is suppressed. The field line is temporarily trapped, with diffusion at the much slower rate characteristic of slab turbulence (or even slower; see Section 6.3). On the other hand, magnetic field lines that start outside islands are rapidly carried far away by the 2D turbulence.

In particular, suppose that particles are injected in a spatially localized region, say a circle of radius  $\rho$ . Then  $z_1 = \rho^2/(4D)$  is a characteristic distance over which field lines outside islands diffuse out of the circle. If an island has diameter  $d$ , then  $z_2 = d^2/(16D_{\text{slab}})$  is the typical distance along the mean field over which field lines escape from the island, given diffusion due to the slab component. If slab diffusion is weak, we can have  $z_1 < z_{\text{obs}} < z_2$ , where  $z_{\text{obs}}$  is the distance of the observer. We suggest that dropouts are observed under these conditions. Magnetic field lines (and the low-energy particles orbiting them) that start deep within islands mostly remain trapped, while those outside the islands rapidly escape from the injection region, leaving gaps with a low density of particles. On the other hand, after a long distance ( $z_{\text{obs}} > z_2$ ) essentially all field lines have escaped their temporary topological traps, corresponding to rapid lateral diffusion of field lines (with the ensemble average diffusion coefficient  $D$ ) and of particles.

This idea is confirmed by computer simulations that trace field line trajectories in representations of 2D+slab turbulence for typical solar wind values, using Cartesian geometry for simplicity. The field line random walk is then a surrogate for particle gyrocenter motion. The simulations involved two steps:

- 1) Generating representations of slab and 2D turbulence with desired

statistical properties, such as the observed Kolmogorov power-law spectrum over the inertial wavenumber range (Jokipii & Coleman 1968), using the power spectrum as we presented in Chapter 3 and random phases, followed by inverse fast Fourier transforms to obtain  $\vec{b}_{slab}(z)$  and  $\vec{b}_{2D}(x, y)$ . The transform in  $z$  used  $2^{22}$  ( $\approx 4.2 \times 10^6$ ) points, representing a length of 25 AU. The transform in  $x$  and  $y$  used 2048 points in each dimension, corresponding to a length of 2.5 AU. The simulations in the present work were for parameters believed to correspond to typical solar wind conditions:  $b/B_0 = 0.5$ , fraction of slab turbulent energy  $f_s = 0.2$  (following Bieber et al. 1994), slab correlation length  $\ell_c = 0.02$  AU, and ultrascale of 2D turbulence  $\tilde{\lambda} \equiv \sqrt{\langle a^2 \rangle / \langle b^2 \rangle_{2D}} = 0.06$  AU. The ultrascale is believed to roughly correspond to the size of the largest islands, and this value corresponds to  $D = 0.02$  AU, as a conservative lower limit. This lower limit is consistent with a previous estimation of  $\tilde{\lambda}$  (Matthaeus, Smith, & Bieber 1999).

2) Tracing magnetic field lines, i.e., solving the coupled ordinary differential equations

$$\frac{dx}{dz} = \frac{b_x(x, y, z)}{B_0} \quad \frac{dy}{dz} = \frac{b_y(x, y, z)}{B_0}. \quad (6.1)$$

We use a fourth-order Runge-Kutta method with adaptive time stepping regulated by a fifth-order error estimate step (Press et al. 1992).

Our computer simulations for several representations (several sets of random phases), different values of  $\tilde{\lambda}$ , and different spectral forms at low wavenumber yielded qualitatively similar results, including structures corresponding to dropouts of  $\sim 0.03$  AU as in the *ACE* observations.

The results shown in Figure 6.5 demonstrate the behavior described above and the realization of 2D turbulence is the same as in Figure 6.4. The upper left

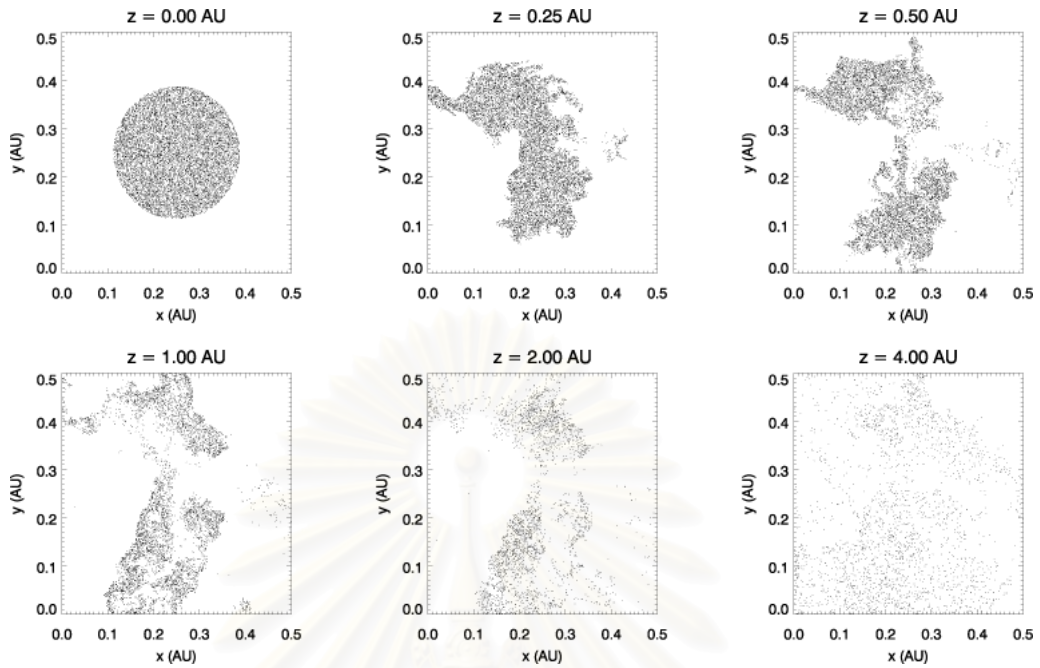


Figure 6.5: Scatter plot of the 10,000 locations of magnetic field lines that are initially (at  $z = 0$ ) located within a circle (simulating the region where particles are injected due to an impulsive solar flare). At intermediate  $z$  values, field lines within islands of the 2D turbulence (around the O-points shown in Figure 6.4) remain trapped, while field lines in other regions spread rapidly. This explains the filamentary distribution of particles as indicated by dropout features. At large  $z$  values all field lines diffuse rapidly, explaining the *Ulysses* and *IMP-8* observations of SEP diffusion throughout the inner solar system.

panel shows random initial locations within a circle, corresponding to the injection region where field lines are populated with SEP. Field lines are then traced from those initial locations as a function of  $z$ . Subsequent panels, cross-sections at longer distances along the mean field, show filamentary structures in the distribution of SEP. A spacecraft near Earth ( $z \approx 1$  AU) samples a transept through this highly inhomogeneous distribution. The simulation results are consistent with observed dropouts of  $\sim 0.03$  AU. At longer distances, essentially all field lines (and particles) have diffused away, leading to the rapid propagation of particles throughout the inner heliosphere at later times. Note that we identify dropouts

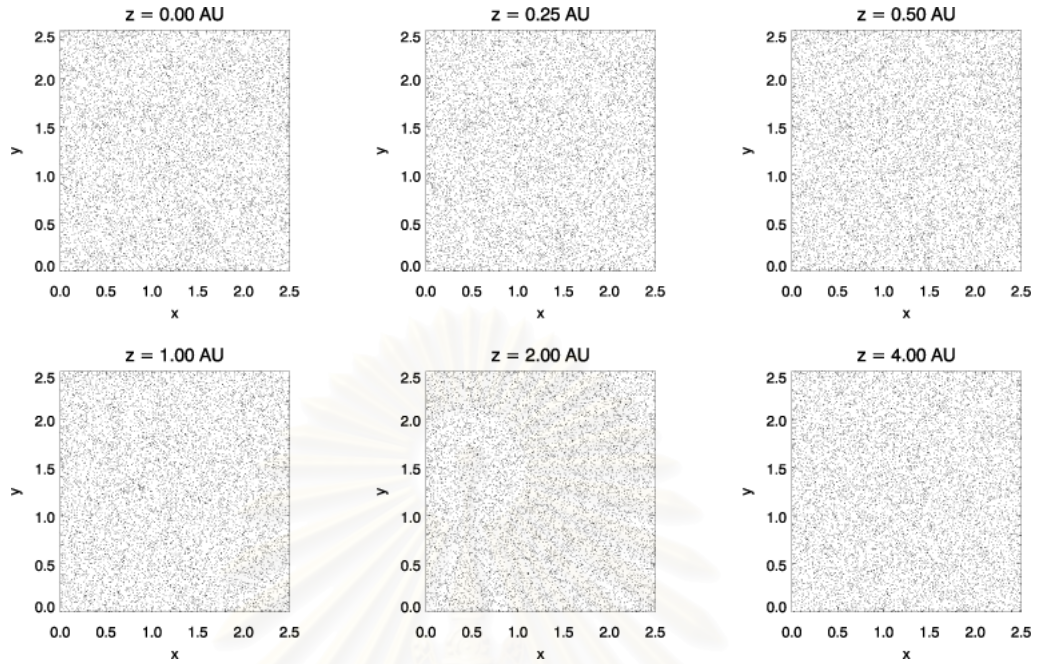


Figure 6.6: Scatter plot of the 10,000 field lines which are initially distributed uniformly through the entire simulation region. The field lines are still uniformly random over any distance. This simulation corresponds to the energetic particles from CME-driven and interplanetary shocks.

with topological structures that develop in solar wind turbulence, not with initial motions at the solar surface. We see effects of islands of various sizes  $d$  due to the self-similar nature of turbulence, including islands within islands, but those much wider than  $\rho$  do not confine particles near the injection region.

Figure 6.6 shows simulation results corresponding to coronal mass ejection (CME) events for which the dropouts cannot be observed. CME events have a wide injection region ( $z_1 > z_{obs}$ ). We set the initial positions of magnetic field lines to be randomly distributed throughout the simulation region. Here we cannot observe inhomogeneous pattern as observed in Figure 6.5. The distribution indeed remains uniformly random at all distances, as required by Liouville's theorem in the context of our model. Therefore, the simulations also confirm that we should



not see the dropouts in this event.

This new view of the perpendicular transport of energetic particles in space plasmas can also reconcile another pair of apparently conflicting observations. Impulsive solar events selected for a strong SEP electron increase were shown to have a narrow distribution in solar longitude (Reames et al. 1990). This indicates only limited lateral spreading for the bulk of SEP, which we attribute to trapping within small-scale topological islands, representing a “core” region of high particle density (Figure 6.7). On the other hand, recent spacecraft observations of Type III radio bursts and associated SEP indicate that SEP electrons and ions can undergo broad lateral motion (up to  $\sim 90^\circ$  in solar longitude) during their transport from the Sun to Earth orbit (Cane & Erickson 2003). In our view, this laterally extended but less intense “halo” of SEP corresponds to particles on field lines initially located outside local islands of 2D turbulence. (Note that particles observed by *Ulysses* do not necessarily correspond to this halo, as they may have undergone lateral diffusion beyond 1 AU.) Indeed, the absence of these halo SEP from the core region is manifest as dropouts.

Finally, we note that the problem considered here is directly analogous with Hamiltonian flow of a dynamical system (in 2D phase space) with time-dependent, random forcing (upon the substitutions  $a \rightarrow H$  and  $z \rightarrow t$ ). Therefore, our qualitative conclusions apply to such systems in general.

### 6.3 Inhibition of Random Walk by Systematic Flow in Two Dimensions

In the two-component model of magnetic turbulence in the solar wind, the slab component causes the field lines to undergo a random walk while the

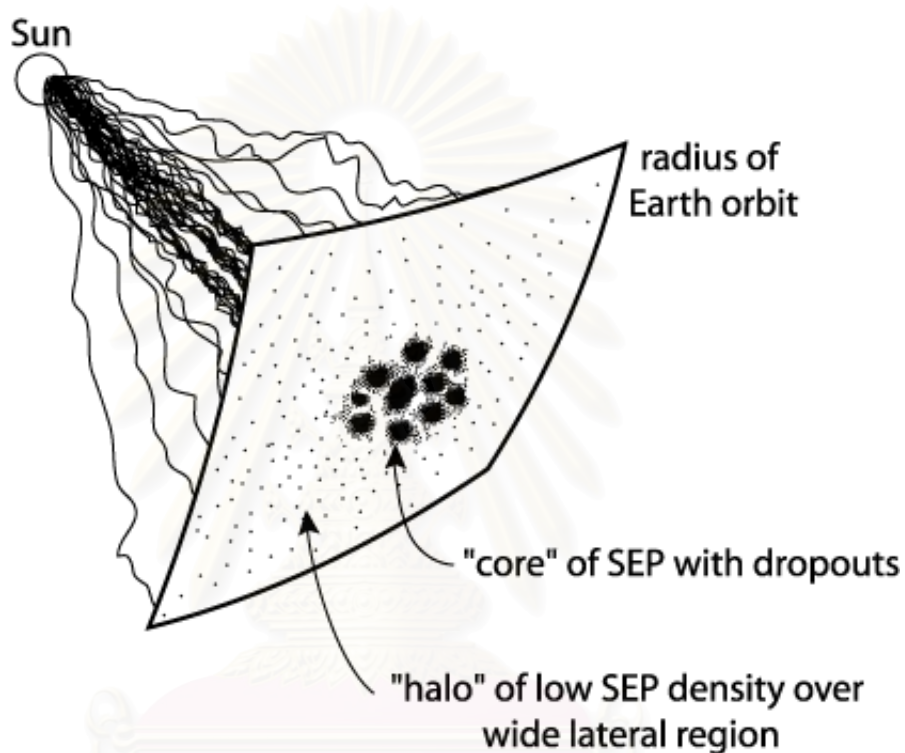


Figure 6.7: Illustration of interplanetary magnetic field lines populated with solar energetic particles (SEP) from a localized source region near the Sun, as expected for an impulsive solar flare. In the 2D+slab model of solar wind turbulence, some field lines are trapped in filaments corresponding to the small-scale topology, i.e., islands of the 2D turbulence, out to Earth orbit, while interstitial field lines spread laterally to large angular distances. This leads to the observed “core” region of SEP with dropouts and an extended “halo” region.

2D turbulence forces the field lines to follow contours of a constant 2D potential function. The previous section showed that the trajectories of field lines depend on the topology of the 2D potential function, and thus were able to explain the filamentation underlying observed dropouts in solar energetic particles (Mazur et al. 2000). The field lines near an O-point are temporarily trapped within 2D islands and field lines near an X-point or outside the 2D islands rapidly travel to other locations.

There are many questions arising from this problem, such as how the field lines diffuse inside and outside the trapping boundaries, how we can define the trapping boundary and what parameters affect the trapping boundary. Instead of immediately examining this complex problem, here we study the field lines in the simpler case of a systematic 2D field for which the potential function contours are circles, and examine the behavior of field line trajectories when adding a turbulent slab component. In addition to our finding that a strong 2D field can suppress the slab diffusion, we provide an explanation in terms of quasilinear theory that can help us to understand the field line trajectories in the general case.

### 6.3.1 Magnetic Field Model

We use a simple model to study the inhibition of the random walk of magnetic field lines. The total magnetic field can be written as  $\vec{B}(x, y, z) = B_0\hat{z} + \vec{b}(x, y, z)$ ; where  $\vec{b}$  is perpendicular to the mean field. The fluctuation is the sum of the 2D the field and slab turbulence, which is

$$\vec{b}(x, y, z) = \vec{b}_{2D}(x, y) + \vec{b}_{slab}(z). \quad (6.2)$$

In general, we can write  $\vec{b}_{2D}(x, y) = \vec{\nabla} \times a(x, y)\hat{z}$ , where  $a(x, y)$  is called the potential function. From this relation, we can see that for the pure 2D case,

the field lines must follow the contour plot of  $a(x, y)$ . Here we set  $a(x, y)$  as a Gaussian function:

$$a(x, y) = A \exp \left[ -\frac{x^2 + y^2}{2\sigma^2} \right] = A \exp \left[ -\frac{r^2}{2\sigma^2} \right], \quad (6.3)$$

where  $A$  is the maximum value at the center of the Gaussian and  $\sigma$  represents the width of the Gaussian. Instead of the irregular contours of  $a(x, y)$  that we used for turbulence earlier in this thesis, a contour of  $a(x, y)$  in this case [eq. (6.3)] is simply a circle. Without the slab field, the field line trajectory is a helical orbit along a cylinder of constant  $a(x, y)$  with a constant angular “velocity” (in terms of the distance  $z$ )  $\Omega^{2D} = a(r_0)/(B_0\sigma^2)$ , where  $r_0$  is the starting radius (see Appendix D).

### 6.3.2 Diffusion Theory

For slab turbulence, the field line trajectories undergo a random walk in space with the perpendicular diffusion rate  $D_{slab} = \ell_c b_{slab}^2 / (2B_0^2)$ , where  $\ell_c$  is the correlation length and  $b_{slab}$  is the root-mean-squared slab energy. The power spectrum of slab turbulence for the  $i$ -component,  $P_{ii}^{slab}$ , that we use in this model is associated with the Kolmogorov spectrum, that is, at high wave number  $k$  the power spectrum is proportional to  $k^{-5/3}$ . We can also rewrite the slab diffusion in terms of the power spectrum at zero wave number,

$$D_{slab} = \sqrt{\frac{\pi}{2}} \frac{P_{xx}^{slab}(k_z = 0)}{B_0^2}. \quad (6.4)$$

When 2D and slab fields are superimposed, the field lines do not follow the contours of  $a(x, y)$  and are also not fully diffusive with the slab rate either. The features of field line trajectories are a kind of combination between the pure 2D and pure slab cases. The field lines should be trapped near the center of

the Gaussian and should rapidly diffuse when the field lines are at a distance  $r \gg \sigma$ . If we consider the region where the 2D field is much stronger than the slab component, we can apply quasi-linear theory to this problem. That means we can assume the orbit of a field line is approximately a circle with angular velocity  $\Omega^{2D}$ . From the two-component model of magnetic turbulence, we can write  $\vec{b}^{slab}(z) = b_x^{slab}(z)\hat{x} + b_y^{slab}(z)\hat{y}$  and

$$\hat{x} = \hat{r} \cos \theta - \hat{\theta} \sin \theta \quad (6.5)$$

$$\hat{y} = \hat{r} \sin \theta + \hat{\theta} \cos \theta \quad (6.6)$$

$$\hat{z} = \hat{z}, \quad (6.7)$$

so the slab fluctuation can be written as

$$\vec{b}^{slab}(z) = (b_x^{slab}(z) \cos \theta + b_y^{slab}(z) \sin \theta) \hat{r} \quad (6.8)$$

$$+ (-b_x^{slab}(z) \sin \theta + b_y^{slab}(z) \cos \theta) \hat{\theta}. \quad (6.9)$$

We can rewrite the 2D part in polar coordinates as

$$\vec{b}^{2D}(r) = -\frac{da(r)}{dr} \hat{\theta} = \frac{ra(r)}{\sigma^2} \hat{\theta}, \quad (6.10)$$

where  $a(r)$  is the Gaussian potential function. Therefore the field line equations for this problem are

$$\frac{dr}{dz} = \frac{b_r}{B_0} = \frac{b_x^{slab} \cos \theta + b_y^{slab} \sin \theta}{B_0} \quad (6.11)$$

$$\frac{d\theta}{dz} = \frac{1}{r} \frac{b_\theta}{B_0} = -\frac{1}{rB_0} \frac{da(r)}{dr} + \frac{b_y^{slab} \cos \theta - b_x^{slab} \sin \theta}{rB_0} \quad (6.12)$$

$$= \Omega^{2D} + \frac{b_y^{slab} \cos \theta - b_x^{slab} \sin \theta}{rB_0}. \quad (6.13)$$

For the case that  $b^{slab} \ll b^{2D}$ , we can use quasi-linear theory (QLT) to find the diffusion coefficient. That means the orbits of field lines undergo little change

due to the slab field. Then  $\Delta\theta \approx \Omega^{2D} \Delta z$ . Next we calculate  $\langle \Delta r^2 \rangle$  from (6.11),

$$\Delta r = \frac{1}{B_0} \int_0^{\Delta z} b_x^{slab}(z) \cos \theta(z) + b_y^{slab}(z) \sin \theta(z) dz \quad (6.14)$$

$$\begin{aligned} \langle \Delta r^2 \rangle &= \frac{1}{B_0^2} \int_0^{\Delta z} \int_0^{\Delta z} \langle (b_x^{slab}(z') \cos \theta(z') + b_y^{slab}(z') \sin \theta(z')) \\ &\quad \times (b_x^{slab}(z'') \cos \theta(z'') + b_y^{slab}(z'') \sin \theta(z'')) \rangle dz' dz'' \end{aligned} \quad (6.15)$$

Since  $\langle a + b \rangle = \langle a \rangle + \langle b \rangle$  and  $\theta$  is not a random variable,

$$\begin{aligned} \langle \Delta r^2 \rangle &= \frac{1}{B_0^2} \int_0^{\Delta z} \int_0^{\Delta z} [\langle b_x^{slab}(z') b_x^{slab}(z'') \rangle \cos \theta(z') \cos \theta(z'') \\ &\quad + \langle b_y^{slab}(z') b_y^{slab}(z'') \rangle \sin \theta(z') \sin \theta(z'') \\ &\quad + \langle b_x^{slab}(z') b_y^{slab}(z'') \rangle \cos \theta(z') \sin \theta(z'') \\ &\quad + \langle b_y^{slab}(z') b_x^{slab}(z'') \rangle \sin \theta(z') \cos \theta(z'')] dz' dz''. \end{aligned} \quad (6.16)$$

Let  $z'' = z' + \Delta z'$ , so  $\int_0^{\Delta z} dz'' \rightarrow \int_{-z'}^{\Delta z - z'} d\Delta z'$ . Equation (6.16) becomes

$$\begin{aligned} \langle \Delta r^2 \rangle &= \frac{1}{B_0^2} \int_0^{\Delta z} \int_{-z'}^{\Delta z - z'} [R_{xx}(\Delta z') \cos \theta(z') \cos \theta(z' + \Delta z') \\ &\quad + R_{yy}(\Delta z') \sin \theta(z') \sin \theta(z' + \Delta z') \\ &\quad + R_{xy}(\Delta z') \cos \theta(z') \sin \theta(z' + \Delta z') \\ &\quad + R_{yx}(\Delta z') \sin \theta(z' + \Delta z') \cos \theta(z')] d\Delta z' dz', \end{aligned} \quad (6.17)$$

where  $R_{ij}(\Delta z') = \langle b_i^{slab}(z') b_j^{slab}(z' + \Delta z') \rangle$  is the correlation function. Here our system is isotropic and the statistics of  $b_x^{slab}$  and  $b_y^{slab}$  are not related; therefore  $R_{xx}(\Delta z') = R_{yy}(\Delta z')$  and  $R_{xy}(\Delta z') = R_{yx}(\Delta z') = 0$ . Then

$$\begin{aligned} \langle \Delta r^2 \rangle &= \frac{1}{B_0^2} \int_0^{\Delta z} \int_{-z'}^{\Delta z - z'} R_{xx}(\Delta z') [\cos \theta(z') \cos \theta(z' + \Delta z') \\ &\quad + \sin \theta(z') \sin \theta(z' + \Delta z')] d\Delta z' dz' \\ &= \frac{1}{B_0^2} \int_0^{\Delta z} \int_{-z'}^{\Delta z - z'} R_{xx}(\Delta z') \cos [\theta(z' + \Delta z') - \theta(z')] d\Delta z' dz' \\ &= \frac{1}{B_0^2} \int_0^{\Delta z} \int_{-z'}^{\Delta z - z'} R_{xx}(\Delta z') \cos(\Omega^{2D} \Delta z') d\Delta z' dz'. \end{aligned} \quad (6.18)$$

Because  $R_{xx}(\Delta z') \approx 0$  when  $\Delta z' \gg \ell_c$ ,

$$\langle \Delta r^2 \rangle = \frac{1}{B_0^2} \int_0^{\Delta z} \int_{-\infty}^{\infty} R_{xx}(\Delta z') \cos(\Omega^{2D} \Delta z') d\Delta z' dz'. \quad (6.19)$$

Writing the correlation function in terms of the power spectrum,

$$R_{xx}(\Delta z') = \frac{1}{\sqrt{2\pi}} \int_{-\infty}^{\infty} P_{xx}(k_z) e^{-ik_z \Delta z'} dk_z. \quad (6.20)$$

Substituting (6.20) into (6.19),

$$\langle \Delta r^2 \rangle = \frac{1}{\sqrt{2\pi} B_0^2} \int_0^{\Delta z} \int_{-\infty}^{\infty} \int_{-\infty}^{\infty} P_{xx}(k_z) e^{-ik_z \Delta z'} \cos(\Omega^{2D} \Delta z') dk_z d\Delta z' dz'. \quad (6.21)$$

Since  $\int_{-\infty}^{\infty} e^{-ik_z \Delta z'} \cos(\Omega^{2D} \Delta z') d\Delta z' = \pi [\delta(k_z + \Omega^{2D}) + \delta(k_z - \Omega^{2D})]$ , the integral in (6.21) becomes

$$\begin{aligned} \langle \Delta r^2 \rangle &= \frac{1}{\sqrt{2\pi} B_0^2} \int_0^{\Delta z} \int_{-\infty}^{\infty} P_{xx}(k_z) \pi [\delta(k_z + \Omega^{2D}) + \delta(k_z - \Omega^{2D})] dk_z dz' \\ &= \sqrt{\frac{\pi}{2}} \frac{\Delta z}{B_0^2} [P_{xx}(-\Omega^{2D}) + P_{xx}(\Omega^{2D})]. \end{aligned} \quad (6.22)$$

Since the power spectrum is symmetric,  $P_{xx}(-\Omega^{2D}) = P_{xx}(\Omega^{2D})$ . Finally, we have

$$\langle \Delta r^2 \rangle = \frac{2\Delta z}{B_0^2} \sqrt{\frac{\pi}{2}} P_{xx}(\Omega^{2D}). \quad (6.23)$$

Thus the diffusion coefficient of the field line in radial direction is

$$D_{rr} = \frac{\langle (\Delta r)^2 \rangle}{2\Delta z} = \sqrt{\frac{\pi}{2}} \frac{P_{xx}(\Omega^{2D})}{B_0^2}. \quad (6.24)$$

Equation (6.24) tells us that the radial motion of field lines very deep inside the 2D field is diffusive and associated with the slab power spectrum at the wave number that resonates with the 2D angular velocity. In order to completely study the behavior of field lines at various radii and distances, we need computer simulations to trace the field lines in a Gaussian 2D field + slab turbulence and examine their statistics.

### 6.3.3 Numerical Experiments

We numerically study the field lines that start at different radii of the Gaussian function  $a(x, y)$ , including their behavior and how they spread in space. We also confirm the quasilinear diffusion theory for the field lines near the center of the Gaussian 2D field by numerical simulations. To get the field line trajectories, we first generate 2D and slab fields. For the 2D field, we can directly generate the magnetic field in real space from the 2D potential function as in equation (6.3). For the slab turbulence field, we generate the field in wave number space, since the system is random and we know the shape of the slab power spectrum, and then use an inverse fast Fourier transform to convert them back to real space (see Section 3.1). For the slab spectrum, we use

$$P_{ii} = \frac{C}{[1 + (k_z \ell_z)^2]^{5/6}}, \quad (6.25)$$

where  $C$  is a normalization constant and  $\ell_z$  is a coherence length which is related to  $\ell_c$  by  $\ell_c = 0.747\ell_z$ . The spectrum is flat when  $k_z \ll 1/\ell_z$  and it rolls over at  $k_{0z} = 1/\ell_z$ . For  $k_z \gg k_{0z}$ , the shape of the spectrum is proportional to  $k^{-5/3}$ , which becomes a Kolmogorov spectrum, as shown in Figure 3.1.

In the next step, we solve the field line equations,

$$\frac{dx}{dz} = \frac{b_x^{2D} + b_x^{slab}}{B_0}, \quad \frac{dy}{dz} = \frac{b_y^{2D} + b_y^{slab}}{B_0}. \quad (6.26)$$

We use a fourth-order Runge-Kutta method with adaptive time stepping regulated by a fifth-order error estimate step (Press et al. 1992). We randomly generate 10,000 initial positions of the field lines starting at a particular radius around the center of the Gaussian and trace the field lines by (6.26). The outputs from solving the field line equations are the positions  $(x, y, z)$  of the field line trajectories.



To confirm the diffusion theory [Eq. 6.24] when  $r \ll \sigma$ , we trace 10,000 field lines which start at a certain radius  $r = 5$  and set  $\sigma = 10$  for the strong 2D field. Figure 6.8 shows an example trajectory of a field line in this problem presented in the  $x$ - $y$  plane. We can see that the field line is temporarily trapped in circular orbits around the 2D island, and then when it is outside the 2D island, the trajectory becomes irregular due to the slab turbulence. Figure 6.9 is a plot of radius  $r$  vs. distance  $z$  for the field line shown in Figure 6.8. For small  $z$  and  $\langle \Delta r^2 \rangle$ ,  $D_{rr}$  is defined by  $\langle (\Delta r)^2 \rangle / (2z)$ . Figure 6.10 shows the numerical calculation of this ratio inside the boundary as eq. (6.24) compared with the theoretical value for  $D_{rr}$ . The numerical ratio initially matches the theory, and later deviates due to the spread in the field line locations, i.e., no longer measuring diffusion at the initial radius.

We perform more simulations to examine the spread of field lines in space as defined by the function  $R'(z) = R(z) - R(0)$ , where  $R(z) = \langle [x(z) - \bar{x}(z)]^2 + [y(z) - \bar{y}(z)]^2 \rangle$  and  $\bar{x}$ ,  $\bar{y}$  are the average positions at a given  $z$ . We can define the effective diffusion coefficient  $D_{eff}$  from  $R'(z)$ ,

$$D_{eff} = \frac{R'(z)}{4z}. \quad (6.27)$$

The effective diffusion coefficient  $D_{eff}$  and  $D_{rr}$  from (6.24) are related by

$$D_{eff} = D_{rr} + \frac{r_0}{2} \frac{dD_{rr}}{dr_0}. \quad (6.28)$$

where  $r_0$  is the radius where the field lines start. Therefore, from QLT and the spectrum we use in simulations, we expect two diffusive regions; one is where the field lines start near the center of the Gaussian ( $r_0 \ll \sigma$ ) as we showed in Figure 6.10 and another one is where the field lines start outside the 2D island

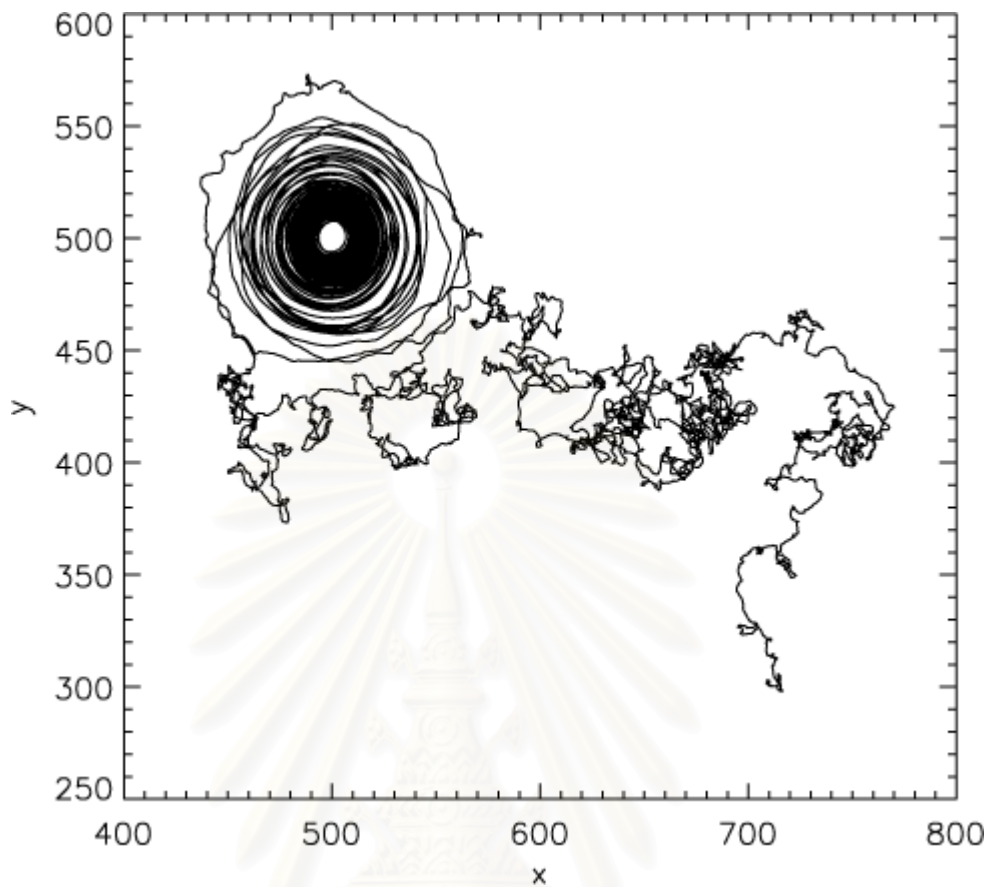


Figure 6.8: Orbit in the  $x - y$  plane of a selected field line that lies deep in the trapping island, showing the predominantly cyclic trajectory, which gradually is transported out of the trapping region, whereupon the motion becomes highly irregular, and is an almost unconstrained random walk.

( $r_0 \gg \sigma$ ) as the slab rate. Figures 6.11 and 6.12 show the relationship between the diffusion coefficients and  $r_0$  from theory.

From the simulation results, we found that for field lines starting inside such a boundary, the diffusion of field lines systematically changes, with a delay at the beginning due to the strong 2D field, while field lines starting outside the boundary immediately diffuse at the slab rate, as in the  $R'$  vs.  $z$  plot shown in Figure 6.13. The suppression of diffusion arises because the rapid motion around circles effectively decorrelates the radial component of the slab field. From the

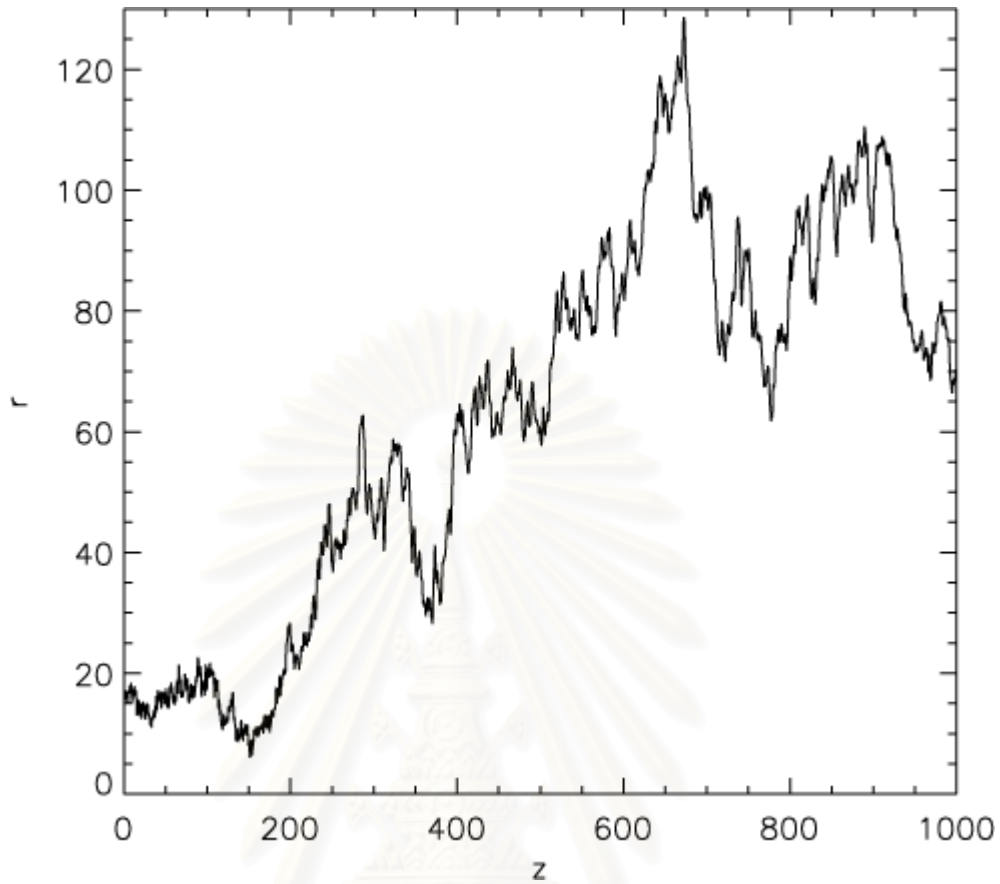


Figure 6.9: Plot of the radial coordinate  $r = \sqrt{x^2 + y^2}$  of a field line vs. the parallel coordinate. At short distances the radial position remains near its initial value  $r = 15$ . After around  $z = 150$  the field line breaks out of the trapping structure and random walks with a much larger amplitude.

simulation results, there are two length scales that we are interested in; the boundary of trapping  $r_c$  and  $L_{trap}^{max}$  which is calculated from  $L_{trap}$  for each initial radius. To evaluate both of them, we trace the straight line at long  $z$  in the  $R'(z)$  plot, where it reflects the slab rate of diffusion, and find the  $x$ -intercept, which is called  $L_{trap}$ , for each initial radius  $r_0$ . Next, we plot  $L_{trap}$  vs.  $r_0$  and then fit the low- $r_0$  portion to a straight line. The  $L_{trap}$ -intercept is identified as  $L_{trap}^{max}$  and the  $r_0$ -intercept is called  $r_c$ , as in Figure 6.12. After we fit the data, we obtain the values of  $L_{trap}^{max}$  and  $r_c$ .

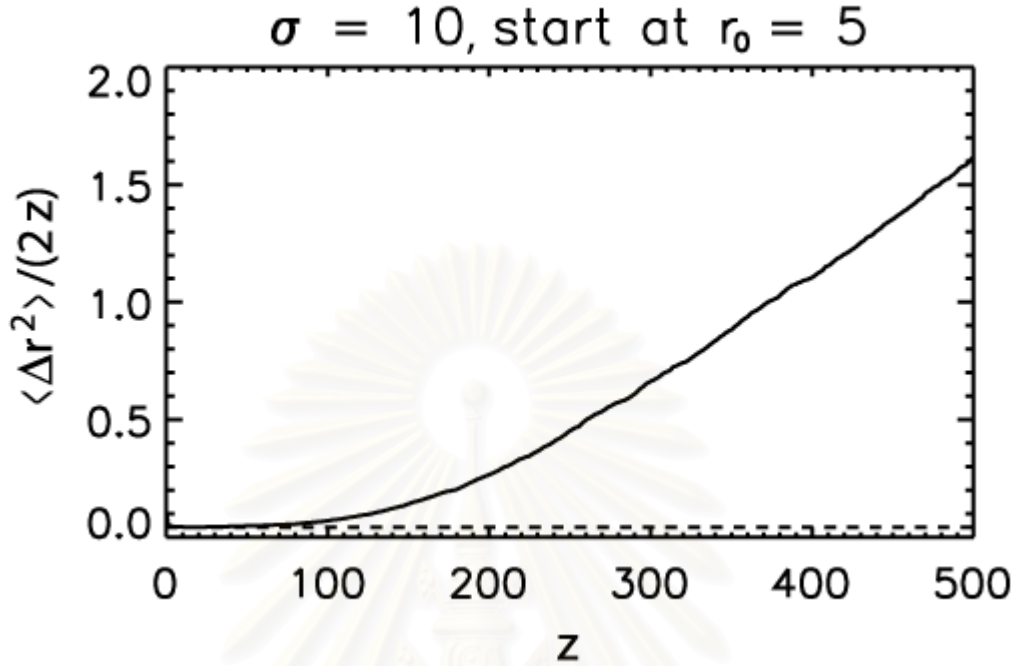


Figure 6.10: Plot of  $\langle \Delta r^2 \rangle / (2z)$  vs.  $z$ , which confirms the theory at small radius, where the dashed line is the theoretical value.

We also vary magnetic parameters such as  $\ell_z$ ,  $\sigma$ ,  $b_{2D}/B_0$ , and  $b_{slab}/B_0$  and look at  $R'$  plots. Note that in this part we define  $b_{2D}$  and  $b_{slab}$  as the root-mean-squared 2D field and slab fluctuation, respectively. The trapping boundary for this case,  $r_c$ , depends only  $\sigma$  and  $\ell_z$  and it is independent of  $b_{2D}/B_0$  and  $b_{slab}/B_0$ , as shown in Figures 6.15 and 6.16. From Figures 6.17 and 6.19, when we increase  $\sigma$  and  $\ell_z$ , the trapping boundary also increases. The trapping boundary  $r_c$  and  $\sigma$  are linearly related and can be fit with the function  $r_c = 1.58\sigma + 1.2$ . For example, if  $\sigma = 1$ , we get  $r_c \approx 2.8$ . We also make the scatter plots for  $\sigma = 1$  shown as Figure 6.18. We can see from the simulation that the trapping boundary is very sharp at  $r \approx 2.5$ . It is close to the relation from the linear fit. Figure 6.19 shows that  $r_c$  vs.  $\ell_z$  can be fit with the relation  $r_c = 17.33\ell_z^{0.1}$ . We also investigate  $L_{trap}^{max}$

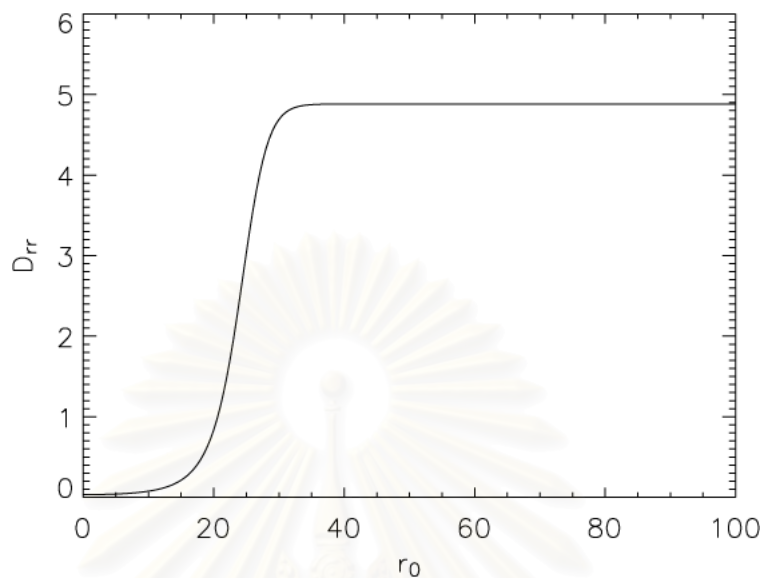


Figure 6.11:  $D_{rr}$  vs.  $r_0$  expected from quasilinear theory.

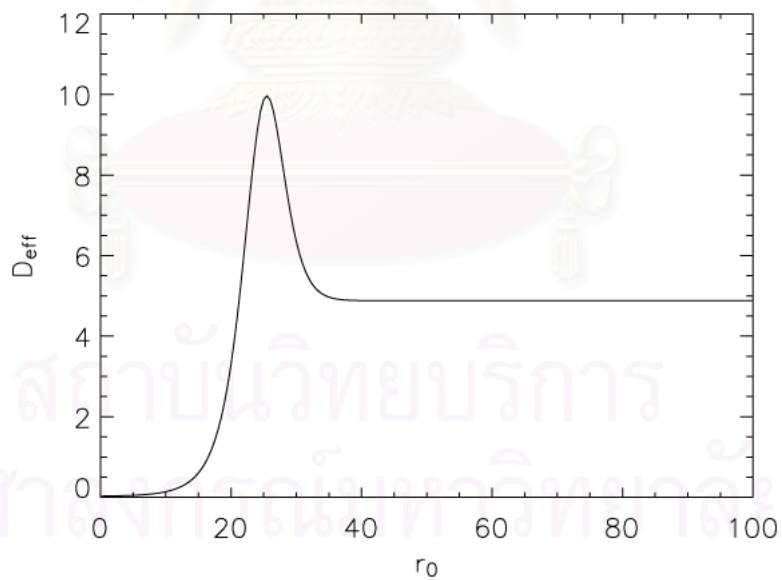


Figure 6.12:  $D_{eff}$  vs.  $r_0$  as derived from Figure 6.11 by equation 6.28.

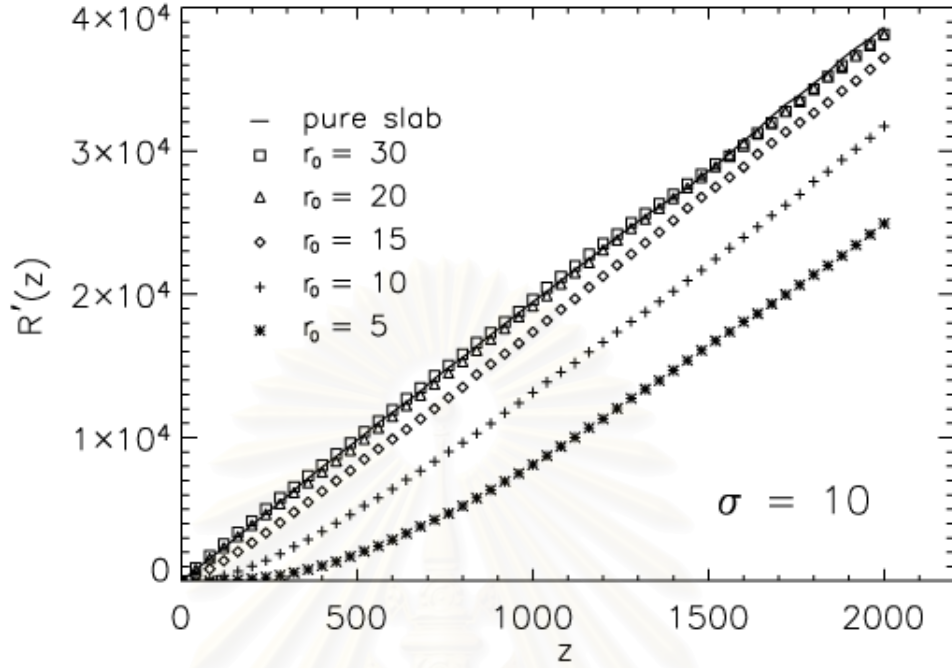


Figure 6.13:  $R'(z)$  vs.  $z$ , showing how the field lines spread from starting points near the center when we set  $\sigma = 10$ .

versus other parameters (Figures 6.21, 6.22, 6.23, and 6.24), and we can simply estimate  $L_{trap}^{max}$  by

$$L_{trap}^{max} \approx L_0^2 \frac{[(b_{2D}/B_0)^2]^{0.62} \ell_z^{0.5}}{[(b_{slab}/B_0)^2]^{0.74} \sigma^{1.5}}. \quad (6.29)$$

In conclusion, we apply quasi-linear theory to the problem of the magnetic field line in the Gaussian 2D field plus slab turbulence. We find that the strong 2D field can inhibit the random walk of the field lines due to the slab component. The field lines located near the maximum of the 2D potential function diffuse at a lower rate than when they are outside the 2D island. The simulations show that when we start the field lines inside the 2D island, the diffusion of field lines systematically changes with a delay at the beginning due to the strong 2D field.

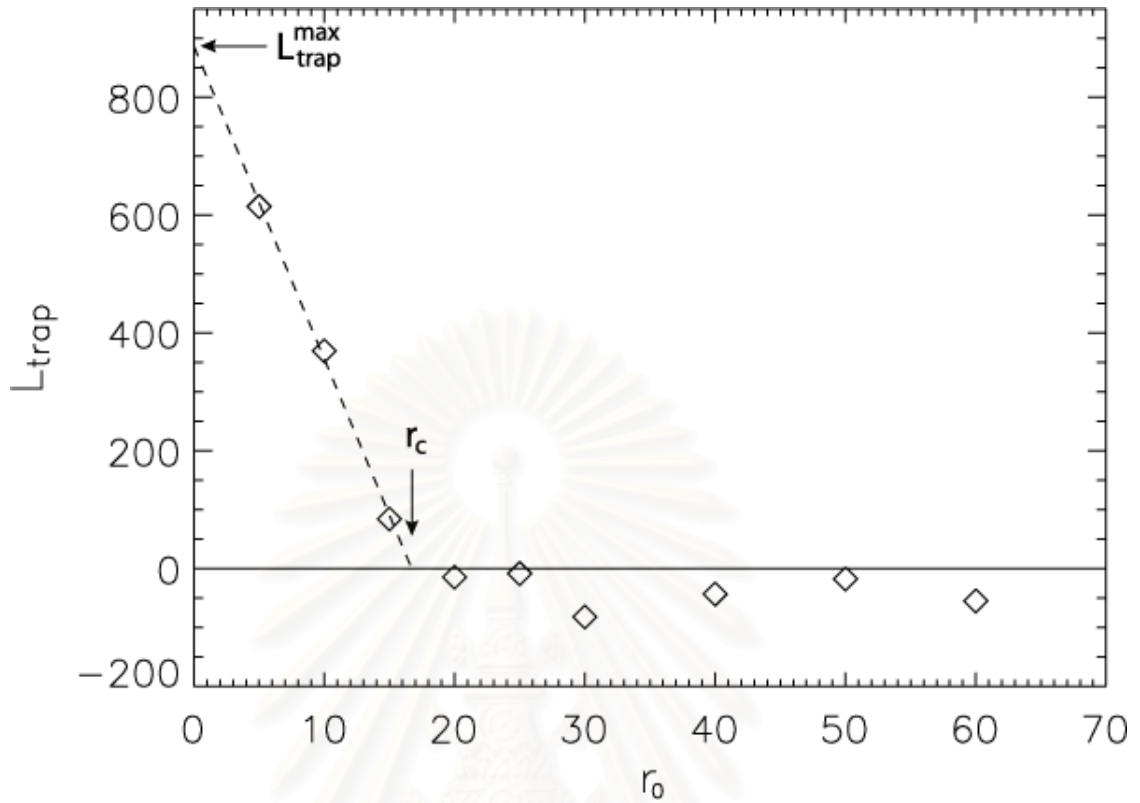


Figure 6.14: Illustration of the definitions of  $r_c$  and  $L_{\text{trap}}^{\text{max}}$  for  $\sigma = 10$  and  $\ell_z = 1$ .

We found that the trapping boundary depends only on the topological scale  $\sigma$  of the 2D island and the characteristic length scale  $\ell_z$  of slab turbulence.

## 6.4 Summary

We try to reconcile the paradox of two types of SEP observations. One is the observation of the dropout phenomena from the *ACE* spacecraft, in which the density of SEPs in space is highly inhomogeneous and there is very little lateral diffusion. In contrast, in *Ulysses* and *IMP-8* observations, the SEPs seem to spread rapidly throughout the entire inner the solar system within a few days, with very a similar intensity at these two spacecraft located opposite sides of the

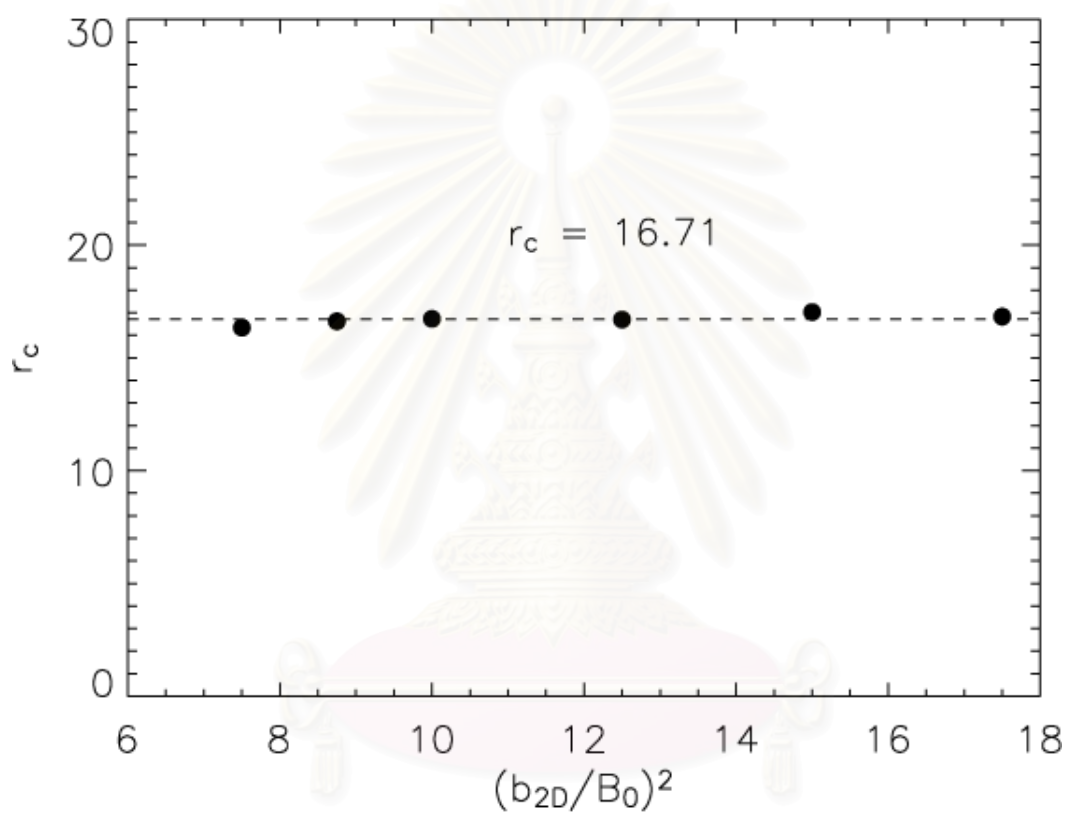


Figure 6.15: Critical radius  $r_c$  vs.  $b_{2D}^2/B_0^2$ . The dashed line is the average value.

สถาบันวิทยบริการ  
จุฬาลงกรณ์มหาวิทยาลัย



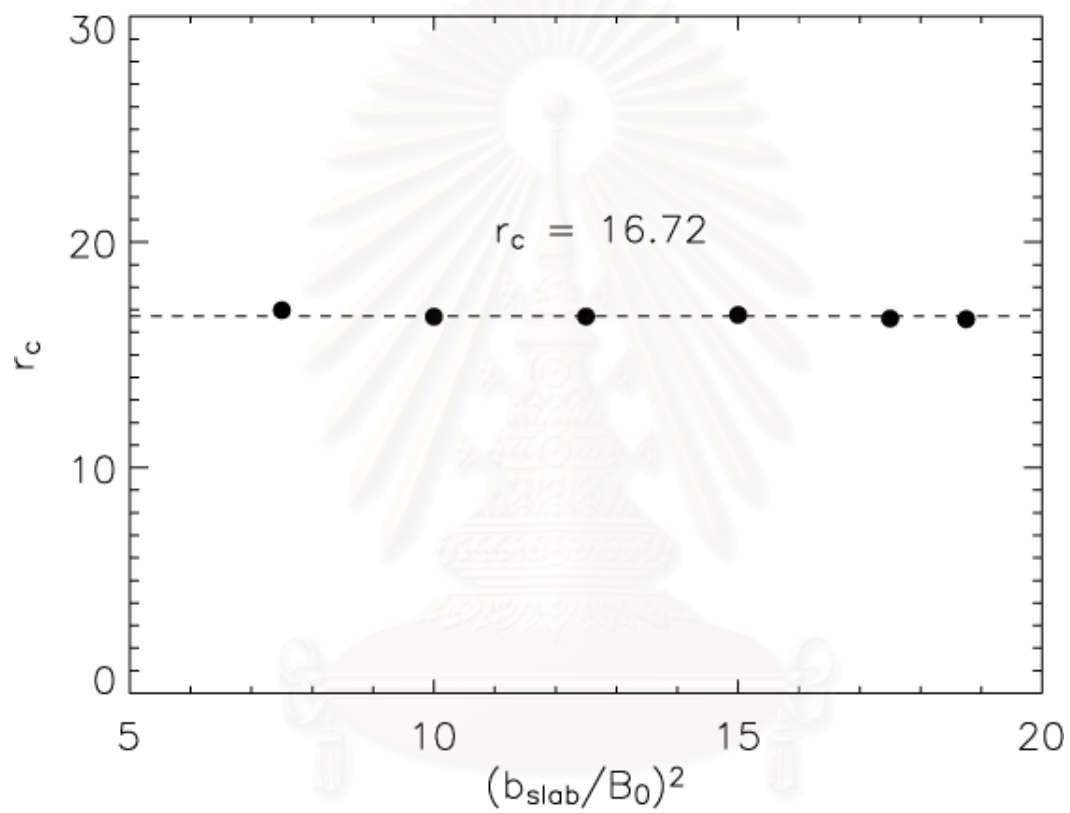


Figure 6.16: Critical radius  $r_c$  vs.  $b_{\text{slab}}^2/B_0^2$ . The dashed line is the average value.

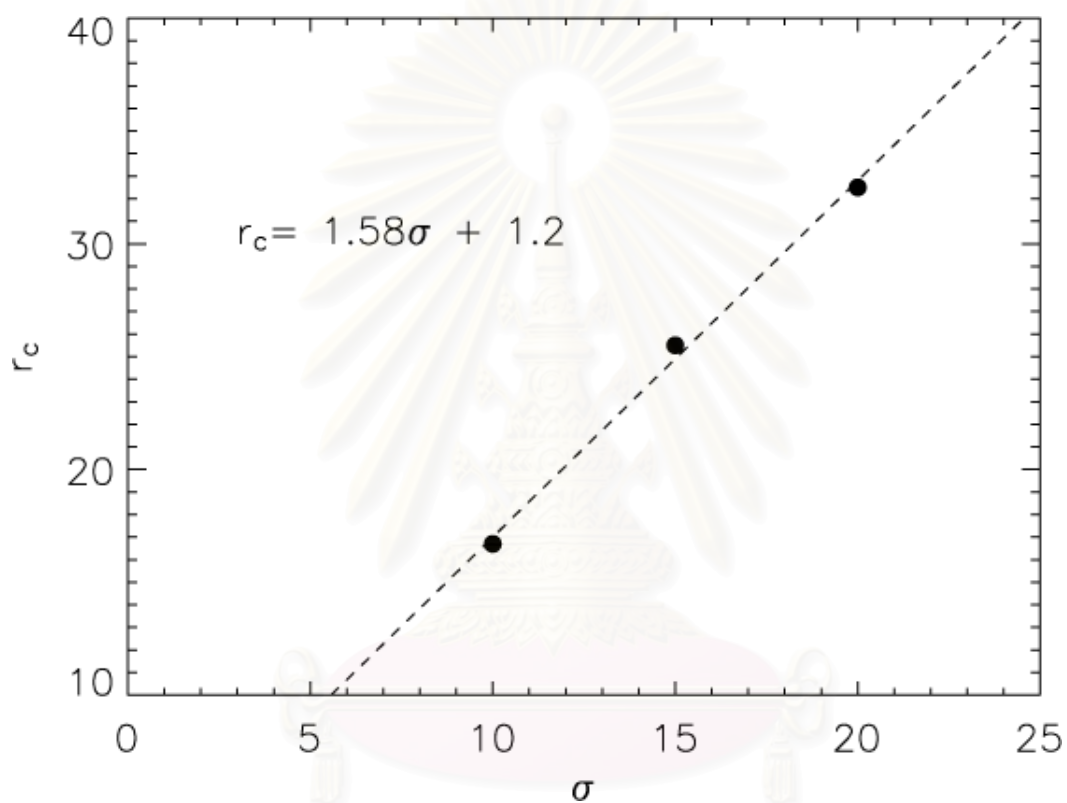


Figure 6.17: Critical radius  $r_c$  vs.  $\sigma$ . The dashed line is the best linear fit to the data.

สถาบันวิทยบริการ  
จุฬาลงกรณ์มหาวิทยาลัย

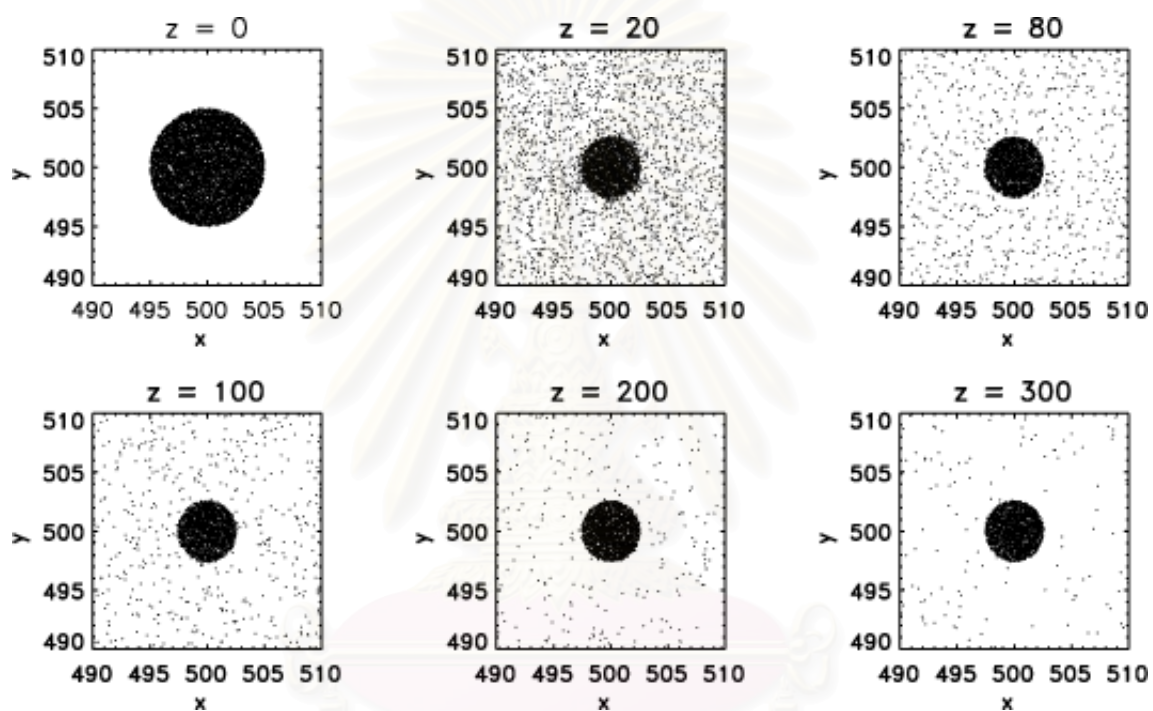


Figure 6.18: Snapshot of 10,000 field lines in Gaussian 2D field + slab turbulence at each  $z$ . Here we set  $\sigma = 1$  for the 2D field.

สถาบันวิทยบริการ  
จุฬาลงกรณ์มหาวิทยาลัย

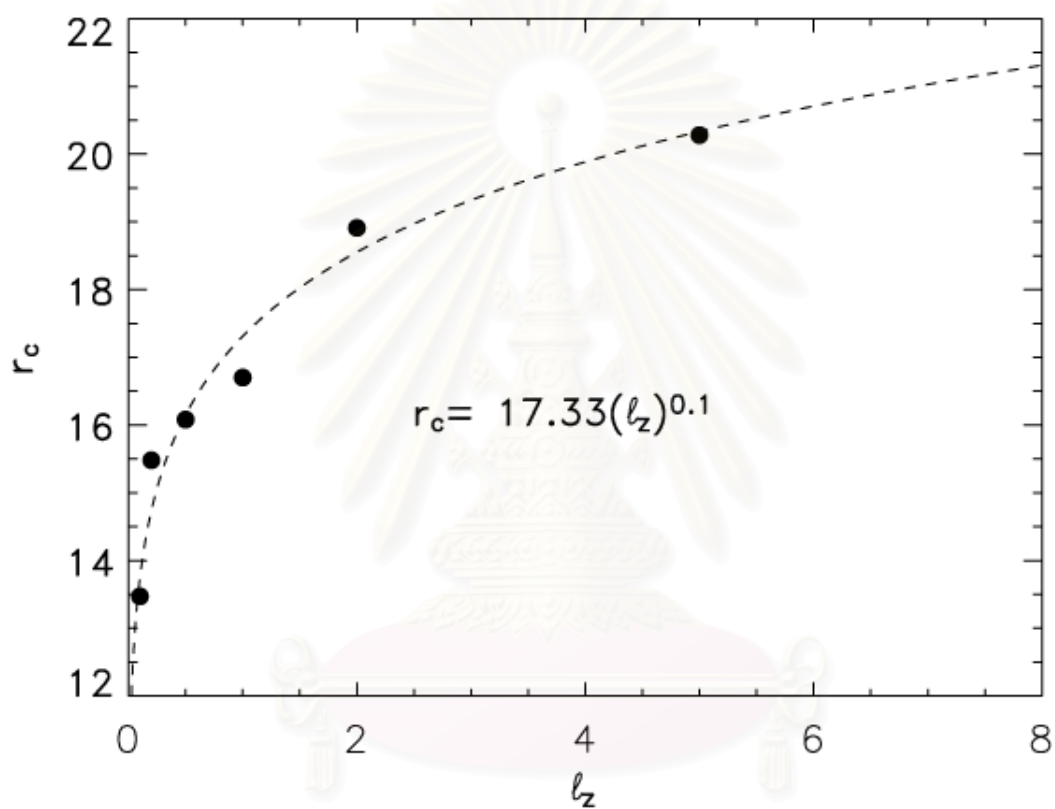


Figure 6.19: Critical radius  $r_c$  vs.  $l_z$ . The dashed line is the best power-law fit.

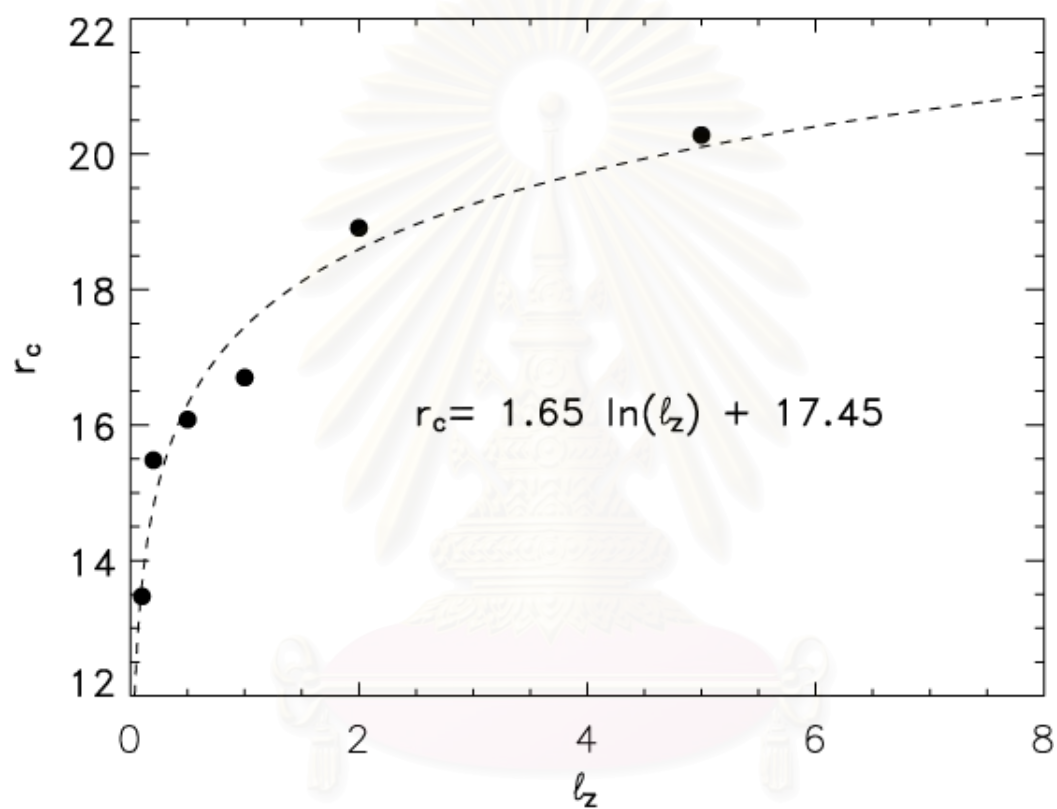


Figure 6.20: Critical radius  $r_c$  vs.  $l_z$ . The dashed line is the best logarithmic fit.

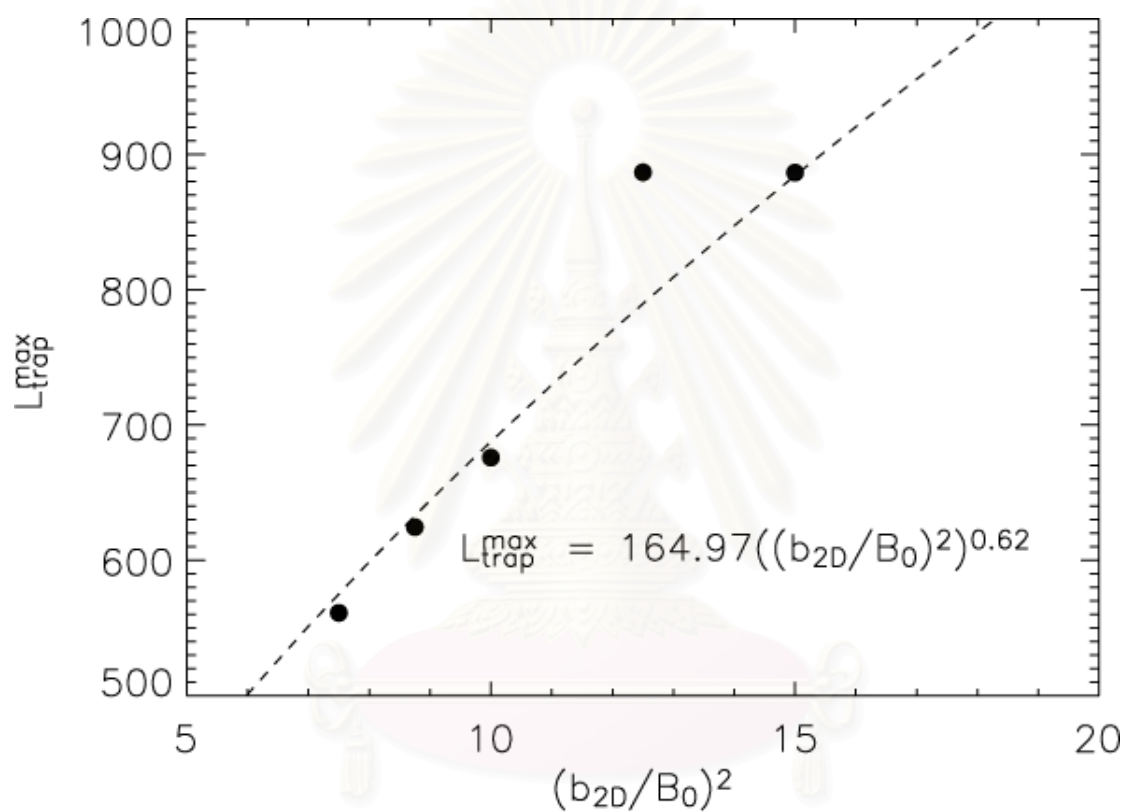


Figure 6.21:  $L_{trap}^{max}$  vs.  $b_{2D}^2/B_0^2$  and the best power-law fit.

สถาบันวิทยบริการ  
จุฬาลงกรณ์มหาวิทยาลัย

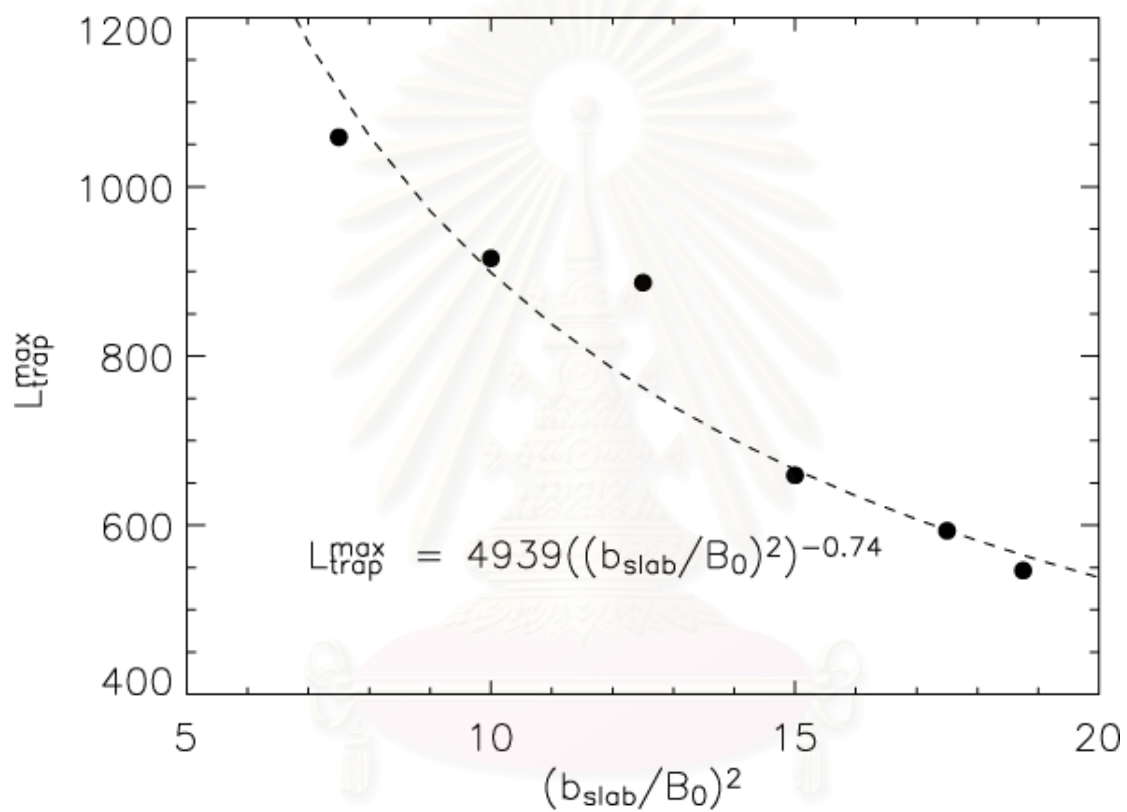


Figure 6.22:  $L_{trap}^{max}$  vs.  $b_{slab}^2/B_0^2$  and the best power-law fit.

สถาบันวิทยบริการ  
จุฬาลงกรณ์มหาวิทยาลัย

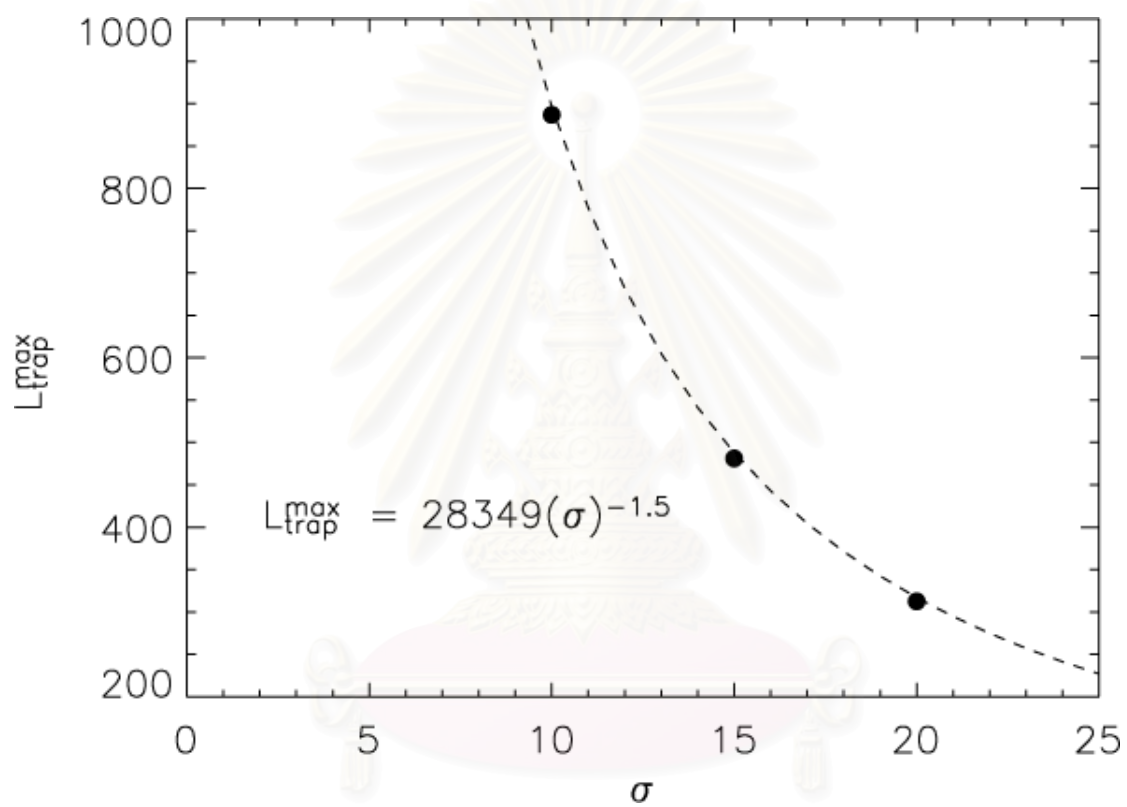


Figure 6.23:  $L_{\text{trap}}^{\text{max}}$  vs.  $\sigma$  and the best power-law fit.

สถาบันวิทยบริการ  
จุฬาลงกรณ์มหาวิทยาลัย



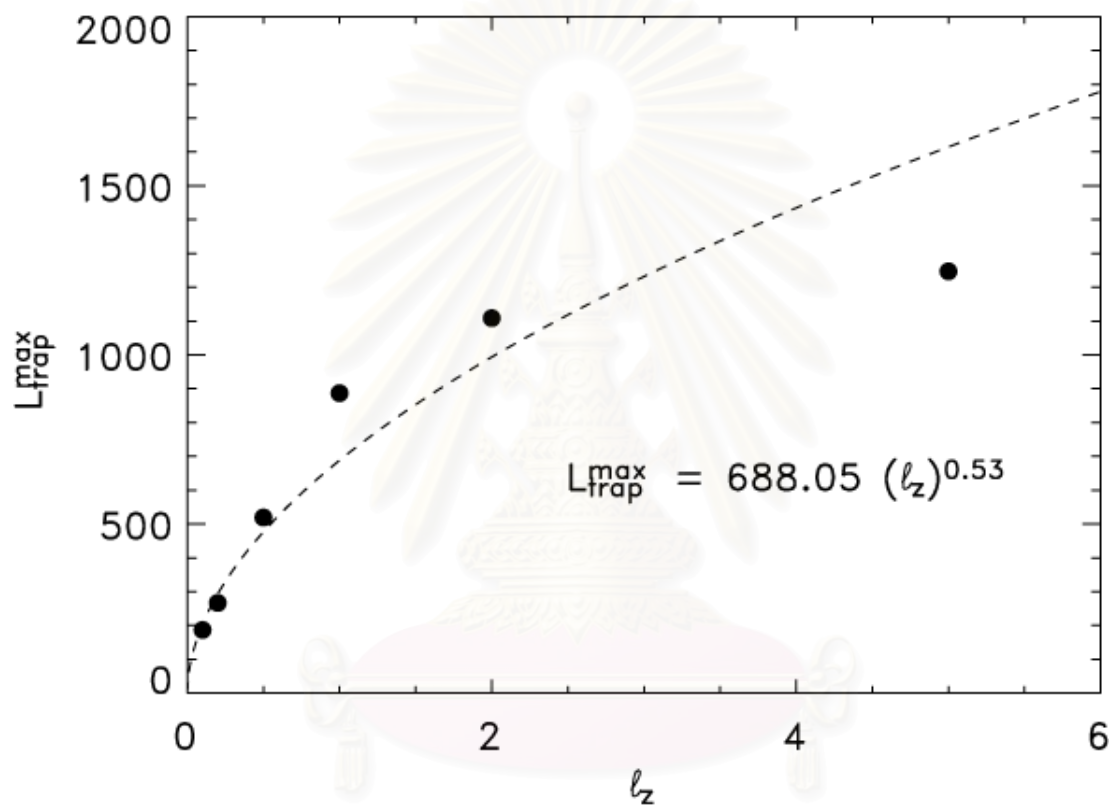


Figure 6.24:  $L_{trap}^{max}$  vs.  $l_z$  and the best power-law fit.

สถาบันวิทยบริการ  
จุฬาลงกรณ์มหาวิทยาลัย

Sun. We propose the idea of conditional statistics of the turbulent magnetic field lines in the two-component model to explain this contradiction. We assume that the trajectories of the magnetic field lines represent the motion of the guiding centers of the charged particles. The idea of the conditional statistics is that magnetic field lines which are initially located near the local O-points of the 2D islands are temporarily trapped and spread with a slower diffusion rate ( $\sim D_{slab}$ ) while the field lines starting near X-points rapidly diffuse like the two-dimensional turbulence ( $\sim D$ ). Thus, with these different rates of diffusion, we can estimate the range of the observation of dropouts from knowing the sizes of injection regions of SEPs and 2D islands. We confirm the idea by the numerical simulations. The simulation results show that the dropout feature occurs over intermediate distance scales and all magnetic field lines escape from 2D islands and undergo substantial lateral diffusion in the long distance limit.

In Section 6.3, we still consider a 2D+slab model but we instead use a systematic model for the 2D component, with contours of the potential function as circles, to study the diffusion of the field lines inside and outside the trapping boundary. The classical quasi-linear theory has been used for derivation of the diffusion coefficient of field lines in the radial direction. We found that the strong 2D field can suppress the field line random walk, with diffusion at a much slower rate than  $D_{slab}$ . When the field lines are far away from the 2D island, the diffusion approaches the slab rate. We again use numerical simulations to explore the behavior of the field lines for this simple case. The simulations show that the boundary of trapping is sharp and depends on the length scales of slab and 2D fields. Starting the field lines inside such boundary, the diffusion of the field lines systematically changes with a delay at the beginning due to the strong 2D field.

Furthermore, the simulations also confirm a quasilinear theory of suppression of diffusion when the field lines are deeply inside the 2D island. We expect that this study should also be relevant to a turbulent system as in Section 6.2. Finally, our study of suppression of field line random walk is also useful for other applications, such as any system that consists of a systematic flow in two dimensions that is superimposed on a random walk process.



สถาบันวิทยบริการ  
จุฬาลงกรณ์มหาวิทยาลัย

# Chapter 7

## Conclusions

We examine the magnetic field line random walk in the two-component model of magnetic turbulence, which is a useful description of the solar wind turbulence. The model includes a mean field in the  $z$  direction plus the transverse fluctuations, which are a mixture of 2D and slab turbulence. We worked on both theoretical and numerical analysis and also discussed the results with regard to relevant observations from spacecraft. The work is separated into three topics: the non-axisymmetric field line random walk, field line separation in axisymmetric turbulence, and the conditional statistics of turbulent field lines.

We have developed theoretical formulae for the field line random walk in non-axisymmetric turbulence and the field line separation in axisymmetric turbulence. Since the system is turbulent, ensemble averaged statistics have been considered. Our derivation is based on homogeneity, the diffusion approximation, and Corrsin's hypothesis. Our solutions are non-perturbative, which means we can apply the formulae to an arbitrary amplitude of the fluctuations. We confirm the theoretical derivation by the numerical simulations. We numerically solve the field line equation by a fourth-order Runge-Kutta method with adaptive step size control to trace the field line trajectories and then directly compute the statistics.

For the non-axisymmetric field line random walk we presented in Chapter 4, we explicitly make the parallel correlation length ( $\ell_c$ ) and slab fluctuations different in  $x$  and  $y$  components for anisotropic slab turbulence and, for 2D turbulence, we set the contours of constant power spectrum  $A(k_x, k_y)$  along ellipses in  $(k_x, k_y)$  space via a specific ellipticity parameter. We obtain the analytical

solution in the simple form of coupled bi-quadratic equations for the diffusion coefficients in  $x$  and  $y$  directions. We also show closed-form expressions for special cases. The simulations are performed for several cases to verify the theory. The results have good agreement with theory. That means the approximations we use for derivation of the theory work well for this problem. However, there are some cases having some difference (not more than 15%) between theoretical and numerical values, more than other cases, and this seems to be associated with the increase of the 2D energy.

For the field line separation in Chapter 5, although we consider the diffusion of the displacement between two adjacent field lines in axisymmetric turbulence, the diffusion coefficients we derived are anisotropic. We found that random field trajectories can separate in general through three regimes of the behavior of the running diffusion coefficient: slow diffusive separation at short distances, an intermediate regime of superdiffusion, and fast diffusive separation at large distances. The slow diffusion and onset of superdiffusion in the mean squared separation  $\langle \Delta X^2 + \Delta Y^2 \rangle$  can be identified as an exponential growth of the mean squared distance between two field lines. We confirm fast and slow diffusive regimes by the computer simulations. The exponential growth for the case that shows the slow diffusive separation can fit well with the expression from the theory.

In Chapter 6, we use the idea of the conditional statistics to explain the apparent contradiction between two sets of SEP observations from spacecraft. One set of observations shows that the intensity of particles repeatedly appears and reappears near the distance of 1 AU. However, in another set of observations, the SEPs seem to rapidly spread to the entire inner solar system within a few days.

In our work, we assume that the trajectories of the particles follow the magnetic field lines which are connected to the injection region at the Sun. The idea is that the magnetic field lines which are initially located near the O-points of 2D turbulence are temporarily trapped while the field lines near X-points rapidly diffuse to other locations. We support this idea by performing the numerical simulations. The simulation results show the dropout features over intermediate distance and, at long distance, all magnetic field lines escape from the 2D islands and undergo substantial lateral diffusion. Furthermore, we study the trapping and escape of field lines due to the 2D field by setting a simple model for the magnetic field. That is the 2D potential function as a Gaussian 2D field plus the slab turbulence. We derive a quasi-linear theory in order to obtain the analytical expression for the diffusion coefficient in the radial component. We found that the strong 2D field can suppress the random walk of field lines. The field lines located deep inside the 2D island spread at a slower rate than the field lines located outside the island, for which the diffusion approaches the slab rate.

Our research leads to many open questions for future work and is useful to explain physical phenomena in space and related problems. Here are some examples. For the non-axisymmetric work, we can apply the theory to solar modulation of galactic cosmic rays and perform the simulations for charged particles in non-axisymmetric turbulence. In the field line separation work, we can continue developing more theoretical techniques for the superdiffusive regime and confirm them by simulations. For conditional statistics work, we can study the suppression in general, when both 2D and slab are turbulent, and also study this directly by the simulations of charged particles in 2D+slab turbulence in spherical coordinates which is closer to the real situation in the heliosphere. Our study

can apply to other situations such as any flows that have patterns similar to a 2D flow and slab turbulence.



สถาบันวิทยบริการ  
จุฬาลงกรณ์มหาวิทยาลัย

# References

- Barge, P., Millet, J., and Pellat, R. Importance of transverse diffusion for cosmic-ray propagation, *Astrophys. J.* **284** (1984): 817-826.
- Barghouty, A. F. and Jokipii, J. R. Turbulent diffusion of magnetic field lines in astrophysical plasmas, *Astrophys. J.* **470** (1996): 858-863.
- Batchelor, G. K. *The theory of homogeneous turbulence* Cambridge: Cambridge University Press, 1953.
- Bieber, J. W., Matthaeus, W. H., Smith, C. W., Wanner, W., Kallenrode, M.-B., and Wibberenz, G. Proton and electron mean free paths: The Palmer consensus revisited, *Astrophys. J.* **420** (1994): 294-306.
- Bieber, J. W., Wanner, W., and Matthaeus, W. H. Dominant two-dimensional solar wind turbulence with implications for cosmic ray transport, *J. Geophys. Res.* **101** (1996): 2511-2522.
- Burger, R. A. and Hattingh, M. Toward a realistic diffusion tensor for galactic cosmic rays, *Astrophys. J.* **505** (1998): 244-251.
- Cane, H. V. and Erickson, W. C. Energetic particle propagation in the inner heliosphere as deduced from low-frequency (<100 kHz) observations of type III radio bursts, *J. Geophys. Res.* **108(A5)** (2003): SSH 8-1.
- Cane, H. V., Richardson, I. G., von Rosenvinge, T. T., and Wibberenz, G. Cosmic ray decreases and shock structure: A multispacecraft study, *J. Geophys. Res.* **99** (1994): 21429-21441.
- Cane, H. V., Wibberenz, G., Richardson, I. G., and von Rosenvinge, T. T. Cosmic ray modulation and the solar magnetic field, *Geophys. Res. Lett.* **26** (1999): 565-568.



- Chandran, B. D. G. Confinement and isotropization of galactic cosmic rays by molecular-cloud magnetic mirrors when turbulent scattering is weak, *Astrophys. J.* **529** (2000): 513-535.
- Corrsin, S. in *Advance in Geophysics, Volume 6: Atmospheric diffusion and air pollution* ed. F. Frenkel and P. Sheppard, New York: Academic Press, 1959.
- Gradshteyn, I. S. and Ryzhik, I. M. *Tables of Integrals, Series and Products* New York: Academic Press, 1980.
- Dröge, W. Particle scattering by magnetic fields, *Space Sci. Rev.* **93** (2000): 121-151.
- Dröge, W., Wibberenz, G., and Klecker, B. A dual spacecraft study of the injection and propagation of energetic particles following the 7 June 1980 gamma ray flares, *Proc. 21st Int. Cosmic Ray Conf. (Adelaide)* **5** (1990): 187.
- Erdős, G., Balogh, A., and Kóta, J. Separation rate of the magnetic field lines observed by ULYSSES at high latitude, *Adv. Space Res.* **19** (1997): 843-846.
- Evenson, P., Meyer, P., and Yanagita, S. Solar flare shocks in interplanetary space and solar flare particle events, *J. Geophys. Res.* **87** (1982): 625-631.
- Fisk, L. A. Motion of the footpoints of heliospheric magnetic field lines at the Sun: Implications for recurrent energetic particle events at high heliographic latitudes, *J. Geophys. Res.* **101** (1996): 15547-15554.
- Giacalone, J., Jokipii, J. R., and Mazur, J. E. Small-scale gradients and large-scale diffusion of charged particles in the heliospheric magnetic field, *Astrophys. J. Lett.* **532** (2000): L75-L78.
- Goldreich, P. and Sridhar, S. Magnetohydrodynamic turbulence revisited, *Astrophys. J.* **485** (1997): 680-688.
- Gray, P. C., Pontius, D. H., Jr., and Matthaeus, W. H. Scaling of field-line random walk in model solar wind fluctuations, *Geophys. Res. Lett.* **23** (1996): 965-968.

- Isichenko, M. B. Effective plasma heat conductivity in ‘braided’ magnetic field-I. Quasi-linear limit, Plasma Phys. Controlled Fusion **33** (1991a): 795-807.
- Isichenko, M. B. Effective plasma heat conductivity in ‘braided’ magnetic field-II. Percolation limit, Plasma Phys. Controlled Fusion **33** (1991b): 809-826.
- Jokipii, J. R. Cosmic-ray propagation. I. Charged particles in random magnetic field, Astrophys. J. **146** (1966): 480-487.
- Jokipii, J. R. The rate of separation of magnetic lines of force in a random magnetic field, Astrophys. J. **183** (1973): 1029-1036.
- Jokipii, J. R. Rate of energy gain and maximum energy in diffusive shock acceleration, Astrophys. J. **313** (1987): 842-846.
- Jokipii, J. R. and Coleman, P. J. Cosmic-ray diffusion tensor and its variation observed with Mariner 4, J. Geophys. Res. **73** (1968): 5495.
- Jokipii, J. R., Kóta, J., and Giacalone, J. Perpendicular transport in 1- and 2-dimensional shock simulations, Geophys. Res. Lett. **20** (1993): 1759-1761.
- Jokipii, J. R., Kóta, J., Giacalone, J., Horbury, T. S., and Smith, E. J. Interpretation and consequences of large-scale magnetic variances observed at high heliographic latitude, Geophys. Res. Lett. **22** (1995): 3385-3388.
- Jokipii, J. R. and Parker, E. N. Random walk of magnetic lines of force in astrophysics, Phys. Rev. Lett. **183** (1968): 44-47.
- Jones, F. C., Jokipii, J. R., and Baring, M. G. Charged-particle motion in electromagnetic fields having at least one ignorable spatial coordinate, Astrophys. J. **509** (1998): 238-243.
- Kadomtsev, B. B. and Pogutse, O. P. Electron heat conductivity of the plasma across a ‘braided’ magnetic field, in Plasma physics and controlled nuclear fusion research, Proc. 7th Int. Conf. (Vienna: IAEA) **1** (1979): 649-662.
- Kirk, J. G., Duffy, P., and Gallant, Y. A. Stochastic particle acceleration at shocks in the presence of braided magnetic fields, Astron. Astrophys. **314** (1996): 1010-1016.

- Kolmogorov, A. N. The local structure of turbulence in incompressible viscous fluids for very large Reynolds numbers, Dokl. Akad. Nauk SSSR **30** (1941b): 299-303.
- Kóta, J. and Jokipii, J. R. Corotating variations of cosmic rays near the south heliospheric pole, Science **268** (1995): 1024-1025.
- Kunow, H., Dröge, W., Heber, B., Müller-Mellin, R., Röhrs, K., Sierks, H., Wibberenz, G., Ducros, R., Ferrando, P., Rastoin, C., Raviart, A., and Paizis, C. High energy cosmic ray nuclei results on Ulysses: 2. Effects of a recurrent high speed stream from the southern coronal hole, Space Sci. Rev. **72** (1995): 397-402.
- Lithwick, Y. and Goldreich, P. Compressible magnetohydrodynamic turbulence in interstellar plasmas, Astrophys. J. **562** (2001): 279-296.
- Maron, J., Chandran, B. D. G., and Blackman, E. Divergence of neighboring magnetic-field lines and fast-particle diffusion in strong magnetohydrodynamic turbulence, with application to thermal conduction in galaxy clusters, Phys. Rev. Lett. **92** (2004): 045001.
- Matthaeus, W. H., Goldstein, M. L., and Roberts, D. A. Evidence for the presence of quasi-two-dimensional nearly incompressible fluctuations in the solar wind, J. Geophys. Res. **95** (1990): 20673-20683.
- Matthaeus, W. H., Gray, P. C., Pontius, D. H., Jr., and Bieber, J. W. Spatial structure and field-line diffusion in transverse magnetic turbulence, Phys. Rev. Lett. **75** (1995): 2136-2139.
- Matthaeus, W. H., Qin, G., Bieber, J. W., and Zank, G. P. Nonlinear collisionless perpendicular diffusion of charged particles, Astrophys. J. Lett. **590** (2003): L53-L56.
- Matthaeus, W. H., Smith, C. W., and Bieber, J. W. Correlation lengths, the ultra-scale, and the spatial structure of interplanetary turbulence, in AIP Conf. Proc. Solar Wind Nine **471** (1999): 511-514.

- Mazur, J. E., Mason, G. M., Dwyer, J. R., Giacalone, J., Jokipii, J. R., and Stone, E. C. Interplanetary magnetic field line mixing deduced from impulsive solar flare particles, *Astrophys. J. Lett.* **532** (2000): L79-L82.
- McComas, D. J., Bame, S. J., Barraclough, B. L., Feldman, W. C., Funsten, H. O., Gosling, J. T., Riley, P., Skoug, R., Balogh, A., Forsyth, R., Goldstein, B. E., and Neugebauer, M. Ulysses' return to the slow solar wind, *Geophys. Res. Lett.* **25** (1998): 1-4.
- McComas, D. J., Elliott, H. A., Gosling, J. T., Reisenfeld, D. B., Skoug, R. M., Goldstein, B. E., Neugebauer, M., and Balogh, A. Ulysses' second fast-latitude scan: Complexity near solar maximum and the reformation of polar coronal holes, *Geophys. Res. Lett.* **29** (2002): 1-4
- McComb, W. D. *The physics of fluid turbulence* Oxford: Clarendon, 1990.
- McKibben, R. B., Connell, J. J., Lopate, C., Zhang, M., Balogh, A., Dalla, S., Marsden, R. G., Sanderson, T. R., Tranquille, C., Anglin, J. D., Kunow, H., Müller-Mellin, R., Heber, B., Raviart, A., and Paizis, C. ULYSSES COSPIN observations of the energy and charge dependence of propagation of solar energetic particles to the Sun's south polar regions, *Proc. 27th Int. Cosmic Ray Conf. (Hamburg)* **8** (2001): 3281-3284.
- McKibben, R. B., Simpson, J. A., Zhang, M., Bame, S., and Balogh, A. ULYSSES out-of-ecliptic observations of "27-day" variations in high energy cosmic ray intensity *Space Sci. Rev.* **72** (1995): 403-408.
- Moraal, H. Observations of the eleven-year cosmic-ray modulation cycle, *Space Sci. Rev.* **19** (1976): 845-920.
- Palmer, I. D. Transport coefficients of low-energy cosmic rays in interplanetary space, *Rev. Geophys. Space Phys.* **20** (1982): 335-351.
- Parker, E. N. Dynamics of the interplanetary gas and magnetic fields, *Astrophys. J.* **128** (1958): 664-676.

- Parker, E. N. Interplanetary dynamical processes New York: Wiley-Interscience, 1963.
- Parker, E. N. The passage of energetic charged particles through interplanetary space, Planet. Space Sci. **13** (1965): 9-49.
- National Research Council (NRC) Plasma physics of the local cosmos National Academies Press, 2004.
- Press, W. H., Teukolsky, S. A., Vetterling, W. T., and Flannery, B. P. Numerical recipes in FORTRAN: The art of scientific computing Cambridge: Cambridge University Press, 1992.
- Rax, J. M. and White, R. B. Effective diffusion and nonlocal heat transport in a stochastic magnetic field, Phys. Rev. Lett. **68** (1992): 1523-1526.
- Reames, D. V. Acceleration of energetic particles by shock waves from large solar flares, Astrophys. J. Lett. **358** (1990): L63-L67.
- Reames, D. V., Cane, H. V., and von Rosenvinge, T. T. Energetic particle abundances in solar electron events, Astrophys. J. **357** (1990): 259-270.
- Rechester, A. B. and Rosenbluth, M. N. Electron heat transport in a Tokamak with destroyed magnetic surfaces, Phys. Rev. Lett. **40** (1978): 38-41.
- Reid, G. C. A Diffusive model for the initial phase of a solar proton event, J. Geophys. Res. **69** (1964): 2659-2667.
- Reinecke, J. P. L., McDonald, F. B., and Moraal, H. Cosmic radiation in the heliosphere at successive solar minima 5. Modulation of anomalous cosmic ray helium during the three consecutive solar minimum periods of 1977/1978, 1987, and 1997, J. Geophys. Res. **105** (2000): 27439-27446.
- Richardson, L. F. Water prediction by numerical process Cambridge: Cambridge University Press, 1922.
- Ruffolo, D., Matthaeus, W. H., and Chuychai, P. Trapping of solar energetic particles by the small-scale topology of solar wind turbulence, Astrophys. J. Lett. **597** (2003): L169-L172.

- Ruffolo, D., Matthaeus, W. H., and Chuychai, P. Separation of magnetic field lines in two-component turbulence, *Astrophys. J.* **614** (2004): 420-434.
- Sagdeev, R. Z., Usikov, D. A., and Zaslavsky, G. M. *Nonlinear physics: From the pendulum to turbulence and chaos* Chur: Harwood, 1988.
- Salu, Y. and Montgomery, D. Turbulent diffusion from a quasi-kinematical point of view, *Phys. Fluids* **20** (1977): 1-3.
- Sanderson, T. R., Erdös, G., Balogh, A., Forsyth, R. J., Marsden, R. G., Gosling, J. T., Phillips, J. L., and Tranquille, C. Effect of magnetic discontinuities on the propagation of energetic particles: Ulysses observations of the onset of the March 1991 solar particle event, *J. Geophys. Res.* **105** (2000): 18275-18284.
- Sanderson, T. R., Marsden, R. G., Wenzel, K.-P., Balogh, A., Forsyth, R. J., and Goldstein, B. E. High-latitude observations of energetic ions during the first ULYSSES polar pass, *Space Sci. Rev.* **72** (1995): 291-296.
- Scholer, M. and Morfill, G. Simulation of solar flare particle interaction with interplanetary shock waves, *Sol. Phys.* **45** (1975): 227-240.
- Similon, P. L. and Sudan, R. N. Energy dissipation of Alfvén wave packets deformed by irregular magnetic fields in solar-coronal arches, *Astrophys. J.* **336** (1989): 442-453.
- Simnett, G. M., Sayle, K. A., Tappin, S. J., and Roelof, E. C. Co-rotating particle enhancements out of the ecliptic plane, *Space Sci. Rev.* **72** (1995): 327-330.
- Simpson, J. A., Anglin, J. D., Bothmer, V., Connell, J. J., Ferrando, P., Heber, B., Kunow, H., Lopate, C., Marsden, R. G., McKibben, R. B., Müller-Mellin, R., Paizis, C., Rastoin, C., Raviart, A., Sanderson, T. R., Sierks, H., Trattner, K. J., Wenzel, K.-P., Wibberenz, G., and Zhang, M. Cosmic ray and solar particle investigations over the south polar regions of the Sun, *Science* **268** (1995): 1019-1023.

Zimbardo, G., Veltri, P., and Malara, F. Diffusion coefficient and Kolmogorov entropy of magnetic field lines, J. Plasma Phys. **32** (1984): 141-158.



สถาบันวิทยบริการ  
จุฬาลงกรณ์มหาวิทยาลัย



## Appendices

สถาบันวิทยบริการ  
จุฬาลงกรณ์มหาวิทยาลัย



# Appendix A

## Test of Accuracy of Streamline Code for Constant + Slab Fields

The “streamline” code is written by using parallel programming with MPI for solving the equations of field lines and the equations of motion for charged particles in magnetic and electric fields. The numerical method that we use to solve the differential equations in the code is a fourth-order Runge-Kutta method with adaptive step size control (Press et al. 1992). The advantage of this method is that users can control the level of accuracy of the results. The input parameter related to the desired accuracy is named “*racc.*”

To test the accuracy of the code, we choose 3 cases for charged particles moving in magnetic and electric field. These are

- **Case 1:** The particles in a uniform magnetic field.
- **Case 2:** The particles in a uniform magnetic field and uniform electric field.
- **Case 3:** The particles in a slab magnetic field.

From Cases 1 and 2, we already know the exact solution. Therefore we can directly compare the energy of the particles which we get from numerical simulations with the value from theory. For the slab field case, we know that particles moving in a magnetic field always conserve their kinetic energy. Then, in this case, we compare the energy of particles with the energy at  $t = 0$ .

## A.1 The equation of motion and analytical solutions

The equation of motion of a charged particle in magnetic and electric fields is

$$\frac{d^2\vec{v}}{dt^2} = \frac{q}{m}(\vec{v} \times \vec{B} + \vec{E}) \quad (\text{A.1})$$

Since we use the numerical method to solve this equation, we reduce the second order ODE to a set of first order ODEs and write it for each component.

Therefore, equation (A.1) becomes

$$\frac{dx}{dt} = v_x \quad (\text{A.2})$$

$$\frac{dy}{dt} = v_y \quad (\text{A.3})$$

$$\frac{dz}{dt} = v_z \quad (\text{A.4})$$

$$\frac{dv_x}{dt} = \frac{q}{m}(v_y B_z - v_z B_y + E_x) \quad (\text{A.5})$$

$$\frac{dv_y}{dt} = \frac{q}{m}(v_z B_x - v_x B_z + E_y) \quad (\text{A.6})$$

$$\frac{dv_z}{dt} = \frac{q}{m}(v_x B_y - v_y B_x + E_z). \quad (\text{A.7})$$

Next, we will consider the analytic solution and characteristics of the particles in the field of each case that we use for testing.

### Case 1: Particles in a Uniform Magnetic Field

The magnetic field is

$$\vec{B} = B_0 \hat{z} \quad (\text{A.8})$$

where  $B_0$  is constant. The analytic solution of this problem is

$$v_x(t) = v_{x0} \cos \Omega t + v_{y0} \sin \Omega t \quad (\text{A.9})$$

$$v_y(t) = v_{y0} \cos \Omega t - v_{x0} \sin \Omega t \quad (\text{A.10})$$

$$v_z(t) = v_{z0}, \quad (\text{A.11})$$

where  $\Omega = mv/qB$  and  $v_{x0}$ ,  $v_{y0}$ , and  $v_{z0}$  are the initial velocities in  $x$ ,  $y$ , and  $z$ , respectively. For this case, the particles move around a magnetic field line as a circle in  $x$ - $y$  the plane with constant pitch angle and constant velocity in the  $z$  direction. The total energy is conserved and equal to  $\frac{1}{2}m(v_{x0}^2 + v_{y0}^2 + v_{z0}^2)$ .

### Case 2: Particles in a Uniform Magnetic Field and Electric Field

We set the fields in the form

$$\vec{B} = B_0 \hat{z} \quad \text{and} \quad \vec{E} = E_0 \hat{x}, \quad (\text{A.12})$$

where  $B_0$  and  $E_0$  are constant. The analytic solution of this problem is

$$v_x(t) = v_{x0} \cos \Omega t + \left( v_{y0} + \frac{E_0}{B_0} \right) \sin \Omega t \quad (\text{A.13})$$

$$v_y(t) = \left( v_{y0} + \frac{E_0}{B_0} \right) \cos \Omega t - v_{x0} \sin \Omega t - \frac{E_0}{B_0} \quad (\text{A.14})$$

$$v_z(t) = v_{z0}. \quad (\text{A.15})$$

Since an electric field is present in the  $x$  direction in this case, the particles drift in the  $y$  direction. The trajectories of particles have a cycloidal shape. From the analytic solution, we can see that the energy in this case is not constant as in the first case. The energy oscillates.

### Case 3: Particles in a Slab Magnetic Field

A slab magnetic field can be written as

$$\vec{B} = B_0 \hat{z} + \delta b_x(z) \hat{x} + \delta b_y(z) \hat{y}. \quad (\text{A.16})$$

Because the magnetic field is random, we cannot derive the analytical solution for this case. However, we know that a static magnetic field does no work on a charged particle in a magnetic field, so the energy will be conserved. Therefore, we can compare the energy for each time with the initial energy. Since the particles have to conserve  $v_x^2 + v_y^2 + v_z^2$ , only the pitch angle is scattered, and not the magnitude of the velocity.

## A.2 Relative Error

We define the relative error as

$$\text{Relative Error} = \frac{|v_{\text{num}}^2 - v_{\text{th}}^2|}{v_{\text{th}}^2}, \quad (\text{A.17})$$

where  $v_{\text{th}}$  is the magnitude of velocity from theory for Cases 1 and 2 and is equal to the magnitude of initial velocity for Case 3 and  $v_{\text{num}}$  is the magnitude of the velocity from numerical results.

## A.3 Results and Discussion

We test 10 particles with random initial points and the initial velocities in each case are  $v_{x0} = 10$ ,  $v_{y0} = 0$ , and  $v_{z0} = 0$ . Since we put 10 particles in the program,  $v_{\text{num}}$  in (A.17) is the average velocity for 10 particles.

For Case 1, the particles moving in a uniform magnetic field, we have the results at various  $racc$  as shown in Figure A.1. The relative error increases linearly in a log-log scale with the slope=1.

For the second case, the particles moving in uniform magnetic field and electric field, we also have the results at various  $racc$  as shown in Figure A.2. In this case the accuracy oscillates a little bit and, for  $racc = 10^{-16}$ , we can see

round-off effects. In Figure A.3, we overlay Figures A.1 and A.2. This shows that the error grows with the same slope in both cases.

However, the relative error increases linearly at only the beginning. When we increase the running time or decrease  $racc$  as in Figure A.4, the error increases exponentially.

For particles moving in a slab field, the results surprise us since the accuracy in this case is better than in the first two cases at the same  $racc$  as shown in Figures A.5-A.9. In Figure A.10, we plot the relative error at  $t = 1000$  gyroperiods with various  $\delta b/B_0$ .

From the accuracy tests we can see that the relative error depends on the parameter  $racc$  and increases linearly at the beginning. At  $10^5$  gyroperiods, for  $racc=10^{-9}$ , we get a relative error of order  $10^{-4}$  for Cases 1 and 2. Surprisingly, for particles moving in a slab field, the relative errors are lower than in the first two cases although the system has more complexity. Therefore, when we perform the simulations, we usually set  $racc$  lower than  $10^{-9}$ . The increased error depends on how long we trace the particles or how far we trace the field lines.

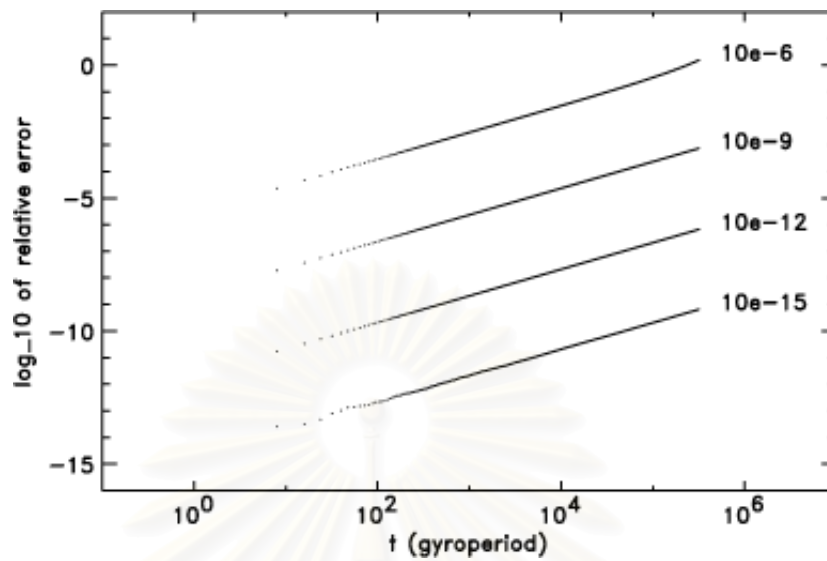


Figure A.1: Accuracy of particle orbits in a uniform magnetic field at various *racc*.

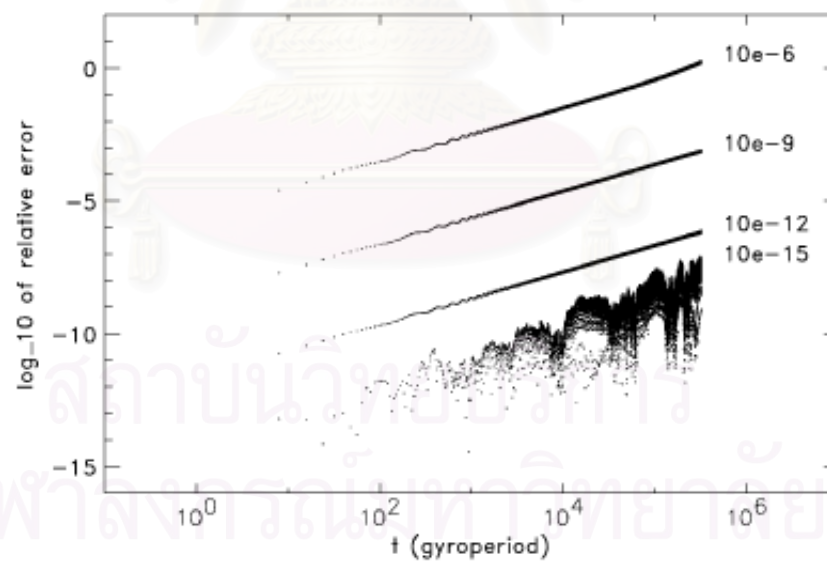


Figure A.2: Accuracy of particle orbits in a uniform magnetic and electric fields at various *racc*.

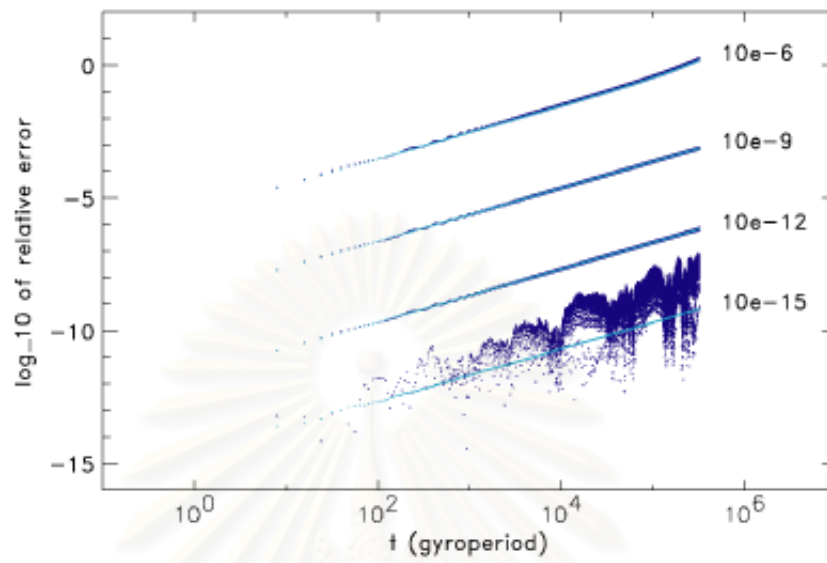


Figure A.3: Overlay of Figures A.1 (black) and A.2 (gray).

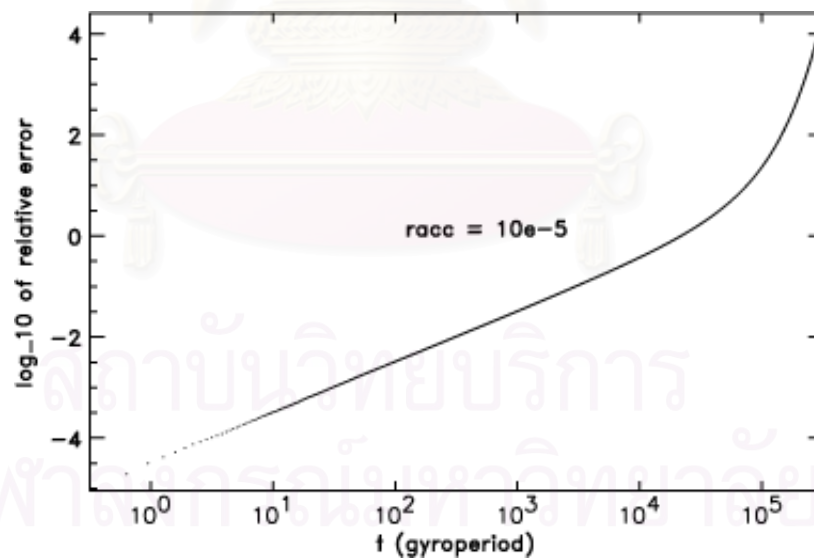


Figure A.4: Accuracy of particle orbits in a uniform magnetic field when we use  $racc = 10^{-5}$ .

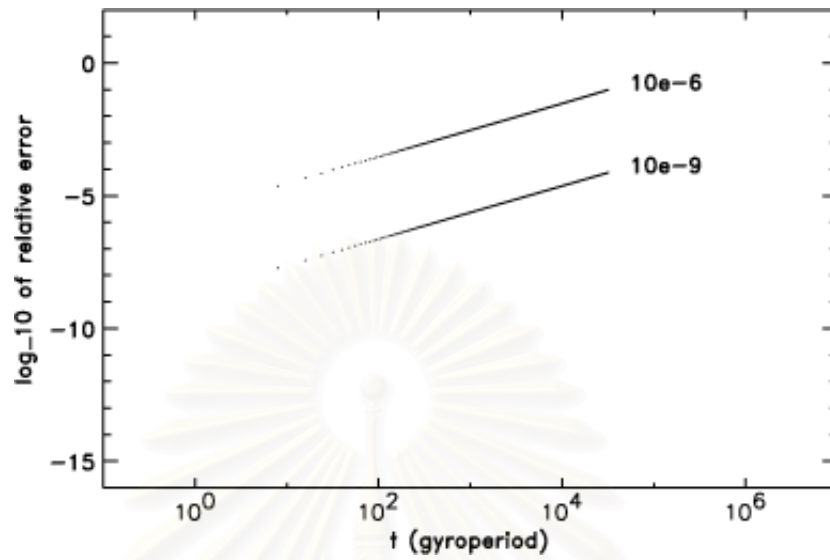


Figure A.5: Accuracy of particle orbits in a slab magnetic field with  $\delta b/B_0 = 0$ .

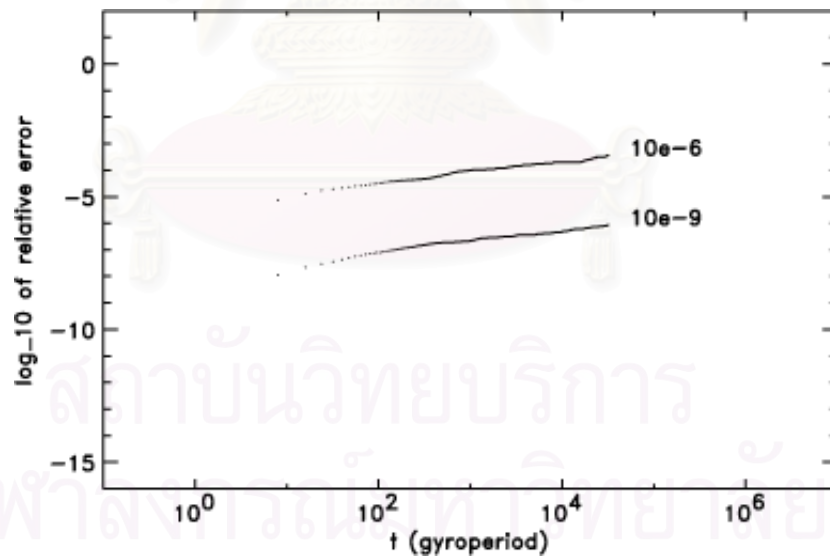


Figure A.6: Accuracy of particle orbits in a slab magnetic field with  $\delta b/B_0 = 0.001$ .



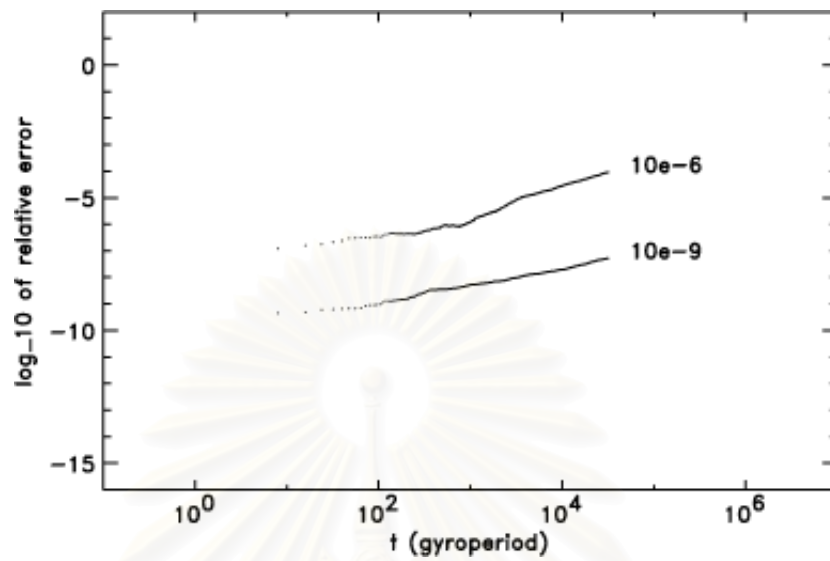


Figure A.7: Accuracy of particle orbits in a slab magnetic field with  $\delta b/B_0 = 0.01$ .

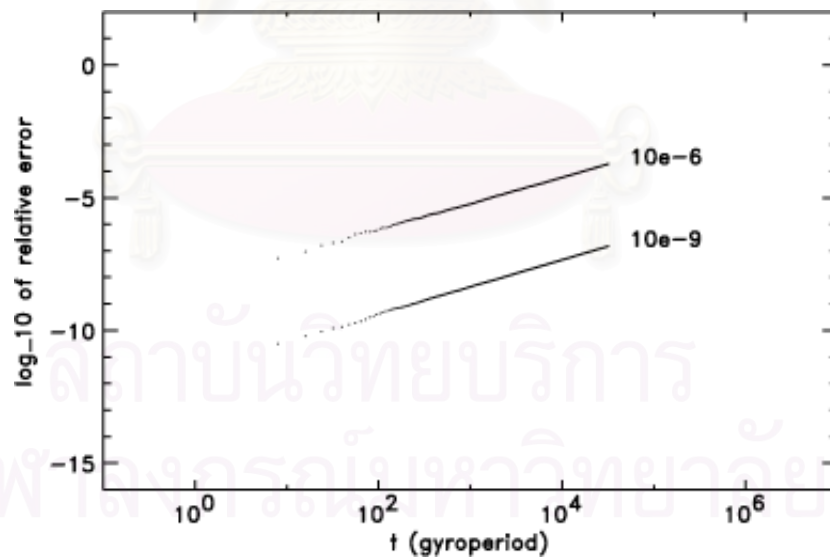


Figure A.8: Accuracy of particle orbits in a slab magnetic field with  $\delta b/B_0 = 0.1$ .

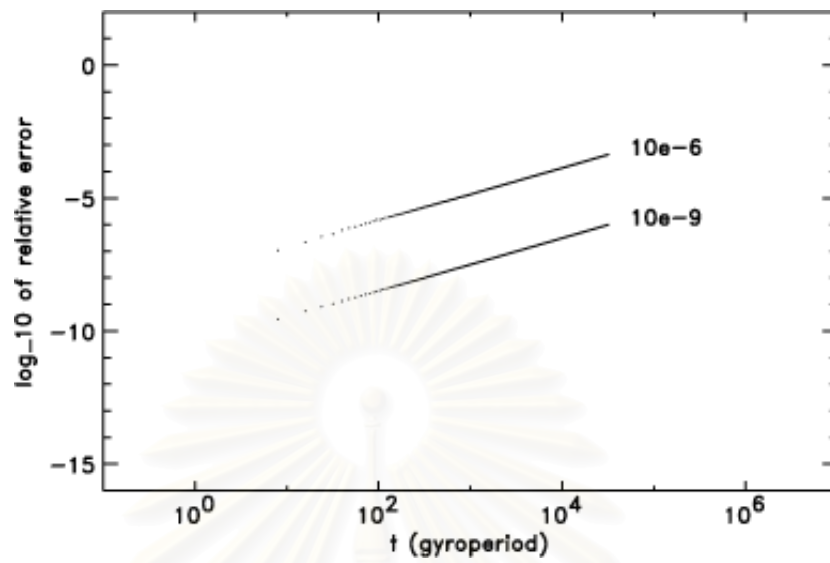


Figure A.9: Accuracy of particle orbits in a slab magnetic field with  $\delta b/B_0 = 1.0$ .

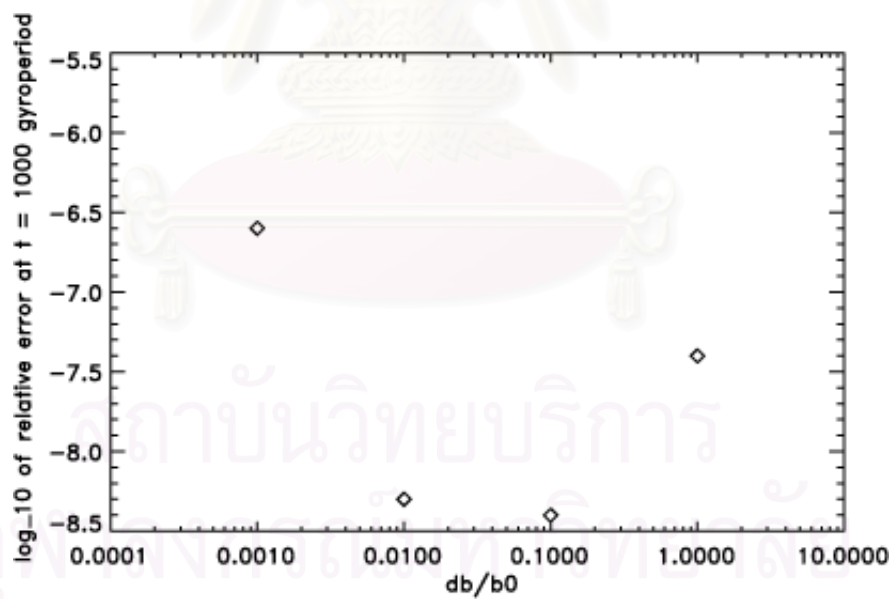


Figure A.10: Accuracy of particle orbits in a slab magnetic field at  $t = 10^3$  gyroperiods and various  $\delta b/B_0$ .

# Appendix B

## Numerical Evaluation of Analytic Expressions for Field Line Separation

The present work yields somewhat complicated analytic expressions for the separation between two magnetic field lines in two-component turbulence (Section 5.2), which are interpreted in Section 5.3. We found it useful to verify that interpretation by numerically evaluating the integrals in equations (2.66), (2.67), (5.15), and (5.16) with the Mathematica program (Wolfram Research, Inc.) for some special cases. Those results, plotted in Figures 5.4 and 5.5, are found to agree with the interpretation of the analytic expressions in Section 5.3. In contrast, the comparison in Figures 5.6 and 5.8 with numerical simulations, which do not incorporate the analytic theory in any way, is an independent test of the validity of the analytic theory itself and its underlying assumptions.

For the numerical evaluation of analytic expressions, the following power spectra were used:

$$P_{xx}^{slab}(k_z) = P_{yy}^{slab}(k_z) \propto \frac{1}{(1 + k_z^2/k_{0z}^2)^{5/6}} \quad (\text{B.1})$$

$$A(k_\perp) \propto \frac{1}{(1 + k_\perp^2/k_{0\perp}^2)^{7/3}}. \quad (\text{B.2})$$

These forms roll off to a constant at low  $k$ , and far above  $k_{0z}$  or  $k_{0\perp}$  they follow a Kolmogorov law, with the omnidirectional power spectrum (OPS) varying as  $k^{-5/3}$ . To see this, note that for slab (1D) fluctuations the OPS is simply  $P_{xx}^{slab} + P_{yy}^{slab}$ , which has the correct dependence, and for 2D fluctuations at a

given magnitude  $k_{\perp}$ , the OPS  $\propto k_{\perp}(P_{xx}^{2D} + P_{yy}^{2D}) = k_{\perp}^3 A$ , which varies as  $k_{\perp}^{-5/3}$  for large  $k_{\perp}$ . However, we stress that the results described in the main text do *not* require power spectra of these specific forms.

For convenience,  $B_0$ ,  $\ell_c$ ,  $k_{0\perp}$ , and  $\ell_{\perp}$  were all set to 1. Effectively, the calculations are for  $B$  in units of  $B_0$ , and  $x$  and  $z$  in units of  $\ell_{\perp}$  and  $\ell_c$ , respectively. For the slab turbulence spectrum of equation (B.1), setting  $\ell_c = 1$  implies that  $\ell_z = 1/k_{0z} = 1.339$ , and for the 2D spectrum of equation (B.2),  $\ell_{\perp} = 1$  implies an ultrascale  $\tilde{\lambda} = 0.577$ . Figure 5.4 used  $X_0 = 0.1$ . For Figure 5.4a, the slab and 2D turbulence energies were set to  $\langle b^2 \rangle^{slab} = 7.07 \times 10^{-7}$  and  $\langle b^2 \rangle^{2D} = 7.5 \times 10^{-9}$ , yielding  $D_{\perp}^{slab} = 3.54 \times 10^{-7}$  and  $D_{\perp}^{2D} = 3.54 \times 10^{-5}$ , for a random walk dominated by the 2D component. For Figures 5.4b and 5.5, the only difference was that the slab energy (i.e.,  $\langle b^2 \rangle^{slab}$ ) was set to 0.01, or  $1.41 \times 10^4$  times stronger, for  $D_{\perp}^{slab} = 5 \times 10^{-3}$ , so that slab turbulence dominates the random walk. These values were chosen for clarity, to separate the various physical régimes, and not to correspond to any specific physical situation such as the solar wind.

Using Mathematica, we first directly calculated  $\langle \Delta x^2 \rangle_{slab}$  for various values of  $\Delta z$  and then iteratively calculated  $\langle \Delta x^2 \rangle$  and  $D_{\perp}$ . Next  $D_{sx}$  and  $D_{sy}$  were calculated iteratively and simultaneously by a secant method (using “Find-Root”). Care was required to ensure precision and accuracy fine enough to yield good results, yet coarse enough to allow the integrals and iterations to converge.

จุฬาลงกรณ์มหาวิทยาลัย

# Appendix C

## Fitting the Data from the *Ulysses* Spacecraft

We focus on event 6 of *Ulysses* as shown in Figure 6.3. It was a gradual event on November 8, 2000. The figure shows a comparison between the 30-70 MeV protons observed from *Ulysses*, which was located near 90°S heliospheric latitude and a longitude opposite that of the Earth, at a radial distance of 2.35 AU (see Figure 6.2), and from *IMP-8*, which was near the Earth. The data decay with the same intensity after a few days. That means the SEPs from the gradual event diffused throughout the inner solar system within a few days. Here we try to find the perpendicular diffusion coefficient of the particles by fitting the *Ulysses* data.

Because McKibben et al. (2001) provide the information of the flare and *Ulysses* locations with respect to the Earth, we first find the footpoint of the magnetic field line that connects to the Earth. Since we assume that the interplanetary magnetic field has a Archimedean spiral shape as shown in Figure C.1, we use the relation

$$\phi_0 - \phi = \frac{\Omega R}{v_{sw}}, \quad (\text{C.1})$$

where  $\phi$  is the angle of the magnetic field line at radius  $R$ ,  $\phi_0$  is the angle of the footpoint at the Sun,  $\Omega$  the angular speed of the Sun which is  $2.92 \times 10^{-6}$  rad/s, and  $v_{sw}$  is the solar wind speed which is approximately equal to 400 km/s. The Earth is located at  $R = 1$  AU and we set  $\phi = 0^\circ$ . Using (C.1), the footpoint of the magnetic field line that connects to the Earth has  $\phi_0 = 62.45^\circ$ . Next we

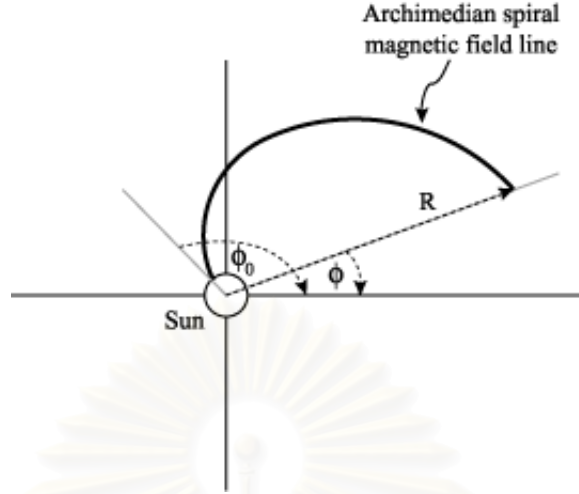


Figure C.1: The coordinates of an Archimedean spiral magnetic field line connected to the Sun.

calculate the position of *Ulysses*. From McKibben et al. (2001), we know that the difference between footpoints of the magnetic field lines that connect to *Ulysses* and to the Earth ( $\Delta\phi_{fp}$ ) is about  $98^\circ$  and *Ulysses* was located at  $R = 2.35$  AU and latitude  $-79.6^\circ$ . Therefore, the footpoint of the magnetic field line that connects to *Ulysses* is at

$$\begin{aligned}\phi_{0(\text{of } Ulysses)} &= \phi_{0(\text{of Earth})} - \Delta\phi_{fp} \\ &= -35.55^\circ \text{ or } 324.45^\circ.\end{aligned}\tag{C.2}$$

Thus the position of *Ulysses* in spherical coordinates is  $\theta = 90^\circ + 79.6^\circ = 169.6^\circ$ ,  $R = 2.35$  AU, and, from (C.1),  $\phi = 177.62^\circ$ .

We next consider the position of the magnetic field line at 2.35 AU that connects to the flare location. From McKibben et al. (2001), the flare from event 6 occurred at N10W77. Converting to spherical coordinates, the flare site is located at  $\theta = 80^\circ$  and  $\phi_0 = 77^\circ$ . We assume that the flare particles transport into space by mainly following the magnetic field line connected to the flare site.

Therefore, the location of the flare's magnetic field line at 2.35 AU is  $R = 2.35$  AU,  $\theta = 80^\circ$ , and  $\phi = 289.96^\circ$ .

Now imagine that the flux of protons that *Ulysses* detected at  $R = 2.35$  AU would diffuse from the flare in two dimensions while also following the connecting field line at flare site. Thus the model that we use to fit the data here is based on the diffusion process on the sphere at 2.35 AU including the flux loss to outside the sphere. This is similar to the concept of the Reid profile (Reid 1964). In that model,

$$f = \frac{c}{t - t_0} \exp \left[ -\frac{L^2}{4\kappa_\perp(t - t_0)} - \frac{t - t_0}{\tau} \right], \quad (\text{C.3})$$

where  $f$  is the flux of the observed particles,  $L$  is the curvilinear distance between *Ulysses* and the flare's magnetic field line at 2.35 AU,  $\kappa_\perp$  is the perpendicular diffusion coefficient of the particles,  $t_0$  is the time when the flare occurred,  $\tau$  is a time constant related to the loss of particles, and  $c$  is a normalization constant. Eq. (C.3) is the solution of the 2D diffusion equation with a loss term,

$$\frac{\partial f}{\partial t} = \kappa_\perp \nabla^2 f - \frac{f}{\tau}. \quad (\text{C.4})$$

From the known locations in spherical coordinates of the flare's magnetic field line and *Ulysses* at 2.35 AU, the angle between them is  $103.89^\circ$ . Thus the arclength between the flare and *Ulysses* ( $L$ ) is about 4.26 AU. Figure C.2 shows the function (C.3) that fits with event 6 from the *Ulysses* data. Here we use  $L = 4.26$  AU,  $c = 5$  in the units of flux  $\times$  days,  $t_0 = 313.5$  days,  $\tau = 2.7$  days, and  $\kappa = 0.5$  AU<sup>2</sup>/day or  $1.30 \times 10^{17}$  m<sup>2</sup>/s.

We now know the approximate diffusion coefficient of the particles. From the field line random walk, the relationship between the perpendicular diffusion coefficient of particle and magnetic field line is

$$\kappa_\perp = \frac{v}{2} D_\perp, \quad (\text{C.5})$$

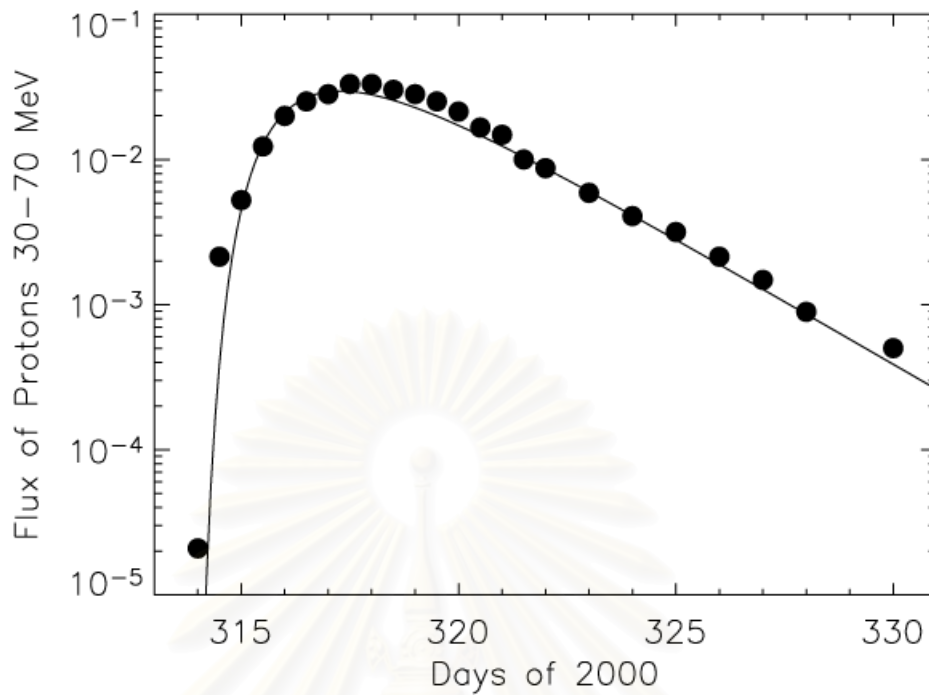


Figure C.2: The dots shows the data from *Ulysses* on November 8-26, 2000 and the line is the function from the Reid profile that can best fit the data.

where  $v$  is the particle speed. We are considering the protons at 30-70 MeV which correspond to particle speeds of  $\sim 9 \times 10^7$  m/s. Therefore, the estimated diffusion coefficient of the field line is  $2.9 \times 10^9$  m or 0.02 AU.

สถาบันวิทยบริการ  
จุฬาลงกรณ์มหาวิทยาลัย



# Appendix D

## Trajectories of Magnetic Field Lines in a Gaussian 2D Field

Here we consider the trajectories of a magnetic field line in a mean field plus pure 2D field where the potential function of the 2D field is a Gaussian function. We can write the total magnetic field as

$$\vec{B}(x, y) = B_0 \hat{z} + \vec{b}^{2D}(x, y). \quad (\text{D.1})$$

In general, we can write  $\vec{b} = a(x, y) \hat{z}$ . For this case,

$$a(x, y) = A_0 \exp\left(-\frac{x^2 + y^2}{2\sigma^2}\right), \quad (\text{D.2})$$

or

$$a(r) = A_0 \exp\left(-\frac{r^2}{2\sigma^2}\right), \quad (\text{D.3})$$

where  $A_0$  is the value of  $a(x, y)$  at the center of the Gaussian and  $\sigma$  is the width of the Gaussian.

To find  $\vec{b}^{2D}$ , we use the relation  $\vec{B} = \vec{\nabla} \times \vec{A}$ , where  $\vec{A}$  is the vector potential. Since  $a(x, y)$  is in the  $z$  direction and can be written as a function of radius, it is convenient to calculate  $\vec{b}^{2D}$  in cylindrical coordinates  $(r, \theta, z)$ . For cylindrical coordinates, each component of  $\vec{B} = \vec{\nabla} \times \vec{A}$  can be determined from

$$B_r = (\vec{\nabla} \times \vec{A})_r = \frac{1}{r} \frac{\partial A_z}{\partial \theta} - \frac{\partial A_\theta}{\partial z} \quad (\text{D.4})$$

$$B_\theta = (\vec{\nabla} \times \vec{A})_\theta = \frac{\partial A_r}{\partial z} - \frac{\partial A_z}{\partial r} \quad (\text{D.5})$$

$$B_z = (\vec{\nabla} \times \vec{A})_z = \frac{1}{r} \frac{\partial(rA_\theta)}{\partial r} - \frac{1}{r} \frac{\partial A_r}{\partial \theta}. \quad (\text{D.6})$$

Therefore, from (D.4)-(D.6) we get

$$b_r^{2D} = 0 \quad (\text{D.7})$$

$$b_\theta^{2D} = -\frac{da(r)}{dr} = \frac{ra(r)}{\sigma^2}. \quad (\text{D.8})$$

The total magnetic field becomes

$$\vec{B} = B_0 \hat{z} + \frac{ra(r)}{\sigma^2} \hat{\theta}. \quad (\text{D.9})$$

The equation of field line in cylindrical coordinates can be written in the form

$$\frac{dr}{B_r} = \frac{rd\theta}{B_\theta} = \frac{dz}{B_z}. \quad (\text{D.10})$$

From (D.10), we obtain the differential equations of field lines as

$$\frac{dr}{dz} = \frac{B_r}{B_z} = 0 \quad (\text{D.11})$$

$$\frac{d\theta}{dz} = \frac{B_\theta}{rB_z} = \frac{a(r)}{B_0\sigma^2}. \quad (\text{D.12})$$

Now we can see that the trajectories of field lines must keep the radial coordinate constant and have a constant angular velocity ( $\Omega^{2D} \equiv d\theta/dz$ ). Thus, for a given initial point  $(r_0, \theta_0, z_0)$ , the trajectory of the field line is

$$r = r_0 \quad (\text{D.13})$$

$$\theta = \Omega^{2D}(z - z_0) + \theta_0, \quad (\text{D.14})$$

where  $\Omega^{2D} = a(r_0)/(B_0\sigma^2)$ . Note that  $r$  is measured from the center of the Gaussian function.

# Vitae

**Name:** Miss Piyanate Chuychai

**Born:** January 15<sup>th</sup>, 1979 in Bangkok, Thailand

**Address:** 7 Soi Watchirathamsatit 13, Bangjak, Prakanong, Bangkok, Thailand

## Education:

**1998** Bachelor's Degree of Science in Physics (2nd class honors)  
Chulalongkorn University, Bangkok, Thailand

## Scholarship:

**2003-2004** Received a grant from the Thailand Research Fund to build a 9-node cluster for the "Motion of Turbulent Magnetic Field Lines in Space" project.

**1999-2004** Received a Royal Golden Jubilee Fellowship from the Thailand Research Fund.

**1996-1998** Received a scholarship from Chulalongkorn University.

## International Publications:

**2004** Ruffolo, D., Matthaeus, W. H., and Chuychai, P., "Separation of Magnetic Field Lines in Two-Component Turbulence," *Astrophys. J.*, 614, 420

**2003** Ruffolo, D., Matthaeus, W. H., and Chuychai, P., "Trapping of Solar Energetic Particles by Small-Scale Topology of Solar Wind Turbulence," *Astrophys. J. Lett.*, 597, L169